

# UNCLASSIFIED

AD NUMBER
AD827596
NEW LIMITATION CHANGE
TO Approved for public release, distribution unlimited
FROM Distribution authorized to U.S. Gov't. agencies and their contractors; Administrative/Operational Use; JAN 1968. Other requests shall be referred to Air Force Weapons Laboratory, Kirtland AFB, NM.
AUTHORITY
AFWL ltr dtd 1 Mar 1972

THIS PAGE IS UNCLASSIFIED

LOAN

AFWL

TR

67-91

C.5

AD-827 596



# ULTRASONIC AND THERMAL STUDIES OF SELECTED PLASTICS, LAMINATED MATERIALS, AND METALS

Lt James R. Asay

Dr. S. R. Urzendowski

Dr. Arthur H. Guenther

LIBRARY  
DO NOT REMOVE FROM LIBRARY

TECHNICAL REPORT NO. AFWL-TR-67-91

January 1968

AIR FORCE WEAPONS LABORATORY

Air Force Systems Command

Kirtland Air Force Base

New Mexico

APPROVED FOR PUBLIC RELEASE,  
DISTRIBUTION UNLIMITED.



16 Feb 1968  
2000  
2000  
2000

AIR FORCE WEAPONS LABORATORY  
Air Force Systems Command  
Kirtland Air Force Base  
New Mexico

When U. S. Government drawings, specifications, or other data are used for any purpose other than a definitely related Government procurement operation, the Government thereby incurs no responsibility nor any obligation whatsoever, and the fact that the Government may have formulated, furnished, or in any way supplied the said drawings, specifications, or other data, is not to be regarded by implication or otherwise, as in any manner licensing the holder or any other person or corporation, or conveying any rights or permission to manufacture, use, or sell any patented invention that may in any way be related thereto.

This report is made available for study with the understanding that proprietary interests in and relating thereto will not be impaired. In case of apparent conflict or any other questions between the Government's rights and those of others, notify the Judge Advocate, Air Force Systems Command, Andrews Air Force Base, Washington, D. C. 20331.

DO NOT RETURN THIS COPY. RETAIN OR DESTROY.

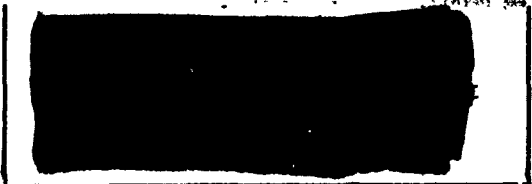
**2153**

ULTRASONIC AND THERMAL STUDIES OF SELECTED  
PLASTICS, LAMINATED MATERIALS, AND METALS

Lt James R. Asay  
Dr. S. R. Urzendowski  
Dr. Arthur H. Guenther

TECHNICAL REPORT NO. AFWL-TR-67-91

APPROVED FOR PUBLIC RELEASE,  
DISTRIBUTION UNLIMITED.





FOREWORD

This research was performed under Program Element 6.16.46.01.D, Project 5710, Subtask 15.018, and was funded by the Defense Atomic Support Agency (DASA). The research was performed in-house, partially under Contract F29(601)-67-C-0042 with the University of Albuquerque. Inclusive dates of research were September 1965 to June 1967. The report was submitted 11 October 1967 by the AFWL Project Officer, Lt James R. Asay (WLRE).

This document is intended for technical personnel who are familiar with the mechanical and thermal properties of solids.

This research is the result of a continuing program to obtain hydrodynamic and equation of state parameters by means of ultrasonic and thermal techniques. In obtaining the data reported herein, the authors wish to express gratitude to the following: James W. Page and Mark F. Middleton for performing many of the measurements, Miss Leonie D. Boehmer for computational assistance, Mr. W. E. Kunzler for metrological support, and to the many others at the Air Force Weapons Laboratory who have supported this research program.

This technical report has been reviewed and is approved.

*James R. Asay*

JAMES R. ASAY  
1Lt, USAF  
Project Officer

*William N. Jackomis*

WILLIAM N. JACKOMIS  
Major, USAF  
Chief, Effects Branch

*Claude K. Stambaugh*

CLAUDE K. STAMBAUGH  
Colonel, USAF  
Chief, Research Division



## ABSTRACT

(Distribution Limitation Statement No. 2)

Ultrasonic and thermal investigations of several common plastics, nose cone materials, and alloys are presented. The ultrasonic data consist of measurements of the acoustic shear and longitudinal velocities in the frequency range of 1 to 10 MHz and as a function of temperature (to  $\sim 125^{\circ}\text{C}$  for most of the plastics and to  $\sim 250^{\circ}\text{C}$  for most of the alloys). Some information is presented regarding the dependence of acoustic velocities on uniaxial stress in two aluminum alloys. The temperature dependent ultrasonic data are used to calculate the temperature dependence of the elastic moduli for the materials studied.

The thermal analyses describe a differential thermal technique (DTA) used to study the phase transitions and chemical transformations of the reported materials. This approach was used to measure the linear coefficient of expansion and the specific heat at constant pressure over a temperature range of  $\sim -100$  to  $200^{\circ}\text{C}$  for the expansion characteristics, and  $\sim -100$  to  $700^{\circ}\text{C}$  for the specific heat measurements. In addition, heats of fusion are reported. In some cases, the thermal behavior of the reported materials is listed to approximately  $1200^{\circ}\text{C}$ . The thermal and ultrasonic data are combined to calculate the Grüneisen ratio as a function of temperature.

The application of ultrasonic and thermal investigations to the determination of the equation of state of solids is also presented. The present study shows that such applications are of significant importance to high pressure equation-of-state determinations. The study also illustrates that many more applications to the equation of state can be obtained through ultrasonic and thermal measurements as a function of hydrostatic pressure.

This page intentionally left blank.

## CONTENTS

<u>Section</u>		<u>Page</u>
I	INTRODUCTION	1
II	ULTRASONIC VELOCITY STUDIES	3
	Experimental Method	3
	Shear Velocity Techniques	3
	Pulse-Echo Technique	4
	Immersion Technique	5
	Uniaxial Stress Technique	9
	Experimental Results	13
	Longitudinal and Shear Velocities in Common Plastics	13
	Longitudinal and Shear Velocities in Nose Cone Materials	27
	Longitudinal and Shear Velocities in Metals and Alloys	39
III	THERMAL ANALYSES	63
	Experimental Method	63
	Differential Thermal Analysis Techniques	63
	Thermal Expansion Techniques	68
	Specific Heat Techniques	70
	Discussion	71
	First-Order Transitions	72
	Second-Order Transitions	75
	Thermal Expansion	77
	Experimental Results	80
	Thermal Properties of Common Plastics	80
	Thermal Properties of Polymers and Laminated Materials	101
	Thermal Properties of Refractories, Metals, and Alloys	138
IV	APPLICATIONS	155
	The Theoretical and Experimental Determination of Grüneisen Ratios from Ultrasonic and Thermal Relations	155
	Determinations of the High Pressure Equation of State From Ultrasonic Techniques	163
	Determination of the Shock Velocity and Particle Velocity Versus Pressure by the Ultrasonic Technique	173

## CONTENTS (cont'd)

<u>Section</u>		<u>Page</u>
IV	APPLICATIONS (cont'd)	
	Additional Thermodynamic Applications to the Equation of State	187
V	CONCLUSIONS AND RECOMMENDATIONS	193
<u>Appendixes</u>		
I	THE RELATIONSHIP BETWEEN THE BULK MODULUS AND THE ACOUSTIC VELOCITIES FOR TRANSVERSE ISOTROPIC MEDIA	195
II	DERIVATION OF THE MURNAGHAN EQUATION	204
III	ESTIMATION OF THE PRESSURE DERIVATIVE OF THE GRÜNEISEN RATIO	209
IV	THE USE OF THE MURNAGHAN EQUATION IN ESTIMATING THE SHOCK AND PARTICLE VELOCITIES AT HIGH PRESSURE	214
V	DERIVATION OF THE NONLINEAR RELATION BETWEEN SHOCK VELOCITY AND PARTICLE VELOCITY	216
VI	THEORETICAL EQUATIONS OF DIFFERENTIAL THERMAL ANALYSIS	222
VII	THERMAL CALCULATIONS AND THERMODYNAMIC APPLICATIONS	225
VIII	DEFINITIONS AND APPLICATIONS OF THERMAL EXPANSIVITY MEASUREMENTS	232
	REFERENCES	239
	DISTRIBUTION	246

## ILLUSTRATIONS

<u>Figure</u>		<u>Page</u>
1	Schematic Diagram of the Immersion Technique	6
2	Details of the Immersion Technique. (The transducers used here are lead zirconate titanate (PZT-5) which are plated with a chrome-gold vacuum deposit. The active center of the transducers is approximately 5/8 inch.)	6
3	Calibration Curve for the Immersion Method at 22°C	9
4	Schematic Diagram of Circuitry Used for Determining Small Changes in Transit Time Occurring in the Uniaxial Technique	10
5	Experimental Arrangement in the Uniaxial Stress Technique	12
6	Longitudinal Velocity Versus Temperature in Delrin Acetal	15
7	Shear Velocity Versus Temperature in Delrin Acetal	16
8	Shear Velocity Versus Temperature in Poly Penco Nylon	18
9	Shear Velocity Versus Temperature in TFE Teflon	20
10	Shear Velocity Versus Temperature in Type G Plexiglas	20
11	Shear Velocity Versus Temperature in High Density Polyethylene (density, 0.967 g/cc)	22
12	Shear Velocity Versus Temperature in Low Density Polyethylene (0.922 g/cc)	23
13	Longitudinal Velocity Versus Temperature in Lexan	25
14	Shear Velocity Versus Temperature in Lexan	26
15	Coordinate System Used for Materials Exhibiting Transverse Isotropy	30
16	Longitudinal Velocity Versus Lamination Angle in Carbon Phenolic (The experimental data are from Reference 4. The solid line is the theoretical prediction of Equation (8).)	34
17	Temperature Dependence of the Shear Velocity in Carbon Phenolic	35
18	Longitudinal Velocity Versus Lamination Angle in General Electric Fiberglas (The solid curve is the theoretical prediction of Equation (8).)	37
19	Temperature Dependence of the Shear Velocity in General Electric Fiberglas	39
20	Temperature Dependence of the Longitudinal and Shear Velocities in Avcoat II	40
21	The Variation of the Longitudinal Velocity in Magnesium-Thorium Alloy to 350°C	41
22	The Variation of the Shear Velocity in Magnesium-Thorium Alloy to 225°C	41

## ILLUSTRATIONS (cont'd)

<u>Figure</u>		<u>Page</u>
23	The Temperature Variation of the Shear Modulus, G, and the Adiabatic Poisson's Ratio in Magnesium-Thorium Alloy	44
24	The Temperature Variation of the Adiabatic Young's Modulus and the Adiabatic Bulk Modulus in Magnesium-Thorium Alloy	44
25	Temperature Dependence of the Longitudinal and Shear Velocities in Gold	46
26	The Longitudinal Velocity Versus Temperature in Lead	48
27	The Relative Change in Transit Time Versus Uniaxial Stress for the Two Shear Modes in 6061-T6 Aluminum at 25°C (See the text for the notation used here.)	49
28	Relative Change in Transit Time Versus Uniaxial Stress for the Longitudinal Mode in 6061-T6 Aluminum	51
29	Temperature Dependence of the Longitudinal and Shear Velocities in 6061-T6 Aluminum	53
30	Relative Change in Transit Time Versus Uniaxial Stress for All Three Velocity Modes in 1060 Aluminum at 25°C	54
31	Yielding Behavior in 1060 Aluminum at 25°C	57
32	Temperature Dependence of the Longitudinal and Shear Velocities in 1060 Aluminum	58
33	Schematic Diagram of the Differential Thermal Analyzer	64
34	The Cell Used for High Temperature Studies	66
35	Definition of Terms Used in Thermogram Characterization	67
36	Schematic Diagram of the Thermomechanical Analyzer Used for Expansivity Measurements	69
37	Differential Thermogram of High Density Polyethylene	81
38	Expansivity Versus Temperature for High and Low Density Polyethylene	81
39	Heat Capacity Versus Temperature for High Density Polyethylene	85
40	Differential Thermogram of Low Density Polyethylene	85
41	Differential Thermogram of the Polyamide, Nylon 6	88
42	Expansivity Versus Temperature for Nylon 6, Teflon, and Plexiglas	88
43	Differential Thermogram of Polytetrafluoroethylene (Teflon)	94
44	Differential Thermogram of Polymethylmethacrylate (Plexiglas)	94
45	Differential Thermogram of Delrin Acetal (DA 500)	98
46	Similarities Between the Heat Capacity and Thermal Expansion Profiles of Delrin Acetal	98
47	Differential Thermogram of Polyethylene Terephthalate (Mylar)	102
48	Differential Thermogram of Avcoat 1	102

## ILLUSTRATIONS (cont'd)

<u>Figure</u>		<u>Page</u>
49	Linear Coefficient of Expansion Versus Temperature for Avcoat 1 and Avcoat 19	106
50	Differential Thermogram of Avcoat 19	106
51	Differential Thermogram of Castable 124	109
52	Expansivity Versus Temperature Profiles of Two Epoxides (Castable 124 and Foam #20)	109
53	Differential Thermogram of Foam #20	112
54	Differential Thermogram of Avco Phenolic Fiberglas	114
55	Linear Coefficient of Expansion Profiles for Avco Phenolic Fiberglas, G.E. Phenolic Fiberglas, and Oblique Tapewound Refrasil ( $\alpha_{  }$ , parallel to axis.)	117
56	Linear Coefficient of Expansion Profiles for Avco Phenolic Fiberglas, G.E. Phenolic Fiberglas, and Oblique Tapewound Refrasil ( $\alpha_{\perp}$ , perpendicular to axis.)	117
57	Differential Thermogram of G.E. Phenolic Fiberglas	122
58	Differential Thermogram of Oblique Tapewound Refrasil	122
59	Differential Thermogram of Carbon Phenolic	126
60	Linear Coefficient of Expansion Versus Temperature for Carbon Phenolic (Parallel and Perpendicular to the Axis)	126
61	Differential Thermogram of Chopped Nylon Phenolic	128
62	Expansivity Versus Temperature Curves for Chopped Nylon Phenolic (CNP) and Tapewound Nylon Phenolic (TWNP) (Parallel to the Axis)	129
63	Expansivity Versus Temperature Curves for Chopped Nylon Phenolic (CNP) and Tapewound Nylon Phenolic (TWNP) (Perpendicular to the Axis)	129
64	Differential Thermogram of Tapewound Nylon Phenolic	132
65	Differential Thermogram for Rad 60	135
66	Linear Coefficient of Expansion Profiles for Rad 60 (Parallel and Perpendicular to the Axis)	135
67	Differential Thermogram of Pyrolytic Graphite	139
68	Linear Coefficient of Expansion Profiles for Pyrolytic Graphite, Quartz, and Fused Silica (Parallel to Axis)	139
69	Heat Capacity Versus Temperature for Pyrolytic Graphite and Quartz	144
70	Differential Thermogram of Fused Silica	144
71	Expansivity Versus Temperature Curves for 6061-T6 Aluminum, 1060 Aluminum, and HM-21A Magnesium-Thorium Alloys	151
72	Grüneisen Ratio, $\gamma$ , as a Function of Temperature for 1060 Aluminum, 6061-T6 Aluminum, HM-21A Magnesium-Thorium, and Gold	151



## ILLUSTRATIONS (cont'd)

<u>Figure</u>		<u>Page</u>
73	Grüneisen Ratios Versus Temperature for Various Materials	161
74	Relative Volume Versus Pressure for 6061-T6 Aluminum (Density, 2.704 g/cc) at 25°C	168
75	Relative Volume Versus Pressure for 1060 Aluminum (Density, 2.703 g/cc) at 25°C	168
76	Relative Volume Versus Pressure for Teflon (Density, 2.19 g/cc)	172
77	Relative Volume Versus Pressure for Polystyrene (Density, 1.07 g/cc) (The ultrasonic work of Hughes and Kelly (Ref. 33) was used to calculate the pressure dependence of the bulk modulus.)	172
78	Shock Velocity Versus Pressure in Cadmium	176
79	Shock Velocity Versus Pressure in Potassium	177
80	Shock Velocity Versus Pressure in Sodium	178
81	Shock Velocity Versus Pressure in Sodium Chloride	179
82	Shock Velocity Versus Pressure in Aluminum Oxide	180
83	Shock Velocity Versus Pressure in Magnesium	181
84	Shock Velocity Versus Pressure in Magnesium Oxide	182
85	Shock Velocity Versus Pressure in Polystyrene	183
86	Shock Velocity Versus Pressure in Iron	184
87	Shock Velocity Versus Pressure in Aluminum	185
88	Particle Velocity Versus Pressure in Aluminum	186
89	Differential Temperature Versus Time Curve Illustrating Reaction Rates	224

## TABLES

<u>Table</u>		<u>Page</u>
1	Shear Velocities in Common Plastics Versus Temperature	28
2	Longitudinal Velocities in Common Plastics Versus Temperature	28
3	The Expansion Coefficients of the Bulk Modulus Versus Temperature in Common Plastics	29
4	The Expansion Coefficients of the Bulk Modulus Versus Temperature in Carbon Phenolic, GE Fiberglass, and Avcoat II	36
5	Elastic Properties of 6061-T6 Aluminum	52
6	Elastic Properties of 1060 Aluminum	56
7	Second- and Third-Order Elastic Coefficients for an Isotropic Medium Under Hydrostatic and Uniaxial Pressure	59
8	Third-Order Elastic Constants of 6061 Aluminum	61
9	The Expansion Coefficients of the Bulk Modulus Versus Temperature in Four Metals	62
10	Fusion and Decomposition Peak Temperatures for the Polymers Studied	74
11	Glass Transition ( $T_g$ ) and Additional Secondary Transition Temperatures of Polymers Studied	78
12	Linear Thermal Expansion Data for High-Density Polyethylene	82
13	Heat Capacity Data for High-Density Polyethylene	82
14	Heat Capacity Data for Low-Density Polyethylene	84
15	Linear Thermal Expansion Data for Low-Density Polyethylene	86
16	Heat Capacity Data for Nylon 6	90
17	Linear Thermal Expansion Data for Nylon 6	90
18	Linear Thermal Expansion Data for Teflon	92
19	Heat Capacity Data for Teflon	93
20	Linear Thermal Expansion Data for Plexiglas	91
21	Heat Capacity Data for Plexiglas	97
22	Linear Thermal Expansion Data for Delrin Acetal	99
23	Linear Thermal Expansion Data for Avcoat 1	103
24	Heat Capacity Data for Avcoat 1	104
25	Linear Thermal Expansion Data for Avcoat 19	107
26	Heat Capacity Data for Avcoat 19	108
27	Linear Thermal Expansion Data for Castable 124	110

## TABLES (cont'd)

<u>Table</u>		<u>Page</u>
28	Heat Capacity Data for Castable 124	111
29	Linear Thermal Expansion Data for Foam #20	113
30	Heat Capacity Data for Foam #20	114
31	Linear Thermal Expansion Data for Avco Phenolic Fiberglas	116
32	Heat Capacity Data for Avco Phenolic Fiberglas	118
33	Linear Thermal Expansion Data for G.E. Phenolic Fiberglas	120
34	Heat Capacity Data for G.E. Phenolic Fiberglas	121
35	Heat Capacity Data for Oblique Tapewound Refrasil	121
36	Linear Thermal Expansion Data for Oblique Tapewound Refrasil	123
37	Linear Thermal Expansion Data for Carbon Phenolic	125
38	Heat Capacity Data for Carbon Phenolic	127
39	Linear Thermal Expansion Data for Chopped Nylon Phenolic	130
40	Heat Capacity Data for Chopped Nylon Phenolic	131
41	Linear Thermal Expansion Data for Tapewound Nylon Phenolic	133
42	Heat Capacity Data for Tapewound Nylon Phenolic	136
43	Linear Thermal Expansion Data for Rad 60	137
44	Heat Capacity Data for Rad 60	138
45	Heat Capacity Data for Pyrolytic Graphite	140
46	Linear Thermal Expansion Data for Pyrolytic Graphite (Parallel to Axis)	141
47	Linear Thermal Expansion Data for Quartz (Parallel to Axis)	143
48	Heat Capacity Data for Quartz	145
49	Linear Thermal Expansion Data for Fused Silica	145
50	Chemical Composition of Metals and Alloys Studied	146
51	Heat Capacity Data for 1060 Aluminum, 6061-T6 Aluminum, HM-21-A Magnesium Thorium, Lead, and Gold	148
52	Linear Polynomial Equations Describing the Expansivity Data of Various Metals and Alloys	149
53	Elongation Versus Temperature for Several Metals and Alloys	149
54	Complete Tabulation of Data Used to Calculate the Grüneisen Ratio in Several Metals and Alloys	152
55	Heat Capacity at Constant Volume for the Metals Studied	154
56	Grüneisen Ratio Versus Temperature for Various Materials	160
57	The Relationship Between the Grüneisen Ratio and the Pressure Derivative of the Bulk Modulus in Aluminum	167
58	Estimation of the Second Derivative of the Adiabatic Bulk Modulus for Several Materials	221

## ABBREVIATIONS AND SYMBOLS

$V_l$	Longitudinal velocity
$V_t$	Shear velocity
$U_s(P)$	Shock velocity at pressure $P$ ; $U_s(0) = c_0$
$U_p(P)$	Particle velocity at pressure $P$
$P$	Pressure
$T$	Temperature
$v$	Specific volume
$\rho$	Density ( $\rho_0$ represents the density at atmospheric pressure or $0^\circ\text{C}$ ; this will be defined in the equation)
$S$	Entropy
$U$	Internal energy
$\epsilon_{ij}$	Components of strain
$\sigma_{ij}$	Components of stress
$c_{ij}$	Second order elastic stiffness constants which are the coefficients of the strains in the linearized form of Hooke's law. In matrix form $\sigma_{ij} = c_{ij} \epsilon_{ij}$
$\nu_i$	Third order elastic stiffness coefficients for isotropic media ( $i = 1, 2, 3$ ). Defined as the isothermal strain derivatives of the adiabatic second order elastic stiffness coefficients, $c_{ij}$
$\mu$	Lame' constant which, for isotropic media, is identical with the shear modulus, $G$
$\lambda$	Lame' constant for isotropic media
$B^S$	Adiabatic bulk modulus for arbitrary pressure and temperature [defined as $-v \left( \frac{\partial P}{\partial v} \right)_S$ ]
$B^T$	Isothermal bulk modulus for arbitrary pressure and temperature [defined as $-v \left( \frac{\partial P}{\partial v} \right)_T$ ]
$B^S_0$	Adiabatic bulk modulus at atmospheric pressure and arbitrary temperature

## ABBREVIATIONS AND SYMBOLS (cont'd)

$\chi$	Compressibility ( $= \frac{1}{B}$ ). Superscript s or T refers to the value at constant entropy or temperature, respectively
E	Young's modulus (superscript s or T implies the adiabatic or isothermal value, respectively)
G	Shear modulus ( $G^s = G^T$ )
$\sigma$	Poisson's ratio
$B_{OT}^{s'}$	Pressure derivative of the adiabatic bulk modulus at constant temperature, evaluated at atmospheric pressure $\left[ = \left( \frac{\partial B^s}{\partial P} \right)_{P=0, T} \right]$  In all of the following quantities, the first entry of the double subscript refers to the parametric value of pressure and the second refers to the value of temperature. A subscript P or T represents constant pressure or temperature, respectively.
$B_{OS}^{s'}$	Pressure derivative of the adiabatic bulk modulus at constant entropy, evaluated at atmospheric pressure $\left[ = \left( \frac{\partial B^s}{\partial P} \right)_{P=0, s} \right]$ . See equation 52 for relation between $B_{OT}^{s'}$ and $B_{OS}^{s'}$ .
$B_{OT}^{s''}$	Second derivative of the adiabatic bulk modulus with respect to pressure at constant temperature, evaluated at atmospheric pressure $\left[ = \left( \frac{\partial^2 B^s}{\partial P^2} \right)_{P=0, T} \right]$ . See equation 168 for the relationship to $B_{OT}^{s'}$
$\left( \frac{\partial B^s}{\partial T} \right)_P$	Temperature derivative of the adiabatic bulk modulus at constant pressure. The temperature derivative of the isothermal modulus is obtained by replacing s with T.
$\alpha$	Linear coefficient of expansion, defined as $\alpha = \frac{1}{l} \left( \frac{\partial l}{\partial T} \right)$ where l is the specimen length
$\beta$	Volume coefficient of expansion defined as $\beta = \frac{1}{v} \left( \frac{\partial v}{\partial T} \right)$ For isotropy $\beta = 3\alpha$
$\left( \frac{\partial \beta}{\partial T} \right)_P$	Temperature derivative of the expansion coefficient at constant pressure
$\left( \frac{\partial \beta}{\partial P} \right)_T$	Pressure derivative of the expansion coefficient at constant temperature
$c_p$	Specific heat at constant pressure. $\left( \frac{\partial c_p}{\partial T} \right)_P$ is the temperature derivative at constant pressure and $\left( \frac{\partial c_p}{\partial P} \right)_T$ is the pressure derivative at constant temperature.

## ABBREVIATIONS AND SYMBOLS (cont'd)

$c_v$	Specific heat at constant volume
$\gamma$	Grüneisen ratio, defined thermodynamically as $\gamma = v \left( \frac{\partial P}{\partial U} \right)_v$ , which reduces to $\gamma = \frac{\beta B^S}{\rho c_p}$
$\left( \frac{\partial \gamma}{\partial P} \right)_T$	Pressure derivative of the Grüneisen ratio at constant temperature
$\left( \frac{\partial \gamma}{\partial T} \right)_P$	Temperature derivative of the Grüneisen ratio at constant pressure
$F_G$	Gibbs free energy
$F_H$	Helmholtz free energy
$H$	Enthalpy or heat content
$\theta_D$	Debye temperature
$\omega$	Atomic vibrational frequency

This page intentionally left blank.

## SECTION I

## INTRODUCTION

Within the last few years, considerable interest has been evidenced regarding the equation of state of materials subjected to extreme pressure and temperature conditions. These conditions occur, for example, when engineering materials are exposed to the environment resulting from a nuclear weapon detonation, and lead to the requirement that the physical properties of such materials be precisely known. A knowledge of physical properties then allows a prediction of how a composite system of various materials will react to a nuclear environment, and, thus, is a mandatory prerequisite in nose cone vulnerability programs.

In the resulting prediction program, a knowledge of various mechanical properties (such as the bulk modulus and sound velocities), and of thermal properties (such as the specific heat and linear expansion coefficient) allows the determination of some parameters which are necessary in computer calculations. Of primary importance among these is the Grüneisen ratio, which relates a change in internal energy to a corresponding pressure change. It has previously been shown (Ref. 4) that this ratio can be accurately determined through a knowledge of the longitudinal and shear acoustic velocities in combination with the thermal expansion and specific heat of a specimen.

The temperature dependence of the Grüneisen ratio is likewise necessary in determining the applicability of components in operational reentry systems. Although the temperature dependence of this ratio can be easily determined through the temperature dependence of thermo-mechanical properties, this information is generally not available for most of the polymeric materials and reinforced plastics. In view of this lack of information, this report supplies detailed thermodynamic data on a wide variety of polymers, and some metals, which are necessary for defining the thermal limits of these materials with respect to their applicability as components in reentry systems.

The thermal analyses reported here were obtained with a differential thermal analysis technique (DTA), in which the temperature of a specimen is continuously compared with that of a reference. This approach allows the determination of the temperature dependence of the specific heat capacity and thermal coefficient of



expansion, in addition to a detailed description of such thermal properties as crystallization, fusion, glass transitions, and decomposition temperatures. Techniques are presented in the text regarding the application of the reported thermal data in estimating the pressure and temperature dependence of the Grüneisen ratio and other shock wave parameters, such as the slope of shock velocity-particle velocity curves. Information is also presented regarding endothermal and exothermal changes in polymers, post-curing of thermosetting resins, polymerization of monomers, and oxidative decompositions.

Ultrasonic data are reported for a wide variety of polymers and a few alloys. The reported data include temperature determinations of the shear and longitudinal velocities (for acoustic frequencies in the low megacycle range) in isotropic and anisotropic materials, and the relations between the propagation velocities and the elastic moduli for materials of arbitrary symmetry. A uniaxial stress technique is illustrated, which when used in conjunction with the ultrasonic approach can yield the third-order elastic stiffness coefficients in solids (Ref. 3). The third-order elastic constants of 6061-T6 aluminum were obtained with this technique and are presented in the text. In addition, a detailed section is presented which illustrates how the ultrasonic technique can be employed to determine the pressure derivatives of the acoustic velocities under hydrostatic compression. This technique originated with the early compressibility measurements on solids by P. W. Bridgman (Ref. 1), and extended by D. Lazarus (Ref. 2) who employed an ultrasonic method to measure the pressure dependence of the acoustic velocities in several metals. However, the text extends the approach by illustrating how the ultrasonic results obtained at low pressures (about 10 kbars) can be extrapolated in some cases to estimate the extremely high pressure equation of state of solids (500 to 1000 kbars).

Section II reports the temperature dependence of the acoustic velocities for several materials and the resulting determinations of the bulk moduli in these materials. Section III is concerned with the thermal description of the same materials, and Section IV is devoted to the application of thermal and ultrasonic data to the determination of the high pressure equation of state of solids. These applications include (1) estimations of the volume pressure relationships, (2) estimations of shock and particle velocities versus pressure, and (3) estimations of the temperature and pressure dependence of the Grüneisen ratio for materials of arbitrary symmetry.

## SECTION II

## ULTRASONIC VELOCITY TECHNIQUE

1. Experimental Method

## a. Shear Velocity Techniques

The techniques for determining the acoustic velocity in the materials investigated in the present study has been described in detail in a previous report (Ref. 4). Basically, the techniques consist of measuring the transit time of pulsed acoustic waves through various thicknesses of solid materials. This method, as illustrated in Reference 4, was used to determine the longitudinal velocity versus temperature in several plastics and nose-cone materials. As shown in that report and Section IV of this report, it is also necessary to know the temperature dependence of the shear velocity to calculate many of the parameters necessary in equation of state studies. This section includes the measurements of shear velocities for most of the materials studied in Reference 4.

Shear velocities are determined with essentially the same technique as that used for measuring longitudinal velocities. With the shear measurements, however, AC-cut quartz transducers were used to excite transverse vibrations within the specimen. The transducers were bonded to the samples with several types of viscous bonding techniques. The various bonding agents found most effective in the present study for shear wave transmission are the following:

Sodium Silicate (water glass)--effective bond from room temperature to approximately 200°C. Most effective for metals and glasses.

Eastman 910 Adhesive--good bond from room temperature to at least 200°C. The transducer can be removed from the specimen by heating to approximately 300°C for a few minutes.

Phenyl Salicylate--thin bonds possible at room temperature. Melts at 42°C.

Dow Chemical Resin 276-V9--thin bonds obtainable by bonding the transducer under moderate pressure at 60°C. Shear rigidity is good to approximately 60°C.

For most of the measurements reported here the shear velocity was obtained for frequencies of interest at 1 and 3 MHz. The velocity was measured by observing the unrectified transmitted pulses for sample thickness ranging from  $\sim 1$  to 10mm (Ref. 4).

#### b. Pulse-Echo Technique

For most of the longitudinal velocity analyses reported here the techniques used in Reference 4 were employed. However, two additional methods were found more appropriate for certain applications. One of these is the pulse-echo technique which is particularly useful in increasing the accuracy of velocity measurements for low loss materials, such as some of the metals and alloys reported in this report. This method can likewise be used for shear velocity measurements, and consists of applying a pulsed signal to a single longitudinal or shear transducer located on the specimen surface, and observing the reflected echoes from the specimen free surfaces with the transmitting transducer. The net transit time for any one echo is then obtained by the conventional method of extrapolating between time marks to a reference cycle in the echo pulse. The advantage of this technique is that bonding effects between the transducer and specimen are minimal so that a high degree of accuracy can be obtained without applying any correction for circuit delays or delays in the acoustic bonding. The main disadvantage is that the method is usually suitable only for low loss materials, so that a sufficient number of well separated pulses can be observed. Also, since the leading edges of the reflected acoustic signals become somewhat distorted and reduced in amplitude upon reflections from the rear surface of the specimen, it is sometimes difficult to identify the correct reference peak in the echo with this technique.

Another consideration appropriate to the echo technique is that sample surfaces must be extremely flat and parallel, and that a sufficiently high frequency must be used to reduce diffraction effects. When a sound wave propagates into a semi-infinite medium the plane wave region is essentially limited to a distance given by (Ref. 5)

$$d = \frac{R^2}{2\lambda} \quad (1)$$

where  $R$  is the radius of the transducer and  $\lambda$  is the wavelength of sound in the medium. Beyond this region the wave diverges at an angle  $\alpha$  determined by

$$\sin \alpha = \frac{1.22\lambda}{2R} \quad (2)$$

These effects generally limit the frequency for our studies to a minimum of about 6 MHz with the pulse-echo method. In metals a frequency of 6 MHz poses no serious problems because the attenuation is still small in this region. However, in plastics the attenuation is sufficiently large as well as a strong function of frequency and temperature, so that temperature measurements with the pulse-echo technique become of marginal applicability. Another disadvantage of this technique is that layered structures, such as some of the nose cone materials, produce increased scattering at intermediate layers, making the technique generally inapplicable for these materials. However, the method possesses inherent capabilities of high accuracy and has been used where suitable, as will be discussed in later sections.

#### c. Immersion Technique

Another technique which has proven extremely useful with regard to accuracy and economy of measurement time is an immersion technique. This approach is effectively limited to longitudinal measurements because of the poor shear transmission characteristics of liquids, although it offers the possibility of measuring shear velocity by constructing the sample geometry so that mode conversion from longitudinal to shear waves occurs within the specimen. In this case, the sample is constructed so that the angle the longitudinal wave makes with a sample free surface is beyond the critical angle for longitudinal wave reflection. For this condition only a shear wave is reflected. Careful consideration of the propagation distance of the detected shear wave then allows a calculation of the shear velocity.

Basically, the immersion method is schematically illustrated in Figure 1. Conventional circuitry is used for generation and detection of the acoustic signals. This approach differs, however, from the solid buffer technique described in Reference 4 in that the liquid (water in this case) acts as a buffer. Reproducibility, and hence, precision are significantly increased since a coupling bond (such as oil or one of the viscous bonds) is not required between the transducers and the specimen. The transducers used in this arrangement were 3/4 inch in diameter, and were coaxially plated with a chrome-gold vacuum deposit. The active center (as shown in Figure 2) was 5/8 inch in diameter. The crystals are mounted in an aluminum sample holder, so that the back surface

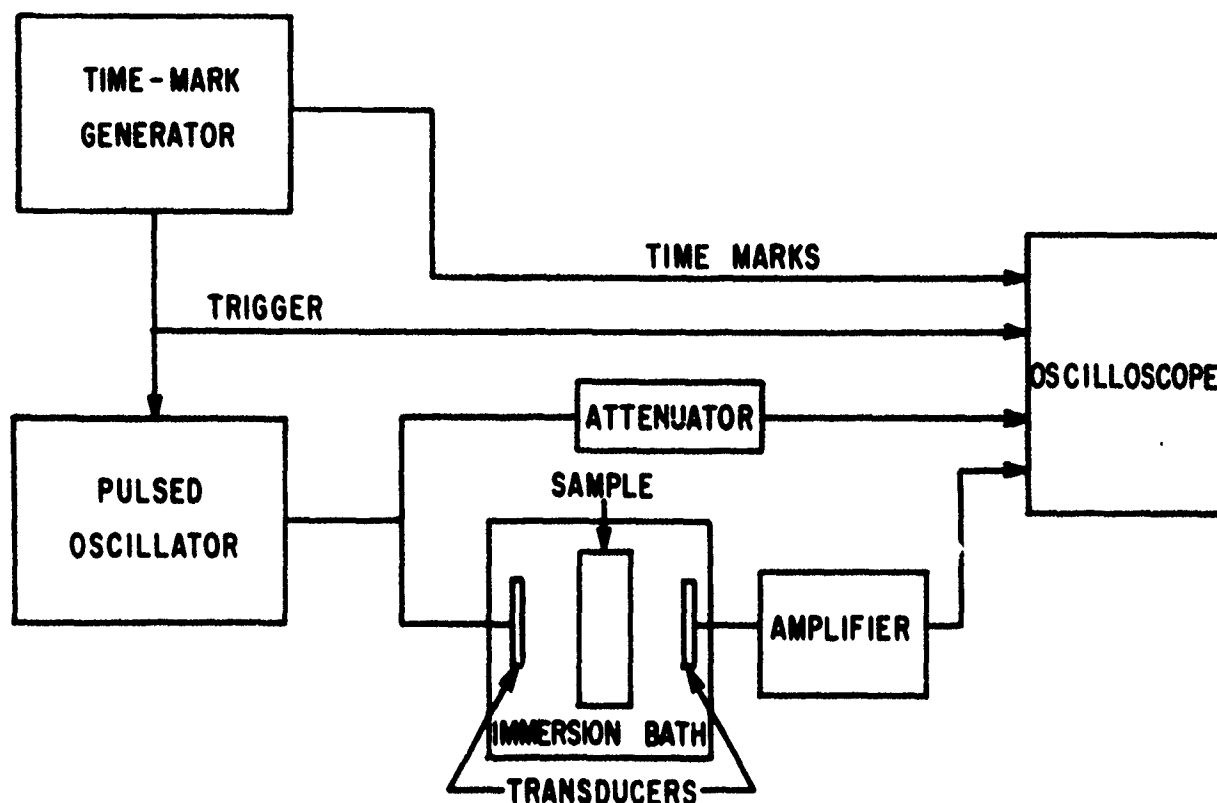


Figure 1. Schematic Diagram of the Immersion Technique.

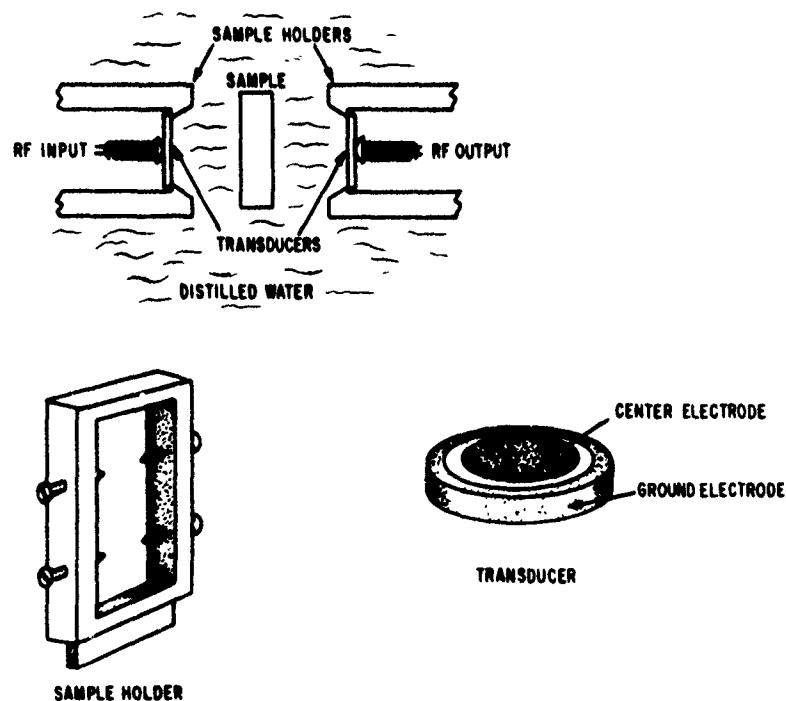


Figure 2. Details of the Immersion Technique.

(The transducers used here are lead zirconate titanate (PZT-5) which are plated with a chrome-gold vacuum deposit. The active center of the transducers is approximately 5/8 inch.)

is exposed to the immersion fluid and the center electrode is air-backed. The contact between the transducer and holder assembly is about 0.02 inch along the radius and over the complete circumference of the transducer. This contact area does not affect the operating characteristics of the transducer or introduce spurious side effects, because the active center is well separated from the point of contact. Electrical contact between the aluminum holder and the back surface of the crystal at the point of contact provides the ground.

The acoustic transit time through the specimen is obtained by inserting the specimens into a sample holder as shown in Figure 2. The holder was then placed in a slot which aligned the sample parallel to the transducers, which were located parallel to each other about one inch apart. No attempt was made to focus the acoustic beam in the path. However, by moving the transducer holders or by probing the area around the acoustic path with a piece of metal and observing the amplitude and transit time change, it was found that diffraction losses are minimal for the separation distances and frequencies employed here. By inserting an empty sample holder it was also found that the holder did not affect the determination of the transit time through the specimen.

The acoustic velocity in a specimen is calculated by separately measuring the transit time through distilled water and the water-sample combination. The velocity in the sample  $V_s$  is then given by

$$V_s = \frac{d_s}{t_i - t_o + \frac{d_s}{V_w}} \quad (3)$$

where

$V_s$  = longitudinal velocity in the specimen

$V_w$  = longitudinal velocity in water

$t_i$  = transit time through the water-sample combination

$t_o$  = transit time through the water only

$d_s$  = sample thickness

In practice, the time difference,  $t_i - t_o$ , was usually directly obtained by measuring the time between corresponding reference peaks with and without the sample inserted. Cedrone and Curran's (Ref. 6) value of  $1.438 + (2.4 \times 10^{-3})T$  mm/ $\mu$ sec ( $T$  in  $^{\circ}\text{C}$ ) for the longitudinal acoustic velocity in distilled water (over the range of from  $20^{\circ}$  to  $30^{\circ}\text{C}$ ) was used to calculate the quantity  $\frac{d_s}{V_w}$ .

The immersion technique has proven especially useful for thin specimens with high acoustic velocities. The main advantage of this method results from the elimination of an acoustic bond required in the solid buffer approach. This bonding can cause appreciable errors, especially at the lower frequencies ( $\sim 0.5$  to  $3.0$  MHz). The results obtained by the two methods are in good agreement above  $3$  MHz. Below this frequency, the reproducibility associated with the solid buffer approach is insufficient to allow valid comparisons.

Figure 3 illustrates the precision demonstrated by the immersion technique. The graph was obtained by measuring the transit time difference when thin pieces ( $1.600$  mm to  $7.953$  mm) of 24ST aluminum were inserted in the bath. These thicknesses of aluminum were chosen as calibration standards because the range of thickness and longitudinal velocity is similar to most of the materials studied with this technique.

Note in Figure 3 that the least-squares line extrapolates to zero when the thickness is zero. This implies that transit time corrections other than those associated with the acoustic velocity in distilled water are not required to calculate the velocity in the specimen. This is not the case for the solid buffer method where time corrections must be applied for the bonding interfaces between various components of the acoustic assembly. The figure also shows that there is no noticeable dispersion effects present in this method at frequencies of  $0.5$  to  $6$  MHz. The least squares slope in Figure 3 is  $6.46 \pm 0.05$  mm/ $\mu$ sec, which is within 1 percent of the handbook value of  $6.42$  mm/ $\mu$ sec for aluminum.

The errors associated with the immersion technique are relatively insensitive to experimental limitations such as sample alignment in the acoustic path, dispersion in the water, or impurity of the water. Calculation shows that the source of error arising from a misalignment of  $5$  degrees in the sample orientation is less than 1 percent, and, therefore, can be considered negligible with this technique because sample alignment was usually within  $2$  degrees. Barthe and Noble (Ref. 7) report a frequency dispersion in distilled water of less than 3 parts in  $10^5$  in this frequency range. They also indicate that the velocity in air-saturated distilled water is only 1 part in  $10^3$  greater than that in degassed water, so that this contribution to the overall error is small. These considerations and the typical error associated with flatness and parallelism of the samples affords an estimated uncertainty on the order of 1 to 2 percent with this technique. The technique has been extremely useful in performing quick analyses, or in measuring the frequency dependence of velocity and acoustic attenuation.

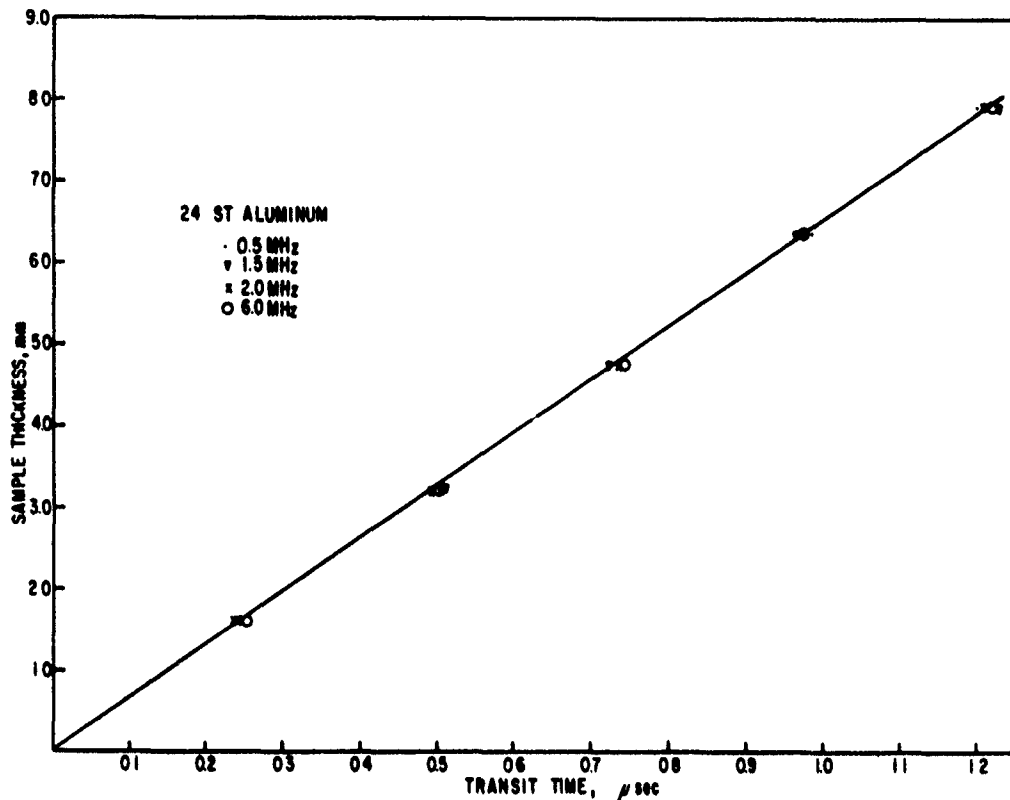


Figure 3. Calibration Curve for the Immersion Method at 22°C

#### d. Uniaxial Stress Technique

Some work is also reported here on the dependence of longitudinal and shear velocities with uniaxial pressure in two aluminum alloys. As explained in Section IV, this technique is a means of determining the third-order elastic constants\* of solids.

Since the velocity, and consequently the roundtrip time, changes only slightly with applied uniaxial stress, it was necessary to precisely detect small changes in transit time. This was accomplished by use of the variable time delay shown in Figure 4. By triggering the oscilloscope just before a preselected echo arrived, the echo could be viewed on an expanded time scale and small changes in transit time could easily be detected with the delay potentiometer. A change of 2 to 3 nsec could be reproducibly measured with this arrangement. Since the total time delays were 30 to 40 μsec, the resulting precision work was about 1 part in  $10^4$ .

\*The third-order elastic stiffnesses are defined as the isothermal strain derivatives of the isentropic second-order stiffnesses as determined at atmospheric pressure.



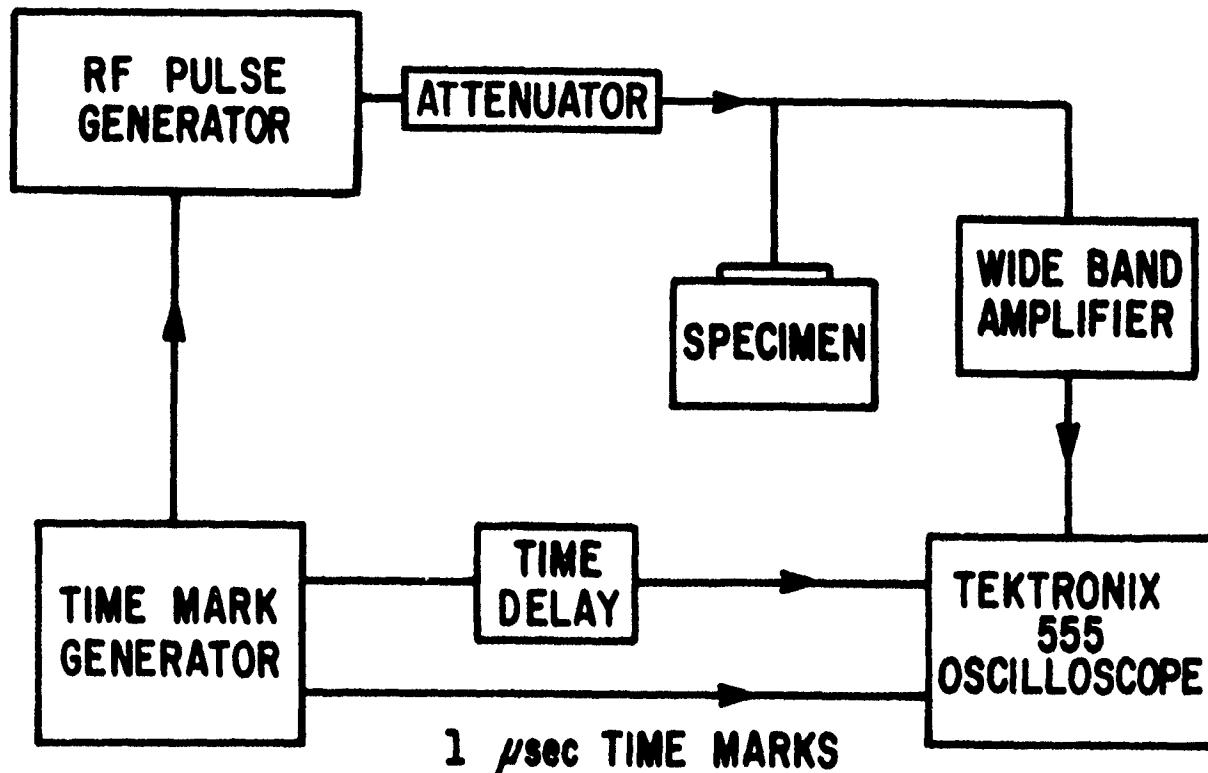


Figure 4. Schematic Diagram of Circuitry Used for Determining Small Changes in Transit Time Occurring to the Uniaxial Technique.

With the uniaxial method the samples were generally prepared as approximately 1-inch cubes and were machined flat and parallel to within  $\sim 0.003$  mm or less than 0.1 milliradians. For the uniaxial measurements it was necessary that the corners be square to ensure one-dimensional stress in the specimen. This was achieved with various degrees of success; however, the corners were generally square to within  $\sim 0.5$  milliradians.

Both quartz and PZT-5 (lead zirconate-titanate) transducers were used in determining the velocity change versus applied uniaxial stress. For most of the measurements the transducers were operated at their fundamental frequencies of 3 MHz. It was found that for both the longitudinal and shear modes the quartz crystals (X-cut for longitudinal measurements and AC-cut for shear measurements) produced cleaner waveforms, and therefore were used for most of the stress measurements. The disadvantage of quartz over PZT is that the generated stress fields for a given input voltage are lower because of the lower piezoelectric coefficients. However, this caused no experimental problems, because the amplified received signals were well above background noise.

For the pressure work some difficulty was encountered in choosing a proper bond for attaching the transducers to the specimens. A rigid bond is necessary for the shear measurements to transmit the transverse motion of the transducer to the specimen. Also, for the stress measurements a bond is necessary which will not affect the pulse waveform as the lateral boundaries of the specimen contract under uniaxial compression. A light-viscosity silicone oil was satisfactory for the longitudinal experiments, and an epoxy resin (Eastman 910) was satisfactory for the shear measurements. Both types of transducers were bonded to the specimen under pressures of  $\sim 5$  psi.

The most important consideration in uniaxial measurements is the provision of a uniform uniaxial load. The system used to accomplish this requirement is shown in Figure 5. The entire system consists of a 20-ton laboratory press driven by a manually operated pump. To eliminate the effect of friction in the hydraulic system, the pressure gauges used in these experiments were calibrated with 10,000 and 50,000-lb proving rings. The rings had been previously calibrated at the National Bureau of Standards and were accurate to within 0.3 percent of full scale. The pressure was maintained to within  $\pm 20$  psi throughout the pressure range of 0 to 11,000 psi. The ball bearing arrangement shown in the figure maintained alignment between the piston and sample.

Furthermore, shear forces arising because of the difference in lateral expansions of the piston and specimen can cause undesirable effects. An analysis by Bogardus (Ref. 8) indicates that these forces can be minimized by matching the ratio of Young's modulus to Poisson's ratio for the sample and piston surface. Measurements were therefore made with a 1/4-inch thick piece of aluminum inserted between sample surface and piston anvil. However, no difference from the original measurements could be detected, so it was concluded that this effect is insignificant in the present study.

Since a temperature change of  $0.5^{\circ}\text{C}$  in aluminum corresponds to a larger change in some of the velocities than a pressure change of 500 psi, it was important to maintain close temperature control during a pressure run. An enclosure around the piston controlled the temperature variation to  $\sim 0.1^{\circ}\text{C}$  during a set of pressure measurements. The variation in temperature from one set of measurements at any given temperature to another was  $\sim 0.5^{\circ}\text{C}$ . However, the present technique was not sensitive enough to detect a difference in slope resulting from a change in environment of  $0.5^{\circ}\text{C}$  so that the data were plotted together.

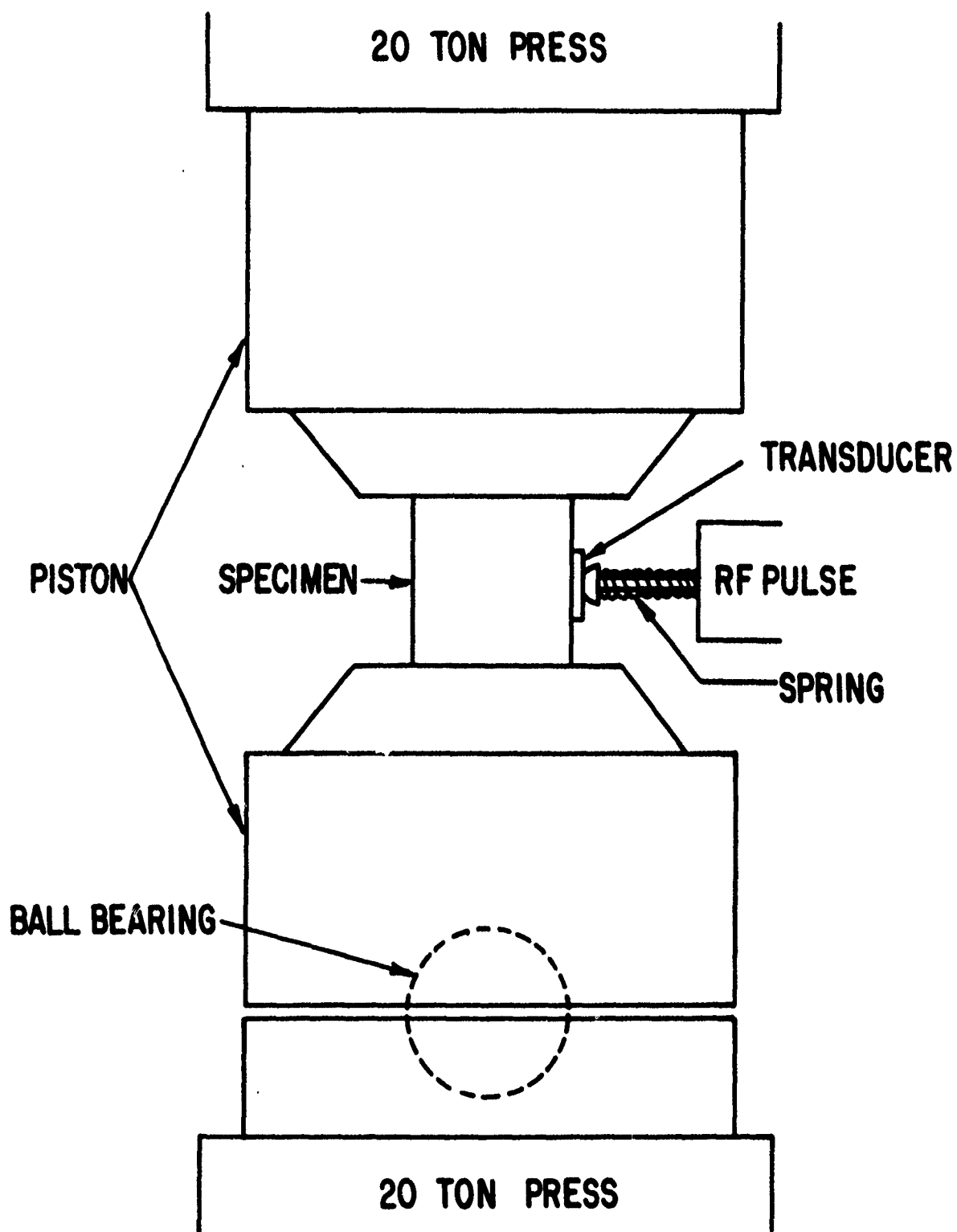


Figure 5. Experimental Arrangement in the Uniaxial Stress Technique.

Indeterminable effects in this technique may lead to errors which are greater than those discussed above, and arise because of misalignment between the piston and the sample, variable stress distribution, and plastic yielding in the specimen. Misalignment between specimen and piston is considered negligible in the present experiments, because the results for any one specimen were reproducible to within the stated limits of precision. Plastic flow, and possibly dislocation movement, can likewise contribute an error to the calculations of the third-order coefficients, because the calculations rely upon purely elastic deformation.

## 2. Experimental Results

### a. Longitudinal and Shear Velocities in Common Plastics

The longitudinal and shear velocities in the materials reported in this section were obtained by measuring the transit times through various sample thicknesses and performing a least-squares plot to obtain the slope. For most of the velocity-temperature data a quadratic function was found to best fit the data.

All of the shear velocities reported herein were obtained by bonding two transducers to either side of a flat and parallel specimen, and measuring the acoustic transmission times for various sample thicknesses. The longitudinal velocities in Delrin Acetal\* and Lexan were obtained with the solid buffer technique (Ref. 4), which likewise requires the use of two separate transducers. The accuracies of all the velocity data reported here are estimated to be 1 to 2 percent.

#### (1) Delrin Acetal

This material is one of the more recently developed plastics which possess material properties comparable with many of those common to metals. It is a highly crystalline, stable form of polymerized formaldehyde (super polyoxymethylene), which exhibits high tensile strength, rigidity, and creep resistance over a wide temperature range. The material used in the present experiments exhibited a mean density of 1.434 g/cc. The variations of the

---

\* Delrin Acetal is a registered trademark of E. I. DuPont de Nemours and Co.

longitudinal and shear velocity with temperature in Delrin Acetal are shown in Figures 6 and 7, respectively, as corrected for thermal expansion.\*

The temperature dependence of the longitudinal velocity was obtained by the solid buffer technique, and the shear velocity versus temperature was obtained by bonding the transducers directly to the specimen. The data for the longitudinal mode of propagation indicate negligible dispersion in the frequency range of 1.5 to 3.0 MHz. The data for the shear velocity are limited to 1 MHz in the present experiments, because the attenuation of the third harmonic was too great to allow accurate velocity measurements at this frequency.

The least-squares fit of the data corresponding to the graphs of Figures 6 and 7 are

$$\text{Longitudinal Velocity, } V_l = 2.58 - (4.21 \times 10^{-3})T - (1.25 \times 10^{-5})T^2, \\ 25^\circ \text{ to } 125^\circ\text{C}$$

$$\text{Shear Velocity, } V_t = 1.19 - (3.69 \times 10^{-3})T - (1.39 \times 10^{-5})T^2, \\ 25^\circ \text{ to } 100^\circ\text{C}$$

where the velocity units are mm/ $\mu$ sec, and temperature T is in  $^\circ\text{C}$ .

The application of the velocity data to the calculations of the elastic moduli is largely limited by the acoustic attenuation arising from internal friction. The dissipation processes which are applicable to the present case are those associated with velocity gradients induced by the acoustic vibrations. These losses may be grouped into two general classes, depending upon whether the mechanical behavior of the specimen corresponds to the Maxwell or Voigt model (Ref. 9).

Based upon the appropriate model, the present data could be used to calculate the frequency dependent moduli in Delrin Acetal. However, the velocity data would have to be supplemented with measurements showing the dependence of velocity and attenuation with frequency to verify the applicable model.

Assuming that the viscous terms are small enough that the mechanical behavior is essentially elastic, the elastic moduli can be derived from the

---

\*All of the thermal expansion coefficients required for velocity correction as used in this section are reported in Section III.

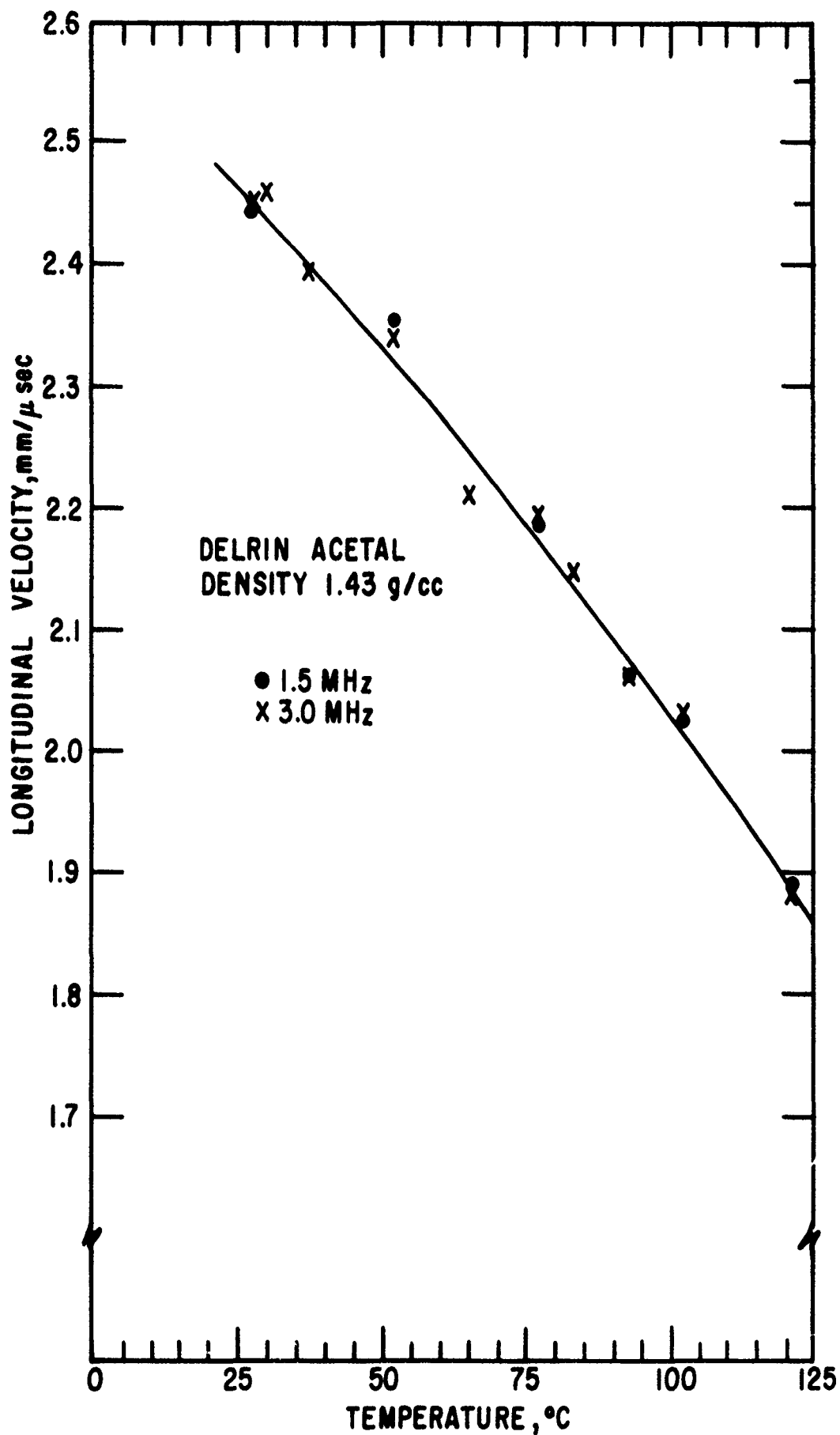


Figure 6. Longitudinal Velocity Versus Temperature in Delrin Acetal.

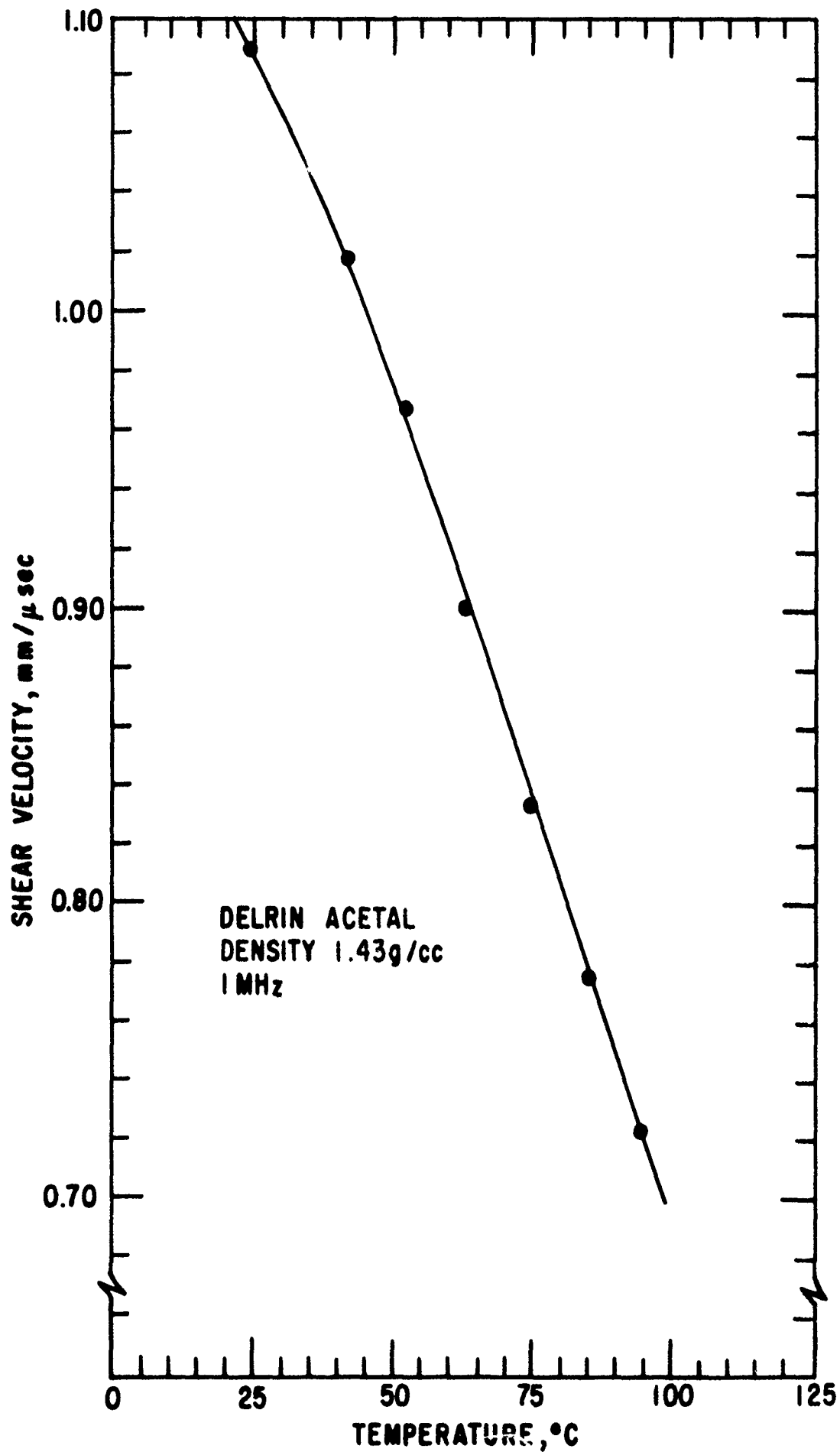


Figure 7. Shear Velocity Versus Temperature in Delrin Acetal.

two sets of reported velocities. In terms of the velocities, Young's modulus  $E$ , the shear modulus  $G$ , and the bulk modulus  $B$  are given as

$$\begin{aligned} E^S &= \rho \frac{v_t^2 (3v_\ell^2 - 4v_t^2)}{v_\ell^2 - v_t^2} \\ G &= \rho v_t^2 \\ B^S &= \rho \left( v_\ell^2 - \frac{4}{3} v_t^2 \right) \end{aligned} \quad (4)$$

In units of dynes/cm<sup>2</sup> and as function of temperature (in °C) the adiabatic moduli (in the range of from 25° to 100°C) for Delrin Acetal are therefore

$$\begin{aligned} E^S &= 5.81 \times 10^{10} - (4.57 \times 10^8)T - (6.25 \times 10^5)T^2 \\ B^S &= 7.00 \times 10^{10} - (2.10 \times 10^8)T \\ G &= 2.13 \times 10^{10} - (1.76 \times 10^8)T - (2.84 \times 10^5)T^2 \end{aligned}$$

The quantities  $B^S$  and  $E^S$  above are the adiabatic moduli. Although the bulk modulus was somewhat nonlinear with temperature as can be seen by inserting the quadratic functions of velocity and density into the equation for  $B^S$ , the linear fit agrees with the experimental data to within 1-1/2 percent over the indicated temperature range. As shown in Section IV, it is necessary to know the temperature derivatives of the bulk modulus in many calculations and a constant derivative introduces significant simplifications. A linear fit of the bulk modulus versus temperature has been found appropriate for all the polymers reported here.

## (2) Poly Penco Nylon\*

Figure 8 shows the dependence of shear velocity on temperature in Poly Penco Nylon (density 1.14 g/cc). The data were obtained over the temperature range of from 25° to 100°C, and are corrected for thermal expansion. The attenuation of the 3 MHz harmonic was too great to allow a reliable determination of the velocity at that frequency. The least-squares fit for the data represented in Figure 8 is

$$v_t = 1.15 - (2.35 \times 10^{-4})T - (4.48 \times 10^{-5})T^2$$

\* Poly Penco Nylon is a registered trademark of The Polymer Corporation.



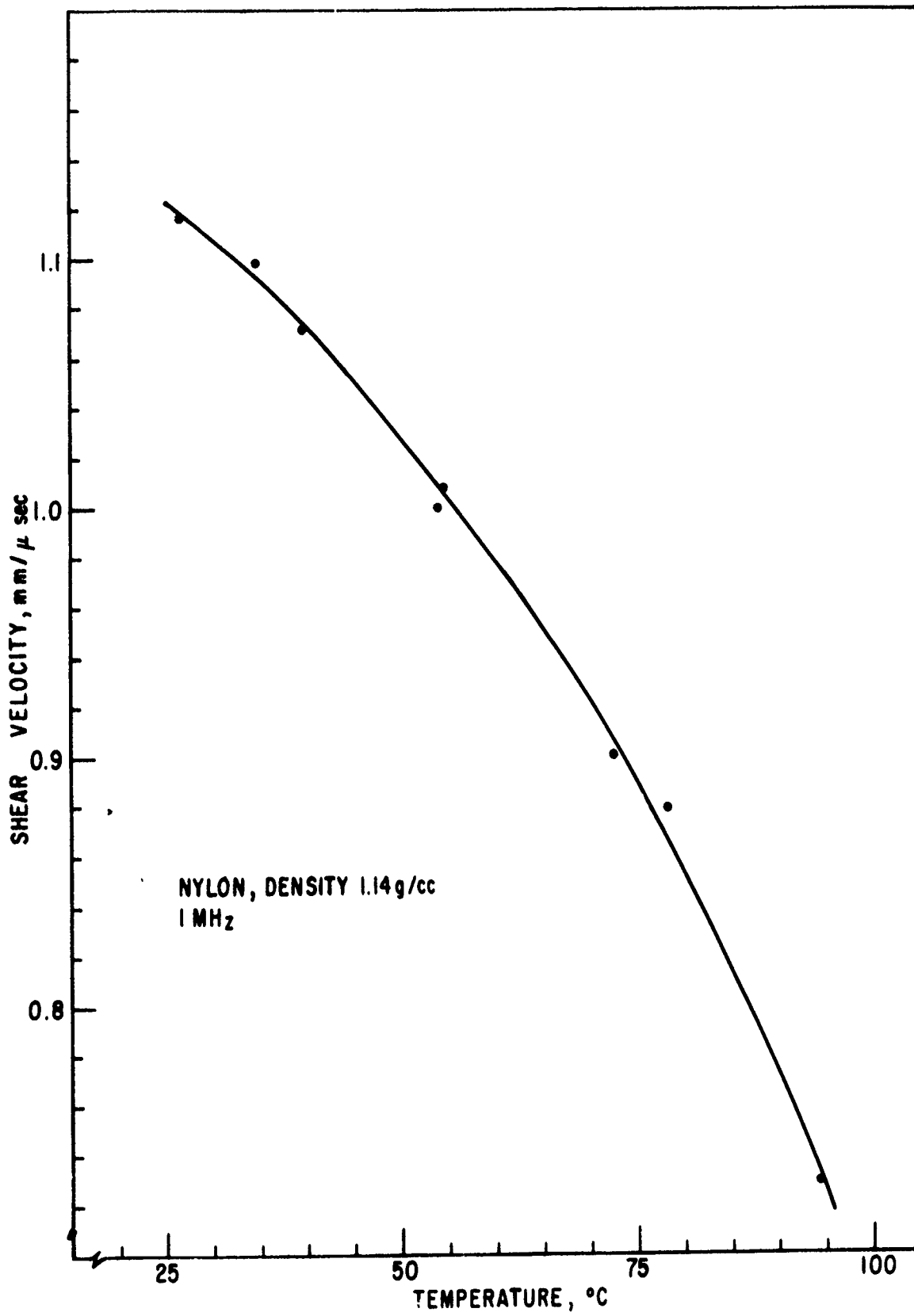


Figure 8. Shear Velocity Versus Temperature in Poly Penco Nylon.

Although the elastic moduli have not been calculated for this material, the velocity data in Tables 1 and 2, in conjunction with thermal expansion data presented in Section III, can be used to calculate all of the moduli as illustrated above for Delrin Acetal. The most important quantity in equation of state calculations is the temperature dependence of the bulk modulus so that a table of this moduli for the plastics studied here is presented at the end of Section II, paragraph 2a.

### (3) Teflon\*

The shear velocity in TFE Teflon (density, 2.19 g/cc) is shown in Figure 9. Again, the experimental technique was not sensitive enough to allow a determination of the velocity of the 3 MHz acoustic wave. Because of the low-friction surface of teflon, some difficulty was experienced in maintaining a good bond between the specimen and transducer. The data therefore show more variation than that experienced in the previous two materials, due to nonreproducibility of bonding.

The variation of the shear velocity near room temperature was too great to allow a reliable observation of the second-order transition as observed by Arnold and Guenther (Ref. 10) in the longitudinal velocity. The data corresponding to the temperature range of from 25° to 150°C were therefore fitted to the following polynomial

$$V_t = 0.581 - (0.345 \times 10^{-2})T + (0.10 \times 10^{-4})T^2$$

### (4) Type G Plexiglas\*\*

Figure 10 exhibits the shear velocity as a function of temperature in Type G Plexiglas. This material, which is a methyl-methacrylate polymer, exhibited a mean density of 1.19 g/cc. As indicated in Figure 10, there is a difference of ~ 1 percent in the velocity at 1.0 and 3.0 MHz. Although this uncertainty approaches the limitations of the techniques, both curves were fitted to separate polynomials. The results are

$$1 \text{ MHz, } V_t = 1.39 + (5.99 \times 10^{-4})T - (2.32 \times 10^{-5})T^2, \quad 25^\circ \text{ to } 125^\circ\text{C}$$

$$3 \text{ MHz, } V_t = 1.43 - (6.47 \times 10^{-4})T - (1.10 \times 10^{-5})T^2, \quad 25^\circ \text{ to } 100^\circ\text{C}$$

\* Teflon is a registered trademark of E. I. DuPont de Nemours and Co.

\*\* Plexiglas is a registered trademark of Rohm & Haas Co.

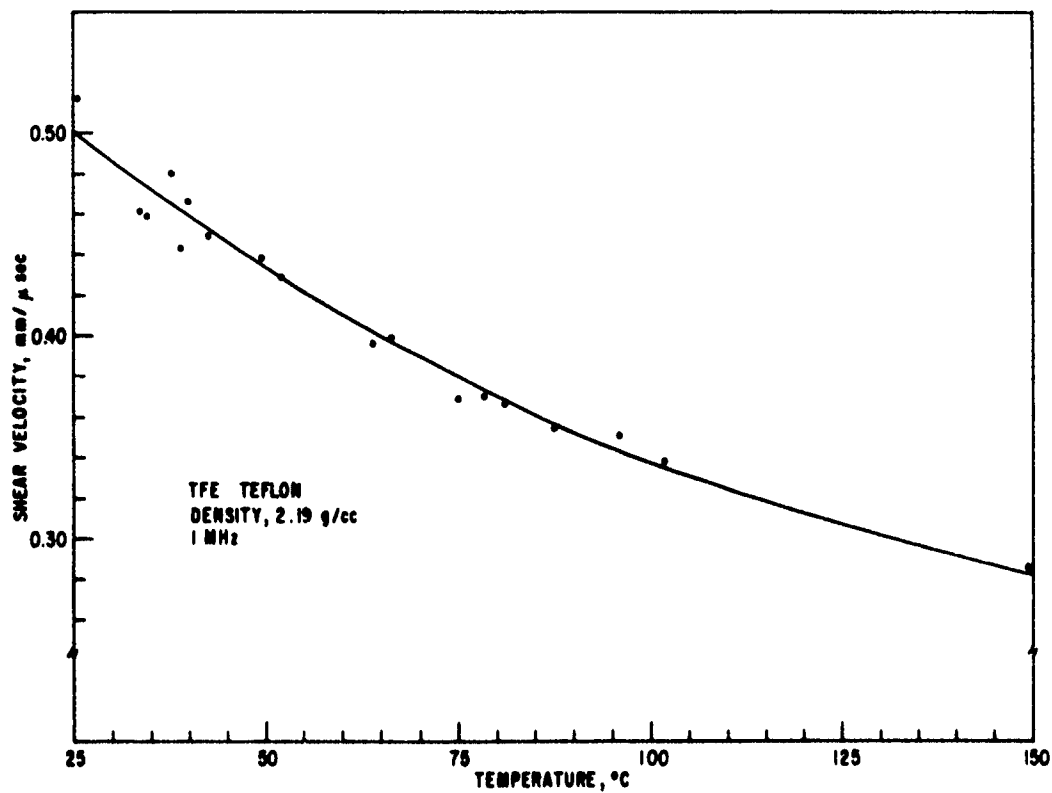


Figure 9. Shear Velocity Versus Temperature in TFE Teflon.

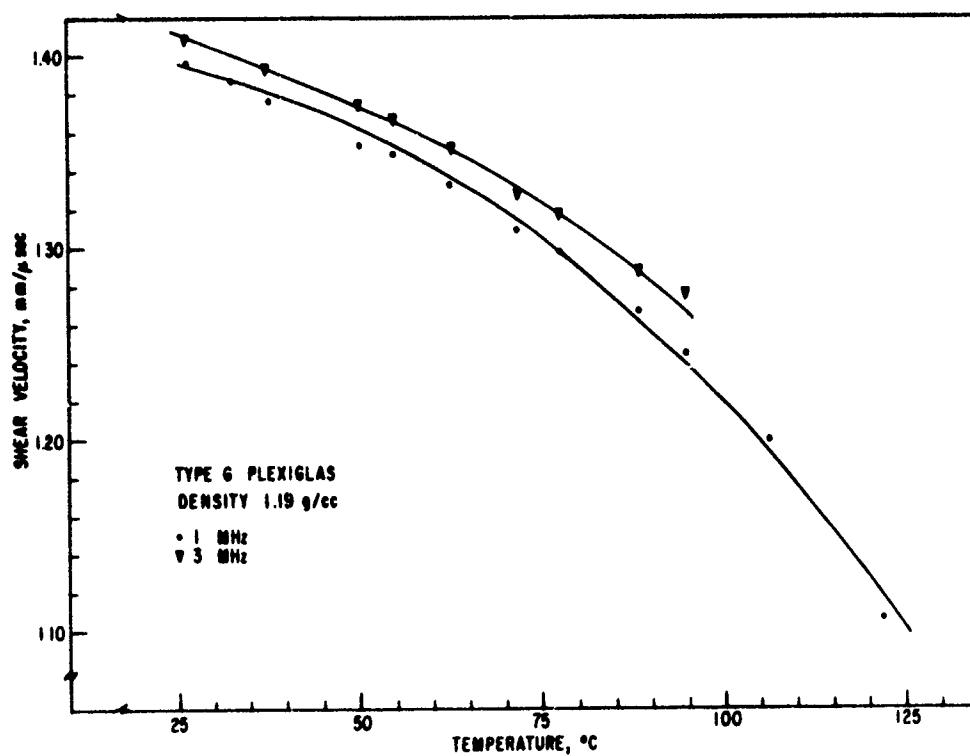


Figure 10. Shear Velocity Versus Temperature in Type G Plexiglas.

It is also noted that the separation in the velocities at  $\sim 100^\circ\text{C}$  appears to be  $\sim 2$  percent. This effect could be due to a frequency dependent relaxation mechanism, because increasing the temperature of a viscoelastic material is equivalent to lowering the frequency (Ref. 9).

#### (5) Polyethylene

Figures 11 and 12 illustrate the variation of shear velocity in two different densities of polyethylene and the dependence of the velocity on temperature. Again, some dispersion in the high-density polyethylene was noted between 1 and 3 MHz (Figure 12), so that separate curves were plotted for the two frequencies.

Of particular interest is the large difference in velocity ( $\sim$  a factor of two) corresponding to a density change of  $\sim 5$  percent. Arnold and Guenther (Ref. 10) have measured the longitudinal velocity corresponding to the two different densities of polyethylene and obtained the results of 1.99 mm/ $\mu\text{sec}$  and 2.55 mm/ $\mu\text{sec}$  at room temperature for the densities of 0.916 g/cc and 0.964 g/cc, respectively. The change in the longitudinal velocity is therefore  $\sim 25$  percent for this change of density. However, the longitudinal velocity is a function of two of the independent elastic constants in an isotropic medium (the Lamé constants,  $\lambda$  and  $\mu$ ), whereas, the shear velocity depends only on the shear modulus or Lamé constant  $\mu$  ( $G$  as used earlier is identical with the constant  $\mu$ ).

The magnitude of variation in the shear velocities observed in the present experiments can be verified through correlation with other elastic properties of the material. Estes (Ref. 11) states that for polyethylene the elastic modulus in tension varies by approximately an order of magnitude for the two densities of polyethylene used here. This modulus cannot be directly related to any dynamically determined modulus, such as the Young's modulus, because of creep and stress relaxation which are present in static tests. However, the effective modulus as reported by Estes is a function of both Lamé constants, and hence, would be influenced significantly by the variation of the shear modulus with density.

More direct support of the reported difference in shear velocities can be obtained by considering Young's modulus in the two materials. Using the previous results (Ref. 4) for the longitudinal velocities and applying the

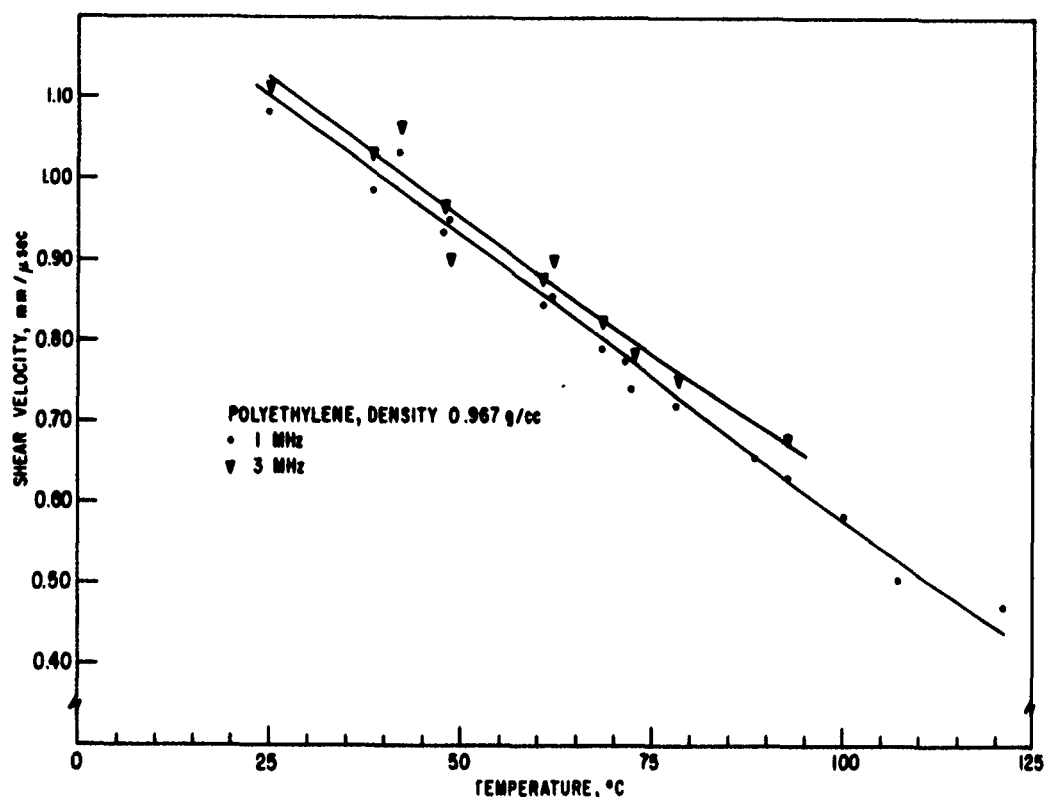


Figure 11. Shear Velocity Versus Temperature in High Density Polyethylene (0.967 g/cc).

elastic relations presented earlier, the reported data give the values of  $3.2 \times 10^{10}$  and  $0.78 \times 10^{10}$  dynes/cm<sup>2</sup>, respectively, for Young's modulus in the high and low density specimens. Young's modulus can also be related to the extensional or thin rod velocity,  $V_{\text{ext}}$ , as  $E = \rho V_{\text{ext}}^2$ . These velocities are calculated from the present data to be 1.8 and 0.91 mm/μsec for the high and low density polyethylene, respectively. The above calculations are in good agreement with Davidse's (Ref. 12) direct measurements of 1.9 and 0.9 mm/μsec for the extensional velocities corresponding to the respective densities of 0.967 and 0.922 g/cc. The least-squares fit of the shear velocities for the densities of polyethylene in the temperature range of from 25° to 100°C as shown in Figures 11 and 12 are

$$\text{density } 0.922 \text{ g/cc, } 1 \text{ MHz, } V_t = 0.554 - (0.81 \times 10^{-4})T - (0.685 \times 10^{-7})T^2$$

$$\text{density } 0.967 \text{ g/cc, } 1 \text{ MHz, } V_t = 1.29 - (7.56 \times 10^{-3})T + (4.36 \times 10^{-6})T^2$$

$$3 \text{ MHz, } V_t = 1.32 - (7.85 \times 10^{-3})T + (9.71 \times 10^{-6})T^2$$

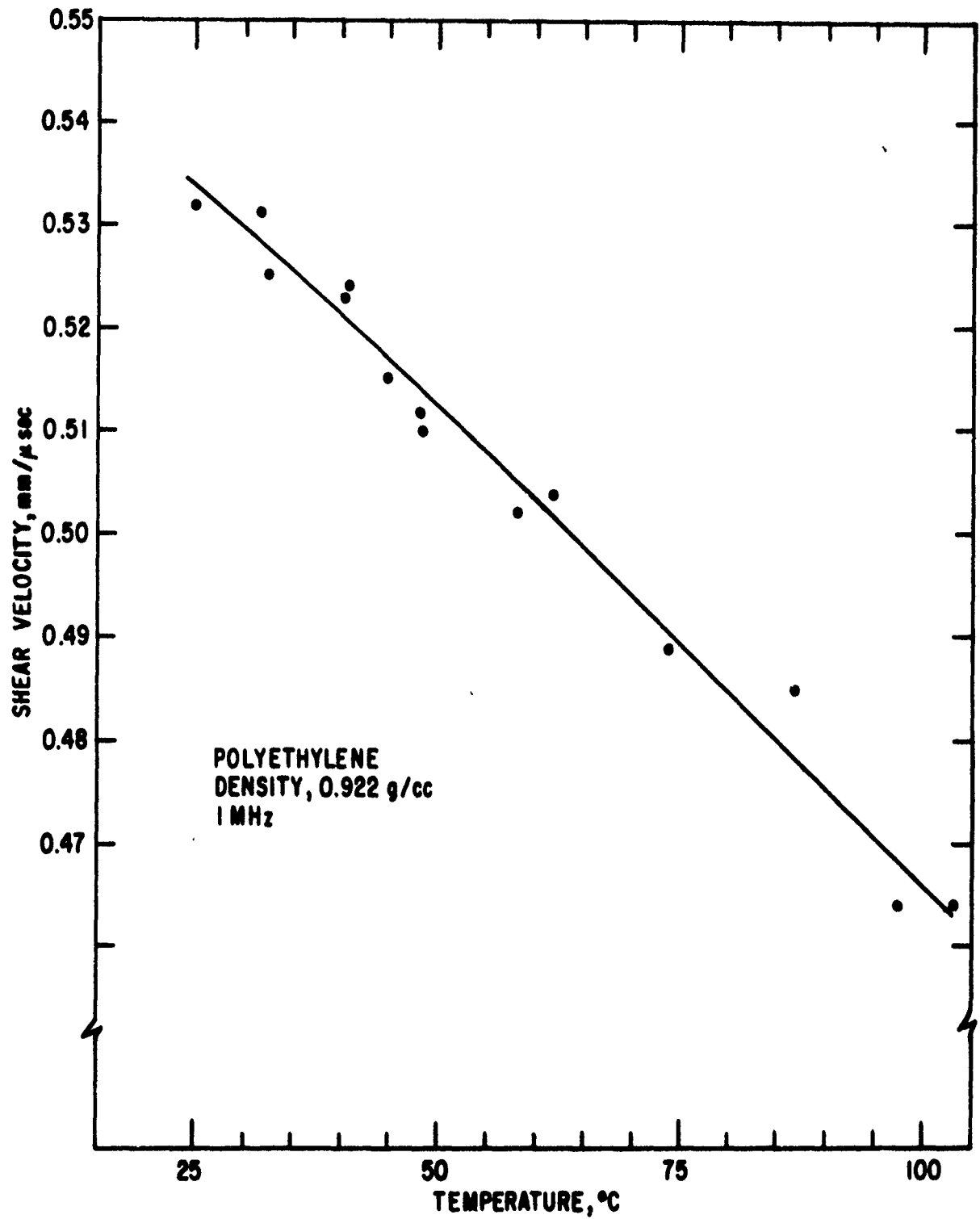


Figure 12. Shear Velocity Versus Temperature in Low Density Polyethylene (0.922 g/cc).

## (6) Lexan\*

Figures 13 and 14 illustrate the variation of the longitudinal and shear velocities with temperature in Lexan (a polycarbonate, density 1.20 g/cc). Both curves were corrected for thermal expansion using the manufacturer's value of  $6.75 \times 10^{-5}/^{\circ}\text{C}$  for the linear coefficient of thermal expansion. The longitudinal velocity was obtained with the solid-buffer technique.

Kunze (Ref. 13) has reported typical compressive and rigidity moduli for polycarbonates as obtained in static tests. His values for the modulus of elasticity and the shear modulus are  $3.40 \times 10^5$  and  $1.16 \times 10^5$  psi, respectively. Using the appropriate equations of elasticity, the present data on the longitudinal and shear velocities yield  $3.73 \times 10^5$  and  $1.45 \times 10^5$  psi for Young's modulus and the shear modulus at  $25^{\circ}\text{C}$ , respectively. This agreement is fair considering the nature of both tests. Kunze does not report the uncertainty of his values nor a specific polycarbonate. Furthermore, static tests, as mentioned earlier, are generally influenced by creep and stress relaxation so that a direct comparison should not be made with the present data. Since the uncertainties for velocities in the present experiments are approximately 1 to 2 percent, the uncertainties in the elastic moduli as calculated above are on the order of 2 to 5 percent. The longitudinal and shear velocities given in terms of temperature for Lexan are

$$V_l = 2.31 - (3.69 \times 10^{-3})T + (6.90 \times 10^{-6})T^2, \quad 25^{\circ} \text{ to } 125^{\circ}\text{C}$$

$$V_t = 0.954 - (0.199 \times 10^{-2})T + (0.528 \times 10^{-5})T^2, \quad 25^{\circ} \text{ to } 90^{\circ}\text{C}$$

## (7) Mylar\*\*

The longitudinal velocity in Mylar was also obtained with the immersion technique. This approach was necessary since the buffer technique does not yield good accuracy with extremely thin samples (e.g., 10 to 14 mils in the case of Mylar) because of the reproducibility of bonding the buffers to the specimen. However, with the immersion technique, reproducibility errors become less important because the fluid (water was used in the present experiments) acts as a buffer and transit times corresponding to different insertions can be reproduced to within a few nanoseconds.

---

\* Lexan is General Electric Company's trademark for polycarbonate resin.

\*\* Mylar is a registered trademark of E. I. DuPont de Nemours and Co.

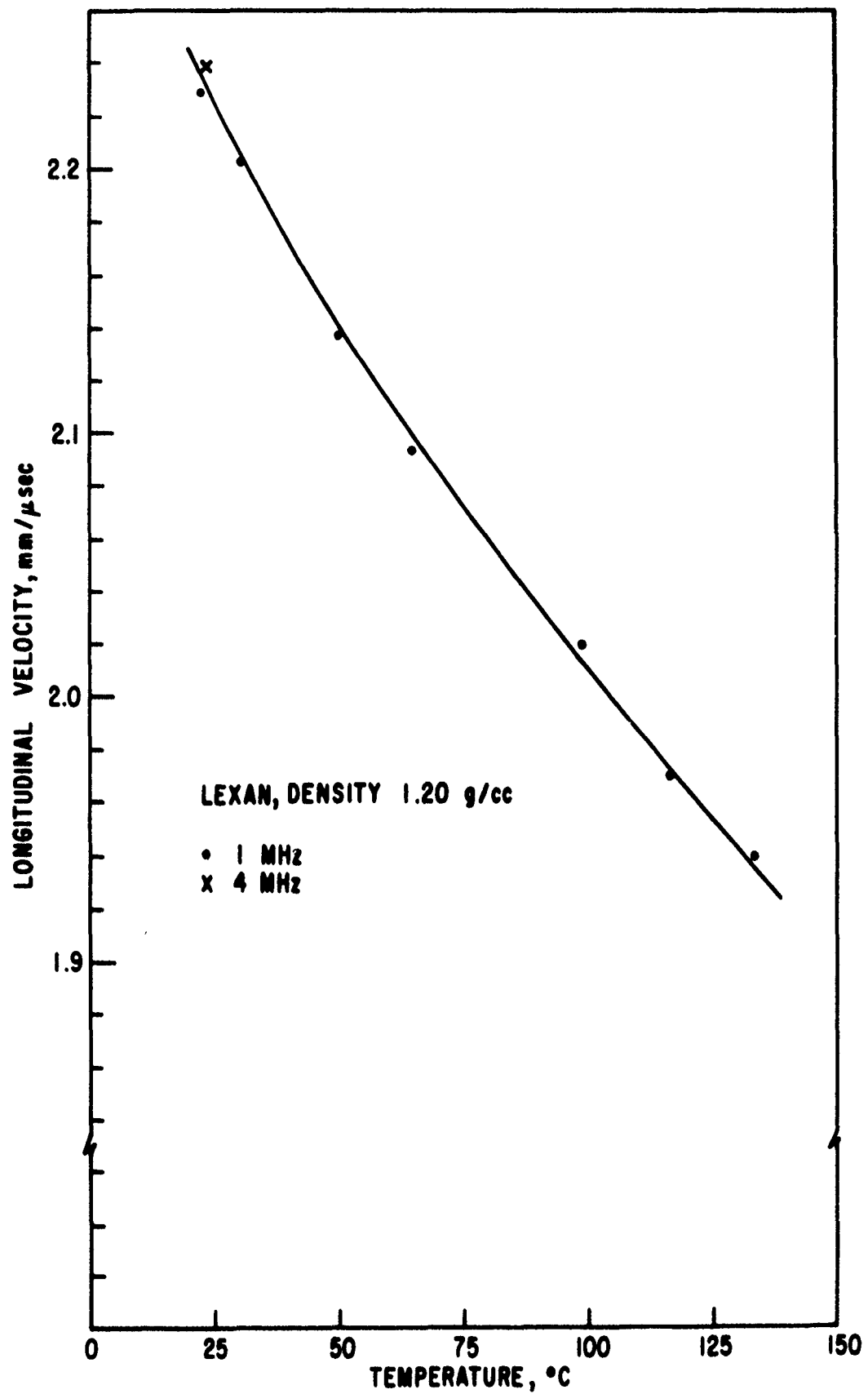


Figure 13. Longitudinal Velocity Versus Temperature in Lexan.



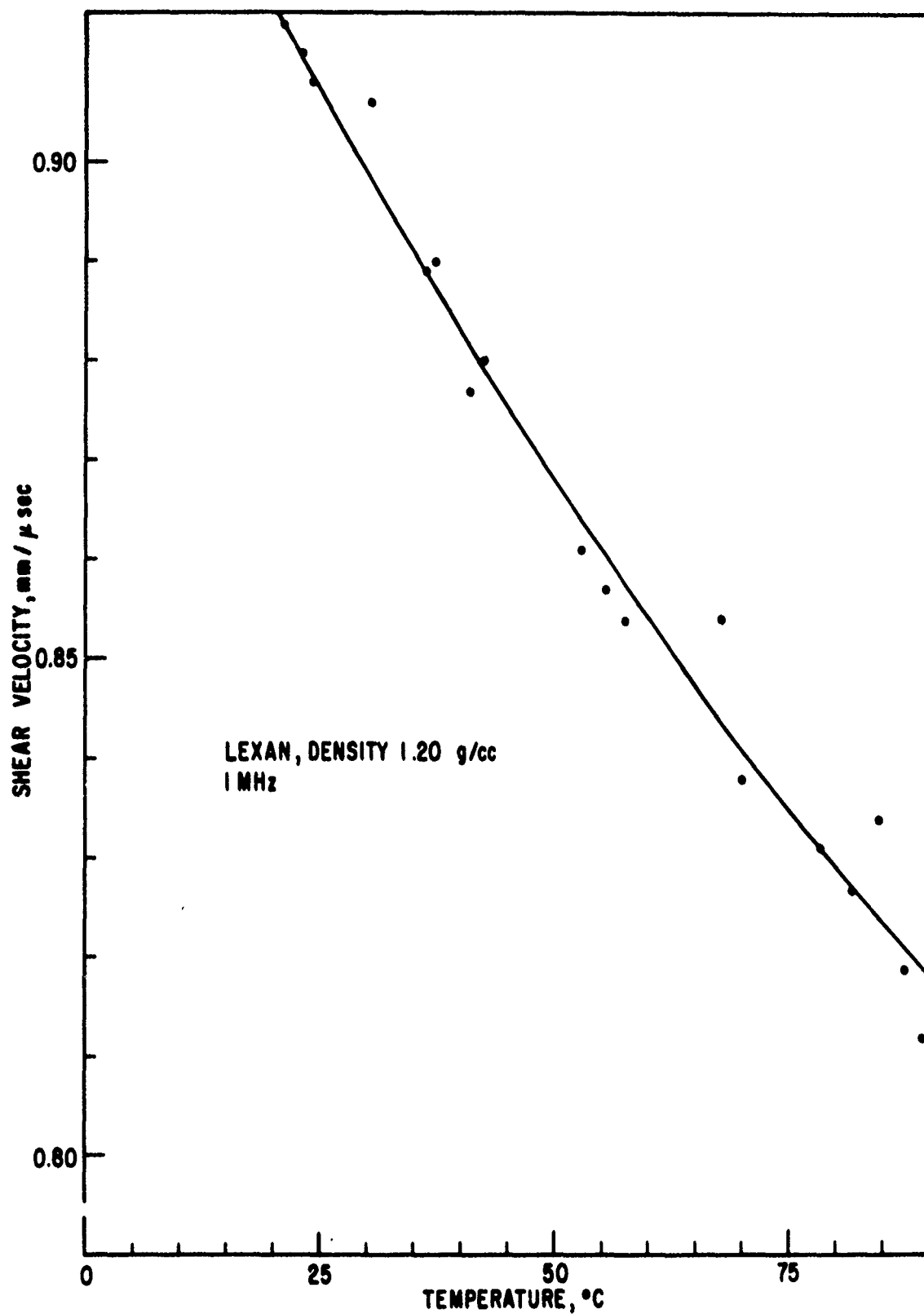


Figure 14. Shear Velocity Versus Temperature in Lexan.

The velocity in Mylar was obtained for the frequencies of 2.0, 4.0, and 12.0 MHz. The acoustic wavelengths ranged from 1 mm to  $\sim 0.2$  mm for these frequencies, with the lowest wavelength corresponding to approximately the sample thickness. For this range of frequencies, a trend in the velocity data was not observed within the limitations of the technique so that the results were averaged together. The average longitudinal velocity in 10 mil Mylar at 21.0°C as obtained in the present experiments is  $2.64 \pm 0.09$  mm/ $\mu$ sec. The velocity in 14 mil Mylar is  $2.29 \pm 0.06$  for the corresponding experimental conditions.

Tables 1 and 2 summarize the least-squares results for the shear and longitudinal velocities in common plastics. Table 3 lists the coefficients for the adiabatic bulk modulus versus temperature for the common plastics listed in Section II, paragraph 2a. The coefficients  $B_{o,o}^s$  and  $(\partial B_o^s / \partial T)_{o,o}$  are defined as the adiabatic bulk modulus at atmospheric pressure ( $P=o$ ; this notation will be explained further in Section IV) and at 0°C, and the temperature derivative of the adiabatic modulus for the corresponding conditions. The bulk modulus expanded in terms of temperature at atmospheric pressure then takes the form

$$B_{o,T}^s = B_{o,o}^s + \left( \frac{\partial B_o^s}{\partial T} \right) T \quad (5)$$

for T in °C.

#### b. Longitudinal and Shear Velocities in Nose Cone Materials

Measurements made on some of the more common nose cone materials are described in this section. The emphasis has been to develop a technique for using the ultrasonic method for determining equation-of-state parameters in some of the recently developed anisotropic layered materials. Of the layered materials studied in Reference 4, carbon phenolic and General Electric Fiberglas exhibited the best reproducibility and uniformity of material structure and were therefore studied first. The study is being continued; however, the results reported in Section II, paragraph 2b illustrate the experimental techniques involved.

##### (1) Carbon Phenolic

The results on the temperature and orientation dependence of the longitudinal velocity in GE carbon phenolic have been reported in Reference 4. The work reported here refers to the dependence of the shear velocity on the corresponding parameters, and a theoretical prediction of the dependence of

Table 1

## SHEAR VELOCITIES IN COMMON PLASTICS VERSUS TEMPERATURE

Temp. °C	Polyethylene		TFE Teflon	Type G Plexiglas	Nylon	Delrin Acetal	Lexan
	0.922 g/cc	0.967 g/cc					
25.0	0.534	1.11	0.501	1.391	1.12	1.090	0.908
30.0	0.529	1.07	0.486	1.388	1.11	1.067	0.899
40.0	0.521	0.999	0.459	1.377	1.07	1.026	0.883
50.0	0.512	0.928	0.434	1.362	1.03	0.975	0.868
60.0	0.503	0.857	0.410	1.343	0.979	0.924	0.854
70.0	0.494	0.787	0.398	1.319	0.919	0.864	0.841
80.0	0.485	0.718	0.370	1.290	0.849	0.808	0.829
90.0	0.475	0.650	0.352	1.256	0.771	0.752	0.818
100.0	0.466	0.583	0.337	1.218	0.683	0.688	
110.0		0.516	0.324	1.176			
120.0		0.451	0.313	1.128			

(All velocities correspond to a frequency of 1.0 MHz.)

Table 2

## LONGITUDINAL VELOCITIES IN COMMON PLASTICS VERSUS TEMPERATURE

Temp. °C	Polyethylene		TFE Teflon	Type G Plexiglas	Nylon	Delrin Acetal	Lexan
	0.922 g/cc	0.967 g/cc					
25.0	1.99	2.56	1.40	2.71	2.72	2.47	2.22
30.0	1.96	2.52	1.36	2.70	2.70	2.44	2.20
40.0	1.88	2.44	1.32	2.68	2.65	2.39	2.17
50.0	1.77	2.35	1.29	2.65	2.61	2.34	2.14
60.0	1.67	2.28	1.26	2.61	2.56	2.28	2.11
70.0		2.20	1.24	2.58	2.51	2.22	2.08
80.0		2.11	1.22	2.54	2.45	2.16	2.06
90.0		2.04	1.20	2.50	2.38	2.10	2.03
100.0		1.96	1.17	2.47	2.30	2.03	2.01
110.0			1.15		2.23	1.97	1.99
120.0			1.12			1.90	1.97

(The data were taken from Reference 4, with the exception of Delrin Acetal and Lexan, and represent average values over the frequency range 1.5 to 3.0 MHz.)

Table 3

THE EXPANSION COEFFICIENTS OF THE BULK  
MODULUS VERSUS TEMPERATURE IN COMMON PLASTICS

Plastic	$B_{o,o}^s$ (kbars)	$\left(\frac{\partial B_o^s}{\partial T}\right)_{o,o}$ (kbars/°C)
Polyethylene, 0.922 g/cc	37.9	-0.262
Polyethylene, 0.967 g/cc	51.8	-0.210
Type G Plexiglas, 1.19 g/cc	58.6	-0.113
Poly Penco Nylon, 1.14 g/cc	69.9	-0.188
Delrin Acetal, 1.434 g/cc	70.0	-0.210
Lexan, 1.20 g/cc	48.3	-0.113

(Temperature range, ~ 25° to 100°C.)

longitudinal velocity upon angle of incidence with respect to the laminae. Carbon phenolic from two different sources was used to determine the shear velocity in the present experiments. The samples from Douglas-McDonnell Aircraft Corporation\* exhibited a structure consisting of approximately 35 layers per centimeter and a density of 1.40 g/cc. The material from General Electric Company indicated a spacing of approximately 30 layers/cm and a density of 1.48 g/cc.

Figure 14 illustrates the nomenclature used to describe the propagation conditions in the layered structures. Both of these materials were essentially isotropic in the plane of the layers (x-y plane). For materials exhibiting such transverse isotropy the stress-strain matrix is significantly simplified and there are only five elastic stiffness coefficients which describe the material. As shown in Appendix I the five measurements which are necessary to yield these coefficients are as follows

\* Santa Monica, California

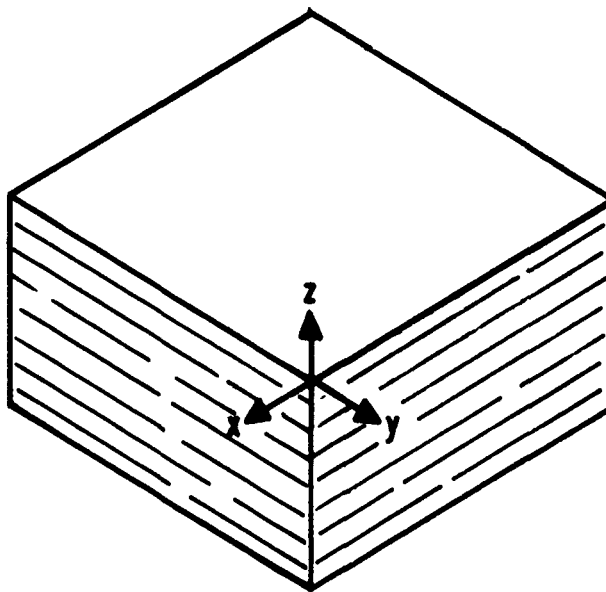


Figure 15. Coordinate System Used for Materials Exhibiting Transverse Isotropy.

$V_{lz}$	longitudinal wave in z-direction
$V_{lx}$	longitudinal wave in x- or y-directions
$V_{l,45}$	longitudinal wave at a $45^\circ$ angle between the x and z plane (or equivalently, the y and z plane)
$(V_{s,z})_x$	shear wave in z-direction with displacement in x- or y-direction
$(V_{s,x})_z$	shear wave in x-direction with displacement in z-direction
$(V_{s,x})_y$	shear wave in x-direction (y-direction) with displacement in y-direction (x-direction)

The relations between the velocities and the corresponding stiffness coefficients are (see Appendix I):

$$v_{lx} = \sqrt{\frac{c_{11}}{\rho}}$$

$$v_{lz} = \sqrt{\frac{c_{33}}{\rho}}$$

$$v_{l,45} = \sqrt{\frac{c_{11} + c_{33} + 2c_{44}}{2}} + \sqrt{\frac{(c_{11} - c_{33})^2}{2} + (c_{13} + c_{44})^2} \quad (6)$$

$$(v_{s,z})_y = (v_{s,z})_x = (v_{s,x})_z = \sqrt{\frac{c_{44}}{\rho}}$$

$$(v_{s,x})_y = \sqrt{\frac{c_{11} - c_{12}}{2\rho}}$$

where  $\rho$  is the density

The most convenient test of the symmetry condition of transverse isotropy is to compare the shear wave velocities obtained for propagation in the z direction with displacements in the x and y directions to that for propagation in the x direction with displacement in the z direction. For transverse isotropy all three velocities should be equal. For the Douglas samples the results for the shear velocities in the various directions are

<u>Propagation Condition</u>	<u>Velocity, mm/<math>\mu</math>sec</u>
$(v_{s,z})_x$	$2.15 \pm 0.03$ (1 MHz)
	$2.19 \pm 0.01$ (3 MHz)
$(v_{s,z})_y$	$2.56 \pm 0.03$ (1 MHz)
	$2.37 \pm 0.01$ (3 MHz)
$(v_{s,x})_z$	$2.23 \pm 0.02$ (1 MHz)
	$2.18 \pm 0.01$ (3 MHz)
$(v_{s,x})_y$	$2.53 \pm 0.04$ (1 MHz)
	$2.49 \pm 0.01$ (3 MHz)

Here the x direction was chosen to lie along one of the weave directions when viewing a layer plane and y was the orthogonal direction in the plane. The results reported here were obtained from the use of the 5th through 9th cycles as reference peaks in the unrectified received pulses for 1 MHz and with the 8th and 9th peaks for 3 MHz. For 1 MHz there was a systematic decrease in the velocity from the 5th through 9th peaks ( $\sim 5$  percent decrease). The peaks were approximately in the center of the pulse, and therefore, should represent attainment of steady-state conditions in the pulse. This decrease in velocity through the use of different reference peaks should therefore be ascribed to experimental uncertainty. A measurement of the shear velocity for propagation along the z axis and displacement at 45 degrees with respect to the x direction yielded a value of 2.17 mm/ $\mu$ sec at 1 MHz.

For the condition of transverse isotropy, the first three results above should be identical, and in general, different from the fourth. This is somewhat illustrated for the 3 MHz data where the results are more consistent and reproducible than those for 1 MHz. However, the data are not consistent enough to definitely distinguish the transverse isotropy condition from either a more general symmetry case or from pure isotropy.

However, the data for the GE specimens are more consistent as shown below:

<u>Propagation Condition</u>	<u>Velocity, mm/<math>\mu</math>sec</u>
$(v_{s,z})_x$	$2.080 \pm 0.016$
$(v_{s,z})_y$	$2.087 \pm 0.010$
$(v_{s,x})_z$	$2.107 \pm 0.011$
$(v_{s,x})_y$	$2.167 \pm 0.030$

The data presented above correspond to 1 MHz and a temperature of  $18 \pm 1^\circ\text{C}$ .

It is observed that the condition of transverse isotropy is verified to within  $\sim 1$  percent for the velocities  $(v_{s,z})_x$ ,  $(v_{s,z})_y$ , and  $(v_{s,x})_z$ . The elastic moduli in Equation (6) were calculated for the GE specimens using the reported longitudinal velocities of

$$v_{l,x} = 4.101 \times 10^5 \text{ cm/sec}$$

$$v_{l,z} = 3.817 \times 10^5 \text{ cm/sec}$$

$$v_{l,45} = 3.878 \times 10^5 \text{ cm/sec}$$

as given in Reference (4) at 25°C. The results for the stiffness coefficients at 25°C are then

$c_{11}$	$c_{12}$	$c_{13}$	$c_{33}$	$c_{44}$
2.49	1.10	0.82	2.16	0.65

in units of  $10^{11}$  dynes/cm<sup>2</sup>. Because of the accumulative effects arising through the use of Equation (6), the estimated uncertainties for  $c_{11}$ ,  $c_{33}$ , and  $c_{44}$  are approximately 5 percent; while for  $c_{12}$  and  $c_{13}$  the estimated uncertainties are  $\sim 10$  percent.

As shown in Appendix I, a knowledge of the five elastic stiffness constants in a transverse, isotropic medium allows a prediction of either the shear or longitudinal velocity as a function of angle of incidence with the lamination layers. The dependence of the longitudinal velocity with lamination angle at 3 MHz has been reported in Reference (4) and is reproduced in Figure 16. In Reference (4) the authors used a semi-theoretical relation derived by Horio and Onogi (Ref. 14) to explain the velocity dependence shown in the figure. This curve is given as

$$\frac{1}{V_{\theta}^2} = \frac{\cos^2 \theta}{V_o^2} + \frac{\sin^2 \theta}{V_{90}^2} \quad (7)$$

where  $\theta$  is the angle between the normal of the specimen surface and the plane of the layers, and  $V_o$  and  $V_{90}$  are the longitudinal velocities for parallel and normal angles of incidence, respectively. Equation (7) was found to predict the velocity at any orientation angle to  $\sim 2$  percent and is represented by the dashed line in Figure 16.

From Appendix I the relation between the longitudinal velocity and the angle of orientation in a transverse medium is given by

$$\begin{aligned} V_{l,\theta} = & \left[ \frac{1}{2\rho} \left( c_{11} \sin^2 \theta + c_{33} \cos^2 \theta + c_{44} \right) \right. \\ & + \frac{1}{2\rho} \left\{ \left[ (c_{11} - c_{44}) \sin^2 \theta - (c_{33} - c_{44}) \cos^2 \theta \right]^2 \right. \\ & \left. \left. + 4 \sin^2 \theta \cos^2 \theta (c_{13} + c_{44})^2 \right\}^{1/2} \right]^{1/2} \end{aligned} \quad (8)$$

where  $\theta$  is the angle between the direction of propagation and the  $z$  axis. Equation (8) was derived for the symmetry condition of transverse isotropy, and thus, provides a further test of this condition in carbon phenolic.



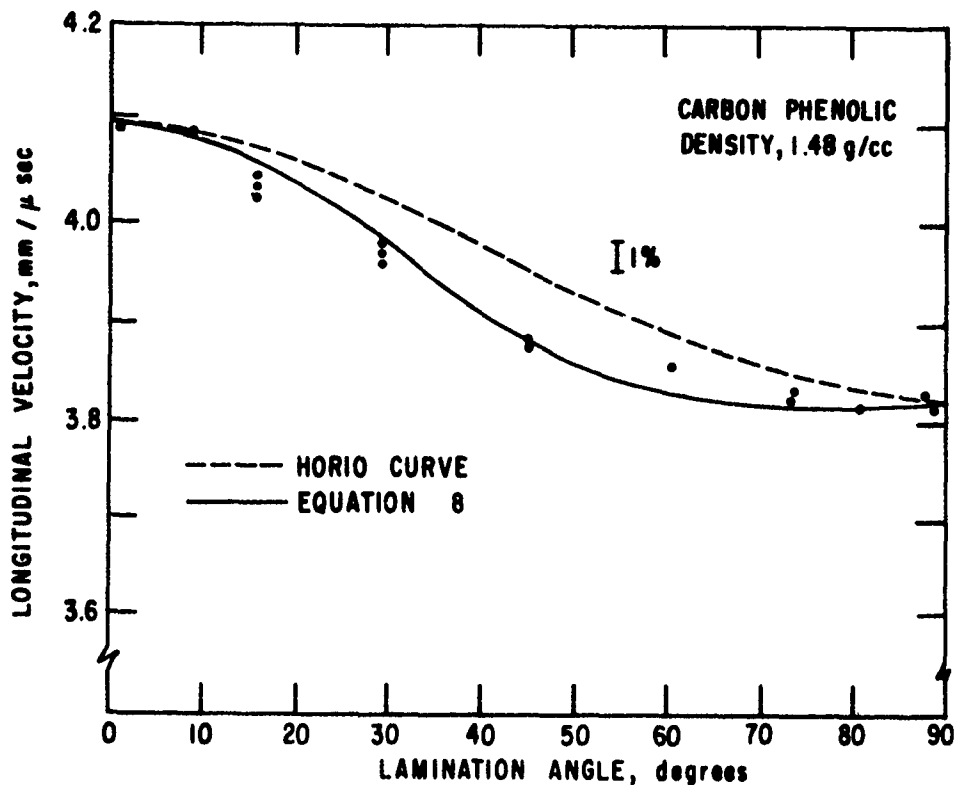


Figure 16. Longitudinal Velocity Versus Lamination Angle in Carbon Phenolic.  
(The experimental data are from Reference 4.  
The solid line is the theoretical prediction of Equation 8.)

As illustrated in Figure 16, there is good agreement between the curve predicted by Equation (8) and the experimental points. In the figure, the lamination angle is defined as the angle between the direction of propagation and the plane of the layers, or the complimentary angle in the notation of Equation (8). The poorest agreement between the theoretical prediction of Equation (8) and the experimental data is  $\sim 0.8$  percent at 60 degrees, whereas the largest separation between the Horio curve and the data is  $\sim 1\text{-}1/2$  percent. In addition, the Horio curve is consistently higher than the actual data, while the data oscillates about the curve of Equation (8). Figure 16 tends to verify Equation (8), and hence, the hypothesis that GE carbon phenolic exhibits transverse isotropy to a high degree.

Figure 17 shows the temperature dependence of the shear velocities in GE carbon phenolic.  $(v_{s,x})_y$  corresponds to propagation parallel to the layers with displacement also parallel to the layers. The curve marked  $(v_{s,z})_x$  was obtained for the combination of propagation directions perpendicular to the layers, with displacements in the two orthogonal directions to the propagation.

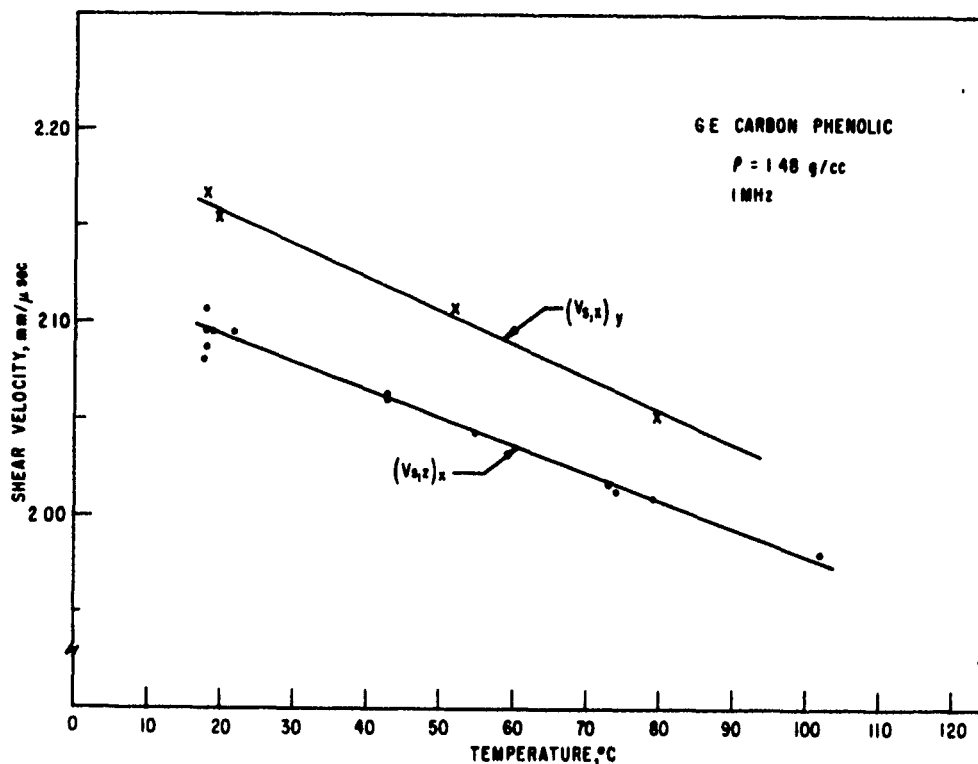


Figure 17. Temperature Dependence of the Shear Velocity in Carbon Phenolic.

Both curves were fitted to a least-squares straight line. The curves for the shear velocities in mm/μsec and T in °C are

$$\begin{aligned} (v_{s,z})_x &= 2.12 - (0.0014)T \\ (v_{s,x})_y &= 2.19 - (0.0017)T \end{aligned}$$

The temperature dependence of the longitudinal and shear velocity allows the determination of the bulk modulus and Grüneisen ratio as functions of temperature. It is shown in Section IV how the elastic stiffness coefficients can be used to calculate the adiabatic bulk modulus in transversely isotropic materials. Using these relations the temperature dependence of the bulk modulus in carbon phenolic has been calculated and is presented in Table 4. The modulus is combined with thermal data in Section III to allow the determination of the temperature dependent Grüneisen ratio.

Table 4

THE EXPANSION COEFFICIENTS OF THE BULK  
MODULUS VERSUS TEMPERATURE IN CARBON  
PHENOLIC, GE FIBERGLAS AND AVCOAT II

(Temperature range,  $\sim 25^\circ$  to  $100^\circ\text{C}$ )

Material	$B_{o,o}^S$ (kbars)	$\left(\frac{\partial B_o^S}{\partial T}\right)_{o,o}$ (kbars/ $^\circ\text{C}$ )
Carbon Phenolic	142	-0.136
GE Fiberglass	174	-0.248
Avcoat II	48.4	-0.263

(2) GE Fiberglass

Figure 18 shows the angular dependence of the longitudinal velocity in GE Fiberglass (abbreviated GEPF; density 1.91 g/cc) as reported in Reference 4. The data were obtained for 3 MHz wave propagation so that the wavelength was much larger than the layer spacing ( $\sim 45$  layers/cm). To apply the technique used for carbon phenolic, the longitudinal velocities for  $0^\circ$ ,  $45^\circ$ , and  $90^\circ$  lamination angle are needed. The results at  $26 \pm 1^\circ\text{C}$  are (Ref. 4):

$$V_{l,x} = 4.331 \text{ mm}/\mu\text{sec}$$

$$V_{l,45} = 3.708 \text{ mm}/\mu\text{sec}$$

$$V_{l,z} = 3.319 \text{ mm}/\mu\text{sec}$$

The results for the shear velocity at  $25^\circ\text{C}$  as obtained in the present study are

<u>Propagation Condition</u>	<u>Velocity, mm/<math>\mu\text{sec}</math></u>
$(v_{s,z})_x$	1.774, 1 MHz 1.780, 3 MHz
$(v_{s,z})_y$	1.765, 1 MHz 1.767, 3 MHz
$(v_{s,x})_z$	1.893, 1 MHz 1.898, 3 MHz
$(v_{s,x})_y$	2.106, 1 MHz 2.094, 3 MHz

The standard deviations of all the shear velocities reported above are approximately 2 percent.

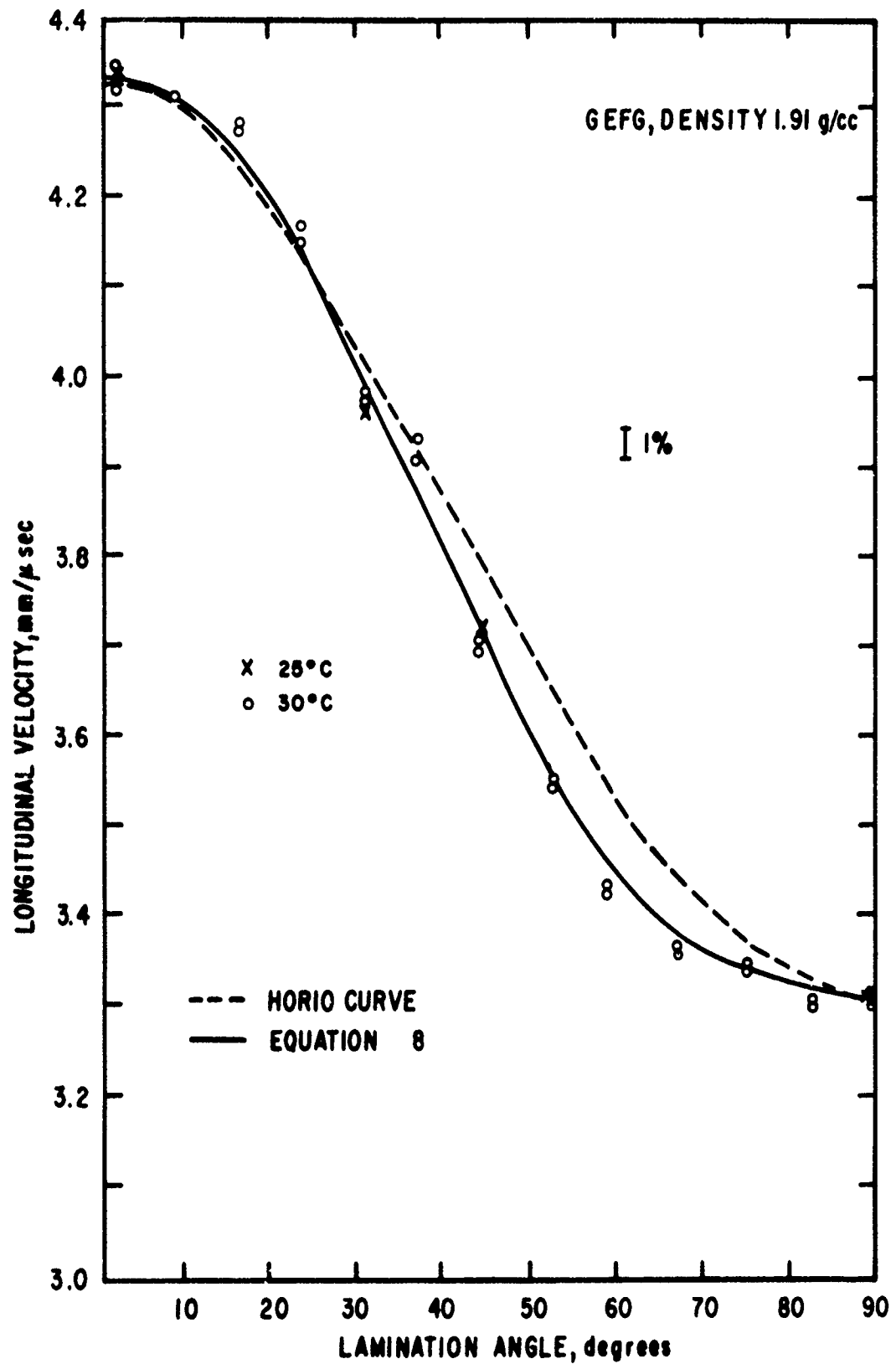


Figure 18. Longitudinal Velocity Versus Lamination Angle in General Electric Fiberglass. The Solid Curve is the Theoretical Prediction of Equation 8.

Figure 18 shows the results of using Equation (8) to predict the longitudinal velocity versus orientation angle in GE Fiberglas. The difference of  $\sim 7$  percent in  $(v_{s,x})_z$  from the other two shear velocities representing  $c_{44}$  indicates that the model of transverse isotropy is not completely valid for GEPF. However, the resulting curve as shown in Figure 18 is still well within 1 percent of the experimental data. The Horio curve represented by Equation (7) shows progressive deviation from the data, particularly for higher lamination angles.

Figure 19 shows the temperature dependence of the shear velocities in GEPF. Over the range of from 20° to 110°C the curves were fitted by least-square methods to the following equations

$$(v_{s,x})_y = 2.13 - (8.3 \times 10^{-4})T - (2.2 \times 10^{-5})T^2$$

$$(v_{s,z})_x = 1.79 - (8.9 \times 10^{-4})T - (1.6 \times 10^{-5})T^2$$

for the velocities in mm/ $\mu$ sec and the temperature T in °C.

### (3) Avcoat II

Figure 20 shows the temperature dependence of the longitudinal and shear velocities in Avcoat II (density, 1.10 g/cc). This material is similar to Avcoat 19 reported in Reference 4, with respect to velocity-temperature behavior. The least-squares fit of the data for the velocity in mm/ $\mu$ sec and the temperature in °C are

$$\text{Longitudinal: } v_l = 2.437 - (0.0097)T, \quad 25^\circ \text{ to } 110^\circ\text{C}$$

$$\text{Shear: } v_s = 1.07 - (0.0084)T, \quad 25^\circ \text{ to } 65^\circ\text{C}$$

Table 4 presents the coefficients for the expansion of the bulk modulus versus temperature in carbon phenolic, GEPF, and Avcoat II. For the layered materials, the determination of the shear coefficient,  $c_{44}$ , was obtained by arithmetically averaging the three velocities obtained through the defining Equation (6). For carbon phenolic the extreme values of the bulk modulus obtained through the use of  $(v_{s,z})_x$ ,  $(v_{s,z})_y$  or  $(v_{s,x})_z$  were within 2 percent of each other. However, for GEPF the extreme values of  $B^S$  at 25°C were 169 kbars and 177 kbars. Therefore, the uncertainty in the bulk modulus in GEPF as obtained through the use of the average value of  $c_{44}$  is about 5 percent due to symmetry approximations alone.

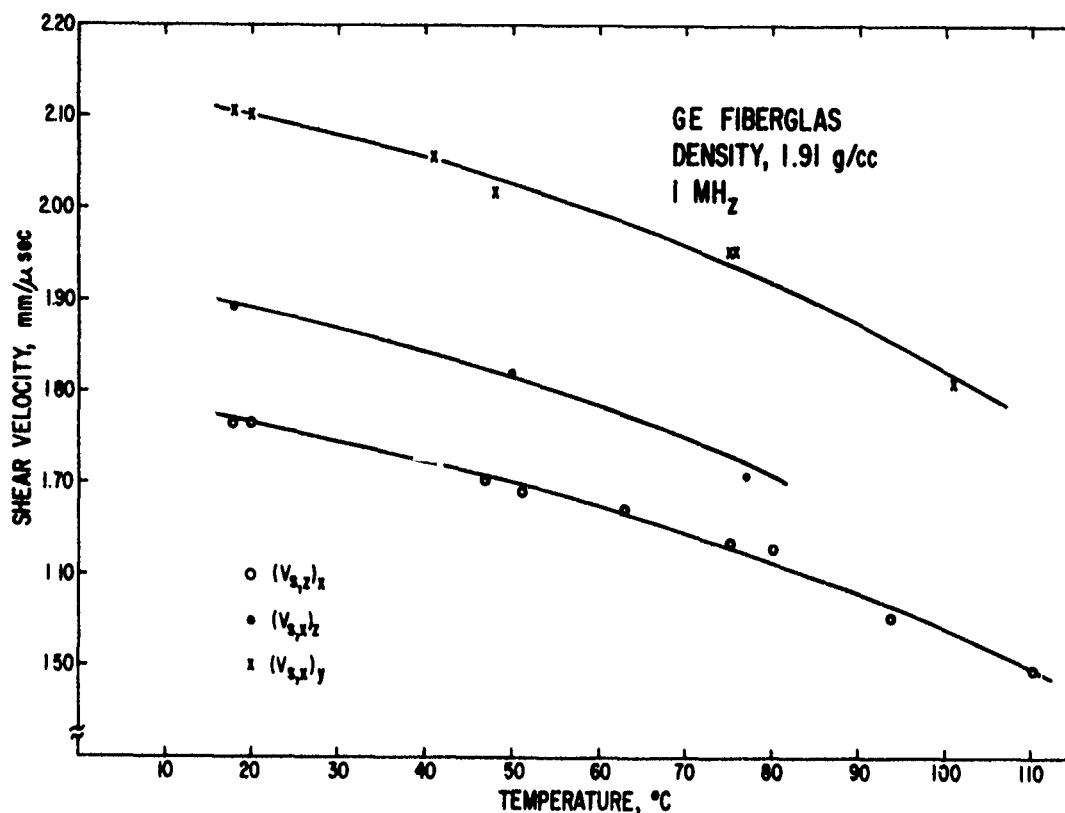


Figure 19. Temperature Dependence of the Shear Velocity in General Electric Fiberglas.

### 3. Longitudinal and Shear Velocities in Metals and Alloys

#### a. Magnesium-Thorium Alloy

This material is one of a recently developed series of heat treatable magnesium alloys containing thorium and manganese as hardeners.\* The composition of this material varies within the following impurity limits: 1.5 to 2.5 percent thorium, 0.45 to 1.1 percent manganese, 0.3 percent total other impurities.

The specimens were prepared as 2-inch square blanks ranging in thickness from 1/4 to 1-1/2 inches. The sample density was determined as  $1.771 \pm 0.006$  gm/cc.

The experimental values of longitudinal and shear velocities as a function of temperature are shown in Figures 21 and 22. The solid curves were obtained

\* Brooks and Perkins Company, Detroit Michigan; commercial designation, HM21 A, T-8 condition.

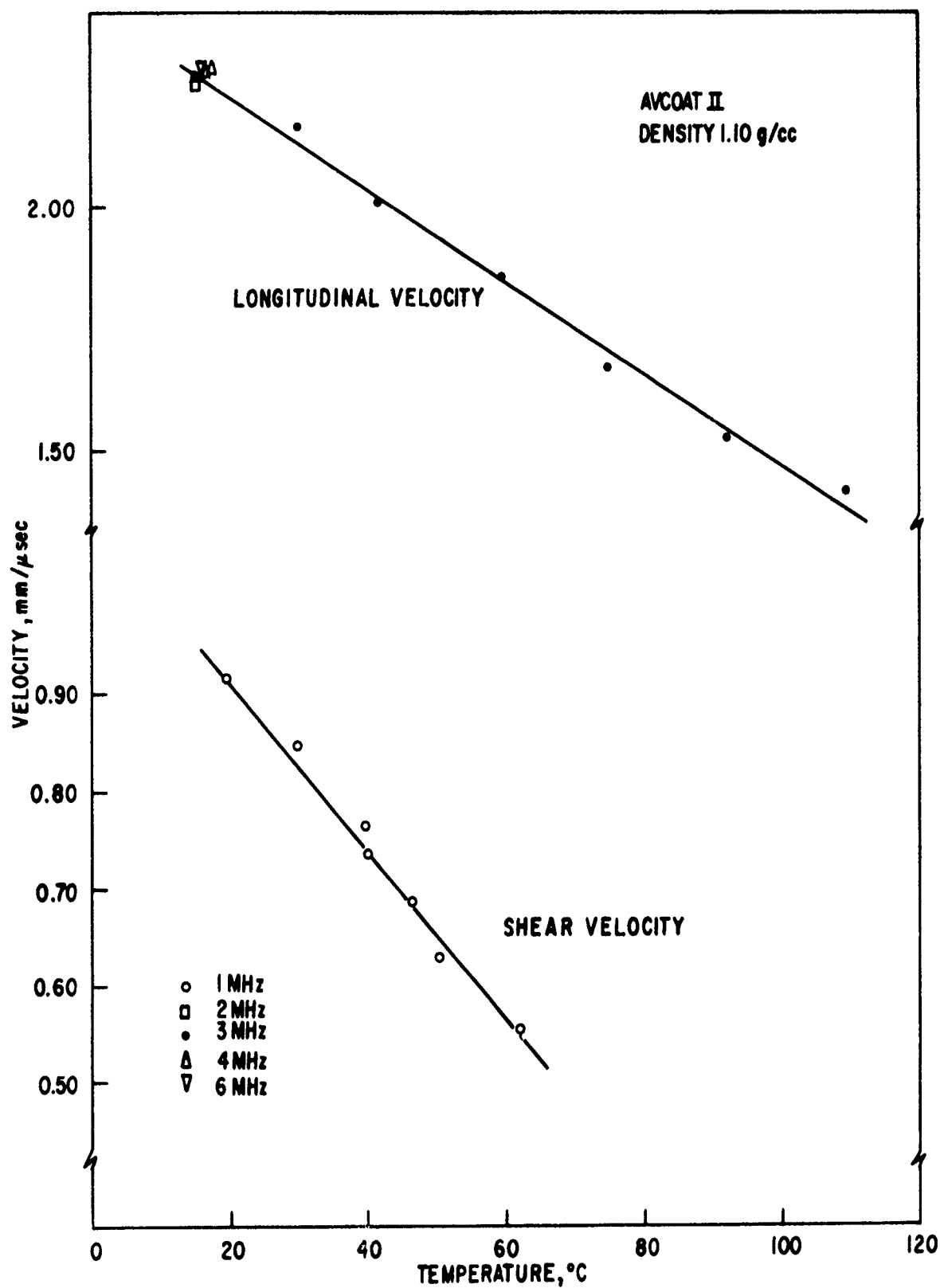


Figure 20. Temperature Dependence of the Longitudinal And Shear Velocities in Avcoat II.

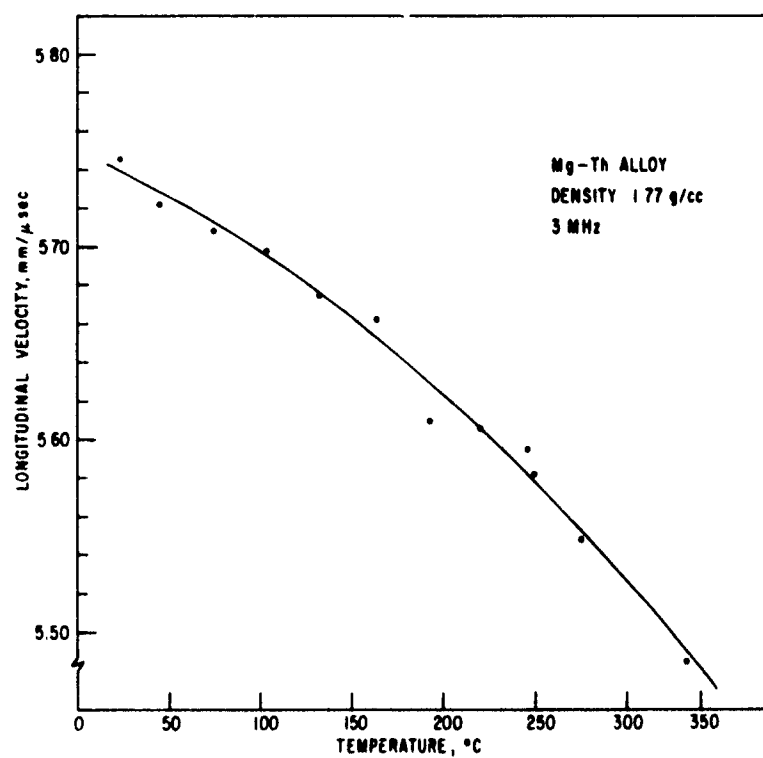


Figure 21. The Variation of the Longitudinal Velocity in Magnesium-Thorium Alloy to 350°C.

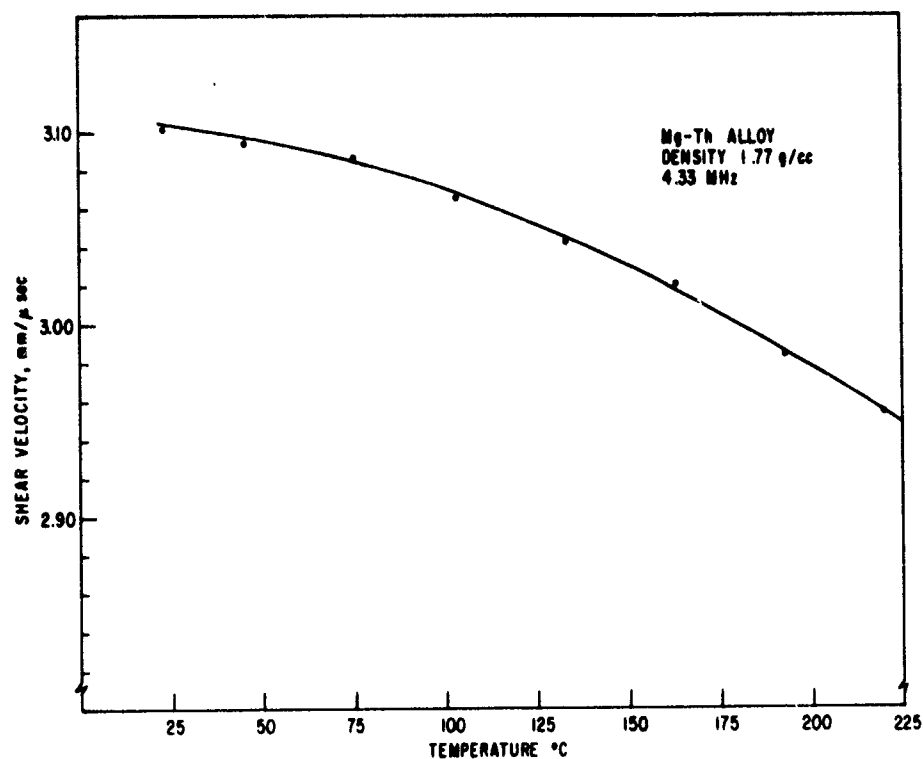


Figure 22. The Variation of the Shear Velocity in Magnesium-Thorium Alloy to 225°C.



by performing a least-squares analysis on the experimental data. In both cases a quadratic function in temperature fitted the experimental data to within the accuracy of the experimental data.

For the longitudinal measurements the estimated sum of errors in length from thermal expansion was  $\pm 0.2$  percent. The random error in transit time measurement was approximately  $\pm 0.4$  percent. Thus, the estimated precision for the velocity curve is  $\pm 0.6$  percent, which is consistent with the maximum deviation of 0.4 percent from the least squares as shown in Figure 21. The variation of the longitudinal velocity with frequency in this material is less than 0.7 percent in the frequency range of 1.5 to 10.0 MHz, with the velocity decreasing with increasing frequency. Some of this variation is due to experimental limitations, but the trend of the data is consistent with geometrical dispersion in this frequency range. The curve for the longitudinal velocity versus temperature was obtained for a frequency of 3.0 MHz. However, since the shear velocity was obtained for 4.33 MHz waves it was necessary to measure the longitudinal velocity at this frequency to calculate the various elastic moduli. It was found that the longitudinal velocity at room temperature and 4.33 MHz was within 0.2 percent of that for 3.0 MHz.

The elastic moduli were calculated by inserting the least-squares coefficients for the longitudinal and shear velocities into the appropriate modulus equations and solving for the new values of the temperature coefficients of the elastic moduli. The coefficients for all the moduli were limited to coefficients of the squared term in temperature. This was justified considering the number of data points and that the coefficients of higher degree terms in temperature decrease rapidly. The acoustic velocities and the associated adiabatic moduli in magnesium thorium alloy are given in terms of the temperature ( $^{\circ}\text{C}$ ) as\*

$$V_l = 5.749 - (3.99 \times 10^{-4})T - (1.14 \times 10^{-6})T^2$$

$$V_t = 3.108 - (1.42 \times 10^{-4})T - (2.59 \times 10^{-6})T^2$$

$$B^S = 3.55 \times 10^{11} - (4.69 \times 10^7)T$$

$$E^S = 4.435 \times 10^{11} - (1.42 \times 10^7)T - (6.04 \times 10^5)T^2$$

$$G = 1.716 \times 10^{11} - (7.99 \times 10^6)T - (2.62 \times 10^5)T^2$$

$$\sigma^S = 0.293 - (6.46 \times 10^{-6})T - (3.39 \times 10^{-7})T^2$$

---

\* Because a shear does not involve a change in volume, there is no difference between the adiabatic and isothermal shear constant G.

for the moduli in dynes/cm<sup>2</sup>, the velocities in mm/μsec, and Poisson's ratio dimensionless. The expansion of the bulk modulus was limited to the linear term in temperature because, as Figure 24 shows, this modulus was essentially constant with respect to temperature variations. A higher order polynomial expansion of the bulk modulus was therefore not required to fit the acoustic data over this temperature range.

As previously noted, the estimated uncertainty in the longitudinal velocity is ~ 1 percent. The error in shear velocity has also been found to be within 1 percent for the type of size samples used here. Hence, the most probable uncertainties in  $G$ ,  $B^S$ ,  $E^S$ , and  $\sigma$ , in whose formulation some accumulation of error occurs, are 2 percent, 3.4 percent, 2.5 percent, and 8 percent, respectively. Some of these errors are as large as the variation of the respective quantity over the indicated temperature range. However, the standard deviation of the velocity measurements was approximately 0.15 percent, for both the longitudinal and shear velocities. Using these values of uncertainty, the uncertainty in predicting the temperature behavior of  $G$ ,  $B^S$ ,  $E^S$ , and  $\sigma$  from the present velocity measurements would be 0.5 percent, 2 percent, 1 percent, and 2 percent respectively.

The temperature dependence of the various elastic moduli is indicated in Figures 23 and 24. The data reveal that the adiabatic Young's modulus and shear modulus in this material decrease over the indicated temperature range, with a curvature which is typical of the behavior in most metals over the indicated range (Ref. 15). Poisson's ratio increases with temperature, which is also typical of most metals. The temperature dependence of the adiabatic bulk modulus is difficult to predict in general and either decreases or increases with temperature, depending on particular material characteristics. As observed in this case, the bulk modulus remains essentially constant over this temperature range.

Fenn (Ref. 16) has measured Young's modulus in this material as a function of temperature by static means. His value of  $4.48 \times 10^{11}$  dynes/cm<sup>2</sup> at room temperature is within ~ 1 percent of the value as obtained here dynamically ( $4.43 \times 10^{11}$  dynes/cm<sup>2</sup> at 25°C). This implies that this material behaves as a purely elastic medium over a large frequency range, i.e., that the stress is directly proportional to the strain. If a significant difference existed in the two methods, the results obtained here would be accompanied by high first order attenuation and second order dispersion, which generally can be explained in terms of relaxation or retardation times.

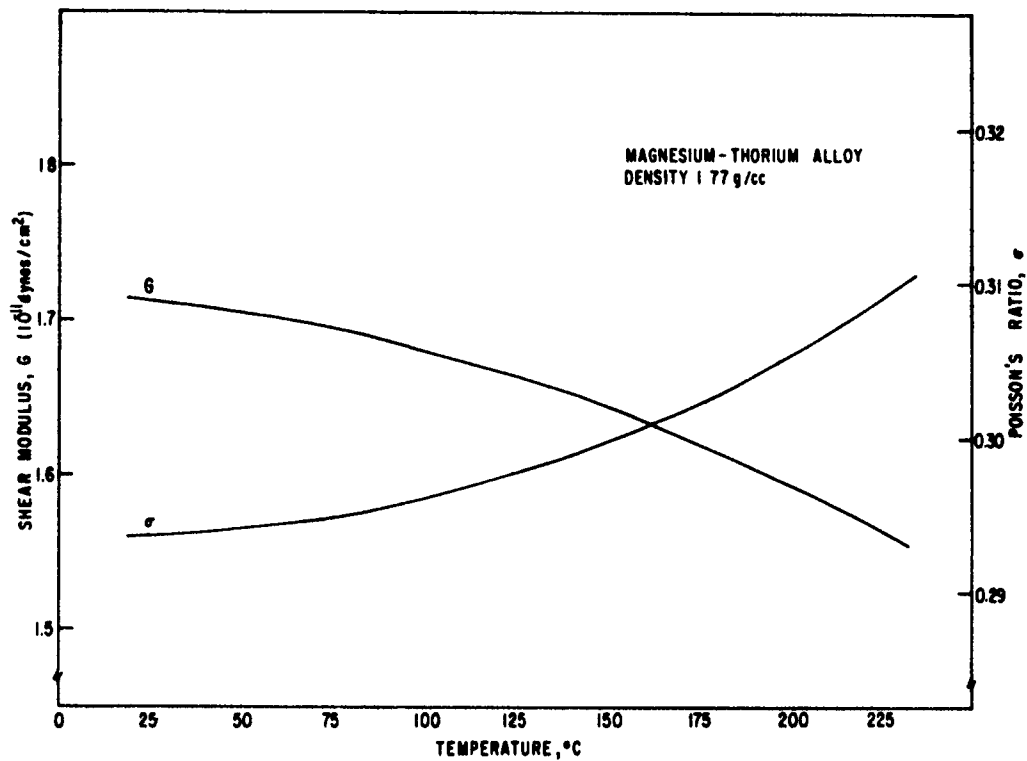


Figure 23. The Temperature Variation of the Shear Modulus,  $G$ , And the Adiabatic Poisson's Ratio in Magnesium-Thorium Alloy.

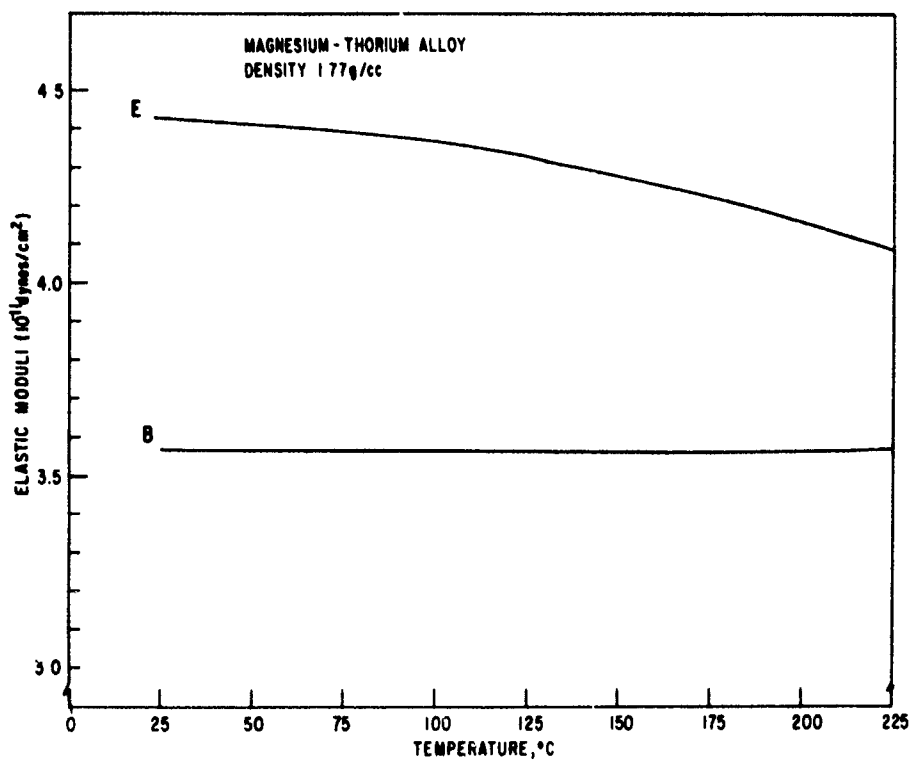


Figure 24. The Temperature Variation of the Adiabatic Young's Modulus and the Adiabatic Bulk Modulus in Magnesium-Thorium Alloy.

Although the correlation may not be exact, it is of interest to compare the adiabatic moduli as obtained here to the corresponding moduli in pure magnesium. Fahey (Ref. 17) has investigated the longitudinal and shear velocities in magnesium (density 1.81 g/cc) in the temperature range of from -232°C to 24°C. His data indicate that over this temperature range, Young's modulus decreases, the bulk modulus remains fairly constant, the shear modulus decreases, and Poisson's ratio increases. The magnitude of these quantities as determined by Fahey at 24°C are

$$E = 4.34 \times 10^{11} \text{ dynes/cm}^2$$

$$B = 3.79 \times 10^{11} \text{ dynes/cm}^2$$

$$G = 1.65 \times 10^{11} \text{ dynes/cm}^2$$

$$\sigma = 0.308$$

which are in fair agreement with the present experimental results. Exact agreement cannot be expected because the purity of magnesium is different in the two cases. However, the data should be similar considering that the material used here is approximately 97 percent magnesium.

#### b. Gold

Figure 25 illustrates the temperature dependence of the longitudinal and shear velocity in gold (density, 18.96 g/cc). The specimens were approximately 99 percent pure, although an analysis of impurities was not performed. The following relations exist between the velocities and temperature for the curves in Figure 23.

$$\text{Longitudinal Velocity: } V_l = 3.292 - (0.00027)T, \quad 25^\circ \text{ to } 280^\circ\text{C}$$

$$\text{Shear Velocity: } V_t = 1.234 - (0.00016)T, \quad 25^\circ \text{ to } 170^\circ\text{C}$$

for  $V$  in mm/ $\mu$ sec and  $T$  in °C.

#### c. Lead

Velocity measurements were performed on lead using the buffer technique. The lead specimens were prepared by melting lead brick (~99 percent lead) and casting into ~1-inch diameter rods. Various thickness specimens were then prepared from the rod. This technique yielded samples which exhibited a significant number of internal voids. The resulting average density of 11.2 g/cc was ~22 percent lower than the value of 11.4 g/cc as reported in the Handbook of Chemistry and Physics (46th edition). This degree of porosity did not affect the longitudinal velocity measurements but did prevent reliable shear wave measurements.

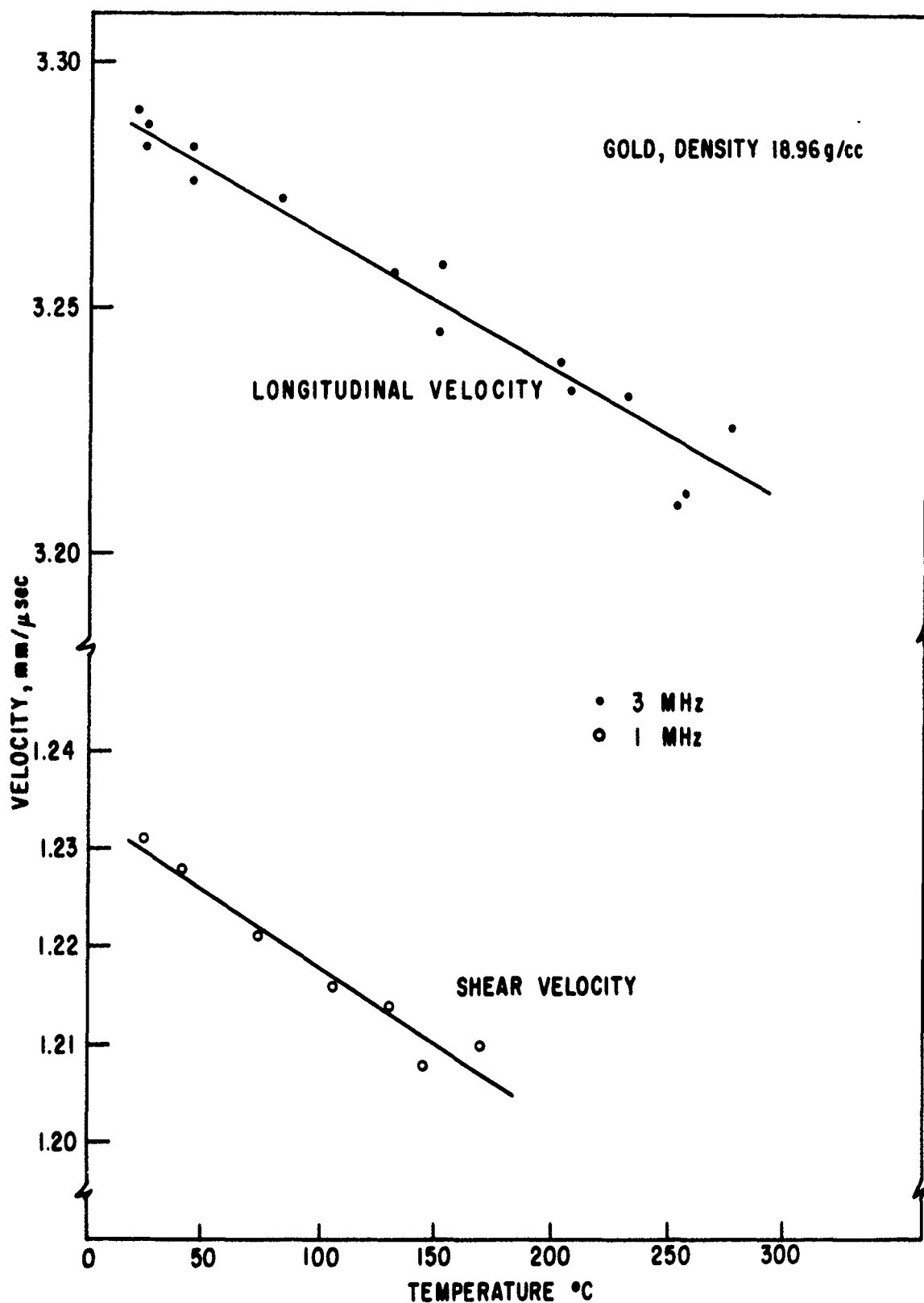


Figure 25. Temperature Dependence of the Longitudinal And Shear Velocities in Gold.

The longitudinal velocity versus temperature with the solid buffer is shown in Figure 26, as obtained from three different samples ranging in thickness from 3 to 9 mm. As shown in the curve there is appreciable scatter. This is probably due to inhomogeneities within the specimens. The velocity data were fitted to a least-squares line of the form

$$V_L = 2.29 - 0.00037T, \quad 25^\circ \text{ to } 250^\circ\text{C}$$

for  $V_L$  in mm/ $\mu$ sec and  $T$  in  $^\circ\text{C}$ .

#### d. Aluminum

Acoustic measurements were performed on two aluminum alloys, 1060 Al (measured bulk density of  $2.703 \pm 0.002$  g/cc) and 6061-T6 Al (bulk density,  $2.704 \pm 0.003$  g/cc). The 1060 alloy is essentially pure aluminum (99.6 percent Al) which exhibits a low yield strength ( $\sim 4000$  psi) when used in the annealed condition, as in the present experiments. The 6061 Al is  $\sim 98$  percent aluminum with minor amounts of magnesium, chromium, silicon, and copper. In the T-6 condition this alloy possesses a yield strength of  $\sim 37,000$  psi. The uniaxial stress arrangement described in Section II was used to apply a one-dimensional stress to  $\sim 1$ -inch cubes of both materials. The longitudinal and shear velocities were then measured for propagation direction perpendicular to the stress. This technique allows the determinations of the third-order elastic constants, if the various wave and displacement vectors are properly oriented with respect to the symmetry of the specimen and the externally applied stress. The third-order constants can be used to calculate the pressure derivative of the adiabatic bulk modulus or to predict anharmonic behavior. This technique is not required to determine the pressure derivative of the bulk modulus, since the pressure derivatives of the second-order elastic constants can also be obtained from hydrostatic pressure measurements on the acoustic velocities. However, this capability is not available at the Air Force Weapons Laboratory at the present, so that an attempt was made to determine the pressure derivatives with a uniaxial stress technique.

Figure 27 shows the dependence of velocity on uniaxial pressure in 6061-T6 Al. The aluminum used for these measurements had been solution heat treated and artificially aged. Most of the measurements were taken on the specimens after machining and without annealing. The data illustrated in the figure correspond to shear wave propagation perpendicular to the stress. Since the degeneracy of the characteristic matrix for the undeformed material is removed

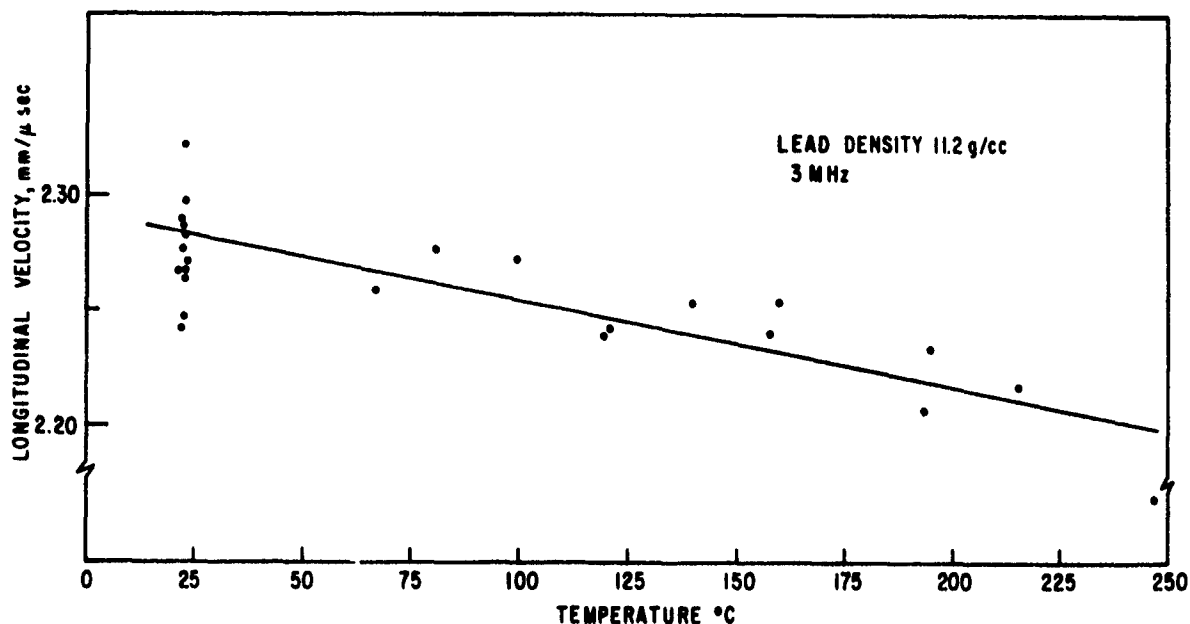


Figure 26. The Longitudinal Velocity Versus Temperature in Lead.

by application of the uniaxial stress, the two transverse modes have different speeds. However, as the figure shows, there is a definite scatter of points, particularly for the shear  $(|||)$  mode. The six slopes shown in Figure 27 for this mode were obtained on one specimen by measuring in the two perpendicular directions for each of the three samples axes. The notation used here corresponds to applied stress ( $M_i$ ), propagation direction ( $N_j$ ), and particle displacement ( $U_k$ ) along the three coordinate axes. Considering a precision of  $\sim 1$  part in  $10^4$  there is a definite separation into at least three different slopes. The effect was reproducible in that measurements for one set of conditions were reproducible after the specimen had been subjected to various other axial loadings. The effect was also consistent, since other specimens exhibited a separation of the shear  $(|||)$  mode into approximately the same slopes. Hysteresis for all the uniaxial measurements was negligible if the maximum stress was kept below the yield strength. Annealing did not produce a detectable change in the slopes, but the range of applied pressure was limited because of lower yield strength.

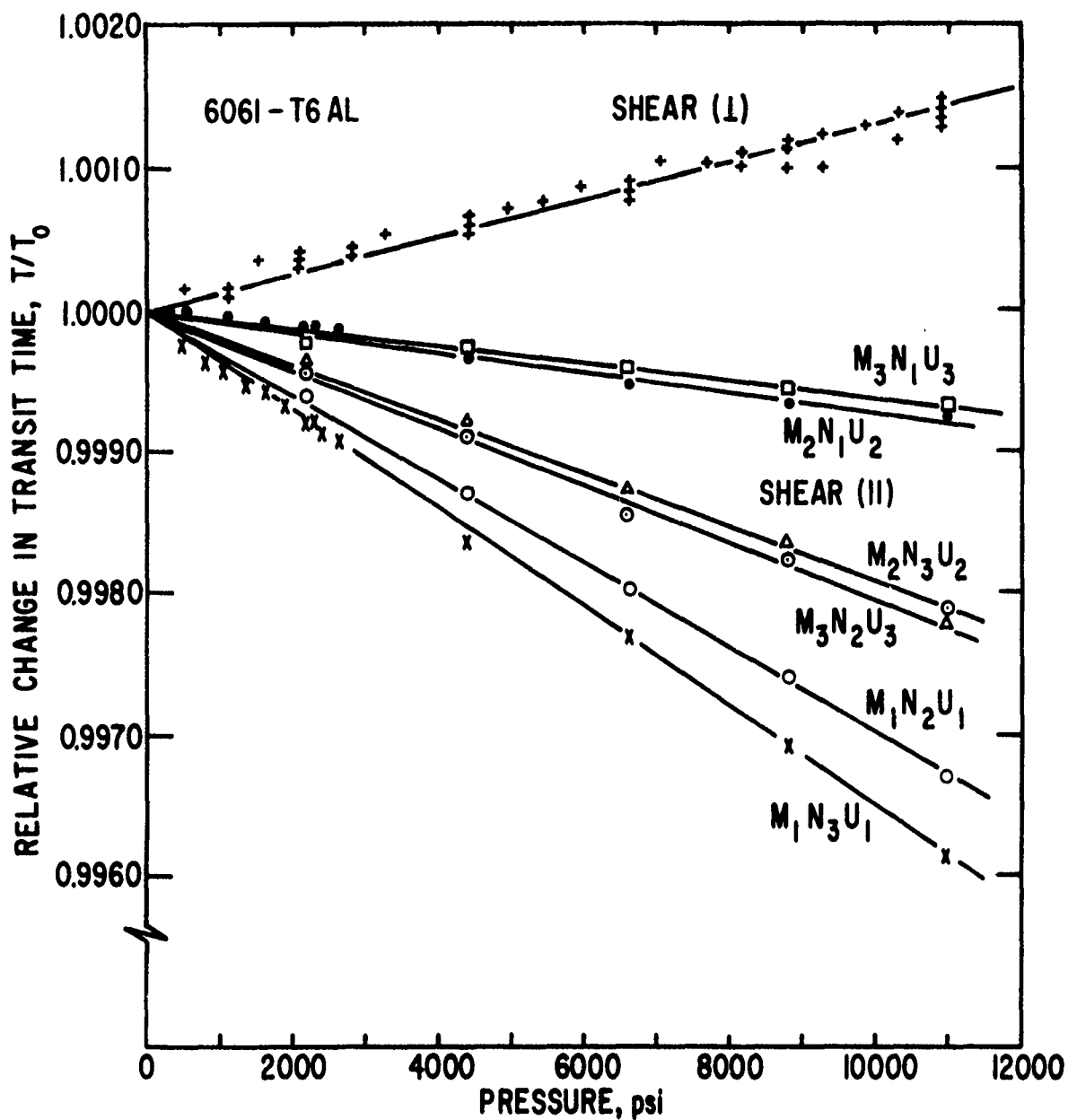


Figure 27. The Relative Change in Transit Time Versus Uniaxial Stress for the Two Shear Modes in 6061-T6 Aluminum at 25°C.  
(See the text for the notation used here.)



The shear ( $\perp$ ) mode did not show a noticeable dependence upon the stress and propagation directions as the shear ( $\parallel$ ) mode did. The shear ( $\perp$ ) data presented in Figure 27 were obtained from a number of different specimens and for different stress directions. All of the data are within 1 part in  $10^4$  of the least-squares lines.

The longitudinal mode gave results similar to the shear ( $\parallel$ ) mode, but was less dependent on sample orientation. Figure 28 indicates the behavior of velocity with uniaxial pressure for the specimen corresponding to the shear ( $\parallel$ ) mode in Figure 27. Although the maximum separation of the longitudinal pressure-slopes is  $\sim 6$  parts in  $10^4$  at 10,000 psi (versus  $\sim 3$  parts in  $10^3$  for the shear ( $\parallel$ ) measurements), this magnitude of variation is well outside experimental uncertainty. The splitting of the slopes was also observed on other specimens, but the data are omitted from the figure for the sake of clarity. Table 5 shows the slopes obtained from a least-squares analysis on all data. The slopes  $\alpha$  are calculated from the relation

$$\left( \frac{t_o}{t} - 1 \right) = \alpha P \quad (9)$$

where the relative transit time  $t_o/t$  is the inverse of the ratios shown in Figures 27 and 28. The maximum range of slopes is given for the shear ( $\parallel$ ) mode, and an average of all samples for the shear ( $\perp$ ) mode and longitudinal modes.

The 6061-T6 aluminum used in these experiments exhibited a grain length of about 1 mm. The material also appeared to exhibit stratification on a microscopic scale. The sample corresponding to the shear ( $\parallel$ ) mode of Figure 27 and the longitudinal mode of Figure 28 exhibited apparent stratification approximately perpendicular to the  $M_1$  axis. In some of the other specimens the stratification appeared at various angles to the specimen axes. However, in these specimens the variation of the slopes for the shear ( $\parallel$ ) mode likewise varied slightly from that in Figure 27.

Texture on a microscopic scale was probably induced in the material during initial rolling, which results in a nonuniform distribution of stresses for an applied uniaxial stress. In any case, the data reported here for uniaxial pressure would have to be supplemented by other information, such as the pressure derivatives of the longitudinal and shear velocities under hydrostatic pressure, in order to reliably calculate the third-order coefficients.

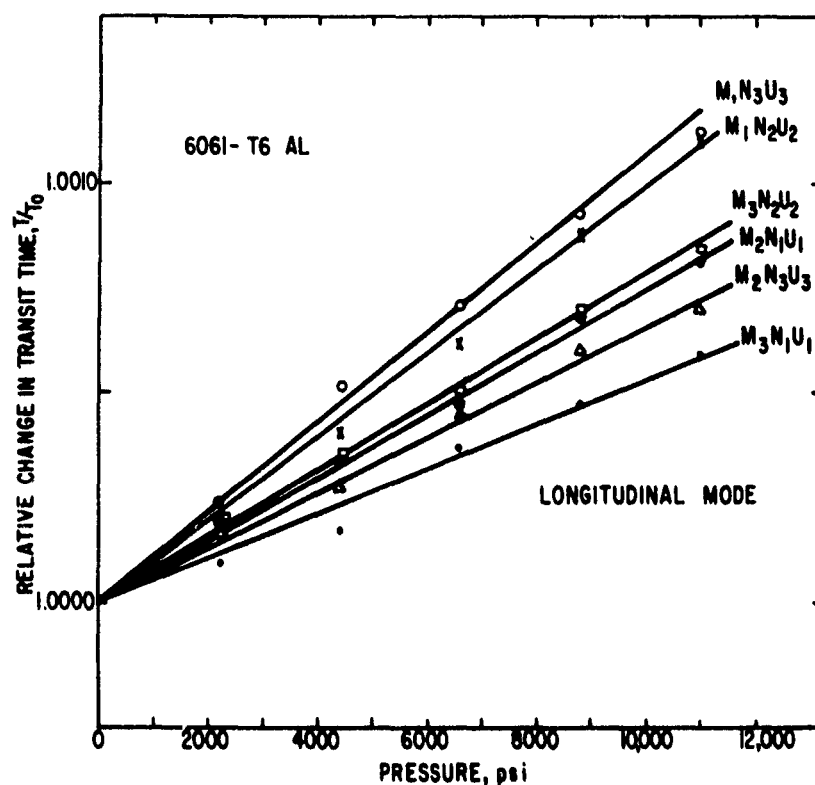


Figure 28. Relative Change in Transit Time Versus Uniaxial Stress for the Longitudinal mode in 6061-T6 Aluminum.

The three separate curves for the shear  $(||)$  mode in Figure 27 are what would be expected if the grain orientation in the specimen was oriented close, but not exactly parallel, to one of the specimen axes. If the observed splitting is a result of only this effect, the results shown here could be used to rotate the coordinate system so that each pair of the three slopes corresponded to the same value of slope. This would give the necessary angular deviation of the specimen symmetry from the three principal axes (Ref. 18).

Metallurgical examination also indicated that the 6061-T6 aluminum used in the present experiments exhibited a higher impurity and porosity than is common in this alloy. However, specimens obtained from two different sources were similar in microscopic detail and velocity variation versus temperature and pressure.

Table 5

## ELASTIC PROPERTIES OF 6061-T6 ALUMINUM

Density, g/cc	2.704
Longitudinal Velocity*, $V_L$ , mm/ $\mu$ sec	$6.426 \pm 0.002 - (0.00091 \pm 0.00001)T$
Shear Velocity, $V_t$ , mm/ $\mu$ sec	$3.188 \pm 0.003 - (0.00086 \pm 0.00003)T$
Young's Modulus, $E^S$ , dynes/cm <sup>2</sup>	$7.35 \times 10^{11} - (4.16 \times 10^8)T$
Shear Modulus, $G$ , dynes/cm <sup>2</sup>	$2.75 \times 10^{11} - (1.67 \times 10^8)T$
Bulk Modulus, $B^S$ , dynes/cm <sup>2</sup>	$7.51 \times 10^{11} - (1.70 \times 10^8)T$
Poisson's Ratio, $\sigma^S$	$0.336 + (0.00011)T$
Grüneisen Ratio, $\gamma$ , at 25°C	2.139
Uniaxial Pressure Slope, $\alpha_L$ , cm <sup>2</sup> /dynes Longitudinal Mode (25°C)	$(-1.17 \pm 0.01) \times 10^{-12}$
Uniaxial Pressure Slope, $\alpha_s$ , cm <sup>2</sup> /dynes Shear (  ) Mode (25°C)	$(1.04 \rightarrow 5.36) \times 10^{-12}$
Uniaxial Pressure Slope, $\alpha_s$ , cm <sup>2</sup> /dynes Shear (⊥) Mode (25°C)	$(-1.927 \pm 0.005) \times 10^{-12}$

\*Temperature in °C

Figure 29 shows the temperature dependence of the longitudinal and shear velocities in 6061-T6 aluminum. The measurements were made on a specimen 1.5 inches long (annealed at 400°C for  $\sim 3$  hours) with both 3 MHz quartz and PZT-5 crystals for the longitudinal mode. Both solid lines in Figure 29 correspond to measurements made along the same specimen axis (which was perpendicular to the apparent stratification layers). For the longitudinal measurements, the velocities in both directions perpendicular to this axis were about 0.4 percent higher, as illustrated by the dashed line. For displacement direction parallel to a cube edge the 6 different shear modes agreed to within 0.2 percent. The elastic moduli were calculated from the usual relations for an isotropic medium and are shown in Table 5 as a function of temperature. The moduli were computed from arithmetic means of the longitudinal and shear modes, and were calculated as linear functions of temperature, since the higher order terms were insignificant to  $\sim 250^\circ\text{C}$ .

Figure 30 illustrates the relative change in transit time for all three velocity modes in 1060 Al. The material used here had been annealed so that the yield strength was much lower than that in 6061-T6 aluminum. The data were therefore confined to lower pressures, leading to somewhat reduced accuracy

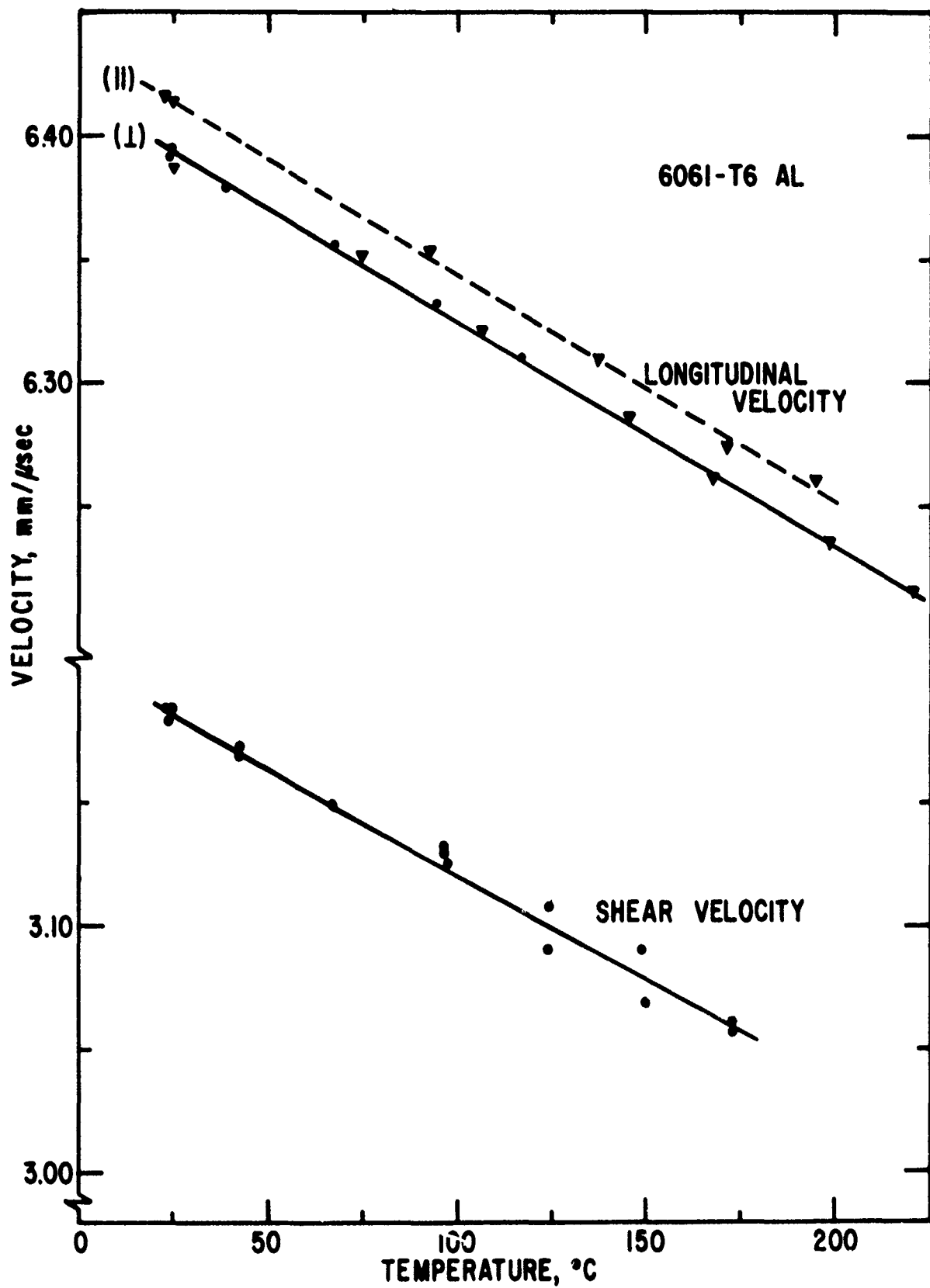


Figure 29. Temperature Dependence of the Longitudinal And Shear Velocities in 6061-T6 Aluminum.

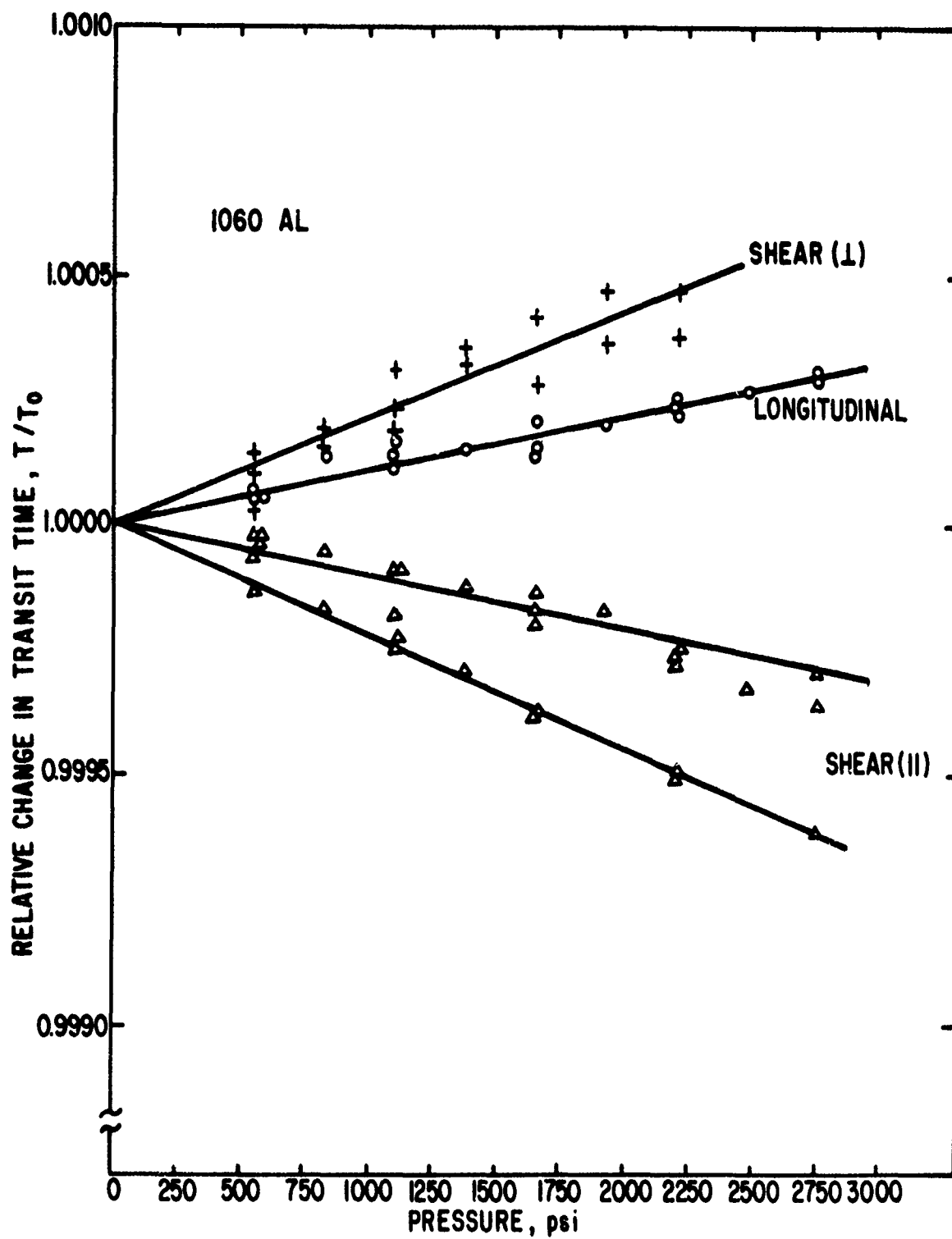


Figure 30. Relative Change in Transit Time Versus Uniaxial Stress for All Three Velocity Modes in 1060 Aluminum at 25°C.

in the slopes. However, as Figure 30 illustrates, the slope for the shear  $(||)$  mode still appears to be split into two components. In Table 6, the range of the two slopes for the shear  $(||)$  mode in Figure 30 are listed and all the data for the shear  $(\perp)$  and the longitudinal mode are tabulated as single slopes.

Figure 31 illustrates yielding behavior in 1060 aluminum. Both solid lines correspond to increasing pressure for two previously unstressed specimens. The dashed line for the shear  $(||)$  mode corresponds to data taken for decreasing pressure after deviation from the straight line fit is significant. As shown, appreciable hysteresis is present ( $\sim 3$  parts in  $10^4$ ) after yielding occurs; however, the relaxation slope is approximately the same as that for increasing pressure before the limit is exceeded. The data for the longitudinal mode were obtained to 8800 psi (the corresponding relative transit time was 1.0091) and indicate departure from linearity at a somewhat different pressure than that for the shear  $(||)$  mode. The data for decreasing pressure (not shown) were essentially linear to zero stress, with a slope of approximately half that for increasing pressure (the zero pressure value of  $t/t_0$  was 1.00882).

The behavior of annealed 6061-T6 aluminum during yielding was similar to that for 1060 aluminum. The slope of the shear  $(||)$  mode in 6061-T6 after annealing was equal to that before annealing, but departure from linearity began at  $\sim 4400$  psi.

The temperature dependences of longitudinal and shear velocities in 1060 aluminum are shown in Figure 32. The data did not indicate a marked dependence of the velocities upon direction of propagation along the axes of the cube as in 6061-T6 aluminum. Microscopic examination revealed elongated grain size, but the stratification was less evident than that observed in 6061-T6. The data in Figure 32 correspond to 3 MHz, but measurements from 2 to 9 MHz indicated negligible dispersion in this frequency range. Table 6 summarizes the results on 1060 aluminum.

Table 7 illustrates the equations which relate a linear change in transit time in an isotropic medium to applied pressure for both hydrostatic and uniaxial compression. The third-order coefficients  $v_1$ ,  $v_2$ , and  $v_3$  correspond to the notation employed by Brugger (Ref. 19). All of the coefficients shown in the table can be calculated from the pressure derivative  $(\rho_0 W^2)'_{p=0}$ , where  $\rho_0$  is the initial velocity and  $W$  is the "natural velocity" (velocity obtained by assuming no length changes when pressure is applied). The natural velocity is related

Table 6

## ELASTIC PROPERTIES OF 1060 ALUMINUM

Density, g/cc	2.703
Longitudinal Velocity*, $V_l$ , mm/ $\mu$ sec	$6.404 \pm 0.003 - (0.00100 \pm 0.00003)T$
Shear Velocity, $V_t$ , mm/ $\mu$ sec	$3.183 \pm 0.002 - (0.00079 \pm 0.00003)T$
Young's Modulus, $E^S$ , dynes/cm <sup>2</sup>	$7.32 \times 10^{11} - (3.92 \times 10^8)T$
Shear Modulus, $G$ , dynes/cm <sup>2</sup>	$2.74 \times 10^{11} - (1.55 \times 10^8)T$
Bulk Modulus, $B^S$ , dynes/cm <sup>2</sup>	$7.43 \times 10^{11} - (2.16 \times 10^8)T$
Poisson's Ratio, $\sigma^S$	$0.335 + (0.000094)T$
Grüneisen Ratio, $\gamma$ , at 25°C	2.113
Uniaxial Pressure Slopes, $\alpha_l$ , cm <sup>2</sup> /dynes (Longitudinal Mode (25°C))	$(-1.49 \pm 0.02) \times 10^{-12}$
Uniaxial Pressure Slopes, $\alpha_s$ , cm <sup>2</sup> /dynes Shear (  ) Mode (25°C)	$(1.55 \rightarrow 3.42) \times 10^{-12}$
Uniaxial Pressure Slope, $\alpha_s$ , cm <sup>2</sup> /dynes Shear (⊥) Mode (25°C)	$(-2.89 \pm 0.06) \times 10^{-12}$

\*Temperature in °C

to the actual velocity  $V(P)$  at pressure  $P$  by

$$W(P) = \frac{l(o)}{l(P)} V(P) \quad (10)$$

where  $l(o)$  is the initial length and  $l(P)$  is the length at pressure  $P$ .

$(\rho_o W)'_{P=0}$  can be obtained from the ultrasonic data as follows

$$\begin{aligned}
 W &= W_o + W'_P, W_o = V_o \\
 \frac{W}{W_o} &= \frac{t_o}{t} \\
 (\rho_o W)'_{P=0} &= 2 \frac{\rho_o V_o^2}{P} \left( \frac{t_o}{t} - 1 \right) \\
 (\rho_o W)'_{P=0} &= 2 \rho_o V_o^2 \alpha \\
 &= 2 \omega \alpha
 \end{aligned} \quad (11)$$

where  $t_o/t$  is the inverse ratio of the transit time at pressure  $P$  to that at atmospheric pressure, and  $\alpha$  is the slope presented in Tables 5 and 6.

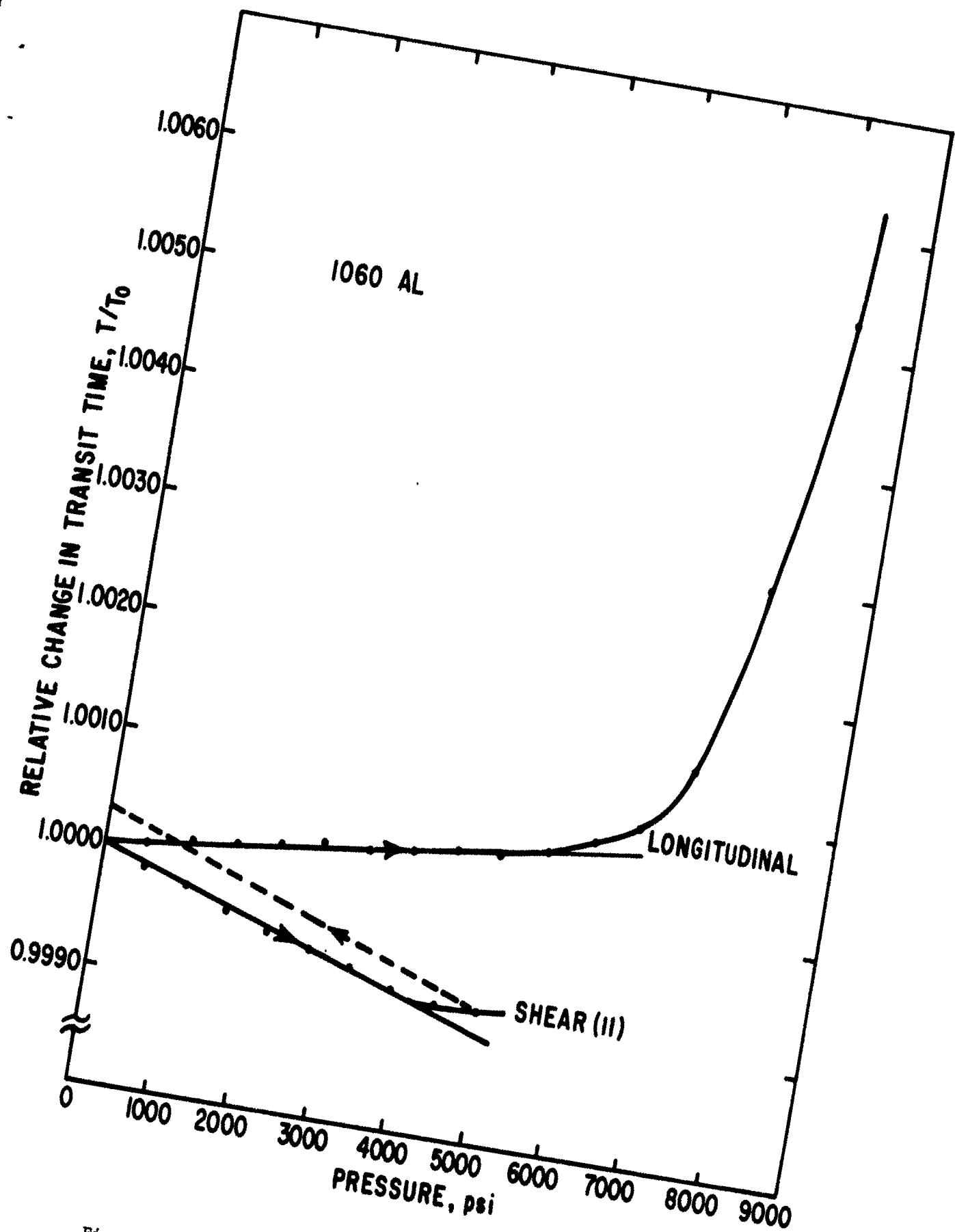


Figure 31. Yielding Behavior in 1060 Aluminum at 25°C.



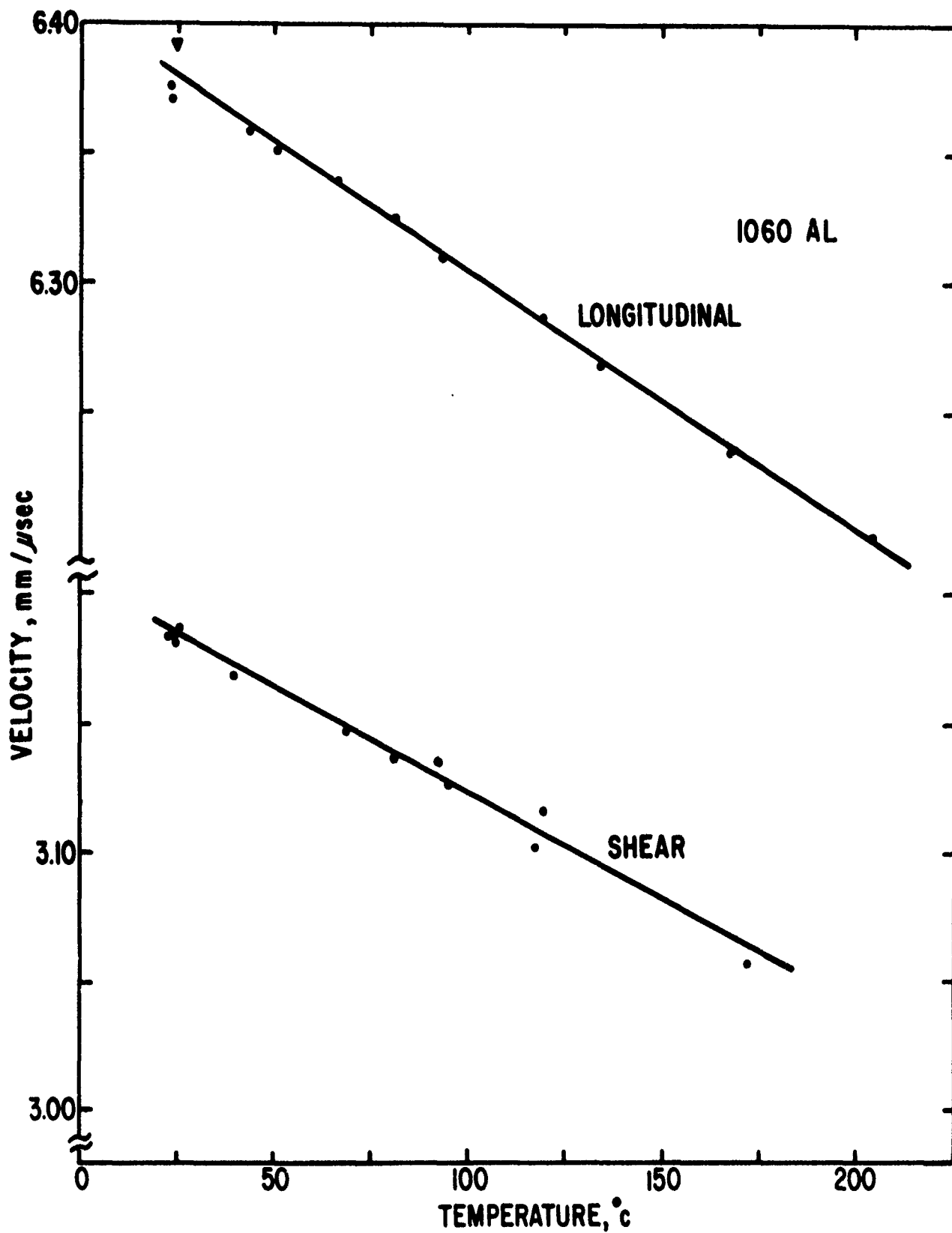


Figure 32. Temperature Dependence of the Longitudinal And Shear Velocities in 1060 Aluminum.

Table 7

SECOND- AND THIRD-ORDER ELASTIC CONSTANTS FOR AN ISOTROPIC  
MEDIUM UNDER HYDROSTATIC PRESSURE AND UNIAXIAL COMPRESSION

Type of Stress	Propagation Direction $\underline{N}$	Mode*	Displacement Direction $\underline{U}$	$\omega \equiv \left( \rho \frac{V^2}{\rho_0} \right)_{P=0}$	$(\rho_0 W^2)'$
Hydrostatic Pressure	arbitrary	L	$\parallel$ to $\underline{N}$	$\lambda^S + 2\mu$	$-1 - \frac{1}{3BT} (2\omega + 3\nu_1 + 10\nu_2 + 8\nu_3)$
Hydrostatic Pressure	arbitrary	S	$\perp$ to $\underline{N}$	$\mu$	$-1 - \frac{1}{3BT} (2\omega + 3\nu_2 + 4\nu_3)$
Uniaxial Compression	$\perp$ to stress	L	$\parallel$ to $\underline{N}$	$\lambda^S + 2\mu$	$\frac{1}{E} \left[ \sigma^T (2\omega + 8\nu_3) + \nu_1 (2\sigma^T - 1) + \nu_2 (8\sigma^T - 2) \right]$
Uniaxial Compression	$\perp$ to stress	S	$\parallel$ to $\underline{M}^{**}$	$\mu$	$\frac{1}{ET} \left[ -2\omega + \nu_2 (2\sigma^T - 1) + 2\nu_3 (\sigma^T - 1) \right]$
Uniaxial Compression	$\perp$ to stress	S	$\perp$ to $\underline{M}$	$\mu$	$\frac{1}{ET} \left[ \sigma^T (2\omega + 4\nu_3) + \nu_2 (2\sigma^T - 1) \right]$

\*L = longitudinal; S = Shear;  $BT = \lambda^T - 2/3\mu$  = isothermal bulk modulus;  $ET = 3\mu BT / (\lambda^T + \mu)$  = isothermal

Young's modulus;  $\sigma^T = \lambda^T / 2 (\lambda^T + \mu)$  = isothermal Poisson's ratio;  $\lambda^T$  and  $\mu$  are Lamé constants

$\lambda^T$  is the isothermal constant whereas  $\mu^T = \mu^S$ , since the shear constant involves no change in volume.

\*\* $\underline{M}$  is the stress direction.

The third-order coefficients can then be used to form the pressure derivative of the adiabatic bulk modulus by

$$\left(\frac{\partial B^S}{\partial P}\right)_{P=0} = - \frac{9v_1 + 18v_2 + 8v_3}{9B^T} - \frac{1}{3} \beta \gamma T \quad (12)$$

where  $\beta$  is the volume coefficient of expansion,  $\gamma$  is the Grüneisen ratio,  $T$  is the absolute temperature, and  $B^T$  is the isothermal bulk modulus, defined in terms of the adiabatic modulus as

$$B^T = \frac{B^S}{1 + \beta \gamma T} \quad (13)$$

Although the pressure derivative  $B^{S'}$  can be obtained through the uniaxial technique, the results are usually not as accurate as those obtained with hydrostatic pressure. This is particularly true of polycrystalline materials where plastic strain, induced by the one-dimensional stress, can lead to changes in the transit time larger than the change caused by elastic deformation. The uniaxial approach is also limited to pressures lower than the elastic limit so that it is difficult to test the linearity of the bulk modulus versus pressure with this technique. However, with hydrostatic pressure the symmetry of the specimen is preserved under pressure, resulting in no change in the relations between the moduli and velocities. The derivative of the bulk modulus can thus be directly obtained from the hydrostatic pressure derivatives of the velocities as follows for an isotropic medium:

$$\begin{aligned} (B^S)_{P=0} &= \rho_0 \left( v_{\ell}^2 - \frac{4}{3} v_t^2 \right)_{P=0} \\ (B^{S'})_{P=0} &= 2\rho_0 \left( v_{\ell 0} v'_{\ell 0} - \frac{4}{3} v_{t 0} v'_{t 0} \right) + 1 + \beta \gamma T \end{aligned} \quad (14)$$

In Equation (14) the derivative of the actual velocities must be known, so that it is necessary to know the length change with pressure. Cook (Ref. 20) shows that the ultrasonic measurement of the compressibility at normal pressure can be used to determine the corresponding length changes under pressure.

Since the slopes of the transit time curves for the longitudinal mode and the shear ( $||$ ) mode are very dependent upon the directions of propagation and particle displacement in the present experiments, uniaxial stress measurements are not reliable for determining third-order coefficients, and hence, the

pressure derivative  $B^S$  through Equation (12) in polycrystalline aluminum. However, hydrostatic measurements would again be useful in this respect, because, as shown in Table 7, ultrasonic data for hydrostatic pressure would yield two equations relating to the three unknown third-order coefficients. The slope of the shear ( $\perp$ ) mode might then be used to calculate the three coefficients. This approach would only be appropriate to first-order because of the microanisotropy due to grain texture. The third-order coefficients in aluminum could also be determined by studying the distortion of sinusoidal ultrasonic waves into higher harmonics as a function of propagation distance (Ref. 21).

Smith, et al. (Ref. 22) have determined the third-order coefficients in several polycrystalline metals, including five alloys of aluminum. Most of their measurements on aluminum were made to  $\sim 12,000$  psi, which is approximately the range for the data on 6061 reported here. They did not observe the orientational effect predominant for the shear ( $\parallel$ ) mode as observed in the present study. However, all of their measurements were made for stress parallel to the preferred orientation (perpendicular to the M axis in this report). Assuming that this direction of stress and shear propagation along the layers most closely approximates elastic behavior, the third-order coefficients were calculated from the reported data on 6061. The results are shown in Table 8 along with the reported results of Smith (Ref. 22). The aluminum alloys in Reference 22 were of the following composition:

2S M	Al, 99.3%
B53S M	Mg, 2.8%; Mn, 0.8%; Cr, 0.1%
B53S P	Mg, 2.8%; Mn, 0.8%; Cr, 0.1%
D54S M	Mg, 4.5%; Mn, 0.8%; Cr, 0.1%
JH77S WP	Zn, 7%; Mg, 2%; Cu, 2%

Table 8  
THIRD-ORDER ELASTIC CONSTANTS OF 6061 ALUMINUM  
(Temperature 22°C)

Aluminum Alloy	Density (g/cc)	$\nu_1$ X $10^{-2}$ kbar	$\nu_2$ X $10^{-2}$ kbar	$\nu_3$ X $10^{-2}$ kbar	$B'_0$	Source
6061 T6	2.704	-30.1	-13.1	-10.4	8.7	This work
2S M	2.737	-22.8	-19.7	-10.2	9.8	Smith, et al.
B53S M	2.677	-24.9	-9.9	-6.9	7.0	Smith, et al.
B53S P	2.687	-9.3	-15.5	-7.5	6.0	Smith, et al.
D54S M	2.719	-37.9	-19.8	-8.0	12.8	Smith, et al.
J477S WP	2.864	-32.0	-17.7	-10.9	10.6	Smith, et al.

Alloys B53S M and P (M and P refer to different heat treatments) and B54S contain approximately the same amount of aluminum as 6061-T6. The third-order constants of 6061 Al as obtained here fall within the range reported by Smith (Ref. 22) for the other five alloys.\*

Smith reports rather high variation ( $\sim 50$  percent) for some of the third-order coefficients. Although the writers did not elaborate on the cause for this variation, it is probably due to microscopic effects, such as plastic deformation, as observed in the present study. Most of the variation among the various alloys listed in Table 8 might then be ascribed to the limitations of the uniaxial pressure technique in determining third-order elastic coefficients in polycrystalline aluminum.

The pressure derivative of the bulk modulus as given in Equation (12) is also listed for each of the alloys in Table 8. The value obtained for 6061 in this study falls within the range reported for the other alloys. However, the agreement between most of the values and the actual value of  $\sim 5.3$  for single crystal aluminum (Ref. 23) is not sufficient for most applications to equation of state studies, as illustrated in the next section.

Table 9 lists the temperature coefficients of the adiabatic bulk modulus for the metals reported in this section. The moduli for lead are omitted, because shear wave data was not obtained in this case.

Table 9  
THE EXPANSION COEFFICIENTS OF THE BULK  
MODULUS VERSUS TEMPERATURE IN FOUR METALS

(Temperature range $\sim 25^\circ$ to $225^\circ\text{C}$ )		
Metal	$B_{0,0}^S$ (kbars)	$\left(\frac{\partial B^S}{\partial T}\right)_{0,0}$ (kbars/ $^\circ\text{C}$ )
1060 Aluminum	743	-0.216
6061-T6 Aluminum	751	-0.170
Magnesium-Thorium Alloy	355	-0.047
Gold	1670	-0.307

\* Because of the uncertainties associated with plastic deformation observed here in 6061-T6 Al, the isothermal moduli in Table 7 were approximated as the adiabatic moduli. For aluminum, this approximation results in an error of  $\sim 4$  to 5 percent.

### SECTION III

#### THERMAL ANALYSIS

##### 1. Experimental Method

###### a. Differential Thermal Analysis Techniques (DTA)

The DuPont 900 Differential Thermal Analyzer\* was used to establish the accurate temperatures of transition of the various polymers studied here. The system is shown schematically in Figure 33. Thermocouples embedded within a sample and reference capillary measure the difference in temperature between the sample, S, and an essentially inert reference, R, (powdered glass beads or powdered alumina), as both are heated in a platinum block by a temperature programmer and controller. The differential amplified thermocouple output,  $\Delta T$ , is coupled to the y-axis of an x-y recorder and the x-axis is driven by the temperature, T, of the sample as indicated by the potential across points A-B. The differential temperature profile,  $\Delta T$ , as a function of temperature, T, is an indication of the energy gains or losses in the sample corresponding to physical changes within the specimen.

Since precision differential thermal analysis is affected by a number of environmental factors, proper experimental techniques were employed to correct or prevent errors associated with (1) particle size and shape differences between sample and reference, (2) differences in heat capacity and thermal conductivity of sample and reference, (3) peak area and temperature measurement, and (4) rate of heating.

Experimentally, the particle size and packing of the sample and reference were matched as closely as possible to control the magnitude of the initial temperature change due to differences in heat capacity and thermal conductivity between the sample and reference.

The two reference materials used for the DTA studies were powdered glass beads and powdered aluminum oxide ( $\text{Al}_2\text{O}_3$ ). With the glass beads as reference, ideal experimental conditions were achieved by diluting the sample with the glass beads until the thermal conductivities of the sample and reference were similar.

\*DuPont 400 Differential Thermal Analysis Instrument Manual, Instrument Products Division, E. I. DuPont de Nemours & Co., Inc., Wilmington, Delaware.

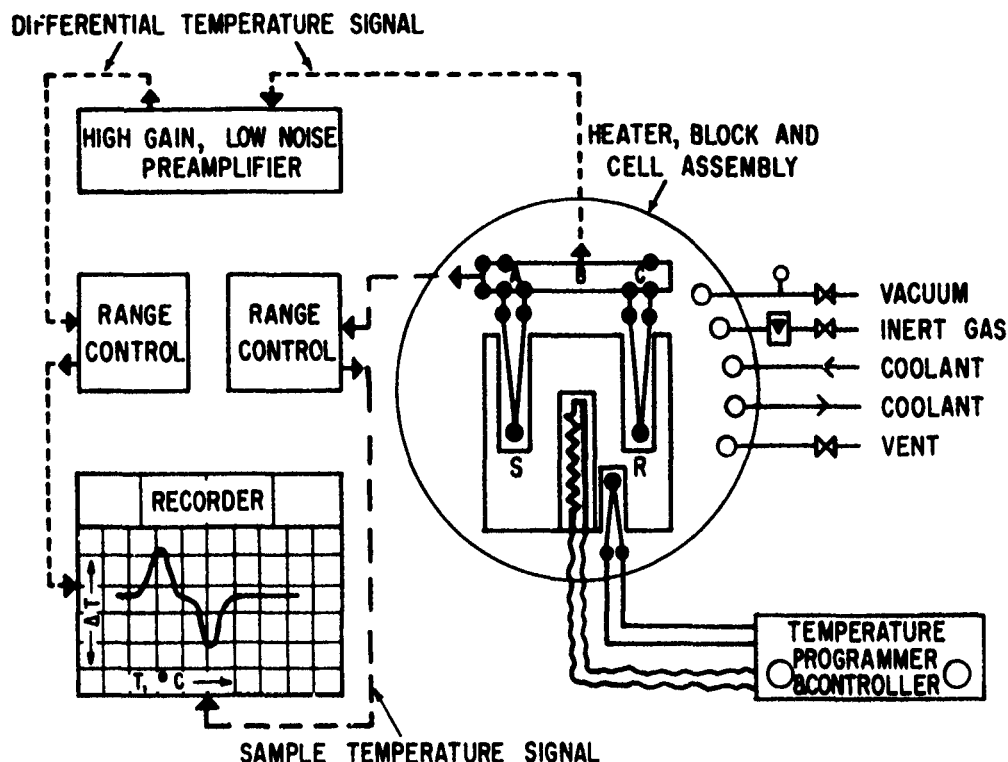


Figure 33. Schematic Diagram of the Differential Thermal Analyzer.

With  $\text{Al}_2\text{O}_3$  as reference, the weights of sample and reference were matched as closely as possible and the baseline slope was positioned by manual adjustment of the  $\Delta T$  zero shift on the instrument panel.\* The proper reference material is necessary to prevent shift of the peak area as illustrated by the theoretical equations of Vold (Ref. 42) in Appendix VI.

Sample size and packing were controlled by using solid cylindrical plugs (approximately 6 to 15 mg) which were placed in 4 mm/pyrex glass holders and inserted in the DTA cell. A small hole drilled in the top of the sample core permitted direct contact between the sample and the thermocouple.

Plots of the transition or fusion peak temperatures versus heating rate of standard samples of tin, lead, mylar, polyethylene, and other related materials, indicated that heating rates of  $5^\circ$  to  $10^\circ\text{C}/\text{min}$  were satisfactory for all DTA measurements. Within this rate interval, no shift of peak temperatures nor

\* Use of the baseline slope has no effect on the value of  $\Delta T$  for it provides a compensating ramp function to return the thermogram baseline to an appropriate horizontal.

peak areas were observed (i.e., for these heating rates, the measured thermal properties were independent of the programmed temperature rate for the size samples employed here).

To avoid oxidation at high temperatures, all thermograms were obtained in an atmosphere of dry nitrogen. Liquid nitrogen was used as the coolant to study polymer characteristics at the lower temperatures.

A DuPont standard cell ( $-100^{\circ}$  to  $500^{\circ}\text{C}$ ) was employed for most of the DTA studies. When a specific polymer was studied at higher temperatures, a DuPont high temperature cell ( $-100^{\circ}$  to  $1300^{\circ}\text{C}$ ) was used (Fig. 34).

The characteristic fusion, decomposition, or polymerization temperatures reported here are the exothermal or endothermal peak temperatures appearing on the respective thermograms. (The terms used in thermogram characterization are illustrated in Figure 35.) Heats of fusion and transition were calculated from quantitative measurements of the peak areas associated with the appropriate phase changes. The application of Vold's equations (Ref. 42, Appendix VI) to the transition peaks of various standards such as benzoic acid,  $\alpha$ -naphthol, silver nitrate, bismuth, and zinc gave the calibration coefficient,  $E$ , of the instrument as a function of temperature. The comparison of heat of fusion values,  $\Delta H$ , obtained for several standard materials with values obtained by the differential calorimetric technique and with values reported in the literature, indicate heats of fusion or transition accurate to approximately 2 to 5 percent. The greater portion of the uncertainty associated with a transition is due to errors occurring with measurement of the peak areas (a planimeter was used in the present study to measure peak areas).

The characteristic glass transition temperature,  $T_g$ , is due to the onset of an internal molecular motion and was evidenced in the present study by a rapid change in the differential temperature between the specimen and reference. It was determined by extrapolating the two lines indicating the first break in the DTA curve, or the temperature at which a change in heat capacity or volume coefficient of expansion occurs. After proper chromel-alumel thermocouple corrections were applied, individual temperature determinations agreed to within  $\pm 0.2^{\circ}\text{C}$  and to within  $2.0^{\circ}$  to  $4.0^{\circ}\text{C}$  of the values reported in the literature.



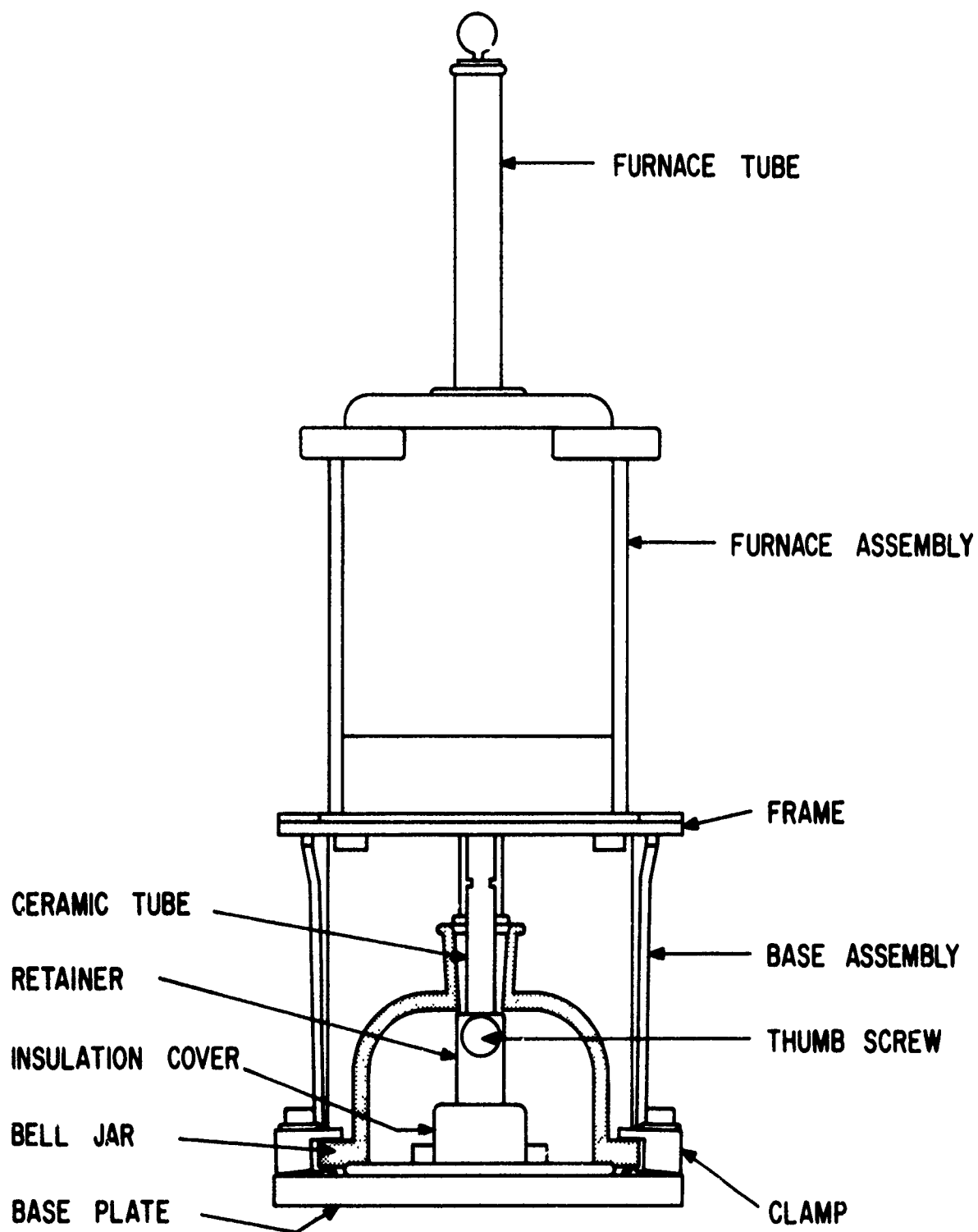
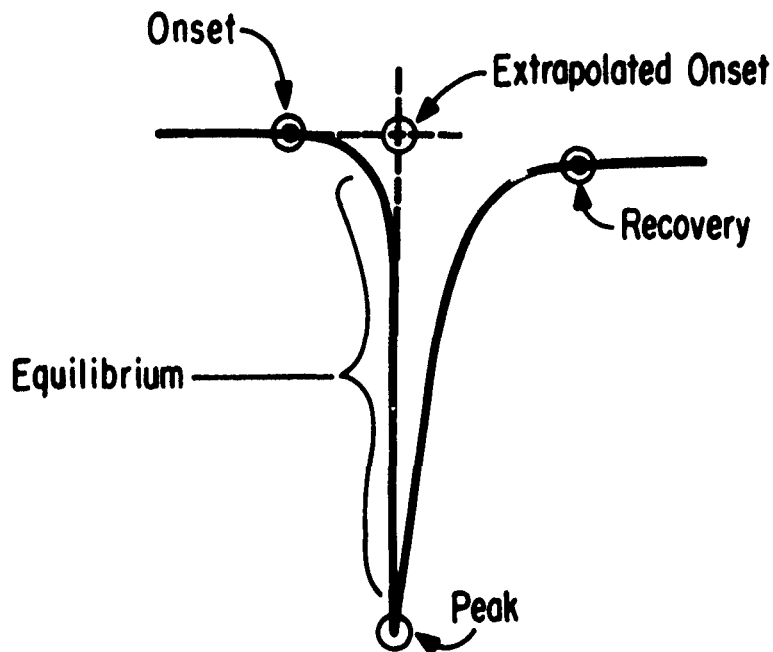


Figure 34. The Cell Used for High Temperature Studies.



#### DEFINITIONS

**Onset:** The temperature at which the thermogram starts to depart from the base line.

**Extrapolated Onset:** The temperature corresponding to the intersection of extrapolations of the base line and the longest straight-line section of the low-temperature side of the peak.

**Peak:** The temperature of reversal.

**Recovery:** The temperature at which the thermogram returns to either the same or a different base line.

**Equilibrium:** The region where the state or form of the sample before transition is in equilibrium with its state or form after transition.

Figure 35. Definition of Terms Used in Thermogram Characterization.

## b. Thermal Expansion Techniques (TMA)

The DuPont 940 thermomechanical analyzer (TMA) plug-in module for the DTA was used to measure the coefficient of linear thermal expansion,  $\alpha$ , of the various polymers reported here. The apparatus (Fig. 36) includes a simplified form of a dilatorimeter which makes use of a linear variable differential transformer and is adaptable to automatic recording of length changes of a specimen versus temperature.

For a typical analysis, a thermocouple embedded in the bottom of a probe is positioned on top of a cylindrical sample (approximately 0.25 inch in diameter by 0.25 inch in height) which rests on a quartz sample holder. Before the run the test specimen is cooled to the desired starting temperature by a bath of liquified nitrogen. The DTA module controls the rate of heating and the absolute temperature of the specimen. As the temperature is increased, sample elongation raises the probe and the linear change in height of the sample is determined as a function of temperature. Values of  $\Delta l/l_0$  are then calculated from the measured change in the graph abscissa  $\Delta l$  (after suitable calibration) and the initial sample length  $l_0$  (the initial specimen lengths were measured with a micrometer at 25°C).

A small correction was applied for the base-line profile of the instrument to compensate for the expansion of the quartz sample holder. This was done by obtaining the expansion profile of the sample holder and a sample of standard (x-cut) quartz, and applying the necessary corrections. The sensitivity of the instrument was then determined by obtaining expansion profiles of pure aluminum for which the expansion coefficient is well known (Ref. 43).

Corrected values of  $\Delta l/l_0$ , adjusted to the adopted reference temperature of 25.0°C, were used to calculate linear expansions as a function of temperature. Values are computed for every 5°C increment by means of Equation (185),  
Appendix VII.

The volume coefficients of expansion,  $\beta$ , and the temperature derivatives,  $\frac{\partial \beta}{\partial T}$ , are given in Section III, paragraph 3. The volume coefficient of expansion of an orientated polymer is about the same as for an isotropic material so that,  $\beta = 3\alpha$  (Appendix VII). The  $\beta$  values for Avcoat, Avcoat 19, Castable 124, Delrin Acetal, Foam #20, high and low density polyethylene, Plexiglas, and Teflon were calculated with this assumption.

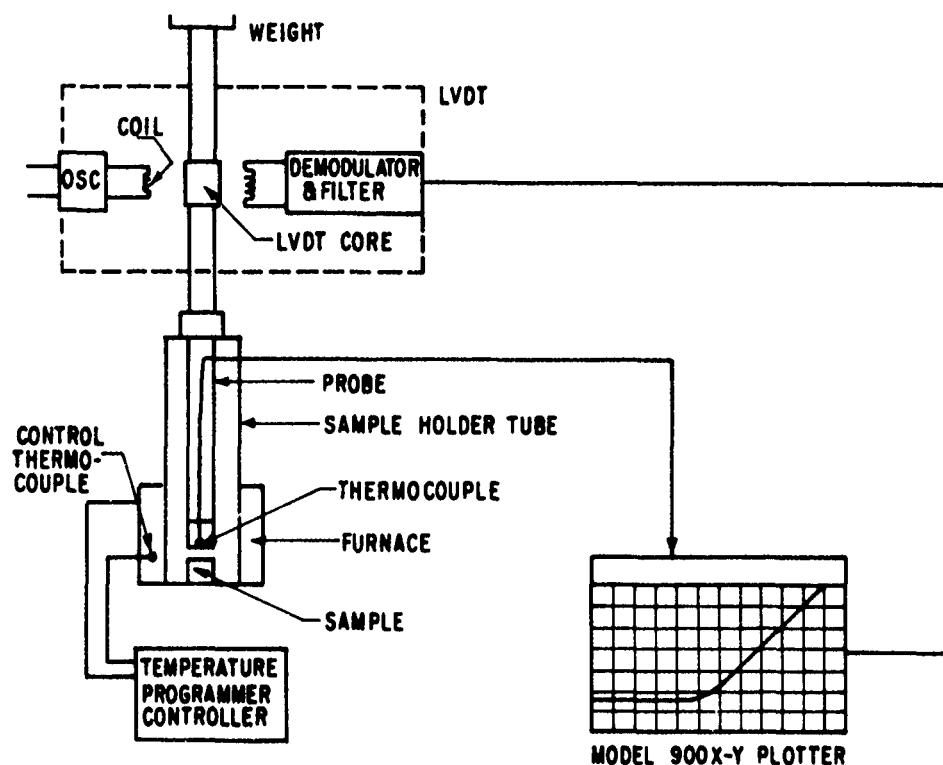


Figure 36. Schematic Diagram of the Thermomechanical Analyzer Used for Expansivity Measurements.

For some of the layered materials the volume coefficients of expansion were calculated from the relation

$$\beta = \alpha_{||} + 2\alpha_{\perp} \quad (15)$$

where  $\alpha_{||}$  is the linear coefficient of expansion in the z-direction (perpendicular to the layers) and  $\alpha_{\perp}$  is the expansion in either of the two other orthogonal directions.

The total probable error for the expansion measurements was calculated as the square root of the summation of all errors associated with each component of the instrument. The error equation takes the form

$$\text{PROBABLE ERROR} = \sqrt{\left(\frac{\Delta E}{E}\right)^2 + \left(\frac{\Delta L}{L}\right)^2 + \left(\frac{\Delta Q}{EQ}\right)^2 + \left(\frac{\Delta T}{T}\right)^2 + \left(\frac{\Delta Tr}{Tr}\right)^2}$$

where

$\Delta E \equiv$  error in measured differential expansion (inches)

$E \equiv$  measured expansion (inches)

$\Delta L \equiv$  error in measured specimen length (inches)

$L \equiv$  original specimen length (inches)

$\Delta Q \equiv$  error in thermal expansion of quartz baseline (inches)

$EQ \equiv$  measured expansion of quartz (inches)

$\Delta T \equiv$  error in measured test temperature ( $^{\circ}\text{C}$ )

$T \equiv$  measured test temperature ( $^{\circ}\text{C}$ )

$\Delta T_R \equiv$  error in room temperature ( $^{\circ}\text{C}$ )

$T_R \equiv$  room temperature ( $^{\circ}\text{C}$ )

For the typical polymers

$$\text{PERCENT PROBABLE ERROR} \equiv \sqrt{\left(\frac{0.0001}{0.1}\right)^2 + \left(\frac{0.001}{0.25}\right)^2 + \left(\frac{0.0001}{0.1}\right)^2 + \left(\frac{3^{\circ}}{200^{\circ}}\right)^2 + \left(\frac{0.5^{\circ}}{25^{\circ}}\right)^2}$$

$$\approx 2.52 \text{ percent}$$

Graphical representations of the length curves for Avco Phenolic Fiberglass, chopped nylon phenolic, carbon phenolic, G.E. Fiberglass, oblique tapewound refrasil, pyrolytic graphite, Rad 60, and tapewound nylon phenolic indicate the presence of varying degrees of anisotropy. For these materials the coefficient of expansion values,  $\alpha$ , were obtained from cylinders cut parallel and perpendicular to the stratification layers.

#### c. Specific Heat Techniques

The latent heat of phase transitions and specific heat data were obtained with an appropriately calibrated calorimetric cell (sensitivity of 0.2 millical/sec-in.) attached to the basic DTA unit. Thermal data obtained by this technique supplement the qualitative data obtained with the DTA 900 cell, and cover the temperature range from  $100^{\circ}$  to  $700^{\circ}\text{C}$ .

The calibration coefficient for a silver sample and the reference holders was obtained by using  $\text{Al}_2\text{O}_3$  as a standard for which the  $c_p$  is known (Ref. 43). An additional check on the calibration of the calorimetric cell was obtained by the application of Vold's equation (Appendix VI) to the fusion peaks of several thermal standards (this technique is identical with that for the differential thermal measurements).

Straight line plots were obtained for each sample when sample weight,  $W$ , versus calibration coefficient,  $E$ , were graphed. The calibration coefficient for each temperature was obtained from these graphs. The present limits of accuracy in the determination of  $\Delta H$  are within 3 to 5.0 percent.

The specific heat of the test specimen (solid plug 30 to 40 mg) was obtained by measuring the temperature lag between sample and reference under "blank" and "sample" conditions. The absolute values of the differential temperature between sample and reference resulting from the heat impulse curve were then substituted into Equation (181), Appendix VII, to calculate  $c_p$ . Because of a temperature lag within the cell, the calorimetric peak temperatures are less accurate ( $3^\circ$  to  $6^\circ\text{C}$ ) than those observed with the DTA standard cell; hence, all reported temperature values were obtained from the DTA measurements.

The specific heat data for the materials studied in the present experiments are listed in Section III, paragraph 3. Linear least-square polynomial equations are given for the metals and alloys and the straight line portions of the polymeric curves. The temperature derivative of the specific heat  $\frac{\partial c_p}{\partial T}$  is also calculated from these equations.

## 2. Discussion

In Section III, paragraph 3, the experimentally determined differential thermal analysis curves, and the thermal expansion and specific heat data are listed and discussed individually for each material studied. The heats of transition and fusion listed were obtained according to the methods outlined in Section III, paragraph 1, and are compared to values obtained by other methods. Because of the existence of an unlimited number of theories defining the mechanical properties of polymeric materials, an attempt is made here to discuss and apply some of the proposed theories to the experimentally determined thermal data.

The effect of a discontinuous change of some property on the thermal behavior was applied to differential studies by Deeg (Ref. 44) and Houldsworth and Cobb (Ref. 45). Since these first studies numerous applications have appeared in the literature with the result that differential thermal analysis is now accepted as a routine tool to solve basic chemical problems. As verified from the differential thermograms (Figures 37 through 70), and expansion plots in Section III, paragraph 2a (Figures 38 through 71), these detectable thermal changes are associated with the first-order crystalline melt transitions or second-order glass transitions.

### a. First-Order Transitions

Pronounced first-order transitions were observed in the present study for highly crystalline materials such as high and low density polyethylene Nylon 6, Delrin Acetal, polymethylmethacrylate, and polytetrafluoroethylene. The melting thermograms of each crystalline polymer exhibit an endothermic peak corresponding to the fusion of the crystalline region of the polymer. The position of the fusion peak was taken as the melting point and the peak area and specific heat data were used to estimate the heat of fusion of the polymer.

The determination of the heat of fusion,  $\Delta H_f$ , provided a method to estimate the percent crystallinity (%C) of several of the polymeric materials. Since the heat of fusion,  $\Delta H_f$ , is expressed by

$$\Delta H_f = H_a - H_c \quad (16)$$

the percent crystallinity was estimated from the relation

$$\%C = \frac{H_a - H}{H_a - H_c} = \frac{\Delta H}{\Delta H_f} \quad (17)$$

where  $H$  is the heat content per gram of the partially crystalline form, and  $H_a$  and  $H_c$  refer to the enthalpies of the amorphous and crystalline regions, respectively. The enthalpy of the amorphous region,  $H_a$ , was obtained from specific heat data well above the melting point at a specified temperature,  $T_a$ , whereas,  $H_c$  was obtained from rearrangement of Equation (16).

The degree of crystallinity was also estimated from specific volume and expansion studies as described in Appendix VIII.

Since the criterion for crystallization is that the free energy,  $\Delta F_f$ , of the crystalline phase must be lower than the free energy of the liquid phase, a knowledge of the contributions to  $\Delta F_f$  from these two phases also defines the degree of crystallinity of the polymer. As the group of molecules in the liquid state unite to form a crystal, a large amount of heat,  $\Delta H_f$ , is evolved which is the result of the tighter association of bonds between the molecules in a crystal versus those in a liquid. Therefore, materials containing strong intermolecular hydrogen bonding, such as Nylon 6 and Delrin Acetal, are expected to show large heats of fusion. (Nylon 6  $\Delta H_f = 15.2$  cal/g; Delrin Acetal,  $\Delta H_f = 39.3$  cal/g.)

The entropy of fusion,  $\Delta S_f$ , defines the lack of order in the liquid which results in the high entropy values found for this state. Since the change in free

energy as liquid changes to crystal is given by  $\Delta F_f = \Delta H_f - T_f \Delta S_f$ , and since at the fusion temperature,  $T_f$ , crystals and liquid are at equilibrium ( $\Delta F = 0$ ), the fusion temperature may be estimated from  $T_f = \Delta H_f / \Delta S_f$ . The observed fusion peak temperatures listed in Table 10 compare favorably with those calculated from fusion phenomena.

The variations in  $T_f$  for the various polymers studied is generally attributed to the complicated effects of surface tension, chain ends, and diluents which lead to a lowering of the fusion temperature below the value expected for a perfect crystal. It was noted that the fusion temperature was high if the heat of fusion was large (i.e., high intermolecular attractions), or if the entropy was low (i.e., material is in a highly crystalline ordered state).

The highly crystalline materials which gave sharp fusion temperatures in the present study were Delrin Acetal, chopped nylon phenolic, Nylon 6, high and low density polyethylene, tapewound nylon phenolic, and polytetrafluoroethylene. The low values of  $\Delta S_f$  also verify the high degree of crystallinity present in these materials.

For a polycrystalline material containing crystallites of various sizes, it is expected that the smallest crystallites will melt at a lower temperature than the larger ones. This effect may be observed by comparing the thermograms of high and low density polyethylene (Figures 37 and 40). A pronounced break in the curve at 70°C for the more highly branched low density polymer is associated with the pre-melt of branched crystallites. The lower  $\Delta H_f$  and  $T_f$  of this material is attributed to the chain ends which decrease the perfect packing within the crystal.

The increase in polarity or cohesive density explains the higher melting points of Nylon 6, polytetrafluoroethylene, chopped nylon phenolic, and tapewound nylon phenolic. The fusion peak for chopped nylon phenolic and tapewound nylon phenolic results from the phenolic component of the polymer, wherein the lamination process lowered the melting temperature  $T_f^0$  of the homopolymer. Fusion temperatures of such composite materials may be estimated from

$$\frac{1}{T_f} = \frac{1}{T_f^0} - \left( \frac{R}{\Delta H_f} \right) \ln X_A \quad (18)$$



Table 10

## FUSION AND DECOMPOSITION PEAK TEMPERATURES FOR THE POLYMERS STUDIED

Polymer	Fusion Peak °C	Fusion Peak Onset, °C	Decomposition Peak, °C	Onset Decompo- sition, °C
Avcoat 1			339 exo., 457	250
Avcoat 19			350 exo., 478	260
Avco Phenolic Fiberglas			210 exo., ~440	~100
Carbon Phenolic			225 exo., ~475	~105
Castable 124			320 exo., 370 exo.	~280
Chopped Nylon Phenolic	255	200	430	~380
Delrin Acetal	75,180	65	349	250
Foam #20			~237 exo., 480	143
Mylar	264	215	455	360
Polyamide (Nylon 6)	225	150	>375, 455	345
Oblique Tapewound Refrasil			230 exo., 320	120
Polyethylene (HDP)	137	110	~490	~420
Polyethylene (LDP)	112	40	~480	400
Polymethylmethacrylate (Plexiglas)			375	~280
Polytetrafluorethylene (Teflon)	25*, 30*, 329	15, 300	560	530
Tapewound Nylon Phenolic	255	225	434	~360

\* Crystalline Transition

wherein the melting point of a polymer composed predominantly of monomer A is lowered. It is assumed that  $X_A$ , the mole fraction of the parent polymer, is interspersed randomly along the chains with the comonomer of mole fraction  $X_B$ .

Conventionally, the degradation of polymers is studied by thermogravimetric analysis, and such TGA studies determine the kinetics of the degradation by measuring the rate of change in weight at constant temperature. Such studies are presently being performed on the materials listed in this report. The differential thermal analysis curves (Figures 37 through 70) were used to establish exothermal or endothermal decomposition peak temperatures as illustrated in Table 10. Examination of the respective thermograms indicates the decompositions proceed at a slow rate over extended temperature ranges.

In general, the highly crystalline materials were completely vaporized, whereas Avcoat 1, Avcoat 19, Castable 124, and Foam #20 were decomposed to tarlike residues. The remaining laminated materials were converted to hard carbonaceous residues upon decomposition.

#### b. Second-Order Transitions

The glass transition temperature,  $T_g$ , of an amorphous polymer is significant in that it is the temperature at which a marked increase in molecular movement gives rise to an incipient change from a rigid solid or glasslike state to a rubberlike or viscous property. Since this second-order transition temperature appears as a discontinuity in the first derivative of a primary thermodynamic quantity, the glass transition temperature may be observed by (1) the change of dynamic elastic moduli and mechanical damping with temperature (References 46 through 49), (2) the sudden increase in specific heat (References 45 through 50), in the coefficient of thermal expansion (References 57 through 59), the compressibility (Ref. 60), and the thermal conductivity (Ref. 61). The glass transition temperatures for the polymers studied were obtained by extrapolating the transition onset (Fig. 35) appearing on the differential thermal analysis thermograms. The observed transition temperatures were likewise verified by specific heat and coefficient of expansion studies. For example, the rotational transition temperature observed for Delrin Acetal, was 40° to 50°C (Fig. 45). This value agrees well with that obtained from the specific heat versus temperature (Fig. 46) and the intersection of the extrapolated linear portions of the elongation versus temperature curve.

The chemical structure of a polymer is known to have a great effect on the glass transition. The presence of highly polar groups along the polymer chain has the effect of increasing the intermolecular forces which pull the chains closer together and reduces the free volume. Comparatively high glass transitions were observed for polar polymers (e.g., Delrin Acetal and Nylon 6), whereas the steric effect of the chain substituent groups was found to affect the glass transition temperatures of composite polymers (e.g., polymethylmethacrylate and low density polyethylene). For polymethylmethacrylate, the stiff and bulky side groups inhibit free rotation of the chain segments and increase the glass transition temperature, whereas, the flexible side groups of low density polyethylene serve to hold the chains apart, free their motions and decrease  $T_g$ . The low glass transition temperatures observed for high and low density polyethylene ( $-120^\circ\text{C}$ ) represent hydrocarbons which have very weak intermolecular forces.

Sharp glass transition temperature were observed on the DTA thermograms and expansion plots of Castable 124 (Fig. 51), Foam #20 (Fig. 53), and polymethylmethacrylate (Fig. 44). Glass transition temperatures of approximately  $34^\circ\text{C}$ ,  $20^\circ\text{C}$ ,  $50^\circ\text{C}$ ,  $-120^\circ\text{C}$ ,  $-122^\circ\text{C}$ , and  $45^\circ\text{C}$ , respectively, were estimated for Avcoat 1 (Fig. 48), Avcoat 19 (Fig. 50), Delrin Acetal (Fig. 45), high density polyethylene (Fig. 37), and Nylon 6 (Fig. 42).

In some instances, it was difficult to identify the glass transition temperature because of the high degree of crystallinity. It is known that since the glass transition is defined as the relaxation of chain segments in the amorphous region of the polymer, the observed differential temperature change would be smaller for crystalline materials.

The inability to observe glass temperatures for the laminated materials was expected, because in fabrication the plasticizing fibers dissolve in the high polymer and lower the glass temperatures or prevent their formation. Werner (Ref. 62) has shown that most plasticizers have glass temperature in the range of from  $-50^\circ\text{C}$  to  $-150^\circ\text{C}$ .

The glass transition of copolymers may have two transition temperatures, one close to the value of  $T_g$  for each homopolymer. If the composition by weight for a series of copolymers is plotted against  $T_g$ , a straight line joins the temperatures of the two homopolymers (References 63, 64, and 65). The glass transition temperature of the copolymer is given by

$$\frac{1}{T_g} = \frac{1}{\left(W_1 + \frac{W_2}{X}\right)} \left[ \frac{W_1}{T_{g1}} + \frac{XW_2}{T_{g2}} \right] \quad (19)$$

where  $W_1$  and  $W_2$  are the weight fractions of the two monomers with transitions at  $T_{g1}$  and  $T_{g2}$  in °K, and  $X$  is a constant.

The rapid rise in the heat capacity curve at the glass transition temperature denotes a second-order transition extending over a small temperature range,  $\Delta T$ , with a heat of transition given by the integral  $\int \Delta c_p dt$  where  $\Delta c_p$  is the excess in heat capacity at the transition. Specific heat data for the metals, alloys, and polymeric materials are listed in Section III, paragraph 3.

The heat capacity of most plastics is about 0.3 to 0.4 cal/g°C. On a mass basis this is considerably more than that of most metals, but the lower density of plastics makes their specific heat on a volume basis less than that of the metals and alloys. Heat capacity data may have small errors due to traces of precuring or evaporation of moisture. Values of the heat capacity of a resin, per monomer unit, can be estimated roughly from additive atomic specific heat values. For polyethylene,  $(-CH_2-CH_2-)_n$ , the estimated value of 0.50 cal/g°C was obtained from the specific heat of 1.8 for carbon and 2.3 for hydrogen, thus

$$c_p = [2(1.8) + 4(2.3)]/28 = 0.50 \text{ cal/g°C}$$

This is within the experimentally reported values of 0.4 to 0.5 cal/g°C, as shown in Section III, paragraph 2c.

#### c. Thermal Expansion

The increase in expansion due to an increase in heat is the result of strains or thermal stresses within the polymer. In accordance with Hooke's law, the axial strain,  $\epsilon$ , originating within the molecule as a result of a temperature stress,  $\sigma_T$ , would be

$$\epsilon = \frac{\sigma_T}{M} = \frac{l - l_0}{l_0}$$

where  $l$  and  $l_0$  refer to the stretched and unstretched sample, respectively, at a temperature,  $T$ , and  $M$  is an effective elastic modulus. The variation of the axial strain,  $\epsilon$ , or the elongation per unit temperature change is discussed in Section III, paragraph 3 for several of the polymers. These values are related to the linear coefficient of expansion,  $\alpha(\Delta T)$  as shown in Appendix VIII.

Many polymers are known to undergo minor secondary transitions (References 66 through 70) but the true nature of these transitions are not clearly understood and in some instances are extremely difficult to identify. Alfrey (Ref. 71) associated the transitions with the restricting (or freezing) of rotational degrees of freedom in polymer chain segments. Boyer and Spencer (Ref. 72) presented evidence that these transitions are associated with kinetic phenomena and attribute the transitions to the existence of a relaxation spectrum corresponding to an isoviscous state. This study does not attempt to define the nature of the transitions, but it does verify the existence of such transitions from calculations of the coefficient of thermal expansion through small temperature intervals (see Section III, paragraph 1, and Appendix VII). Computer plots of the data thus calculated were obtained by adjusting the span between the 5-degree temperature intervals so that only the most significant transitions were prominent. Plots of the coefficient of expansion,  $\alpha$ , (Figures 38 through 71) illustrate the presence of these secondary transitions. The values obtained for  $T_g$  and the additional secondary transitions are tabulated in Table 11 and discussed individually for each material.

Table 11  
GLASS TRANSITION ( $T_g$ ) AND ADDITIONAL SECONDARY  
TRANSITION TEMPERATURES OF POLYMERS STUDIED

Polymer	Density, g/cm <sup>3</sup>	$T_g$ , °C	$T_{sec}$ , °C
Avcoat 1	1.10	34.0	-50,160
Avcoat 19	1.07	~20.0	-50,130
Castable 124	1.23	37.8	-10
Chopped Nylon Phenolic	1.68	40.4	-65
Delrin Acetal	1.43		-40
Foam #20	0.33	137.5	-40,40
Mylar	1.41	70.0	-80
Polyamide (Nylon 6)	1.14	48.0	-20,76
Polyethylene (HDP)	0.97	>-110.0	-20,70
Polyethylene (LDP)	0.92	>-110.0	-20,70
Polymethylmethacrylate (Plexiglas)	1.19	112.0	-25,10,175
Polytetrafluoroethylene (Teflon)	2.19		-78,50
Tapewound Nylon Phenolic	1.21	40.0	-45

An elastic-plastic material has both elastic and plastic strains. This state is typical of most of the polymers studied. In the elastic region, the effect of temperature on strain is twofold; first, to cause a slight modification in the values of the elastic constants, and second, to produce a strain even in the absence of an external mechanical stress.

The thermal strain,  $\epsilon_T$ , is the strain due to the temperature change expressed as

$$\epsilon_T = \alpha(T - T_0) \quad (21)$$

where  $T_0$  refers to a reference temperature.

The strain,  $\epsilon_\ell$ , due to stress is related through a modulus to the stresses imposed on the surface of the material--the origins of such stresses may be thermal or may be forces applied to the object's external surface. (See Appendix VIII for derivation of equations.) Therefore, when an element is subjected to a thermal load, the total strain,  $\epsilon$ , in the material can be considered in two parts: (a) the strain,  $\epsilon_\ell$ , due to a molecular stress, and (b) the strain,  $\epsilon_T$ , due to the change of temperature in the material itself

$$\epsilon = \epsilon_\ell + \epsilon_T = \epsilon_\ell + \alpha T \quad (22)$$

A rigid solid would have insignificant strains due to molecular stresses, regardless of the applied thermal strain,  $\epsilon_m$ . Therefore, at low temperatures, the total strain,  $\epsilon$ , is expected to be small since the thermal expansion is generally small. At the glass transition, both strains contribute to the increased values of  $\epsilon$ .

Polytetrafluoroethylene (Teflon) is considered to be a rigid plastic material for molecular strains are said to be insignificant.

The volume coefficient of expansion was calculated as mentioned in Section III, paragraph 1, and Appendix VIII. Isotropic, molecular oriented, and fibrillar materials were examined and are discussed in Section III, paragraph 3. The molecular oriented and fibrillar arrangements represent low entropy states for the application of heat resulted in disordered masses of higher entropy. The high degree of anisotropy present in these materials depends on the fiber alignment along the main axis of the polymer and the degree of lateral or axial expansion of the fiber as well as of the parent polymer.

### 3. Experimental Results

#### a. Thermal Properties of Common Plastics

##### (1) Polyethylene High Density (HDP)

This material is a thermoplastic resin of very long, nearly branchfree chains made by the polymerization of ethylene. Elemental analysis indicates 86.0 percent carbon and 14.0 percent hydrogen, and a calculated density of 0.967 g/cm<sup>3</sup>.

The DTA thermogram (Fig. 37) yields an endothermic peak at the melting point ( $T_f = 134.5^\circ\text{C}$ ) which agrees well with values given in the literature (Ref. 73). The glass transition temperature (below  $-110^\circ\text{C}$ ) is beyond the range of the instrument. Decomposition occurs at approximately  $492^\circ\text{C}$ . Secondary transitions at  $< -110^\circ\text{C}$ ,  $-20^\circ\text{C}$ , and  $70^\circ\text{C}$  were noted by a change in slope on the DTA thermogram; however, these transitions were more clearly identified by the thermal expansion plots (Fig. 38). Kline, et al. (Ref. 74), Oakes and Robinson (Ref. 75), and Schmieder and Wolf (Ref. 76) report peaks at  $-120^\circ\text{C}$ ,  $-25^\circ\text{C}$ , and  $70^\circ\text{C}$  which they observed upon measuring the shear moduli damping factor  $G''/G'$ . These peaks were identified as alpha, beta, and gamma. The gamma transition refers to the main glass transition at  $-120^\circ\text{C}$ , which is said to be due to long  $\text{CH}_2$  sequences in the amorphous phase containing the branch points or co-monomer units. The alpha phase at approximately  $70^\circ\text{C}$  is attributed to the crystalline phase of the polymer. Nielsen (Ref. 77) has shown that this phase may be correlated with the size of a crystallite or the length of the polyethylene sequences in a crystallite. Nuclear magnetic resonance studies by Rempel, et al. (Ref. 78) also indicate that the alpha phase is related to motion in the crystalline phase. The thermomechanical analyzer does not permit the study of crystallinity except in so far that the crystalline (alpha) transition temperature of the sample is shifted by previous heat treatments.

Table 12 lists the linear coefficient of thermal expansion as a function of temperature. The agreement with earlier work on polyethylene is satisfactory (References 79, 80, and 81).

Heat capacity data derived by fitting linear least-square equations to experimental data gave the information listed in Table 13. The equations define all the transitions present in polyethylene.

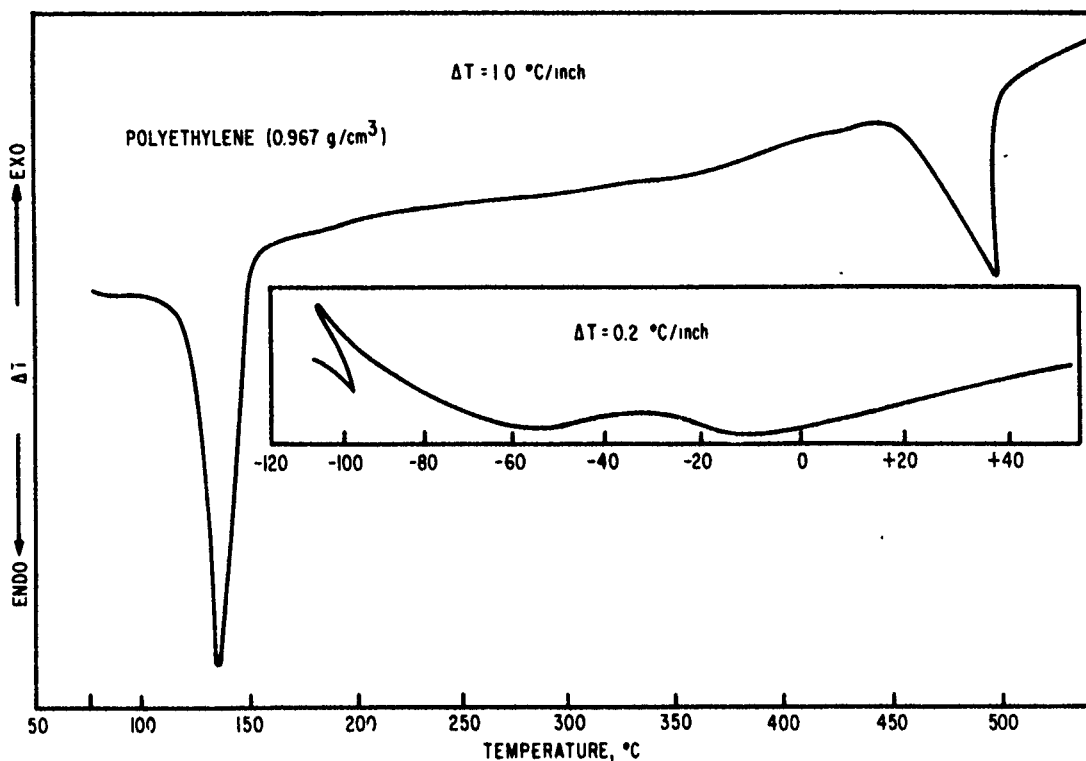


Figure 37. Differential Thermogram of High Density Polyethylene.

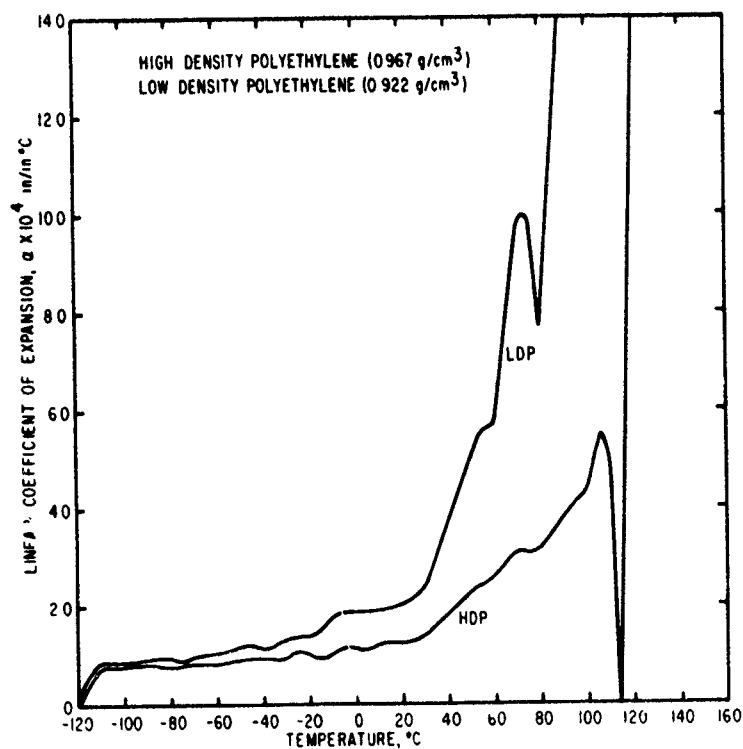


Figure 38. Expansivity Versus Temperature for High and Low Density Polyethylene.



Table 12

## LINEAR THERMAL EXPANSION DATA FOR HIGH DENSITY POLYETHYLENE

Temp. °C	$\alpha \times 10^5 \text{ in/in}^\circ\text{C}$	Temp. °C	$\alpha \times 10^5 \text{ in/in}^\circ\text{C}$
-100	7.688	20	12.680
-90	8.021	30	14.704
-80	7.854	40	18.613
-70	8.021	50	22.822
-60	8.187	60	26.431
-50	8.819	70	31.340
-40	9.019	80	32.249
-30	9.119	90	38.059
-20	9.984	100	43.068
-10	10.683	110	50.453
0	11.282	120	54.979
10	12.347		

## Polynomial Fit for Coefficient of Expansion

$$(\alpha = A + BT)$$

Temp. Range °C	$A \times 10^5 (\text{°C})^{-1}$	$B \times 10^6 (\text{°C})^{-2}$
25 to 100	$2.976 \pm 0.953$	$3.91 \pm 0.14$

Table 13

## HEAT CAPACITY DATA FOR HIGH DENSITY POLYETHYLENE

$$(c_p = a + bT)$$

Temp. Range °C	$a \text{ cal/g}^\circ\text{C}$	$b \times 10^3 \text{ cal/g}^\circ\text{C}^2$	Av Error of $c_p \times 10^2$
-100 to + 50	0.3689	1.54	0.82
50 to 125	0.2800	3.38	0.97
125 to 137	-5.9970	53.59	1.19
137 to 175	8.0974	-40.27	0.89
200 to 325	0.8007	-0.05	1.08
325 to 362	1.1991	-1.32	1.71
362 to 440	-0.0478	2.13	0.70
440 to 492	-18.5400	43.68	11.03
475 to 510	45.3293	-0.89	43.38
510 to 540	0.8106	-1.53	48.99

In this and following tables some of the intercept values of  $c_p$  are negative. This is not to imply a negative value of  $c_p$ , but simply results from extrapolating about  $0^\circ\text{C}$ . This point was chosen as the intercept in temperature because of the ease of expressing the linear least-squares coefficients over different temperature intervals.

Examination of the heat capacity as a function of temperature over the entire temperature range studied (Fig. 39) shows that the average specific heat of the solid at  $-20^\circ\text{C} \rightarrow 50^\circ\text{C}$  is 0.395. The extrapolation of this straight line to  $350^\circ\text{C}$  would eliminate all melting point heat effects and yield a heat capacity for the liquid (along the dashed line in Figure 39) of  $0.539 \text{ cal/g}^\circ\text{C}$ . These values agree well with the data reported by Wunderlich (References 82 and 83) for the annealed solid sample and the liquid. The heat capacity begins to rise above the extrapolated straight line at about  $30^\circ\text{C}$ , but the sharp increase is noted at  $120^\circ\text{C}$ . Most of the melting occurs within a  $25^\circ$  temperature range.

According to Inoue (Ref. 84) the calculated enthalpy of fusion,  $\Delta H_f$ , of high density polyethylene is  $60.2 \text{ cal/g}$  for a material with a density of  $0.988 \text{ g/cm}^3$ . Our value of  $58.8 \text{ cal/g}$  determined from the area measurement of the fusion curve is in excellent agreement with materials having similar densities.

The entropy of fusion,  $\Delta S_f$ , calculated thermodynamically ( $\Delta S = \Delta H_f/T_m$ ) was  $0.044 \text{ cal/g}^\circ\text{C}$ . Using Inoue's value (Ref. 84) of  $64.8 \text{ cal/g}$  as the heat of fusion of the crystalline region,  $\Delta H_c$ , a calculated value of 90.7 percent crystallinity was obtained from

$$x = \frac{\Delta H_f}{\Delta H_c}$$

where  $\Delta H_f$  was the observed heat of fusion and  $\Delta H_c$  that of the pure crystalline material. The high degree of crystallinity obtained (90.7 percent) indicates that polyethylene crystallizes readily due to the simplicity of the size of the repeating ( $-\text{CH}_2-$ ) unit.

## (2) Low Density Polyethylene (LDP)

This material is polymerized ethylene which is of lower molecular weight than the high density sample. Differences in physical properties between high and low density polyethylene are greatly influenced by the density (crystallinity) and the molecular weight (melting point) which are the result of the increased branching present in the low density polymer. The sample studied had a calculated density of  $0.922 \text{ g/cm}^3$ .

Examination of the differential thermogram (Fig. 40) indicates a fusion peak at 112°C with a slight shoulder at approximately 70°C. The latter, not evident on the thermogram of HDP (Fig. 37), is attributed to unfolding of branched chains in the amorphous region and may be correlated with the size of a crystallite or the length of the polyethylene sequences in a crystallite (References 74, 74, 76, and 85).

The heat capacity of low density polyethylene is about 0.599 cal/g°C at 20°C. As the temperature is raised, the heat capacity increases, reaching a value of about 1.220 cal/g°C at 90°C and 1.900 cal/g°C at 112°C. These results indicate a disordering of the structure of the solid beginning below 50°C, and becoming increasingly marked as the temperature is raised and culminating in a relatively sharp change to a liquid structure at about 112°C. Linear least-squares equations for the heat capacity are given as  $c_p = a + bT$  where the constants take the values indicated in Table 14.

Table 14  
HEAT CAPACITY DATA FOR LOW DENSITY POLYETHYLENE  
( $c_p = a + bT$ )

Temp. Range °C	a cal/g°C	b × 10 <sup>3</sup> cal/g°C <sup>2</sup>	Av Error of $c_p$ × 10 <sup>2</sup>
-100 to +25	0.5473	1.98	0.24
25 to 80	0.3741	7.95	0.25
90 to 112	-1.4983	29.15	7.81
112 to 130	10.7919	-71.23	1.53
137 to 220	0.8719	0.43	1.52
225 to 300	1.2013	-1.07	0.47
300 to 375	0.4167	1.52	0.60
390 to 430	-0.7545	4.57	1.02
440 to 485	-24.0177	57.36	5.32

The thermal expansion studies (Table 15 and Figure 38) clearly define secondary transitions at < -110°, -20°, and 70° similar to the high density polymer.

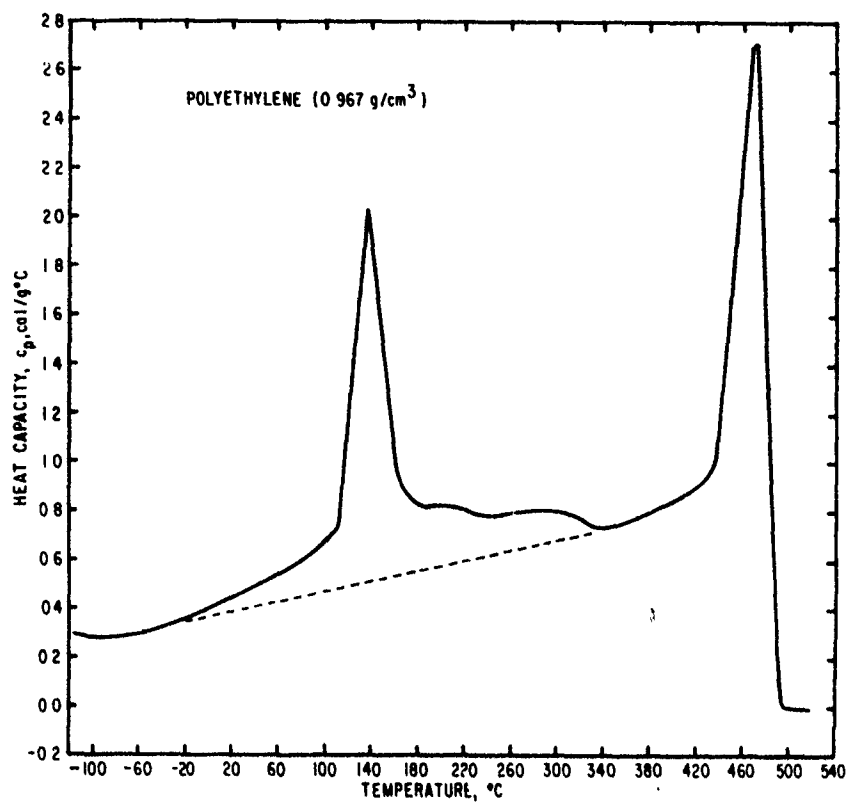


Figure 39. Heat Capacity Versus Temperature for High Density Polyethylene.

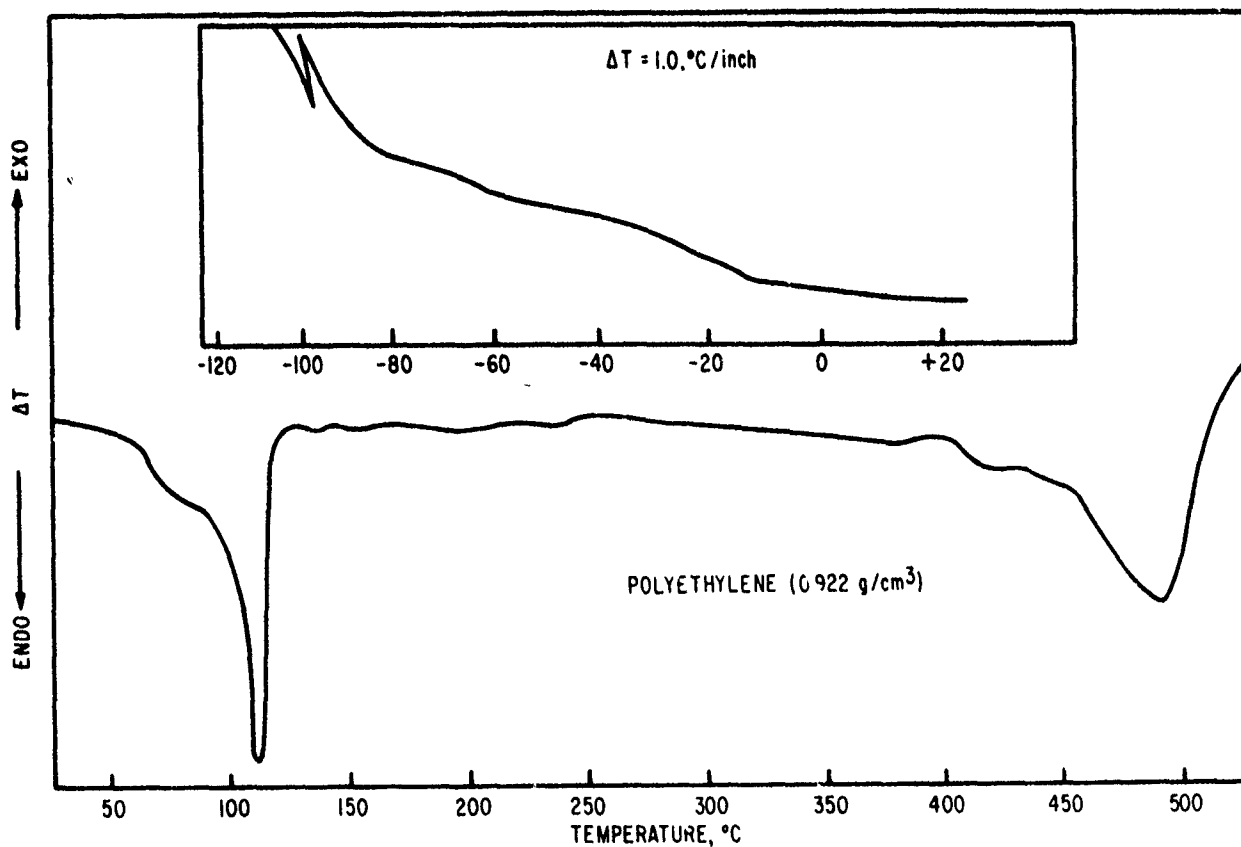


Figure 40. Differential Thermogram of Low Density Polyethylene.

Table 15  
 LINEAR THERMAL EXPANSION DATA FOR LOW DENSITY POLYETHYLENE

Temp. °C	$\alpha \times 10^5$ in/in°C	Temp. °C	$\alpha \times 10^5$ in/in°C
-100	8.046	10	19.332
-90	8.558	20	20.530
-80	8.728	30	24.085
-70	9.410	40	37.267
-60	9.751	50	50.448
-50	10.433	60	57.630
-40	11.456	70	96.761
-30	12.786	80	77.304
-20	13.467	90	222.195
-10	18.616	100	297.077
0	19.025		

Polynomial Fit for Coefficient of Expansion

$$(\alpha = A + BT)$$

Temp. Range °C	$A \times 10^5$ (°C) <sup>-1</sup>	$B \times 10^6$ (°C) <sup>-2</sup>
-100 to -40	13.23 $\pm$ 0.32	0.00 $\pm$ 0.54
-35 to -15	17.40 $\pm$ 0.87	1.63 $\pm$ 0.3
-10 to 20	19.03 $\pm$ 0.06	0.00 $\pm$ 0.47
30 to 60	886.00 $\pm$ 3.93	11.38 $\pm$ 0.85
60 to 75	-132.60 $\pm$ 59.01	31.12 $\pm$ 8.71
75 to 80	322.50 $\pm$ 176.30	56.08 $\pm$ 22.77
80 to 100	-946.50 $\pm$ 180.80	126.40 $\pm$ 20.03

The observed heat of fusion,  $\Delta H_f = 32.9$  cal/g, calculated from heat capacity measurements agrees well with the value of 33.6 cal/g obtained for a similar material by Raine, Richards, and Ryder (Ref. 86). This leads to a thermodynamic entropy value of  $\Delta S_f = 0.29$  cal/g°C as opposed to the value of 0.04 cal/g°C obtained for the high density polymer. The lower heat of fusion or the

higher entropy value is attributed to lower intermolecular attractions, or decreased crystallinity evident in the low density polymer as a result of the increased number of branches present.

The observed crystallinity (see discussion on high density polyethylene for method of calculation) of 50.8 percent compares favorably with other reported values (References 87 and 88).

A heat of decomposition of  $\Delta H = 122.3$  cal/g was obtained by the differential thermal technique. This value is subject to instrumental errors and will be verified by thermogravimetric studies. The observed decomposition temperature (Fig. 40) was 480°C.

### (3) Polyamide (Nylon 6)

This material is a long chain polyamide which is a linear condensation product of caprolactam  $[\text{NH}_2 - (\text{CH}_2)_5 - \text{CO} -]$ . The calculated density of the polymer was 1.14 g/cm in which the repeating unit is  $[(\text{CH}_2)_5 - \text{CO} - \text{NH} -]_x$ .

The thermogram trace presented in Figure 41 exhibits well-defined peak positions and peak areas. The sharp fusion peak temperature at  $T_f = 225^\circ\text{C}$  was taken as the true melting point, whereas, the irregular peak above 345°C indicates decomposition. The sharp, long fusion peak postulates a high degree of crystallinity and/or orientation.

Nielsen (Ref. 73) and Coffman, et al., (Ref. 89) report a second-order glass transition at 50°C. Figure 42 illustrates a similar peak on the thermal expansion versus temperature curve. This second-order transition is not associated with any latent heat; rather, the first derivative of the enthalpy (the specific heat) changes suddenly at this temperature. The transition is attributed to motion of large chain segments in the amorphous regions (References 90 and 91).

The small transition at  $-20^\circ\text{C}$  (Fig. 42) is said to represent the onset of segmental motion involving one or more amide groups in the amorphous regions which are not directly hydrogen bonded to other amide groups in the adjacent chains (Ref. 92). This peak was not seen on the DTA thermogram (Fig. 41).

Figure 41 shows that decomposition occurs above 345°C with a double decomposition peak occurring at  $\sim 385^\circ\text{C}$ . Schwender and Zuccarello (Ref. 91)

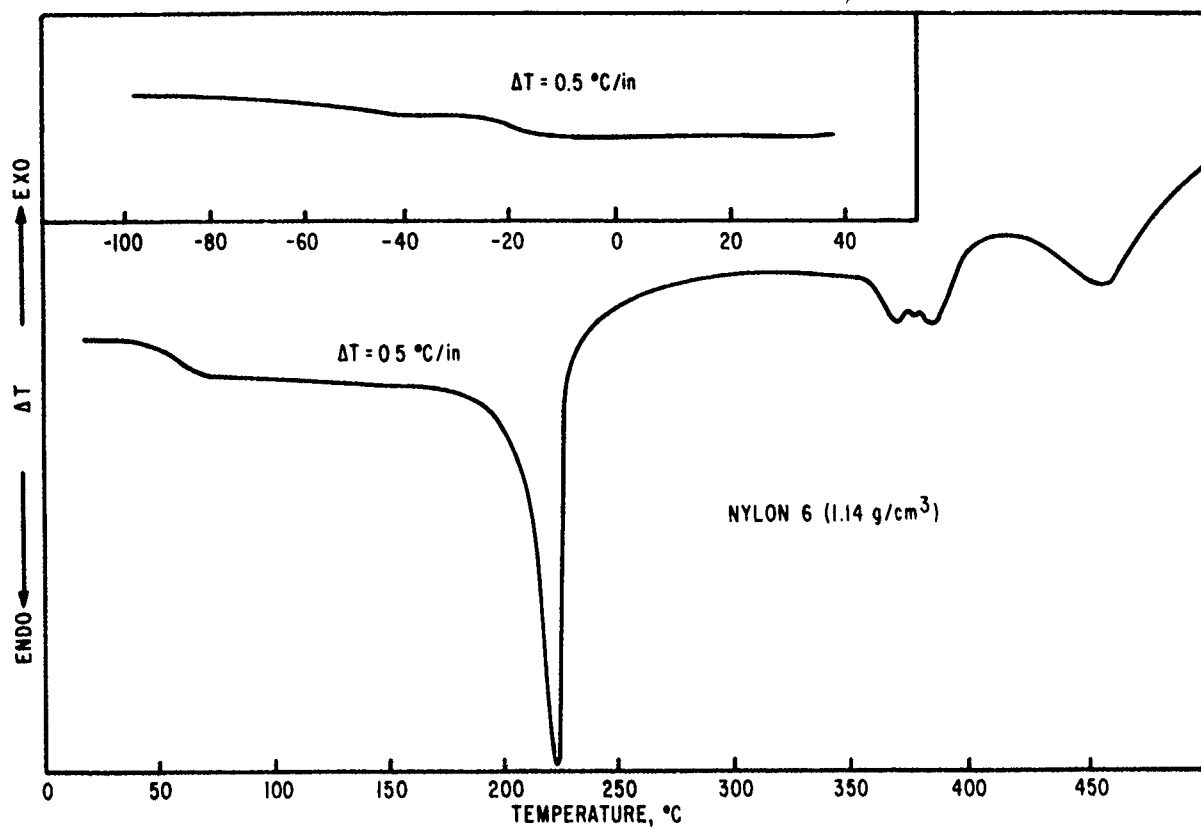


Figure 41. Differential Thermogram of the Polyamide, Nylon 6.

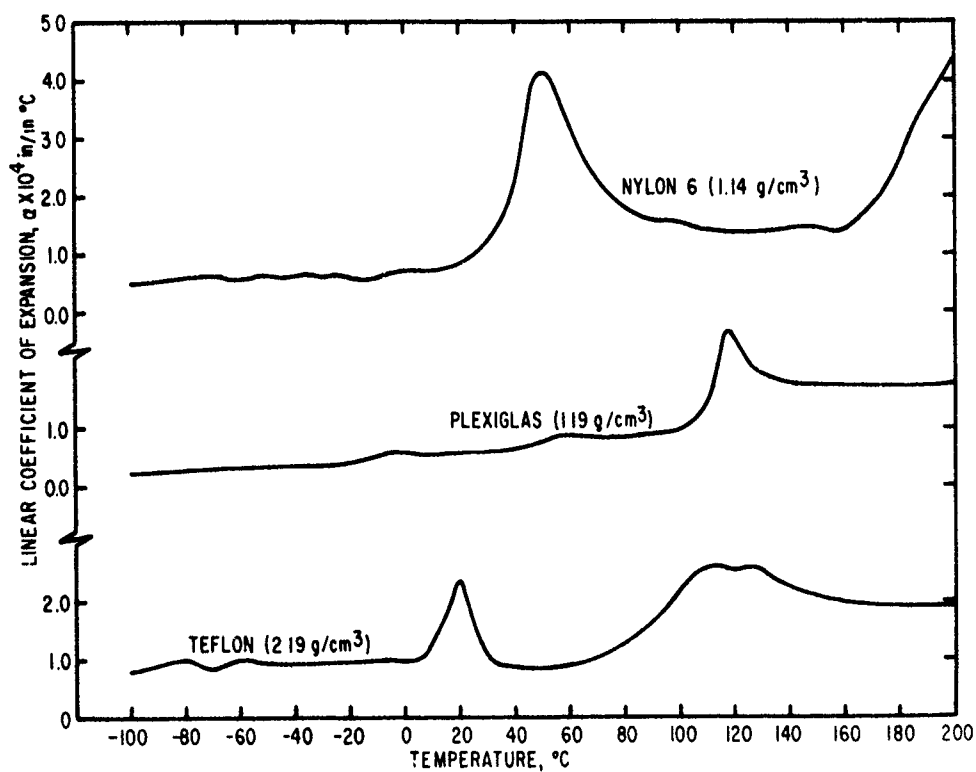


Figure 42. Expansivity Versus Temperature for Nylon 6, Teflon, and Plexiglas.

interpret this small endotherm as resulting from random hydrolytic scission which is followed by degradation with a peak temperature at approximately 455°C.

The heat capacity data defining the important transitions present in Nylon 6 may be represented as  $c_p = a + bT$ . Individual values of  $a$  and  $b$  are shown in Table 16. The data verify the glass transitional temperature at 46°C and the melting temperature of 225°C. The graph of the original data clearly define the peak at 385°C as observed by Schwender and Zuccarello (Ref. 91) with the decomposition peak at  $\sim 448^\circ\text{C}$ . The solid polymer heat capacity could be expressed by the first entry in Table 16 so that the corresponding enthalpy for the solid would be

$$H_{0^\circ} - H_{-100^\circ} = 0.3716T + 5.0 \times 10^{-4} T^2$$

The polymer is said to be in a rubbery phase from 50° to 175°C for which  $\Delta H$  becomes

$$H_{175^\circ} - H_{50^\circ} = 0.4039T + 7.60 \times 10^{-4} T^2$$

The liquid region of the polymer would exist from  $\sim 260^\circ$  to 350°C for which  $\Delta H$  is

$$H_{350^\circ} - H_{260^\circ} = 0.5318T - 0.85 \times 10^{-4} T^2$$

The heat of fusion determined from the measurements of the fusion peak area was  $\Delta H_f = 15.2 \text{ cal/g}$ . Inoue (Ref. 84) has shown the linear relationship between the heat of fusion and the crystallinity to the density. For the pure crystalline material, he gives an extrapolated value of 45.6 cal/g which agrees well with the value reported by Dole and Wunderlich (Ref. 93). For a material of density  $1.14 \text{ g/cm}^3$ , similar to the experimental sample used in this study, a value of 15.8 cal/g was reported for  $\Delta H_f$ , which is in excellent agreement with the value of 15.2 cal/g reported here. The calculated crystallinity for this sample was 30.0 percent. Table 17 lists the thermal expansion data for the polymer.

#### (4) Polytetrafluoroethylene (PTFE) (Teflon)

Teflon is a highly crystalline linear polymer (density  $2.186 \text{ g/cm}^3$ ) which is resistant to change in heat at relatively high temperatures. Elemental analysis of the sample showed 76.0 percent fluorine and 24 percent carbon.



Table 16  
HEAT CAPACITY DATA FOR NYLON 6

$$(c_p = a + bT)$$

Temp. Range °C	a cal/g°C	b × 10 <sup>3</sup> cal/g°C <sup>2</sup>	Av Error of c <sub>p</sub> × 10 <sup>2</sup>
-100 to 0	0.3716	1.00	0.20
-0 to 46	0.3640	2.74	1.78
50 to 200	0.4039	1.52	0.90
200 to 224	-4.9492	0.28	10.01
224 to 265	5.5194	-0.19	5.22
270 to 350	0.5318	-16.68	0.62

Table 17  
LINEAR THERMAL EXPANSION DATA FOR NYLON 6

Temp. °C	α × 10 <sup>5</sup> in/in°C	Temp. °C	α × 10 <sup>5</sup> in/in°C
-100	5.02	60	31.90
-90	5.30	70	23.08
-80	6.24	80	18.54
-70	6.25	90	15.36
-60	5.93	100	15.12
-50	6.60	110	14.88
-40	6.25	120	14.64
-30	5.90	130	14.41
-20	5.97	140	14.15
-10	7.08	150	13.96
0	8.01	160	13.70
10	7.82	170	16.08
20	9.06	180	25.58
30	11.01	190	35.08
40	23.98	200	34.59
50	40.12		

Polynomial Fit for Coefficient of Expansion  
(α = A + BT)

Temp. Range °C	A × 10 <sup>5</sup> °C <sup>-1</sup>	B × 10 <sup>6</sup> °C <sup>-2</sup>
30 to 50	-40.57 ± 7.06	16.14
60 to 75	77.79 ± 7.13	-7.80
80 to 160	17.48 ± 1.02	-0.24
170 to 200	-145.50 ± 15.20	9.50

The DTA thermogram (Fig. 43) shows a first-order transition at 23°C as observed by Rigby and Bunn (Ref. 94). A slight indication of the order-disorder transition at 30°C was also noted on the DTA thermogram. This transition was confirmed by Quinn, Roberts, and Work (Ref. 95) and from specific heat measurements made by Furukawa, McCoskey and King (Ref. 96); Bridgman (Ref. 97) and Weir (Ref. 98) studied the transition at high pressures. X-ray studies (References 94 and 99) indicate no new well-defined crystal structure is revealed above 20°C, but only a disorientation or weakening of the structure that exists below 20°C.

Marx and Dole (Ref. 100) have ascribed a heat of transition of 1.96 cal/g to the 20°C transition and 0.40 cal/g to the 30°C transition. In this study, the total heat capacity for the internal transition calculated from the measurement of the area under the curve with a polar planimeter gave  $\Delta H_{TR} = 1.90$  cal/g, which is in excellent agreement with the above. It is assumed that this value was due to the 20°C transition as postulated by Marx and Dole (Ref. 100). The failure of the 30°C transition to appear for this specific study may have been because of the machining of the sample. The heat generated at this time prevented the reoccurrence of the 30°C transition.

Thermal expansion data (Table 18 and Figure 42) verify the existence of the 20°C transition. The expansion at 20°C is approximately 58.4 percent higher than that at 50°C.

The sharp endothermal peak at 329°C (Fig. 43) corresponds to the melting transition reported by Roff (Ref. 101). This peak is followed by an exothermal process with a major endothermal decomposition beginning at  $\sim 530^\circ\text{C}$ . The decomposition peak temperature ( $T_D \approx 560^\circ\text{C}$ ) is said to be due to free radical depolymerization of the polymer. Further thermogravimetric studies should define this region in greater detail.

The experimental heat capacity was fitted to linear least-squares equations and may be expressed as indicated in Table 19.

The calculated enthalpy of fusion obtained by measuring the area under the curve at 328°C was 10.1 cal/g; when added to the value at 20°C, gives an overall value of 12.0 cal/g. The heat of fusion of polytetrafluoroethylene has been calculated using PVT data and the Clapeyron equation; the published values vary from 9.8 cal/g for the quenched sample to 14.2 cal/g for the powder (References 102 and 103).

Table 18  
LINEAR THERMAL EXPANSION DATA FOR TEFLON

Temp. °C	$\alpha \times 10^5 \text{ in/in}^\circ\text{C}$	Temp. °C	$\alpha \times 10^5 \text{ in/in}^\circ\text{C}$
-100	7.80	60	10.06
-90	8.66	70	10.13
-80	9.42	80	13.05
-70	8.96	90	16.48
-60	9.12	100	22.89
-50	9.36	110	26.48
-40	9.72	120	25.02
-30	9.79	130	26.99
-20	10.05	140	24.14
-10	10.24	150	22.39
0	10.60	160	20.31
10	13.09	170	20.26
20	21.62	180	19.07
30	9.55	190	18.97
40	9.16	200	18.97
50	8.99		

Polynomial Fit for Coefficient of Expansion  
( $\alpha = A + BT$ )

Temp. Range °C	$A \times 10^5 {}^\circ\text{C}^{-1}$	$B \times 10^6 {}^\circ\text{C}^{-2}$
15 to 35	$38.39 \pm 3.48$	-9.14
50 to 90	$-14.60 \pm 1.48$	4.51
130 to 200	$23.20 \pm 1.67$	-0.21

Heat capacity data for the temperature interval  $345^\circ \rightarrow 500^\circ\text{C}$  give a corresponding enthalpy of fusion of 12.67 cal/g. Adding this to the enthalpy obtained at  $20^\circ\text{C}$ , a total enthalpy of 14.59 cal/g is acquired, which agrees to within +6.5 percent of Lupton's value (Ref. 104) and to -5.8 percent of the value calculated by Douglas and Harman (Ref. 105).

Comparison of thermal studies of Teflon with high density polyethylene indicate that thermal stability is enhanced by substitution of hydrogen atoms by fluorine.

Table 19  
HEAT CAPACITY DATA FOR TEFLON  
( $c_p = a + bT$ )

Temp. Range °C	a cal/g°C	b × 10 <sup>3</sup> cal/g°C <sup>2</sup>	Av Error of $c_p$ 10 <sup>2</sup>
-100 to 0	0.1915	33.72	0.13
0 to 20	0.1909	1.31	0.52
20 to 30	0.0904	5.81	0.38
30 to 45	0.3679	-3.56	0.61
50 to 290	0.2003	17.00	0.30
300 to 329	-0.1538	1.35	0.27
330 to 345	-3.5635	11.77	1.88
345 to 355	0.9874	-1.49	0.81
360 to 425	0.5390	-26.98	0.33

(5) Polymethy Methacrylate (PMMA)(Plexiglas)

Plexiglas (density 1.19 g/cm<sup>3</sup>) is a rigid thermoplastic acrylic resin produced by the polymerization of monomeric derivatives of methacrylic acid  $[CH_2 = CCH_3 - COOH]$ . The molecular chain is relatively large in the transverse section and there is evidence it occurs largely in the coiled configuration.

Every second carbon of the chain is asymmetric with resulting d and l arrangements randomly located along the chain. This random arrangement of the  $-CH_3$  and  $-COOCH_3$  groups above and below the chain results in a completely noncrystalline polymer because space-volume or steric effects are not conducive to crystallization. The noncrystalline character of Plexiglas is verified by the thermogram of Figure 44 for which no fusion peak was evident; the latter is characteristic of crystalline or semicrystalline polymers. The main glass transition occurs at 115°C; a broad secondary transition is seen from 0° to 60°C. The expansion plot (Fig. 42) clearly defines the latter at 50°C.

A similar second-order transition was reported by Becker (Ref. 106) and other investigations (References 76, 107, 108, and 109). Nielsen (Ref. 87) has measured the dynamic mechanical properties of PMMA, and reports a broad secondary transition at around 50°C with no distinct drop in the modulus. Heydeman and Grucking (Ref. 107) have noted also that this transition was not affected by hydrostatic pressure while the glass transition temperature was found

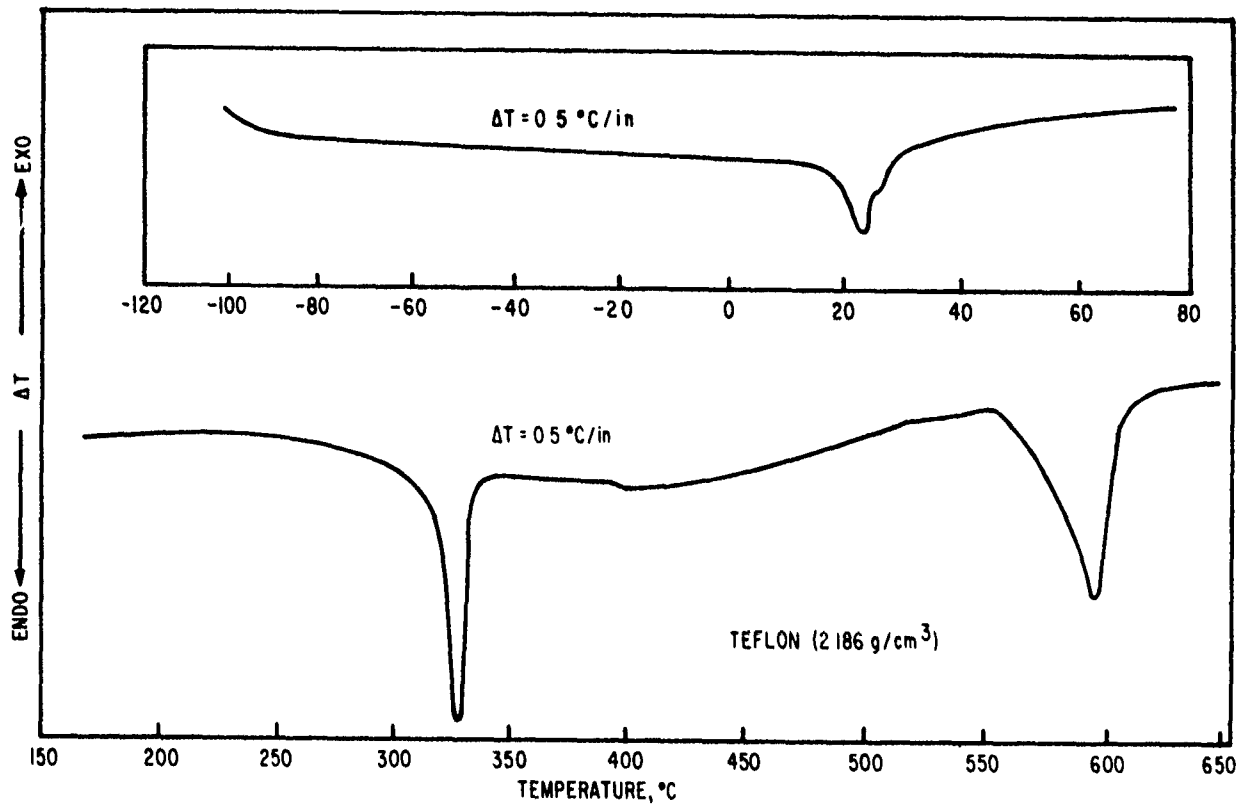


Figure 43. Differential Thermogram of Polytetrafluoroethylene (Teflon).

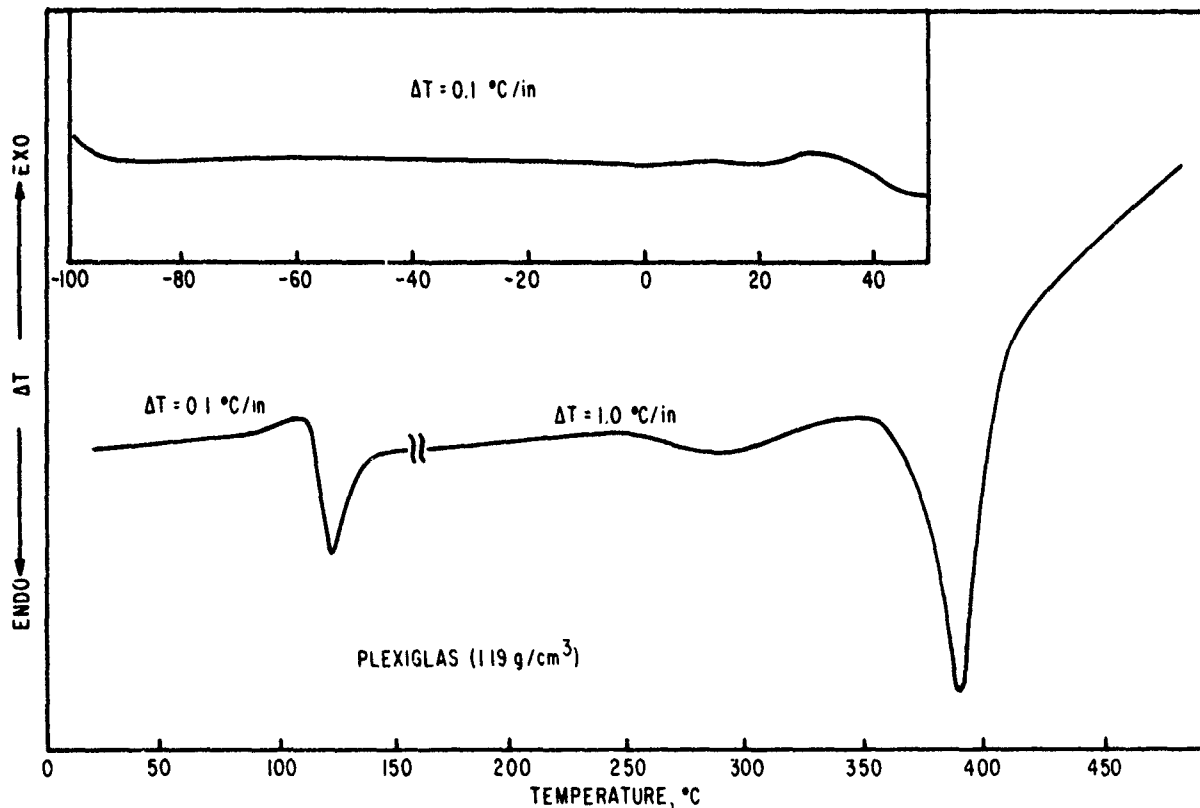


Figure 44. Differential Thermogram of Polymethylmethacrylate (Plexiglas).

to shift by about  $0.018^{\circ}\text{C}/\text{atm}$ . The general conclusion from the above referenced materials is that the transition at  $\sim 60^{\circ}\text{C}$  is attributed to the motion of the side group ( $-\text{COOCH}_3$ ), which becomes mobile at a lower temperature than the main chain.

The thermogram of Figure 44 shows that decomposition is indistinct, with the greatest amount of decomposition occurring at  $375^{\circ}\text{C}$ . Fox, et al., (Ref. 110) and Cowley and Melville (Ref. 111) have demonstrated that thermal degradation is important at  $150^{\circ}\text{C}$  where extensive depolymerization occurs.

Linear thermal coefficient of expansion data are listed in Table 20. All values increase with an increase in temperature, and  $\alpha$  values above the glass transition are doubled over those occurring below. There was no outstanding change in the expansion from  $60^{\circ}\text{C}$ , however, its variation with temperature from  $0^{\circ}$  to  $100^{\circ}\text{C}$  is greater than is expected for a rigid polymer.

The linear description of the isobaric specific heat as a function of temperature is given from  $-100^{\circ}$  to  $200^{\circ}\text{C}$ . Values above this temperature were nonlinear because of the extensive degradation of the polymer. The constants for the equation  $c_p = a + bT$  are defined in Table 21.

The compressibility change,  $\Delta\chi$ , and expansivity change,  $\Delta\beta$ , at the glass transition temperature,  $T_g$ , may be used to determine the effect of pressure on  $T_g$  by Ehrenfest's law (Ref. 112) which states that

$$\frac{dT_g}{dP} = \frac{\Delta\chi}{\Delta\beta} = \frac{1}{\Delta\beta B}$$

where  $B$  is the bulk modulus. Using a value of  $58.6 \times 10^9 \text{ dyne}/\text{cm}^2$  for  $\Delta B$  and  $52.2 \times 10^{-5} \text{ in}/\text{in}^{\circ}\text{C}$  for  $\Delta\beta$ , the change in  $T_g$  may be expressed by

$$dT_g = \frac{1}{\Delta\beta B} dP = 3.27 \times 10^{-8} dP$$

it is known that the glass and secondary transitions cause a stepwise increase of the thermal expansivities and the isothermal compressibilities. Above the glass transition, both expansivities and compressibilities rise in proportion to the temperature.

Table 20  
 LINEAR THERMAL EXPANSION DATA FOR PLEXIGLAS

Temp. °C	$\alpha \times 10^5$ in/in°C	Temp. °C	$\alpha \times 10^5$ in/in°C
-100	2.395	60	7.627
-90	2.564	70	8.092
-80	2.807	80	8.557
-70	2.888	90	9.021
-60	3.239	100	9.486
-50	3.391	110	13.616
-40	3.407	120	26.899
-30	3.205	130	18.545
-20	4.420	140	17.875
-10	4.690	150	17.172
0	5.844	160	17.101
10	5.305	170	17.172
20	5.533	180	17.242
30	6.234	190	17.242
40	6.698	200	17.241
50	7.163		

Polynomial Fit for Coefficient of Expansion  
 $(\alpha = A + BT)$

Temp. Range °C	$A \times 10^5$ °C <sup>-1</sup>	$B \times 10^6$ °C <sup>-2</sup>
10° to 100°	$4.840 \pm 0.199$	0.465
5° to 120°	$-4.450 \pm 12.25$	5.283

(6) Delrin Acetal (DA 500)

This high molecular weight material is a highly crystalline stable form of polymerized formaldehyde, sometimes referred to as an acetal resin because of the repeating oxymethylene units  $(-\text{OCH}_2)_n$  in the polymer structure. Hammer, et al., (Ref. 113) define the polymer as linear rather than branched because of the high degree of crystallinity. The observed density of 1.43 g/cm<sup>3</sup> closely approaches the density of 1.51 g/cm<sup>3</sup> for the pure crystalline material.

Table 21  
HEAT CAPACITY DATA FOR PLEXIGLAS  
( $c_p = a + bT$ )

Temp. Range °C	a cal/g°C	b × 10 <sup>3</sup> cal/g°C <sup>2</sup>	Av Error of $c_p$ × 10 <sup>2</sup>
-100 to 45	0.1974	1.76	1.17
45 to 78	0.1578	3.05	0.56
78 to 112	0.2878	1.42	0.54
112 to 130	-0.0328	4.27	1.20
138 to 150	0.6376	-0.60	0.21
150 to 166	0.4264	0.82	0.38
166 to 200	0.4249	0.92	0.59

The melt endothermal peak at 180°C (Fig. 45) is preceded by a break at 75°C which is attributed to the onset of rotational vibrations. A secondary transition observed on the expansion plot (Fig. 46) at -40°C is said to be due to the motion of the (-O-CH<sub>2</sub>-O-) group. The pronounced transition is not considered to be the glass transition temperature, since the  $T_g$  of highly crystalline materials should occur at lower temperatures. Linton and Goodman (Ref. 114) observed a similar increase in ductility in the 60° to 80°C temperature range from stress-strain studies.

Heat capacity and linear coefficient of expansion plots (Table 22 and Figure 46) show identical breaks or transitional regions at 75° and 150°C. This is expected since the frequency coefficient ( $f = d \log v/dT$ ) and the expansion coefficient ( $\beta = d \log v/dT$ ) is equal to the Grüneisen ratio. Further applications to the Grüneisen ratio will be discussed in Section IV, paragraph 1.

The linear least-square heat capacity equations may be used to define the various regions of interest. For the solid polymer below 50°C the equation takes the form

$$c_p = 0.2384 + 1.00 \times 10^{-3}T$$

where the average error in the  $c_p$  value is  $\pm 0.39 \times 10^{-2}$  cal/g°C.

The 50° to 70° region may be given as

$$c_p = 0.1904 + 2.11 \times 10^{-3}T$$

where the error in  $c_p$  is  $0.02 \times 10^{-3}$  cal/g°C.



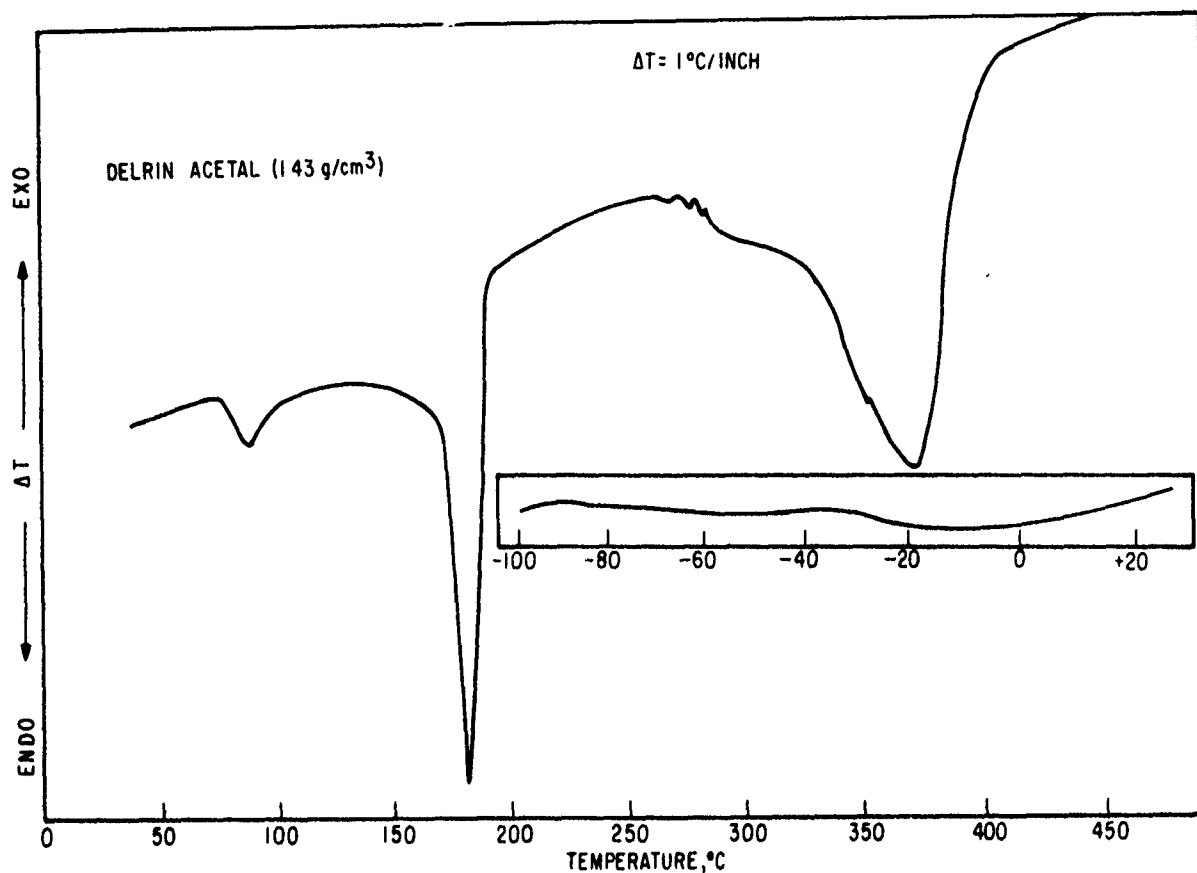


Figure 45. Differential Thermogram of Delrin Acetal (DA 500).

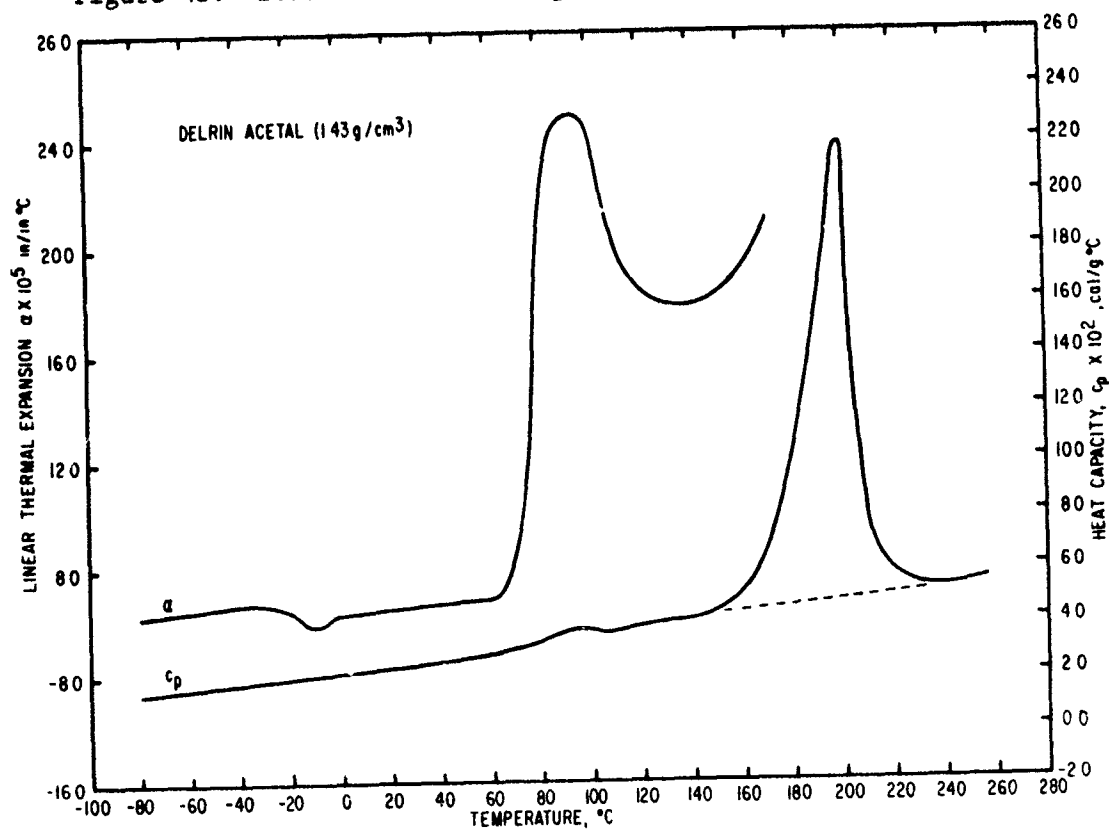


Figure 46. Similarities Between the Heat Capacity and Thermal Expansion Profiles of Delrin Acetal.

Table 22  
LINEAR THERMAL EXPANSION DATA FOR DELRIN ACETAL

Temp. °C	$\alpha \times 10^5$ °C	Temp. °C	$\alpha \times 10^5$ °C
-100	5.30	30	6.75
-90	6.21	40	6.76
-80	6.45	50	8.20
-70	6.61	60	21.66
-60	6.80	70	24.70
-50	6.70	80	24.79
-40	6.42	90	20.19
-30	5.87	100	18.56
-20	6.20	110	17.43
-10	6.31	120	17.82
0	6.43	130	18.99
10	6.54	140	19.15
20	6.66	150	20.90

Polynomial Fit for Coefficient of Expansion  
( $\alpha = A + BT$ )

Temp. Range °C	$A \times 10^5$ °C <sup>-1</sup>	$B \times 10^6$ °C <sup>-2</sup>
25 to +25	$6.43 \pm 0.070$	0.115
30 to 35	$6.74 \pm 0.017$	0.002
55 to 85	$12.06 \pm 7.721$	1.600
125 to 140	$15.54 \pm 1.526$	0.243

The liquid polymer may be described by the heat capacity data obtained above the melting point,  $T_f$ . In equation form this becomes

$$c_p = 0.8659 - 1.48 \times 10^{-3}T$$

where the average error in  $c_p$  is  $\pm 0.14 \times 10^{-2}$  cal/g°C.

Since the change from the solid to the liquid phase is carried out reversibly at constant temperature and fixed pressure at the fusion

temperature,  $T_f$ , the enthalpy of fusion,  $\Delta H_f$ , may be expressed directly from heat capacity data (Appendix VII) as

$$\Delta c_{p,f} = \Delta H_f = 44.805 - 22.43 \times 10^{-2} T_f$$

where  $\Delta c_p = c_p (\text{solid})_f - c_p (\text{liquid})_f$  at the transition temperature,  $T_f = 180^\circ\text{C}$ . Solution of the above equation gives  $\Delta H_f = 41.1 \text{ cal/g}$ . The heat of fusion estimated from the planimeter measurement and summation of peak areas occurring at  $75^\circ$  and  $180^\circ\text{C}$ , respectively, was  $39.8 \text{ cal/g}$ . Both methods yield values which are in excellent agreement with the value of  $41.5 \text{ cal/g}$  reported by Inoue (Ref. 84) for a material density of  $1.421 \text{ g/cm}^3$ .

Using the value of  $\Delta H_c = 58.7 \text{ cal/g}$  (Ref. 84) for the pure crystalline form, a calculated percent crystallinity of 70.0 percent was obtained from  $\%C = \Delta H_c / \Delta H_f$ , where  $\Delta H_f$  refers to the experimentally determined heat of fusion obtained in this study. The resulting thermodynamic entropy of fusion  $\Delta S_f = 0.22 \text{ cal/g}$  indicates disorder brought about by the unfolding of branched chain segments in the amorphous region.

#### (7) Mylar

Commercial polyethylene terephthalate (density =  $1.41 \text{ g/cm}^3$ ) in film form was studied to determine the effects of thermal treatment. For the calorimetric studies, the mylar film (0.005 in. thick) was cut into strips 0.5 inch wide and wrapped around the thermocouple. Annealed samples were obtained by heating the film directly in the cell  $10^\circ$  to  $20^\circ$  above the melting point ( $T_f = 264^\circ\text{C}$ ) and then cooling at a rate of  $0.5^\circ\text{C/min}$ .

Careful examination of the thermal record trace (Fig. 47) shows a glass transition at  $\sim 70^\circ\text{C}$ , followed by a sharp melting endotherm at  $264^\circ\text{C}$ . Decomposition begins at approximately  $360^\circ\text{C}$  with a decomposition peak at approximately  $455^\circ\text{C}$ .

Because the area under the thermogram peak is directly proportional to the amount of heat accompanying the transition, the heat of fusion,  $\Delta H_f$ , could be estimated by determining the peak area and comparing it with the melting peak area of benzoic acid for which the heat of fusion of the latter is  $33.9 \text{ cal/g}$  (Ref. 115).

The estimated  $\Delta H_f$ , thus obtained was  $\Delta H_f = 13.8 \text{ cal/g}$  which was in excellent agreement with values obtained by Ke (Ref. 116). Cobbs and Burton

(Ref. 117) have found that a sample having a measured density of  $1.4 \text{ g/cm}^3$ , corresponds to 60 percent crystallinity. Using this value, the true heat of fusion of the crystalline form would be  $13.8/0.60$ , or  $23.0 \text{ cal/g}$ .

Curve 2 (Fig. 47) is the crystallization exotherm of the polymer. This was obtained by heating the sample to approximately  $20^\circ$  above its melting point and then permitting it to crystallize slowly at a rate of  $3^\circ\text{C/min}$ . Comparison of the area under this curve,  $A_c$ , with that of the area of the fusion peak,  $A_f$ , permits one to estimate the percent crystallinity as

$$\text{Percent Crystallinity} = \frac{A_c}{A_f} \times 100 \quad (23)$$

The area ratios thus obtained were  $\frac{0.620}{1.0334} = 60 \text{ percent}$ .

The thermodynamic fusion entropy,  $\Delta S_f$ , was  $\frac{13.8 \text{ cal/g}}{264^\circ\text{C}} = 0.05$  which indicates a well ordered crystalline structure.

Since the thermomechanical analyzer requires samples 0.23 inch in length no expansivity measurements were attempted on the film.

#### b. Thermal Properties of Polymers and Laminated Materials

##### (1) Avcoat

This material is a light epoxy polyamide (density  $1.10 \text{ g/cm}^3$ ) which is used as an insulator, and has a tendency to become very soft and visibly distorted under moderate pressure. The DTA thermogram (Fig. 48) shows a secondary transition at approximately  $-50^\circ\text{C}$ , followed by a pronounced glass-transition temperature at  $34^\circ\text{C}$ . The great increase in viscoelastic character at the glass-transition temperature made it difficult to prevent the probe penetration of the sample at  $T_g$ . Since the expansion proceeds normally 20 degrees beyond the glass transition temperature, the values of Table 23 were extrapolated to obtain the corrected values at  $T_g$ . It is assumed that the typical glass-transition temperature associated with polyamides ( $T_g \approx 50^\circ\text{C}$ ) has been lowered by the plasticizing effect of the epoxy. The secondary transition at  $160^\circ\text{C}$  is probably due to the evolution of gaseous decomposition products. The decomposition onset at  $275^\circ\text{C}$  (Fig. 48) leads to a peak temperature of approximately  $350^\circ\text{C}$ , which is interrupted by a break at approximately  $330^\circ\text{C}$ , and is related to the decomposition products evolved at this temperature.

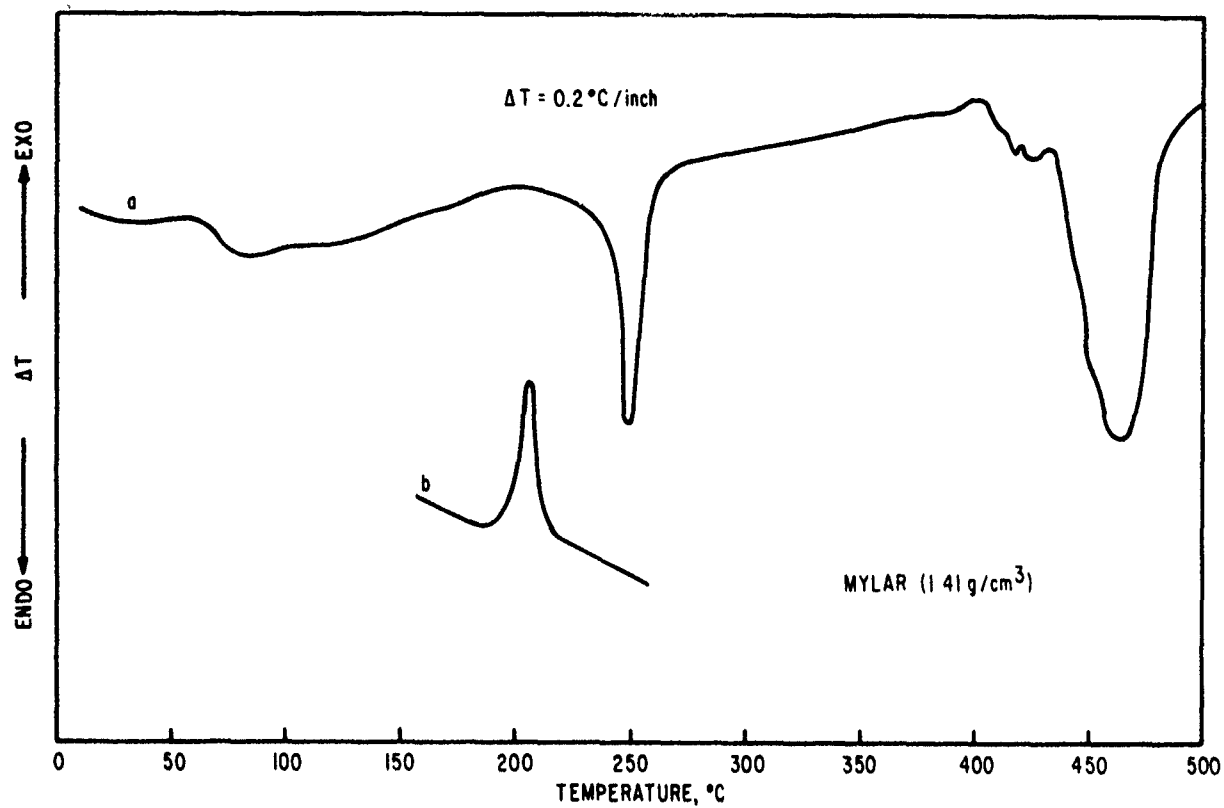


Figure 47. Differential Thermogram of Polyethylene Terephthalate (Mylar).

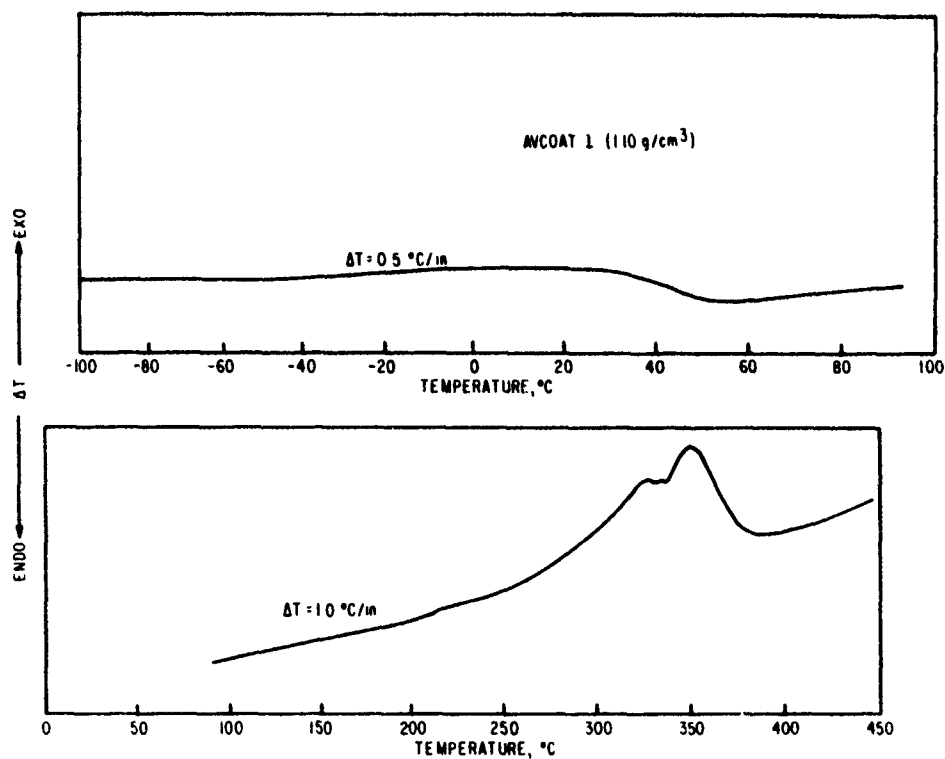


Figure 48. Differential Thermogram of Avcoat 1.

Table 23  
 LINEAR THERMAL EXPANSION DATA FOR AVCOAT 1

Temp. °C	$\alpha \times 10^5 \text{ } ^\circ\text{C}^{-1}$	Temp. °C	$\alpha \times 10^5 \text{ } ^\circ\text{C}^{-1}$
-100	5.91	60	19.85
-90	6.08	70	19.58
-80	6.25	80	19.98
-70	6.42	90	20.35
-60	6.58	100	20.11
-50	6.89	110	20.18
-40	6.50	120	20.24
-30	6.99	130	20.31
-20	7.47	140	20.37
-10	7.96	150	21.10
0	9.22	160	20.57
10	9.10	170	20.83
20	10.34	180	21.42
30	13.86	190	20.21
40	16.04	200	20.22
50	18.74		

Polynomial Fit for Coefficient of Expansion  
 $(\alpha = A + BT)$

Temp. Range °C	$A \times 10^5 \text{ } ^\circ\text{C}^{-1}$	$B \times 10^6 \text{ } ^\circ\text{C}^{-2}$
-40 to 15	$8.441 \pm 0.18$	0.48
15 to 35	$3.307 \pm 0.98$	0.35
60 to 200	$19.47 \pm 0.35$	0.06

The linear coefficient of expansion values (Table 23) vary from a low value of  $5.9 \times 10^{-5} \text{ } ^\circ\text{C}^{-1}$  to  $20.8 \times 10^{-5} \text{ } ^\circ\text{C}^{-1}$  at  $200^\circ\text{C}$ . These values agree well with expansion values presented by Morgan and Overall (Ref. 149). The expansion curve (Fig. 49) closely resembles that of Avcoat 19. The linear least-square equations (Table 23) were obtained from straight line portions of the expansion curves and were used to calculate the Grüneisen ratio of Section IV-1.

Table 24  
HEAT CAPACITY DATA FOR AVCOAT 1  
 $c_p = a + bT$

Temp. Range °C	a cal/g°C	b × 10 <sup>3</sup> cal/g°C <sup>2</sup>	Av Error of $c_p$ × 10 <sup>2</sup>
-100 to 0	0.2786	0.62	0.23
20 to 60	0.2319	3.13	0.59
65 to 150	0.3750	0.85	0.35
160 to 270	0.5558	-0.28	0.62
275 to 347	1.6654	-4.29	0.99
347 to 400	-2.2343	6.75	3.64
400 to 425	0.4015	0.19	0.56

Heat capacity measurements were made on the original solid without previously annealing the sample to verify the secondary transitions observed by the thermal expansion studies. Linear least-square equations were fitted to the straight-line portions of the data given in Table 24.

Examination of the plot of heat capacity versus temperature showed on increase from 30° to 160°C followed by a rapid drop to a minimal peak at ~ 350°C. The latter corresponds to the decomposition exotherm observed in the DTA studies. The broad glass transition interval at 15° to 35°C was therefore more clearly defined by the thermal expansion studies.

The total heat capacity of the decomposition as determined in the present experiment described the heat of decomposition,  $\Delta H_D$ , as

$$c_p = -3.8997 + 11.04T - \Delta H_D$$

where the error in the  $c_p$  is  $\pm 0.03$  cal/g°C. (See Appendix VII for derivation of equations.)

Heat capacity values were greatly affected by the previous heat treatment of the sample. It was observed that the heat associated with the machining of the sample caused heat capacity values to differ by approximately 40 percent in the region above the glass transition. The  $c_p$  data listed above were obtained from a chip cut manually from the original sample. All machining of the sample was avoided.

## (2) Avcoat 19

This material is a light green elastomeric epoxy resin (density 1.07 g/cm<sup>3</sup>). Avocat 19 is similar to Avcoat 1 in that it has a tendency to become soft and distorted at moderate temperatures; however, no evidence of probe penetration of the sample was evident during the expansion studies.

The glass transition temperature ( $T_g = 20^\circ\text{C}$ ), which was slightly lower than that observed for Avcoat 1, was clearly defined on the DTA thermogram (Fig. 50). The latter also defines a decomposition onset temperature at  $260^\circ\text{C}$ , and a decomposition peak temperature at approximately  $478^\circ\text{C}$ . The irregular decomposition curve (Fig. 50) indicates the evolution of decomposition products which will be verified by thermogravimetric studies.

Thermal expansion data (Table 25 and Figure 49) agree well with those obtained by Morgan and Overall (Ref. 149). Although the expansion profiles of Avcoat 1 and Avcoat 19 are similar, linear coefficient of expansion values for the latter are approximately  $1 \times 10^{-5}$  in/in $^\circ\text{C}$  greater than those of Avcoat 1 over the entire temperature range studied. This may be the result of the slightly higher density of the Avcoat 1 sample, which would result in a smaller volume, and hence, a smaller thermal expansion value.

Eiermann (Ref. 118) has shown that the thermal conductivity of amorphous high polymers is mainly determined by the behavior of the van der Waals bonds. From the force constants for the bonds, he derived a relationship between the break in the thermal conductivity and in the thermal expansion curve at the glass transition expressed by

$$\Delta \left[ \frac{1}{\lambda} \left( \frac{\partial \lambda}{\partial T} \right) \right] = -5.8 \Delta \beta \quad (24)$$

where the first term in the equation is the increment of the relative temperature coefficient of the thermal conductivity, and  $\Delta \beta$  is the increment of the coefficient of cubic thermal expansion at the second-order transition temperature. Eiermann found that this relationship is independent of the substance and of the temperature, and that all polymers attain a value of  $-1.3$  to  $-1.5\%$   $^\circ\text{C}^{-1}$  for  $\Delta \left[ \frac{1}{\lambda} \left( \frac{\partial \lambda}{\partial T} \right) \right]$ . For Avcoat 19, the increment of the coefficient of cubic expansion,  $\Delta \beta$ , was found to be  $2.37 \times 10^{-4}$  in/in $^\circ\text{C}$  at the glass transition interval. Equation (24) gave a value of  $-1.38\%$   $^\circ\text{C}^{-1}$  for the increment of the relative temperature coefficient of the thermal conductivity. This calculated value is in good agreement with the experimental results mentioned above.



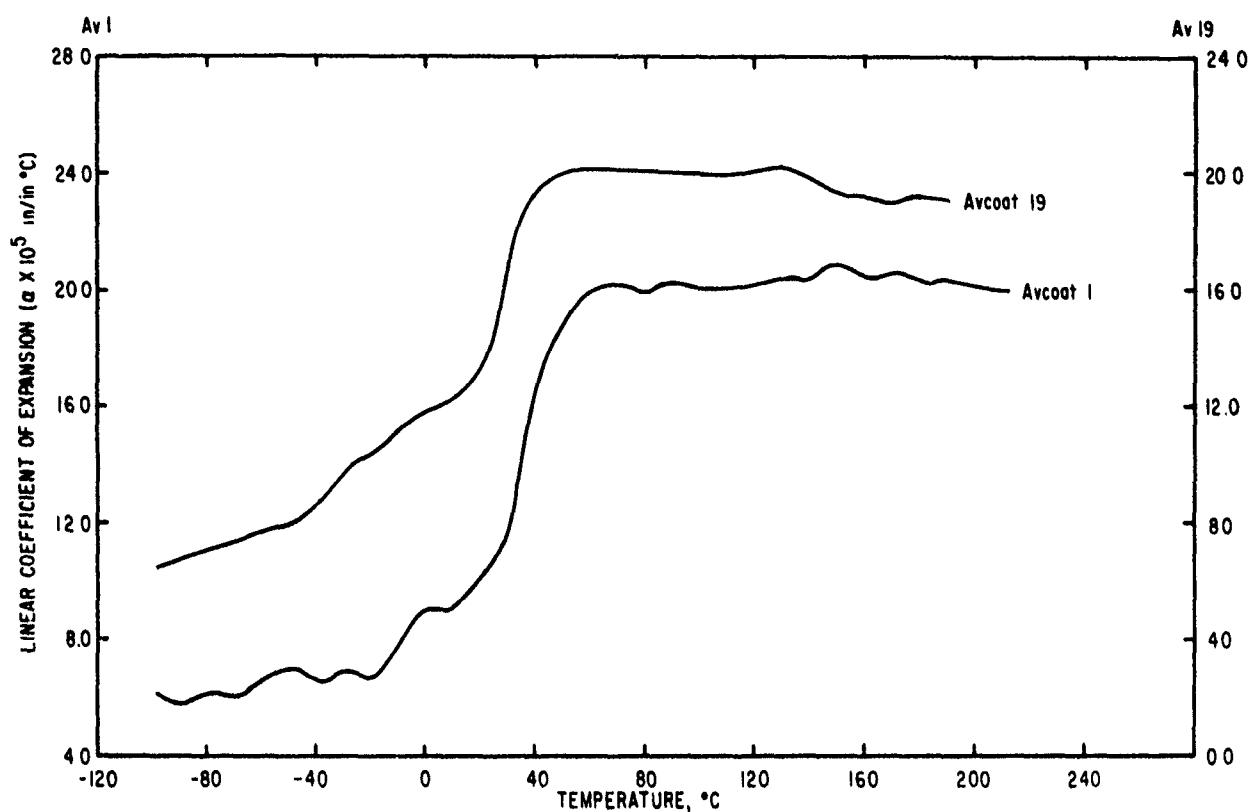


Figure 49. Linear Coefficient of Expansion Versus Temperature for Avcoat 1 and Avcoat 19.

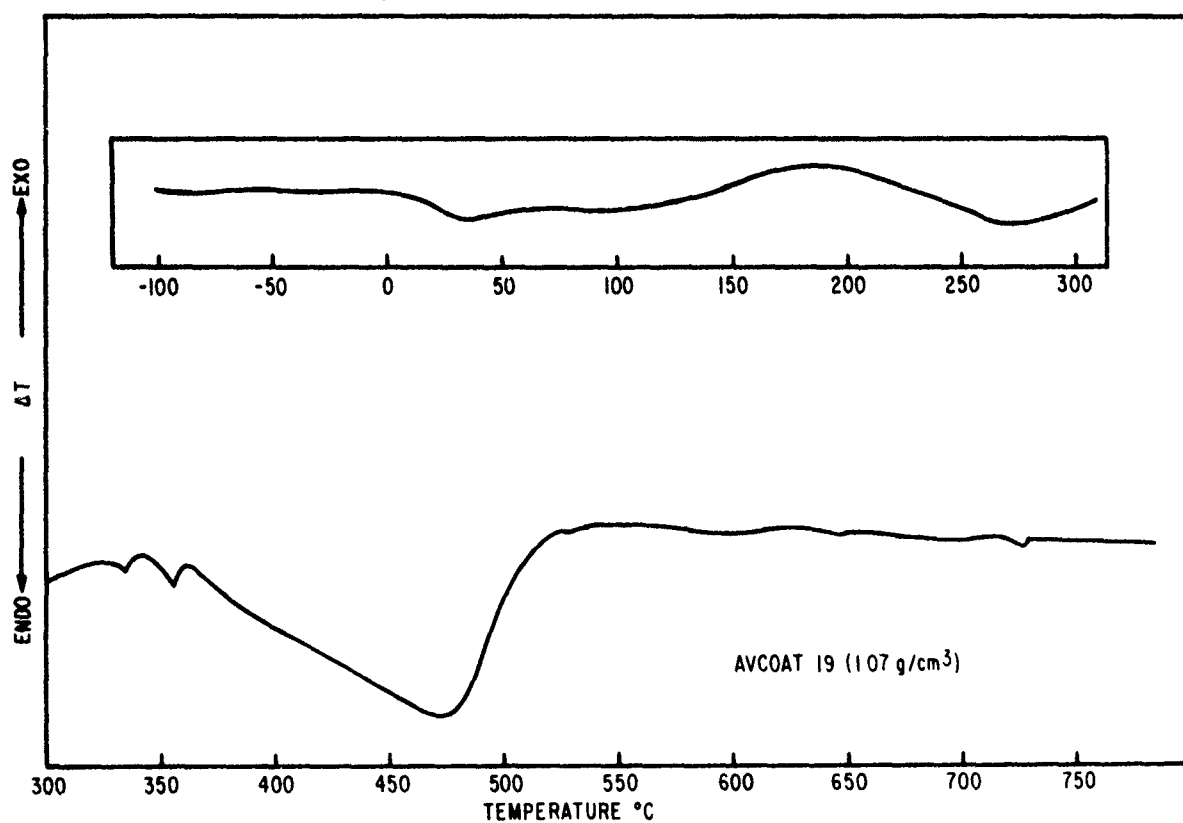


Figure 50. Differential Thermogram of Avcoat 19.

Table 25  
 LINEAR THERMAL EXPANSION DATA FOR AVCOAT 19

Temp. °C	$\alpha \times 10^5$ °C	Temp. °C	$\alpha \times 10^5$ °C
-100	6.51	60	20.15
-90	6.86	70	20.03
-80	7.17	80	20.00
-70	7.38	90	20.01
-60	7.87	100	20.05
-50	7.91	110	19.80
-40	8.92	120	20.09
-30	9.97	130	21.00
-20	10.44	140	19.80
-10	11.41	150	19.20
0	11.87	160	19.10
10	12.21	170	18.90
20	13.26	180	18.99
30	16.78	190	19.21
40	19.52	200	19.21
50	20.08		

Polynomial Fit for Coefficient of Expansion  
 $(\alpha = A + BT)$

Temp. Range °C	$A \times 10^5$ °C <sup>-1</sup>	$B \times 10^6$ °C <sup>-2</sup>
-25 to 20	$11.87 \pm 0.15$	0.717
20 to 45	$8.307 \pm 1.38$	2.83
40 to 100	$19.67 \pm 0.45$	0.04
135 to 200	$20.17 \pm 1.43$	-0.10

Heat capacity data may be represented by  $c_p = a + bT$ , where the constants  $a$  and  $b$  are given in Table 26. As observed from this data, the heat capacity increases approximately 40 percent through the glass transitional region (10° to 40°C). In the same temperature interval a relative specific volume increase of approximately 39 percent was noted from expansivity measurements. The small differences in the percentages may be due to the difficulty in defining the exact boundaries of the transition.

Table 26  
HEAT CAPACITY DATA FOR AVCOAT 19  
( $c_p = a + bT$ )

Temp. Range °C	a cal/g°C	b × 10 <sup>3</sup> cal/g°C <sup>2</sup>	Av Error of $c_p \times 10^2$
-100 to -20	0.2795	1.05	0.15
-20 to 40	0.2988	3.48	1.67
45 to 100	0.4165	1.18	1.13
105 to 175	0.4504	0.83	0.73
200 to 340	1.2215	-3.02	2.95

(3) Castable 124 (C-124)

Castable 124 is a discolored opaque epoxy with a density of 1.23 g/cm<sup>3</sup>. Elemental analysis of the sample gives 66.0 percent carbon, 25.3 percent oxygen, 7.11 percent hydrogen, 1.26 percent phosphorous, and 0.33 percent nitrogen.

The glass transition temperature (Fig. 51) at 37.8°C is much lower than that of the foamed epoxy (Foam #20,  $T_g \approx 137^\circ\text{C}$ ). At approximately -10°C a slight indication of secondary transition occurs, which is attributed to the "freezing in" of chain segments.

Instead of a melting endotherm, there occurs at a peak temperature of 320°C a small exotherm leading to the major exothermic peak at 370°C. The presence of these exotherms suggests the formation of volatile decomposition products. The use of a visual cell likewise indicated sample darkening at this temperature. The slight upward shift of the DTA baseline after 400°C (Fig. 51) suggests loss of weight in the sample at the exothermic reaction. Further thermogravimetric studies will verify this assumption. An estimated heat of decomposition of 25.2 cal/g was derived from a calculated value of 1.75 cal/g for  $\Delta H$  at 320°C and a value of 23.5 cal/g for  $\Delta H$  at 370°C. Numerical values for  $\Delta H$  were obtained by measuring the areas under the curve and applying the equations of Appendix VI.

The graph of the linear coefficient of expansion (Fig. 52) was obtained from the expansion data listed in Table 27. The glass transition temperature at 37.8°C was clearly defined as well as a secondary transition

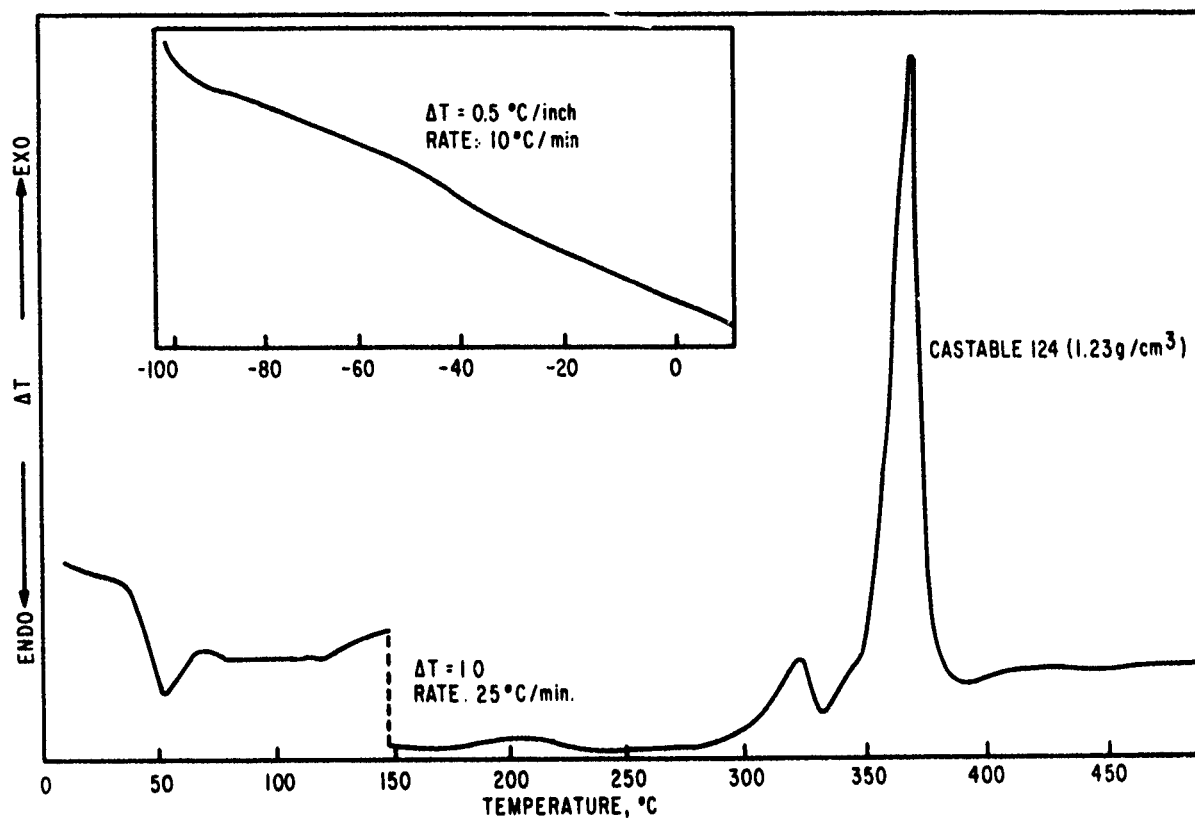


Figure 51. Differential Thermogram of Castable 124.

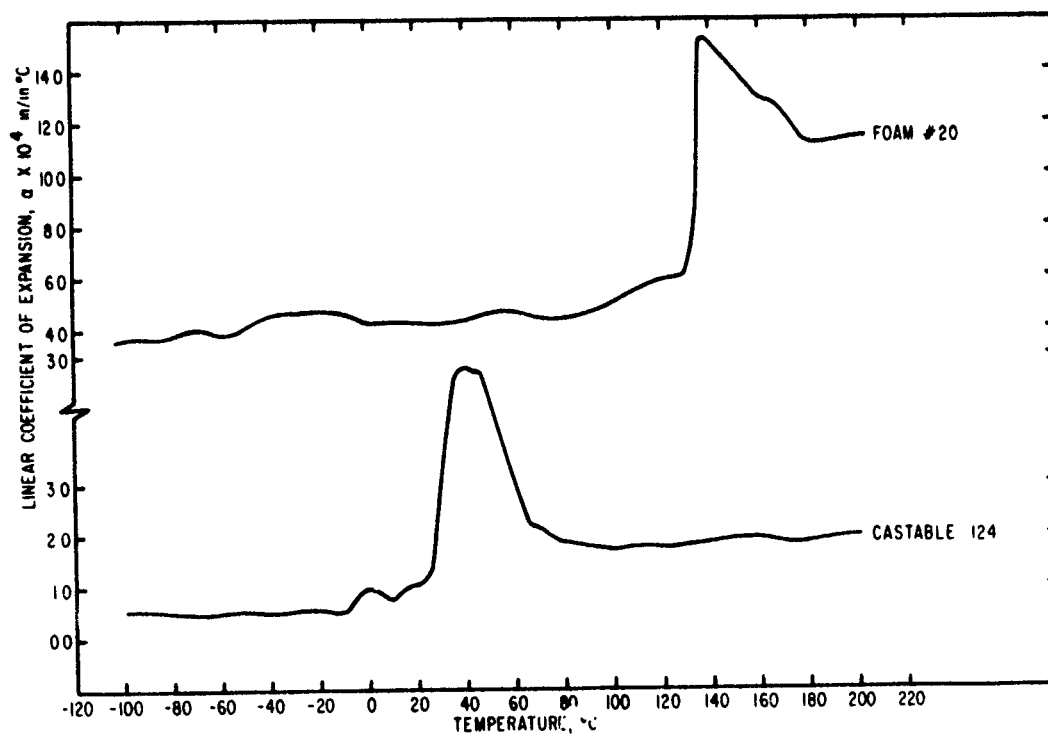


Figure 52. Expansivity Versus Temperature Profiles of Two Epoxides. (Castable 124 and Foam #20).

at  $-10^{\circ}\text{C}$ . These transitions were verified by heat capacity data, which may be represented by the equation,  $c_p = a + bT$ , where  $a$  and  $b$  are constants defined by the expressions in Table 28. The data show a rapid rise after the glass transition temperature ( $T_g = 37.8^{\circ}\text{C}$ ) to  $80^{\circ}\text{C}$  where the heat capacity decreases slightly until the decomposition onset at approximately  $280^{\circ}\text{C}$ .

Table 27  
LINEAR THERMAL EXPANSION DATA FOR CASTABLE 124

Temp. $^{\circ}\text{C}$	$\alpha \times 10^5 \text{ }^{\circ}\text{C}$	Temp. $^{\circ}\text{C}$	$\alpha \times 10^5 \text{ }^{\circ}\text{C}$
-100	5.21	60	28.49
-90	4.40	70	19.14
-80	5.30	80	18.83
-70	4.60	90	18.25
-60	4.95	100	17.55
-50	5.59	110	18.16
-40	5.09	120	17.83
-30	5.59	130	18.29
-20	5.76	140	18.46
-10	4.89	150	19.28
0	7.81	160	19.63
10	7.76	170	19.94
20	10.98	180	19.90
30	31.47	190	19.86
40	52.78	200	20.02
50	45.19		

Polynomial Fit for Coefficient of Expansion  
( $\alpha = A + BT$ )

Temp. Range $^{\circ}\text{C}$	$A \times 10^5 \text{ }^{\circ}\text{C}^{-1}$	$B \times 10^6 \text{ }^{\circ}\text{C}^{-2}$
-100 to -5	$6.517 \pm 0.50$	0.202
30 to 45	$-0.3388 \pm 20.77$	$12.49 \pm 5.48$
50 to 70	$110.6 \pm 7.45$	$-13.41 \pm 1.23$
75 to 200	$16.80 \pm 0.50$	0.161

Table 28  
HEAT CAPACITY DATA FOR CASTABLE 124  
( $c_p = a + bT$ )

Temp. Range °C	a cal/g°C	b × 10 <sup>3</sup> cal/g°C <sup>2</sup>	Av Error of $c_p$ × 10 <sup>2</sup>
-100 to -50	0.2982	0.71	0.05
-50 to -12	0.3104	0.95	0.08
-10 to 35	0.3175	1.41	0.35
37 to 65	0.1954	4.57	0.60
70 to 80	0.5636	-0.93	0.14
90 to 255	0.4291	-0.08	0.39

(4) Epoxy Foam #20

DuRaFoam EA\* is a prefoamed block of thermosetting resin. This material is an epoxy-based formulation with a density of 0.325 g/cc, which has a fine-cell, uniform, nondirectional structure. The epoxy base used in these foams is Epon 834\*\*, which is a glycidyl polyether of a dihydric phenol having an epoxide equivalent weight of 225 to 290 (Ref. 119). This rigid material is completely free from grain and is characterized by excellent machinability and dimensional stability.

The main curve features obtained for the foam (Fig. 53) are identified as: (1) the second-order glass transition,  $T_g$ , at 137°C which is manifested by a well-defined downward shift in the baseline, reflecting an increase in the heat capacity of the polymer, (2) polymer curing--as indicated by the small exothermic curve beginning at approximately 200°C, and (3) polymer fusion, represented by the endothermic curve with a peak temperature at 380°C, followed by decomposition at approximately 430°C.

The presence of an exothermic reaction in an inert atmosphere suggests the formation of secondary decomposition products due to the formation of new covalent bonds.

The high  $T_g$  value indicates a rigid amorphous stable polymer which softens to a flexible rubber-like material in the glass transitional region.

\*DuRaFoam is a registered trademark of D&R Pilot Plants, Inc., Hazardville, Conn.

\*\*Epon 834 is a registered trademark of Shell Chemical Co., Emeryville, Calif.

A repeated run through the glass transition temperature shows a gradual shift in the  $T_g$ . Wunderlich and Bodily (Ref. 120) have proposed that the configuration of  $T_g$  is governed by the rate at which the polymer is cooled.

Values obtained for the thermal expansion (Table 29) show a two-hundred and fifty-percent increase in the expansion at the glass transition over that obtained at room temperature.

The linear heat capacity data which best describe the experimental data are given by the expressions for a and b in Table 30.

The plot of the linear thermal expansion,  $\alpha$ , versus temperature (Fig. 52) shows a minor secondary transition at  $-40^\circ\text{C}$  and  $+40^\circ\text{C}$ , with the glass transition clearly defined at  $137.5^\circ\text{C}$ . Failure of the expansion plot to return to original expansion values observed below the glass temperature indicates a rearrangement of crystallites.

#### (5) Avco Phenolic Fiberglass (APFG)

This material is a phenol-formaldehyde thermosetting resin laminated with glass fibers. The fibers form a regular weave pattern with the resin binder resulting in a density of  $1.71 \text{ g/cm}^3$ .

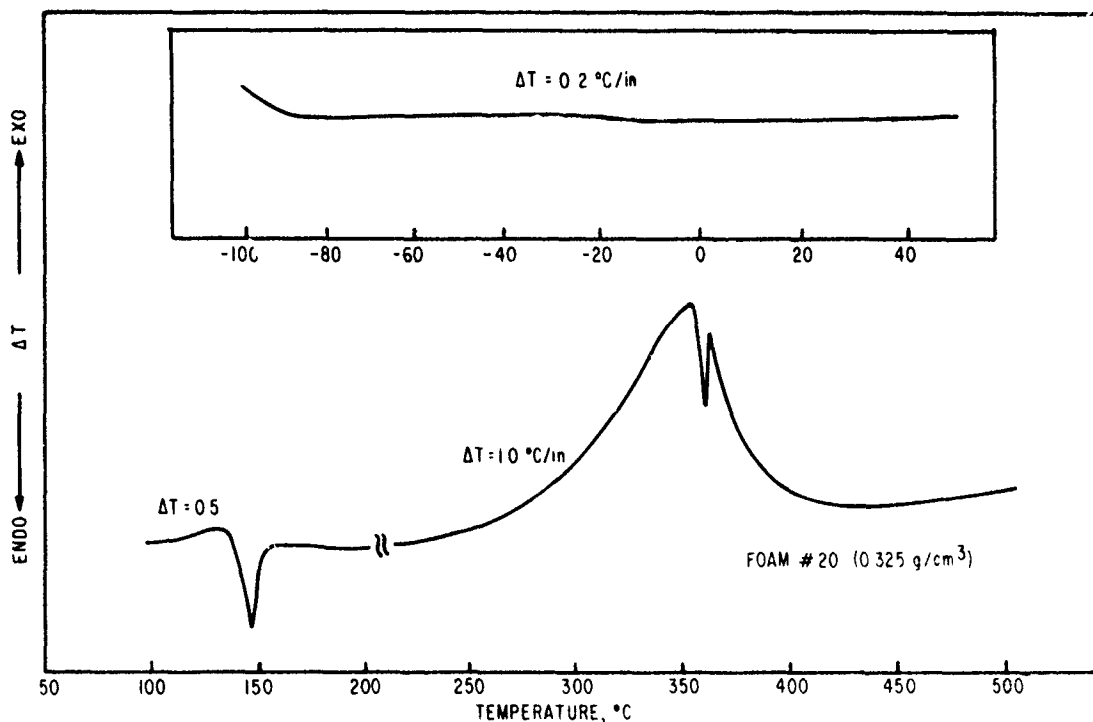


Figure 53. Differential Thermogram of Foam #20.

Table 29  
LINEAR THERMAL EXPANSION DATA FOR FOAM #20

Temp. °C	$\alpha \times 10^5 / ^\circ\text{C}$	Temp. °C	$\alpha \times 10^5 / ^\circ\text{C}$
-100	3.66	60	4.83
-90	3.66	70	4.42
-80	3.72	80	4.35
-70	4.23	90	4.63
-60	3.89	100	4.88
-50	4.27	110	5.07
-40	4.73	120	6.00
-30	4.75	130	6.10
-20	4.77	140	14.98
-10	4.79	150	13.90
0	4.11	160	12.89
10	4.42	170	12.67
20	4.24	180	12.48
30	4.30	190	11.33
40	4.37	200	11.41
50	4.73		

Polynomial Fit for Coefficient of Expansion  
( $\alpha = A + BT$ )

Temp. Range °C	$A \times 10^5 \text{ } ^\circ\text{C}^{-1}$	$B \times 10^6 \text{ } ^\circ\text{C}^{-2}$
-20 to 40	$4.806 \pm 0.11$	.02
60 to 80	$4.885 \pm 1.13$	-.06
95 to 130	$1.643 \pm 0.77$	.34
40 to 200	$23.200 \pm 1.58$	-.62

No significant transitions (Fig. 54) were observed from  $-100^\circ$  to  $125^\circ\text{C}$ , except the thermogram exhibited a steady rise in baseline, indicating an increase in heat capacity. The change in slope after  $125^\circ\text{C}$  may be attributed to phenol melt within the polymer. Partial decomposition occurred at temperatures greater than  $400^\circ\text{C}$ , with a decomposition peak at approximately  $440^\circ\text{C}$ .



Table 30  
HEAT CAPACITY DATA FOR FOAM #20  
( $c_p = a + bT$ )

Temp. Range °C	a cal/g°C	b × 10 <sup>3</sup> cal/g°C <sup>2</sup>	Av Error $c_p \times 10^2$
-100 to -40	0.1884	1.44	0.47
-40 to +20	0.2147	2.17	0.21
20 to 88	0.1323	6.14	1.16
88 to 100	1.0526	-4.64	0.05
100 to 137	0.3202	2.67	0.04
137 to 145	-0.1896	6.40	0.02
145 to 155	-1.2083	13.38	0.55
155 to 170	1.0814	-1.37	0.22
175 to 210	0.5363	1.87	0.33

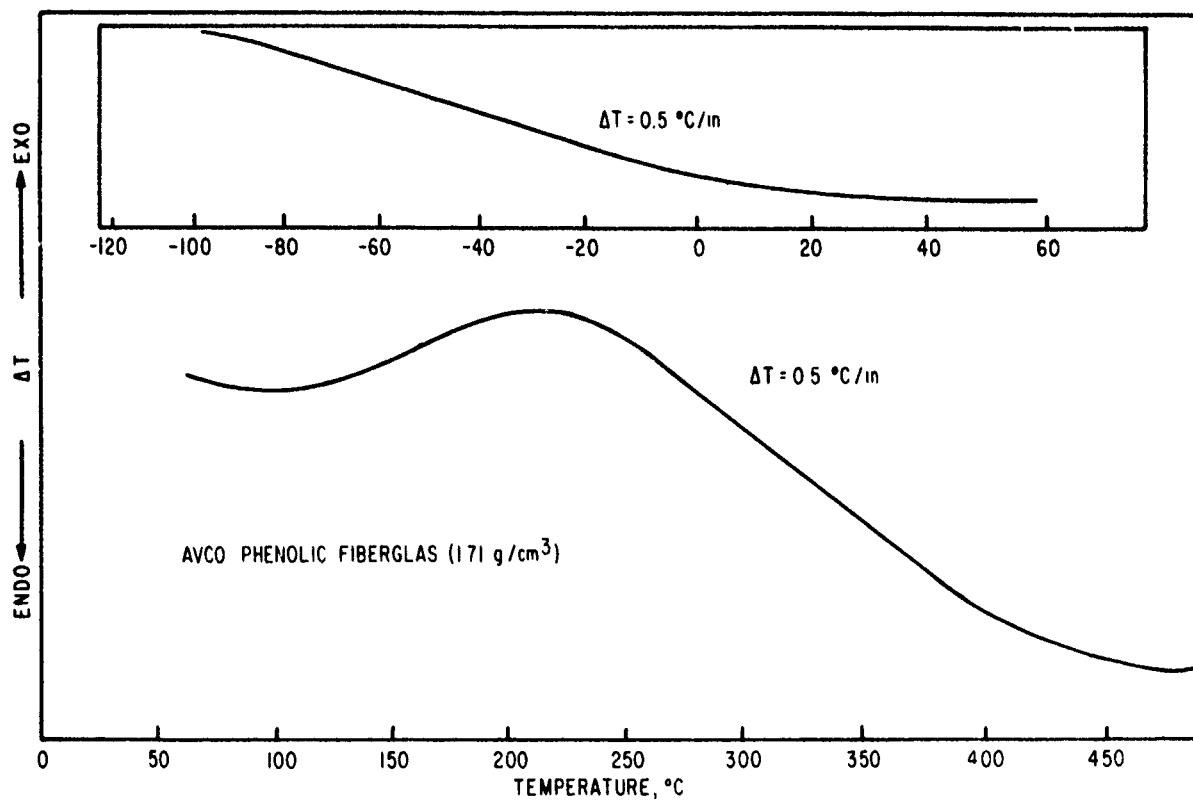


Figure 54. Differential Thermogram of Avco Phenolic Fiberglass.

Linear thermal expansion measurements made in two directions, horizontal and vertical to the weave pattern, are given in Table 31 and graphed in Figures 55 and 56. The change in slope of the horizontal expansion,  $\alpha_{||}$ , (Fig. 55) at 110°C is almost completely eliminated for the vertical expansion,  $\alpha_{\perp}$  (Fig. 56). This illustrates the efficiency of the weave pattern in strengthening the material and preventing the probe penetration of the sample. Due to the lack of information concerning the fiber diameter and length, no attempt will be made to define the amount of expansion resulting from the matrix and the fibers.

Fiber alignment along the main axis is said to account for differences in thermal expansion noted for Avco Phenolic Fiberglass (APFG), GE Phenolic Fiberglass (GEPF), and oblique tapewound refrasil (OTWR). The expansion in the "c" direction (elongation parallel to the weave) ( $\alpha_{||}$ ) follows the order

$$\text{OTWR} < \text{APFG} < \text{GEPF}$$

over the entire temperature range studied. The exception at 200°C where  $\text{GEPF} < \text{APFG} < \text{OTWR}$  is attributed to the probe penetration of the sample, which makes it impossible to obtain an accurate expansion measurement for APFG at this temperature. The linear extrapolation of  $\alpha_{||}$  from 100°C would give values in agreement with the above. The larger diameter of the glass fibers present in APFG accounts for the slightly lower expansion values than those observed for GEPF. As seen in Figure 55, the narrow fibers of GEPF were more efficient in increasing the overall strength of the polymer, because it was much easier to obtain expansion data for this material.

At low temperatures, the expansion in the "a" direction (elongation perpendicular to the weave) ( $\alpha_{\perp}$ ) follows the order

$$\text{APFG} < \text{GEPF} < \text{OTWR}$$

which reverts to  $\text{OTWR} < \text{APFG} < \text{GEPF}$  at higher temperatures. At low temperatures, the regular tight weave patterns of APFG and GEPF are effective in lowering the expansion values over those of OTWR; however, at higher temperatures, the increased concentration of the glass components of APFG and GEPF contribute greatly to the overall expansion values.

The heat capacity data were fitted to linear least-square equations and may be expressed as  $c_p = a + bT$ , where the constants are defined in Table 32. The heat capacity for the entire temperature range (-100° to 450°C) may be expressed by  $c_p = 0.2169 + 3.14 \times 10^{-4}T$  wherein, the average error in the heat capacity is  $1.87 \times 10^{-2}$  cal/g°C.

Table 31  
 LINEAR THERMAL EXPANSION DATA FOR AVCO PHENOLIC FIBERGLAS

Temp. °C	$\alpha_{\perp} \times 10^6 / ^\circ\text{C}$	$\alpha_{  } \times 10^5 / ^\circ\text{C}$	Temp. °C	$\alpha_{\perp} \times 10^6 / ^\circ\text{C}$	$\alpha_{  } \times 10^5 / ^\circ\text{C}$
-100	-0.34	1.58	60	2.34	2.86
-90	-0.34	1.61	70	1.34	2.89
-80	-0.34	1.72	80	1.33	3.09
-70	-0.34	1.75	90	1.00	3.03
-60	-0.34	1.88	100	2.67	3.16
-50	-0.34	1.92	110	2.67	3.43
-40	-0.34	2.02	120	1.34	3.02
-30	-0.20	2.02	130	3.00	2.28
-20	-0.10	2.25	140	4.65	2.18
-10	1.34	2.26	150	3.67	2.08
0	1.00	2.22	160	4.01	1.82
10	1.34	2.18	170	7.34	1.55
20	1.67	2.22	180	6.34	1.88
30	1.34	2.22	190	6.01	2.25
40	2.34	2.49	200	8.00	2.55
50	2.34	2.55			

Polynomial Fit for Coefficient of Expansion  
 $(\alpha = A + BT)$

Temp. Range °C	$A \times 10^5 \text{ } ^\circ\text{C}^{-1}$	$B \times 10^6 \text{ } ^\circ\text{C}^{-2}$
Parallel expansion, $\alpha_{  }$		
-100 to 100	$2.352 \pm .01$	.08
110 to 170	$6.468 \pm .50$	-.30
175 to 200	$-4.520 \pm .48$	.36
Perpendicular expansion, $\alpha_{\perp}$		
-100 to 200	$0.272 \pm .03$	.03

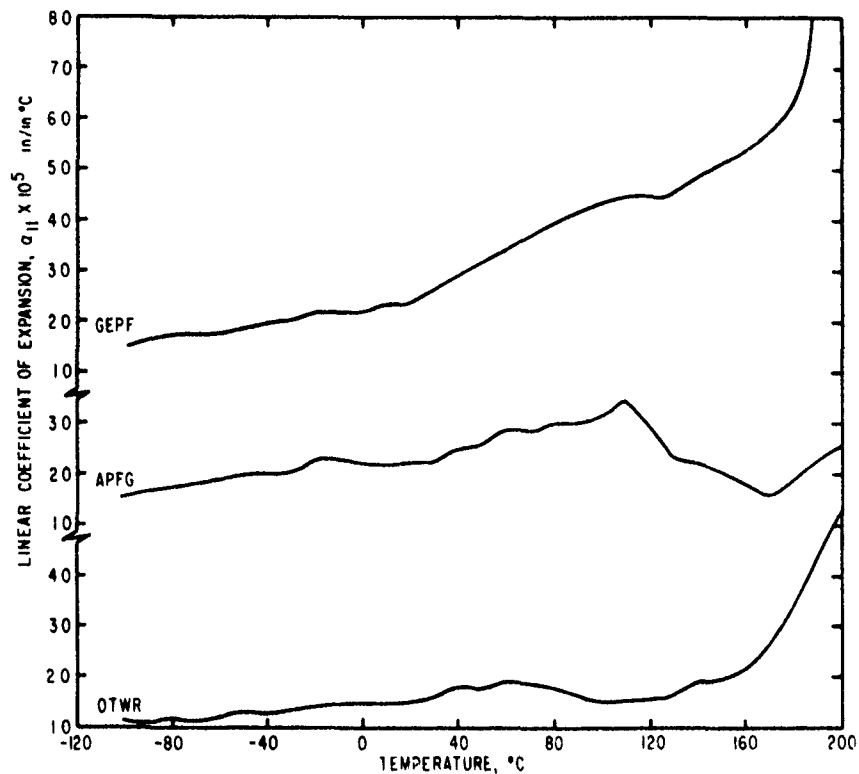


Figure 55. Linear Coefficient of Expansion Profiles for Avco Phenolic Fiberglass, G.E. Phenolic Fiberglass, and Oblique Tapewound Refrasil ( $\alpha_{||}$ , Parallel to Axis)

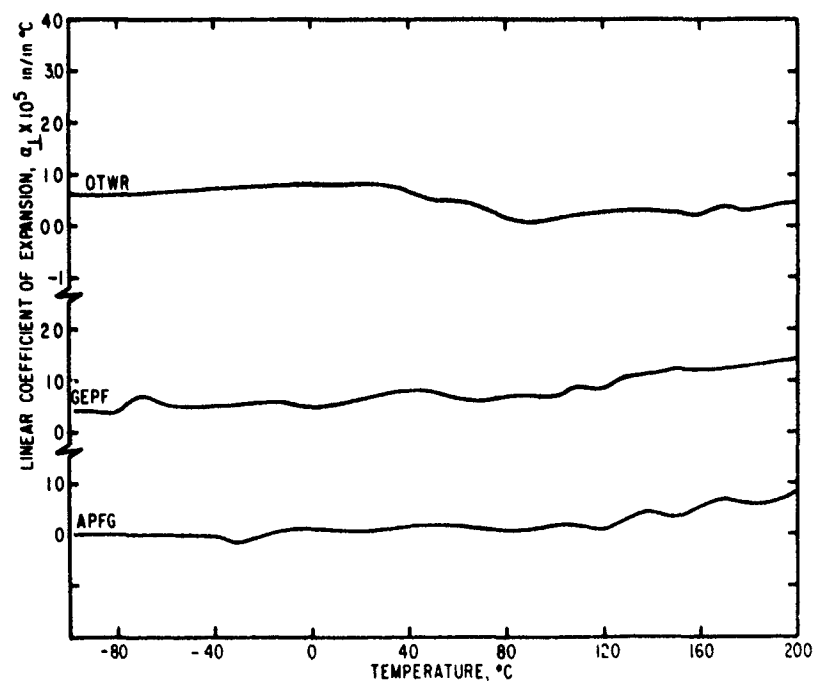


Figure 56. Linear Coefficient of Expansion Profiles for Avco Phenolic Fiberglass, G.E. Phenolic Fiberglass, and Oblique Tapewound Refrasil ( $\alpha_{\perp}$ , Perpendicular to Axis).

Table 32  
HEAT CAPACITY DATA FOR AVCO PHENOLIC FIBERGLAS  
( $c_p = a + bT$ )

Temp. Range °C	a cal/g°C	b × 10 <sup>3</sup> cal/g°C <sup>2</sup>	Av Error $c_p \times 10^2$
-100 to 80	.2231	0.44	0.14
80 to 325	.2311	0.21	1.02
325 to 450	1.1341	0.60	1.77

Examination of the data shows a heat capacity of approximately 0.235 cal/g°C at 25°C which increases to 0.329 cal/g°C at 320°C. The heat capacity expected for a phenol-formaldehyde resin at room temperature is ~ 0.4 cal/g°C, whereas, that of glass is ~ 0.12 cal/g°C. The experimental values obtained may be explained by the Kopp-Neumann law (Ref. 121), which states that the molecular heat of a compound is the sum of the atomic heats of its constituents. In equation form this becomes

$$c_p(P) = a[c_p(M)] + b[c_p(F)]$$

where a and b refer to the molar concentration of the heat capacities of the pure matrix,  $[c_p(M)]$ , and fibers  $[c_p(F)]$ , respectively. The term  $[c_p(P)]$  refers to the heat capacity of the resulting polymer.

Differentiation and integration of the heat capacity data above gave the corresponding enthalpy values for the transition regions below 210°C as

$$(H_{0^\circ\text{C}} - H_{-100^\circ\text{C}}) = 0.2150 T + 2.09 \times 10^{-4} T^2$$

and

$$(H_{210^\circ\text{C}} - H_{20^\circ\text{C}}) = 0.2178 T + 4.55 \times 10^{-4} T^2.$$

The corresponding entropy values may be expressed as

$$(S_{0^\circ\text{C}} - S_{-100^\circ\text{C}}) = 0.2150 \ln T + 2.09 \times 10^{-4} T$$

$$(S_{210^\circ\text{C}} - S_{20^\circ\text{C}}) = 0.2178 \ln T + 9.09 \times 10^{-4} T$$

(6) G. E. Phenolic Fiberglas (GEPF)

The polymer, made from a glass fabric sheet impregnated with a thermosetting resin, shows a regular weave pattern and has a density of 1.91 g/cc. Compared to Avco Phenolic Fiberglas (APFG) the fibers appear to have a smaller

diameter, and hence, a tighter weave. Specification data include: 35.06 percent oxygen, 30.8 percent carbon, 14.87 percent silicon, 8.14 percent calcium, 4.29 percent aluminum, 2.44 percent hydrogen, and 1.86 percent boron, plus other impurities.

The DTA thermogram (Fig. 57) is similar to all phenolic resins in which a slight exotherm at 237°C falls into a valley with a minimum at approximately 425°C. The decomposition peak at approximately 237°C is associated with the phenolic component of the resin. Decomposition is completed at a peak temperature of approximately 480°C.

The linear expansion plot ( $\alpha_{||}$ , Fig. 55) indicates a slight exotherm temperature range of from 40° to 125°C which is probably due to the melting of the phenol component. A deviation of  $\pm 2.0$  percent was noted for the expansion values in this region. As discussed previously (see data for APFG) the binding nature of the fibers cause expansion parallel to the weave to be larger than the perpendicular expansion (see Table 33 and Figures 55 and 56).

The total heat capacity of the polymer can be well represented by the equation,  $c_p = a + bT$ , where the constants  $a$  and  $b$  have values for the various temperature ranges as shown in Table 34. From the data it can be seen that the heat capacity increases linearly to 350°C where the values seem to level off to a constant value of approximately 0.35 cal/g°C. After 450°C they continue dropping to a minimum peak of  $\sim 0.066$  cal/g°C at 480°C. Since the heat capacity values are considered to be additive functions of the individual constituents within the polymer, the data are in accord with what was expected for phenol-formaldehyde glass fiber reinforced systems.

#### (7) Oblique Tapewound Refrasil (OTWR)

This material is a Monsanto SC 1008 phenolic resin (35 percent by weight) laminated with a high silica leached glass fabric (65 percent by weight). The reinforcement contains a boron impurity (0.023 percent) and the tape layup is at an angle of 23 degrees. Additional specification data include: density, 1.54 g/cm<sup>3</sup>; porosity, 6.29 percent; 42.96 percent oxygen, 32.35 percent silicon, 22.6 percent carbon, 2.06 percent hydrogen, and 0.03 percent boron (Ref. 122).

The DTA thermogram (Fig. 58) indicates a slight maximum at a peak temperature,  $T_p = 235^\circ\text{C}$ , dropping into the characteristic phenolic valley at a minimum of approximately 400°C.

Table 33  
 LINEAR THERMAL EXPANSION DATA FOR G. E. PHENOLIC FIBERGLAS

Temp. °C	$\alpha_{\perp} \times 10^6 / ^\circ\text{C}$	$\alpha_{  } \times 10^5 / ^\circ\text{C}$	Temp. °C	$\alpha_{\perp} \times 10^6 / ^\circ\text{C}$	$\alpha_{  } \times 10^5 / ^\circ\text{C}$
-100	3.95	1.53	60	7.01	3.46
-90	4.17	1.60	70	6.01	3.74
-80	4.01	1.73	80	7.23	3.95
-70	6.67	1.73	90	7.25	4.15
-60	5.34	1.80	100	7.35	4.34
-50	4.67	1.90	110	9.02	4.45
-40	5.31	2.00	120	8.68	4.50
-30	5.67	2.03	130	11.01	4.56
-20	5.77	2.13	140	11.68	4.89
-10	6.01	2.16	150	12.35	5.12
0	5.01	2.16	160	12.01	5.39
10	5.90	2.36	170	12.68	5.82
20	6.25	2.40	180	13.35	6.39
30	7.34	2.73	190	13.68	9.38
40	8.01	2.99	200	14.68	26.58
50	8.01	3.10			

Polynomial Fit for Coefficient of Expansion

$$(\alpha = A + BT)$$

Temp. Range °C	$A \times 10^5 \text{ } ^\circ\text{C}^{-1}$	$B \times 10^6 \text{ } ^\circ\text{C}^{-2}$
Parallel expansion, $\alpha_{  }$		
-100 to 30	$2.29 \pm .03$	$7.825 \pm .01$
40 to 170	$2.28 \pm .10$	$.195 \pm .01$
170 to 200	$-108.59 \pm 42.0$	$6.520 \pm 2.26$
Perpendicular expansion, $\alpha_{\perp}$		
-100 to 200	$6.34 \pm .25$	$3.200 \pm .03$

Table 34  
HEAT CAPACITY DATA FOR G. E. PHENOLIC FIBERGLAS  
( $c_p = a + bT$ )

Temp. Range °C	a cal/g°C	b × 10 <sup>3</sup> cal/g°C <sup>2</sup>	Av Error $c_p$ × 10 <sup>2</sup>
-100 to 125	0.2224	0.67	0.58
150 to 325	0.3058	0.23	1.19
338 to 425	0.5256	-0.49	0.56
425 to 478	1.9380	-3.78	1.43
480 to 505	-3.7618	8.02	1.24
505 to 575	0.2105	0.25	0.44

The expansion plots parallel and perpendicular to the layers are given in Figures 55 and 56 and discussed with Avco Phenolic Fiberglass. The irregular weave pattern of the glass fibers accounts for the greatest deviations in the expansion values.

Over the temperature range where the heat capacity is a function of temperature,  $c_p = a + bT$ , the data can be represented by values of the constants given for a and b in Table 35. Heat capacity values are similar to those for G.E. Phenolic Fiberglass with a peak maximum at ~ 230°C which drops to a minimum at ~ 320°C. Table 36 lists the coefficient of expansion values for OTWR.

Table 35  
HEAT CAPACITY DATA FOR OBLIQUE TAPEWOUND REFRASIL  
( $c_p = a + bT$ )

Temp. Range °C	a cal/g°C	b × 10 <sup>4</sup> cal/g°C <sup>2</sup>	Av Error $c_p$ × 10 <sup>2</sup>
-100 to 0	0.2150	4.18	0.20
20 to 210	0.2178	9.09	0.47
220 to 300	0.7049	-14.46	0.93
325 to 425	-0.1350	13.10	0.92
450 to 625	0.2093	3.28	2.68



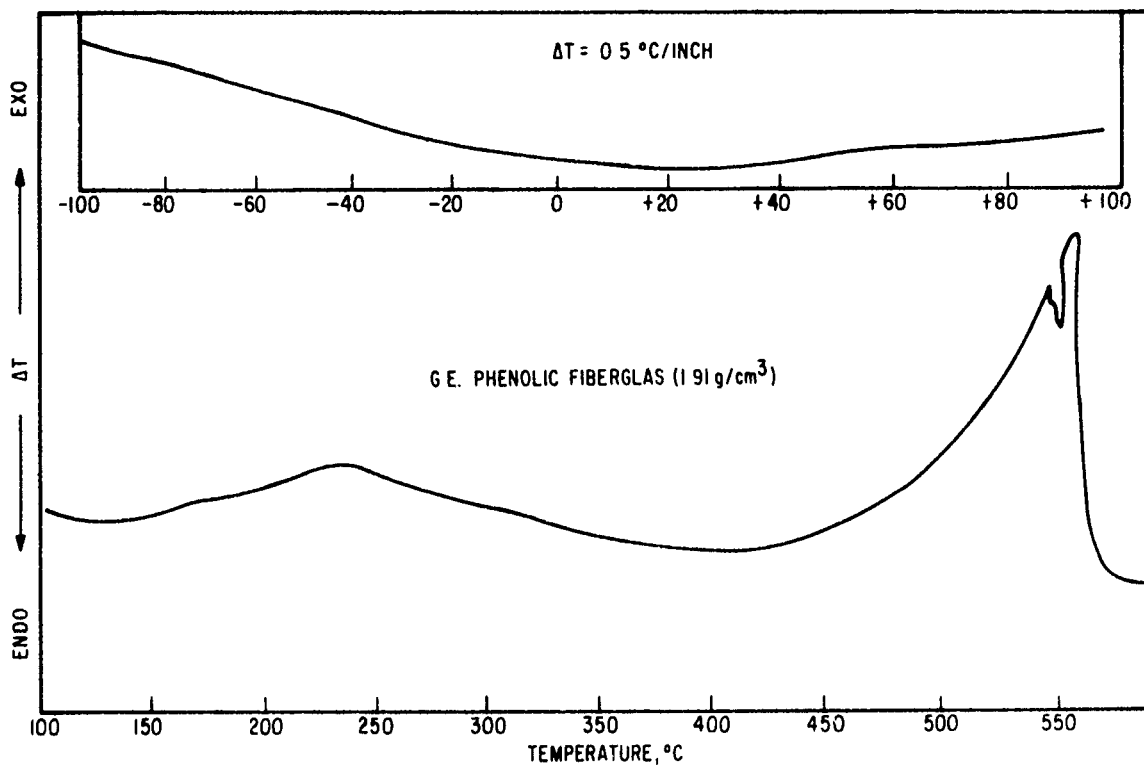


Figure 57. Differential Thermogram of G.E. Phenolic Fiberglass.

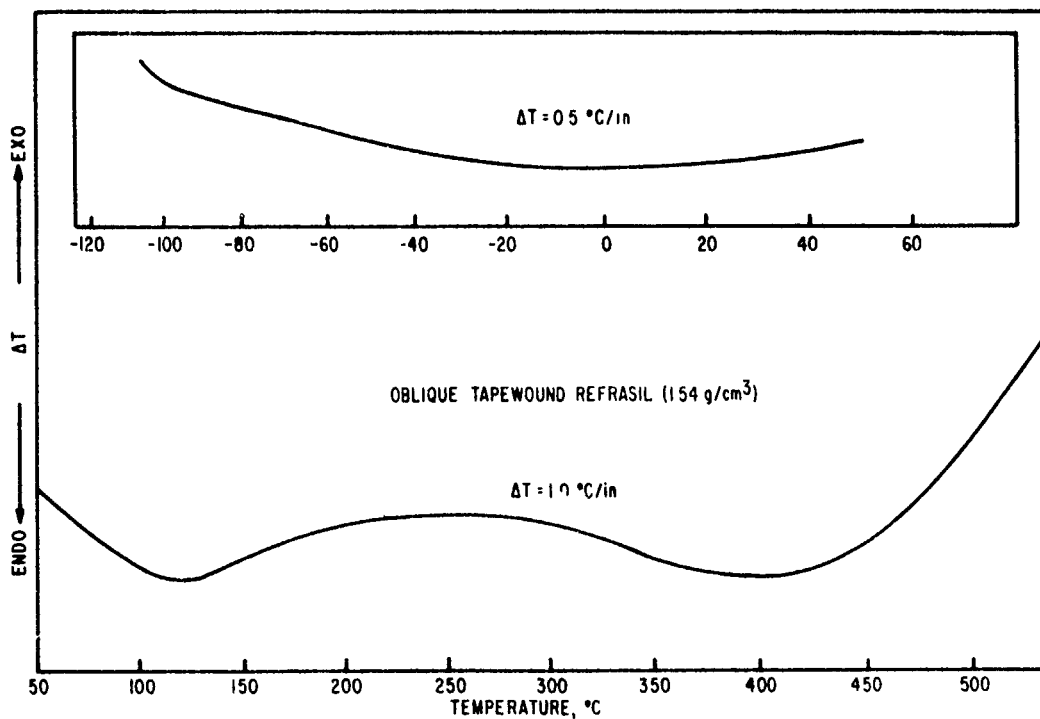


Figure 58. Differential Thermogram of Oblique Tapewound Refrasil.

Table 36  
 LINEAR THERMAL EXPANSION DATA FOR OBLIQUE TAPEWOUND REFRASIL

Temp. °C	$\alpha_{\perp} \times 10^6 / ^\circ\text{C}$	$\alpha_{  } \times 10^5 / ^\circ\text{C}$	Temp. °C	$\alpha_{\perp} \times 10^6 / ^\circ\text{C}$	$\alpha_{  } \times 10^5 / ^\circ\text{C}$
-100	6.00	1.14	60	5.01	1.91
-90	6.01	1.07	70	3.68	1.84
-80	6.20	1.21	80	2.67	1.81
-70	6.20	1.14	90	0.67	1.68
-60	6.66	1.21	100	1.34	1.61
-50	6.90	1.31	110	1.34	1.68
-40	7.00	1.27	120	2.34	1.54
-30	7.20	1.24	130	2.67	1.64
-20	7.76	1.64	140	3.01	1.91
-10	8.25	1.54	150	3.34	2.14
0	8.36	1.51	160	3.30	2.14
10	8.69	1.51	170	3.50	2.72
20	8.30	1.47	180	2.56	3.35
30	8.02	1.47	190	3.79	4.37
40	7.35	1.50	200	4.35	5.36
50	5.54	1.50			

Polynomial Fit for Coefficient of Expansion  
 $(\alpha = A + BT)$

Temp. Range °C	$A \times 10^5 \text{ } ^\circ\text{C}^{-1}$	$B \times 10^6 \text{ } ^\circ\text{C}^{-2}$
Parallel expansion, $\alpha_{  }$		
-100 to 50	$1.51 \pm .03$	0.04
60 to 110	$2.24 \pm .10$	-0.06
115 to 145	$0.66 \pm .67$	0.19
140 to 200	$-7.76 \pm 1.22$	0.66
Perpendicular expansion, $\alpha_{\perp}$		
-100 to 330	$0.802 \pm .01$	0.02
40 to 100	$1.129 \pm .08$	-0.11
or 100 to 200	$-0.088 \pm .07$	-0.03
-100 to 200	$0.595 \pm .04$	-0.02

## (8) Carbon Phenolic (CP)

The General Electric prepregated carbon phenolic studied, contains carbon cloth filaments which appear to be uniaxially orientated. Specification data (Ref. 122) include:

density	1.48 g/cm <sup>3</sup>
resin	34 percent by weight
reinforcement	66 percent by weight
elemental analysis	C 90.8 percent    N 0.6 percent
	H 2.1 percent    O 6.5 percent

This phenolic resin is a very highly crosslinked three-dimensional polymer, since the phenol was able to react with formaldehyde at positions ortho, meta, and para to the alcohol group. The phenolic resin is the base material with carbon fibers as the filler.

The DTA thermogram (Fig. 59) shows an exotherm onset at approximately 105°C with an exothermic peak temperature at 225°C. The latter leads into a decomposition valley with a minimum at approximately 475°C.

Repeated DTA studies of the sample showed that the porosity of the material permitted excessive absorption of moisture, because water and ice points were detected on the initial thermograms. These were removed by predrying the sample in an oven at 100°C for two hours. It is known that ionic impurities coupled with moisture will increase the electrical conductivity of an insulator. It is also known that the thermal conductivity of materials is directly proportional to electrical conductivity and depends on chemical composition, filler, temperature, and moisture. The addition of the carbon filler to the phenolic matrix resulted in a thermal conductivity of 0.002 cal/sec-cm-°C (Ref. 122), as opposed to the value of 0.0003 cal/sec-cm-°C for the unfilled polymer. Because of increased heat dissipation resulting from this high thermal conductivity, it was necessary to perform all thermal studies at a rate of 5°C/min. In this way, temperature equilibration at each point of interest was assured. Reproducible and comparable results were obtained only after the humidity and rate of heating were rigorously controlled.

Moisture and heating rate were also seen to have a pronounced effect on expansion data. In general, the elongation increased as the amount of absorbed moisture increased, but no uniform trend was noted. Expansion values in the "a" and "c" directions (Table 37) were obtained from runs on the predried sample.

Table 37  
 LINEAR THERMAL EXPANSION DATA FOR CARBON PHENOLIC

Temp. °C	$\alpha_{\perp} \times 10^5 / ^\circ\text{C}$	$\alpha_{  } \times 10^5 / ^\circ\text{C}$	Temp. °C	$\alpha_{\perp} \times 10^5 / ^\circ\text{C}$	$\alpha_{  } \times 10^5 / ^\circ\text{C}$
-100	1.05	1.17	60	0.62	1.27
-90	1.24	1.30	70	0.53	1.07
-80	1.14	1.30	80	0.56	1.24
-70	1.02	1.37	90	0.74	1.17
-60	0.90	1.37	100	0.81	1.37
-50	0.99	1.46	110	0.68	1.43
-40	0.93	1.50	120	0.74	1.69
-30	0.96	1.56	130	0.96	1.72
-20	0.99	1.72	140	1.33	1.85
-10	1.02	1.69	150	1.42	2.15
0	1.15	1.72	160	1.55	2.28
10	1.08	1.66	170	1.30	2.99
20	0.93	1.63	180	1.42	4.62
30	1.05	1.37	190	2.07	7.61
40	0.62	1.43	200	2.23	19.90
50	0.68	1.37			

Polynomial Fit for Coefficient of Expansion  
 $(\alpha = A + BT)$

Temp. Range °C	$A \times 10^5 \text{ } ^\circ\text{C}^{-1}$	$B \times 10^6 \text{ } ^\circ\text{C}^{-2}$
Parallel expansion, $\alpha_{  }$		
-100 to 0	$1.75 \pm 0.02$	0.06
10 to 70	$1.75 \pm 0.06$	-0.09
110 to 190	$-6.19 \pm 2.20$	0.61
Perpendicular expansion, $\alpha_{\perp}$		
-100 to -20	$0.87 \pm 0.07$	-0.03
-20 to +30	$1.04 \pm 0.03$	-0.00
40 to 80	$1.12 \pm 0.17$	-0.08
80 to 200	$-5.60 \pm 0.21$	0.13

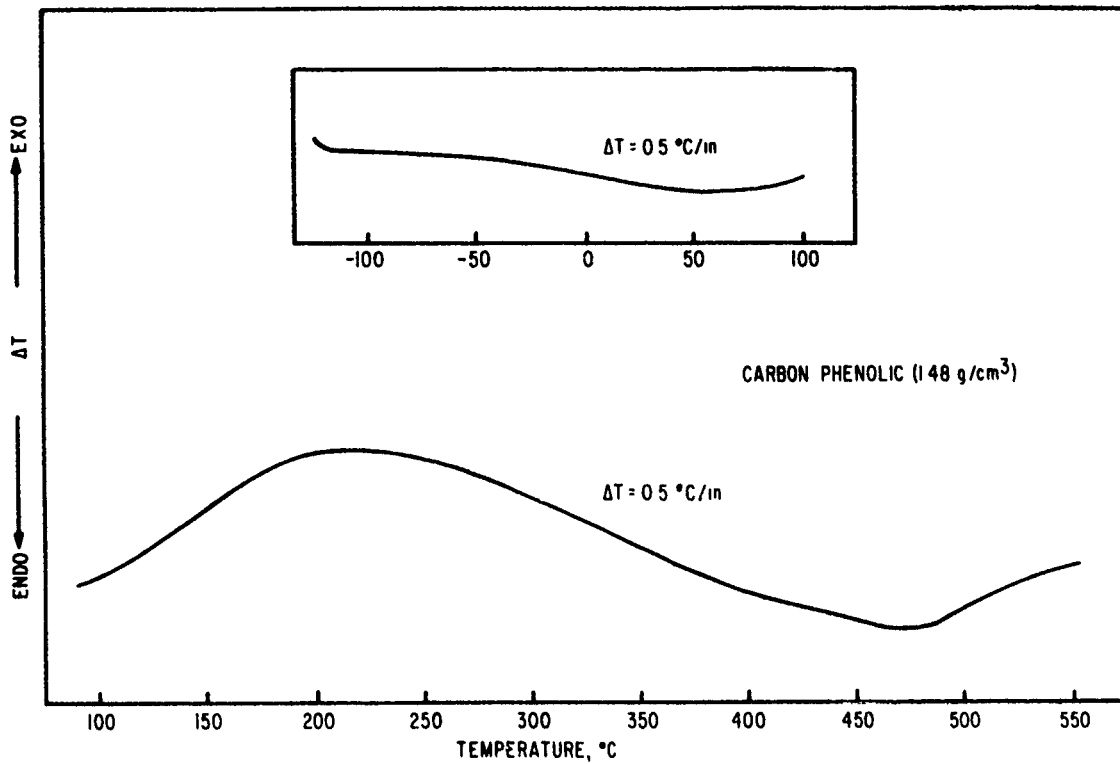


Figure 59. Differential Thermogram of Carbon Phenolic.

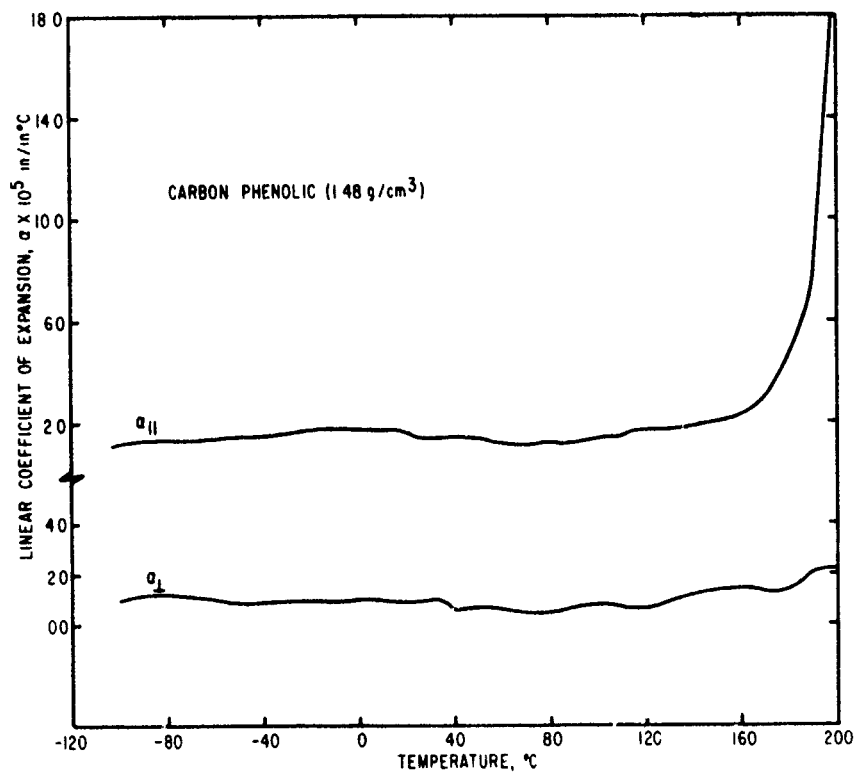


Figure 60. Linear Coefficient of Expansion Versus Temperature For Carbon Phenolic (Parallel and Perpendicular to the Axis).

The plot of  $\alpha$  versus  $T$  (Fig. 60) shows a slight decrease in the expansion from approximately 30° to 80°C. This decrease is less pronounced in the "a" direction and may be the result of decomposition of the phenol component of the polymer.

The heat capacity equations derived from linear least-square curve fitting of the original data give the expressions in Table 38. A 58 percent increase in heat capacity is noted from -100° to 80°C which decreases to ~ 12 percent up to 240°C and levels off to ~ 9.0 percent from 240° to 700°C. The data are consistent with the expectations for the solid-solid, liquid-solid, and solid residue phases, which are prevalent in the three temperature ranges of the polymer.

Table 38  
HEAT CAPACITY DATA FOR CARBON PHENOLIC

$$c_p = a + bT$$

Temp. Range °C	a cal/g°C	b × 10 <sup>3</sup> cal/g°C <sup>2</sup>	Av Error $c_p \times 10^2$
-100 to 75	0.1881	1.07	0.53
80 to 225	0.2263	0.51	0.59
250 to 700	0.3152	0.12	0.15

#### (9) Chopped Nylon Phenolic (CNP)

The chopped nylon phenolic studied is a laminated thermosetting product made of nylon fabric sheet material on which was impregnated a phenolic thermosetting resin binder, and consolidated under high temperatures and pressure into a hard solid product. The nylon fibers tend to line up parallel to the plane of the sheet, but in random direction. The effect of this nonwoven basis of the reinforcement is to introduce a higher level of variability in the mechanical properties. The material had a calculated density of 1.68 g/cm<sup>3</sup>.

As indicated on the DTA thermogram (Fig. 61), no pronounced transitions occur before 200°C; however, a slight break in the curve at approximately 40°C suggests the appearance of the nylon glass transition temperature. At approximately 200°C the characteristic phenolic exotherm onset is observed, which is interrupted by a sharp fusion peak at 257°C. The latter is attributed to the nylon component of the polymer. Decomposition begins at approximately 380°C with the well-defined decomposition peak occurring at ~ 430°C. A charred residue remained after heating to temperatures beyond 700°C.

The coefficient of expansion versus temperature curves (Figures 62 and 63) indicate the presence of the glass transition temperature at approximately 40°C. This temperature was more clearly observed on the original length versus temperature curves. No further secondary transitions were listed for the material, because small irregularities in the expansion curves could be the result of the non-uniformity of the interwoven layers.

Plots of the parallel expansion,  $\alpha_{||}$ , (Fig. 62) of chopped nylon phenolic and tapewound nylon phenolic show that both increase rapidly to about 160°C. Reruns on the materials indicated a softening region from approximately 80° to 350°C, which was more pronounced for chopped nylon phenolic than for the tapewound polymer. The upper limiting temperature was verified by heat capacity data. This "soft region" is indicated by the dotted line on the graph of chopped nylon phenolic (Fig. 62) and suggests that the regular weave pattern of TWNP increased the strength of the polymer to a greater extent than the irregular weave made by the chopped strands. Since increase in polymer strength is not directly related to decreased thermal expansion, results of Table 39 show CNP to be more effective in lowering the expansion of the polymer. Room temperature data parallel and perpendicular to the plane (Table 39 and Figures 62 and 63) indicate

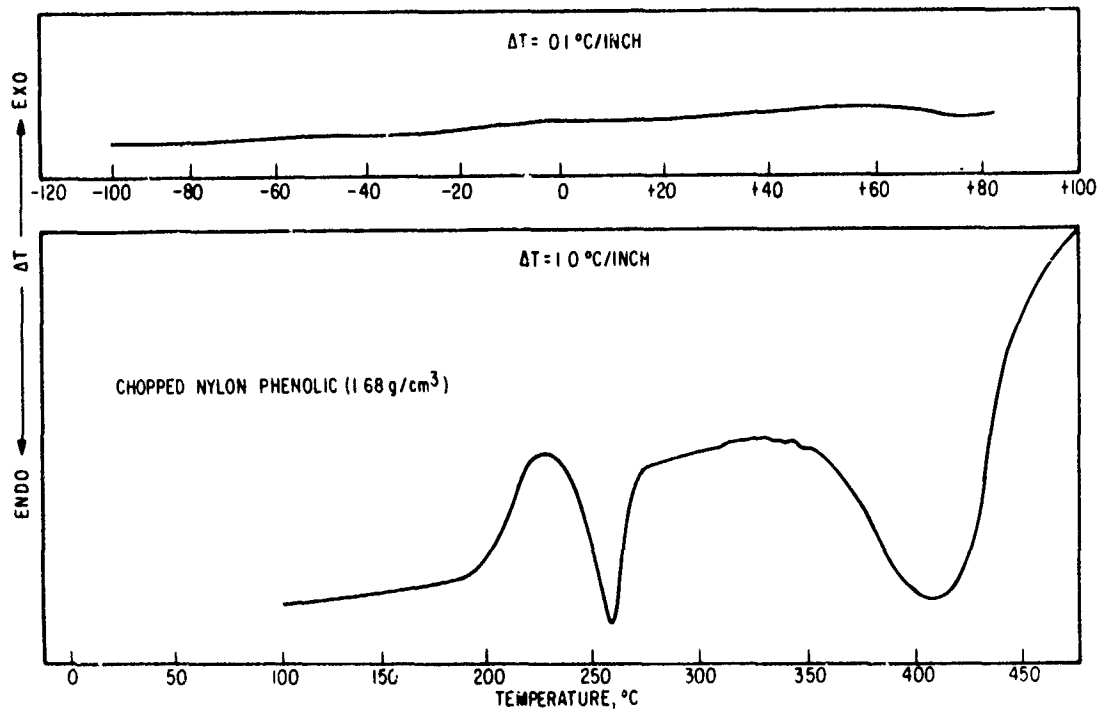


Figure 61. Differential Thermogram of Chopped Nylon Phenolic.

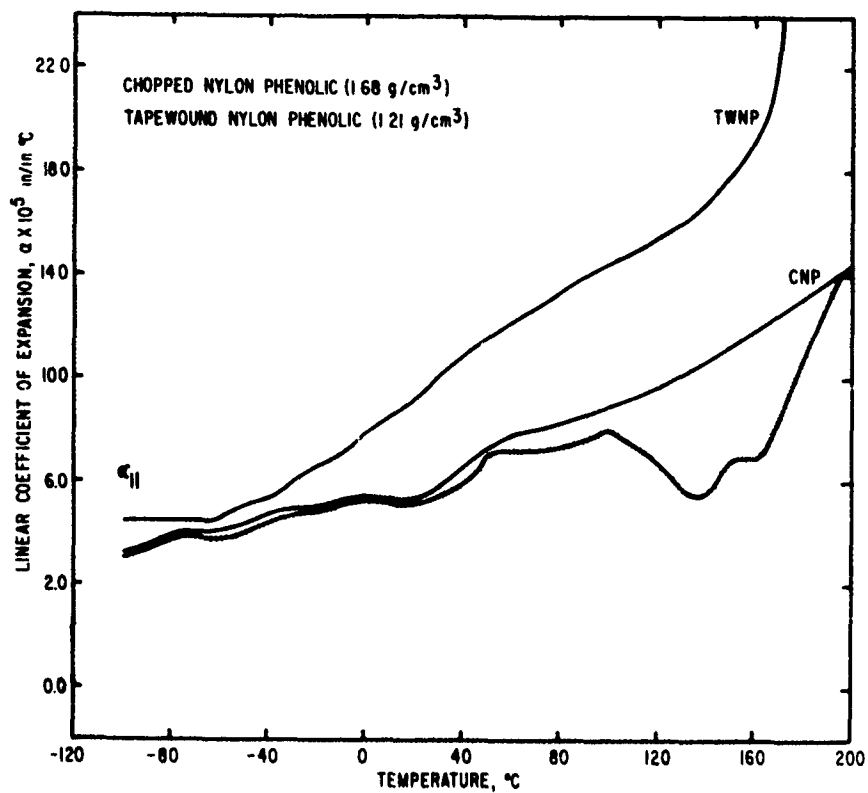


Figure 62. Expansivity Versus Temperature Curves for Chopped Nylon Phenolic (CNP) and Tapewound Nylon Phenolic (TWNP) (Parallel to the Axis).

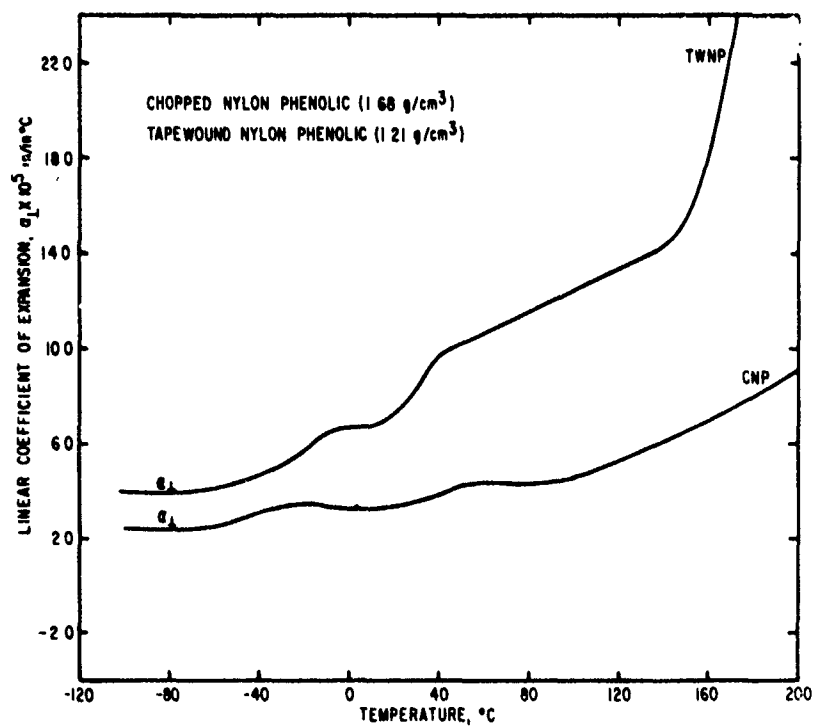


Figure 63. Expansivity Versus Temperature Curves for Chopped Nylon Phenolic (CNP) and Tapewound Nylon Phenolic (TWNP) (Perpendicular to the Axis).



Table 39  
 LINEAR THERMAL EXPANSION DATA FOR CHOPPED NYLON PHENOLIC

Temp. °C	$\alpha_{\perp} \times 10^5 / ^\circ\text{C}$	$\alpha_{  } \times 10^5 / ^\circ\text{C}$	Temp. °C	$\alpha_{\perp} \times 10^5$	$\alpha_{  } \times 10^5 / ^\circ\text{C}$
-100	2.40	3.32	60	4.30	7.80
-90	2.44	3.40	70	4.40	8.00
-80	2.43	3.78	80	4.33	8.42
-70	2.56	4.09	90	4.48	8.66
-60	2.46	4.00	100	4.61	8.98
-50	2.88	4.42	110	4.71	9.23
-40	3.22	4.77	120	5.40	9.63
-30	3.33	4.97	130	5.92	10.22
-20	3.50	5.01	140	5.99	10.79
-10	3.43	5.32	150	6.89	11.38
0	3.43	5.41	160	6.82	11.98
10	3.57	5.38	170	7.69	12.56
20	3.40	5.27	180	7.97	13.20
30	3.60	5.80	190	8.63	13.96
40	3.88	6.42	200	9.01	14.40
50	3.98	7.43			

Polynomial Fit for Coefficient of Expansion

$$(\alpha = A + BT)$$

Temp. Range °C	$A \times 10^5 \text{ } ^\circ\text{C}^{-1}$	$B \times 10^6 \text{ } ^\circ\text{C}^{-2}$
Parallel expansion, $\alpha_{  }$		
-100 to 0	$5.56 \pm 0.07$	$0.24 \pm 0.01$
20 to 60	$3.77 \pm 0.13$	$0.70 \pm 0.00$
70 to 200	$3.90 \pm 0.26$	$0.51 \pm 0.02$
Perpendicular expansion, $\alpha_{\perp}$		
-100 to -55	$3.42 \pm 0.40$	$0.11 \pm 0.05$
-60 to -20	$4.09 \pm 0.14$	$0.25 \pm 0.03$
-40 to 110	$3.51 \pm 0.06$	$0.11 \pm 0.01$
100 to 200	$-0.08 \pm 0.26$	$0.45 \pm 0.02$

chopped nylon phenolic is 40 to 60 percent more efficient in lowering the expansion than tapewound nylon phenolic. The addition of nylon fibers to the phenolic matrix improved the dimensional stability of the molded nylon by reducing the thermal expansion.

The mean observed heat capacity values were smoothed by fitting to them empirical functions of temperature whose coefficients were determined by the method of least squares. The resulting equation,  $c_p = a + bT$ , gives expressions as indicated in Table 40.

The corresponding enthalpy,  $H$ , for the low temperature ranges may be expressed as

$$H_{-50^{\circ}\text{C}} - H_{-100^{\circ}\text{C}} = 0.1794 T + 7.15 \times 10^{-4} T^2$$

$$H_{205^{\circ}\text{C}} - H_{0^{\circ}\text{C}} = 0.1964 T + 1.04 \times 10^{-3} T^2$$

The enthalpy of fusion,  $\Delta H_f$ , (at  $257^{\circ}\text{C}$ ) associated with the nylon component present in the polymer was found to be 8.36 cal/g. Since the exact concentration of the nylon component is unknown, no comparison can be made with known literature values.

Table 40  
HEAT CAPACITY DATA FOR CHOPPED NYLON PHENOLIC  
 $c_p = a + bT$

Temp. Range °C	a cal/g°C	b × 10 <sup>3</sup> cal/g°C <sup>2</sup>	Av Error $c_p \times 10^2$
-100 to -5	0.1784	1.43	1.25
0 to 205	0.1764	2.07	0.22
235 to 260	-4.3005	19.31	3.20
260 to 280	6.5367	-20.88	4.81
285 to 335	0.3364	0.71	0.44

(10) Tapewound Nylon Phenolic (TWNP)

Tapewound nylon phenolic consists of a nylon cloth base with a phenolic resin binder. The nylon fibers are oriented through the matrix to give the effect of a closely woven fabric. The mechanical and thermal properties are highly influenced by the presence of the thermoplastic polyamide threads. The density of the material is 1.21 g/cm<sup>3</sup>.

The DTA thermogram (Fig. 64) is very similar to that of chopped nylon phenolic (Fig. 59); however, the glass transition temperature of nylon was not observed for TWNP. The exothermic onset at approximately 148°C leads to the decomposition peak at 433°C. Preliminary pyrolysis studies show the material to be approximately 11 percent volatilized at 370°C. The typical nylon fusion endotherm was evident at 255°C.

As previously discussed under chopped nylon phenolic, the finely woven structure is less efficient in lowering the thermal expansion of the material than is the nonwoven chopped nylon phenolic. As observed from the expansion data (Table 41 and Figures 62 and 63), the parallel alignment of the woven filaments in the TWNP resin matrix permit the material to withstand greater stresses than the chopped nylon polymer. (For the former, no softening region was evident.)

The perpendicular expansion curve (Fig. 63) shows a slight irregularity at  $\sim 40^\circ\text{C}$ , which is probably because of the glass transition temperature of the nylon component. No such irregularity was noted on the parallel expansion curve (Fig. 62).

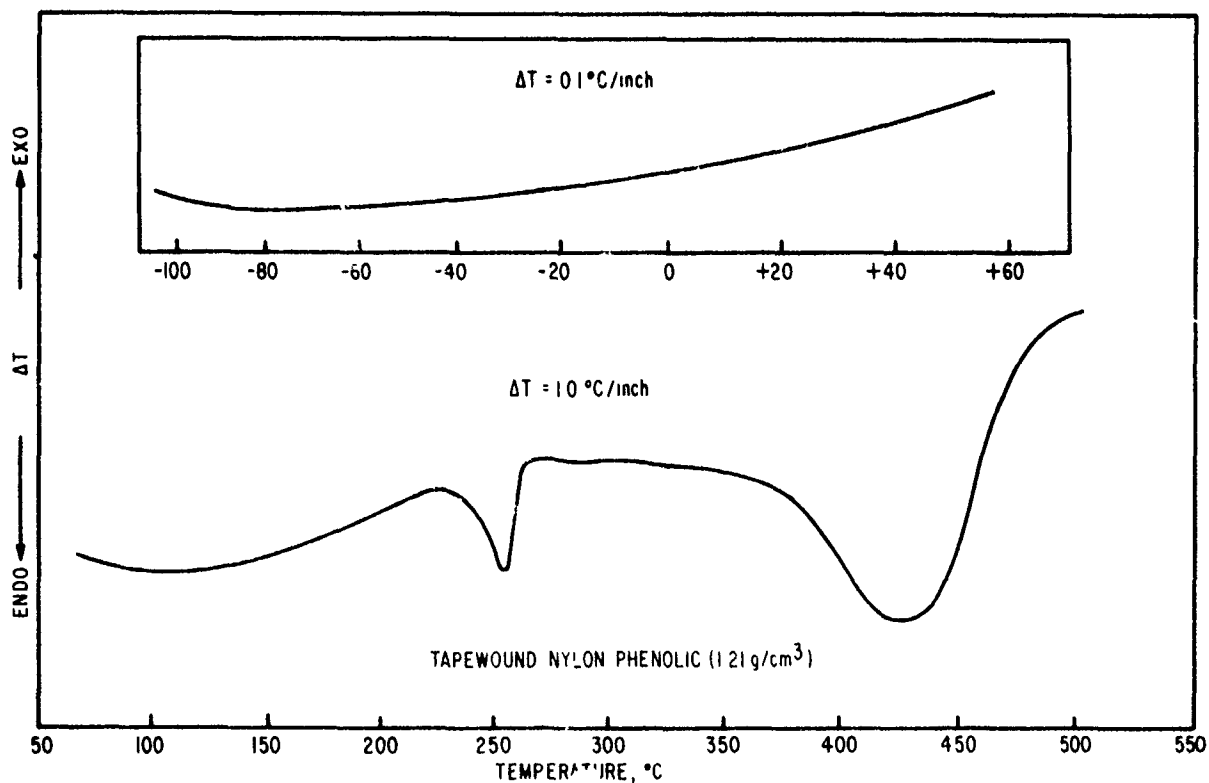


Figure 64. Differential thermogram of Tapewound Nylon Phenolic.

Table 41

## LINEAR THERMAL EXPANSION DATA FOR TAPEWOUND NYLON PHENOLIC

Temp. °C	$\alpha_{\perp} \times 10^5 / ^\circ\text{C}$	$\alpha_{  } \times 10^5 / ^\circ\text{C}$	Temp. °C	$\alpha_{\perp} \times 10^5 / ^\circ\text{C}$	$\alpha_{  } \times 10^5 / ^\circ\text{C}$
-100	3.90	4.54	60	10.82	12.04
-90	3.90	4.54	70	11.19	12.80
-80	3.92	4.54	80	11.69	13.65
-70	3.95	4.54	90	11.96	14.07
-60	4.20	4.54	100	12.63	14.74
-50	4.42	5.21	110	13.00	14.89
-40	4.62	5.21	120	13.30	15.55
-30	5.57	5.84	130	13.80	15.92
-20	5.51	6.84	140	14.34	16.92
-10	6.58	6.88	150	15.59	18.12
0	6.68	7.99	160	18.27	19.01
10	6.68	8.67	170	23.18	23.97
20	7.19	8.81	180	26.54	34.01
30	8.26	10.21	190	26.84	63.35
40	9.67	10.95	200	27.54	67.42
50	10.21	11.82			

## Polynomial Fit for Coefficient of Expansion

$$(\alpha = A + BT)$$

Temp. Range °C	$A \times 10^5 \text{ } ^\circ\text{C}^{-1}$	$B \times 10^6 \text{ } ^\circ\text{C}^{-2}$
Parallel expansion, $\alpha_{  }$		
-100 to -10	$5.93 \pm 0.36$	$0.26 \pm 0.00$
0 to 100	$7.29 \pm 0.30$	$0.54 \pm 0.07$
110 to 160	$1.44 \pm 2.77$	$0.98 \pm 0.20$
160 to 200	$15.50 \pm 9.07$	$2.22 \pm 0.50$
Perpendicular expansion, $\alpha_{\perp}$		
-30 to 160	$7.95 \pm 0.20$	$0.68 \pm 0.02$
0 to 160	$7.99 \pm 0.30$	$0.68 \pm 0.03$

Heat capacity data for the polymer are represented by  $c_p = a + bT$ , where the constants are shown in Table 42.

The heat capacities in Table 42 follow the same trends as observed for chopped nylon phenolic (Table 40). At low temperatures,  $-100^{\circ}\text{C}$  to  $200^{\circ}\text{C}$ , heat capacities differ by approximately 7 percent; beyond  $200^{\circ}\text{C}$   $c_p$  curves are similar, but chopped nylon phenolic has lower  $c_p$  values. As noted for chopped nylon phenolic and several other polymers, previous heat treatments gave varied values for the heat capacities.

The amount of heat absorbed at the  $255^{\circ}\text{C}$  fusion peak was  $\Delta H = 3.8$  cal/g. This value depends upon the concentration of the nylon component in the polymer.

(11) Rad 60

This polymer is a black carbonaceous rigid material which has a density of  $1.41 \text{ g/cm}^3$ . The DTA thermogram (Fig. 65) shows no significant transitions, except a slight rise in the baseline is noted at approximately  $140^{\circ}\text{C}$  with a more rapid increase at approximately  $475^{\circ}\text{C}$ .

Expansivity data in the "c" direction, parallel to the axis (Table 43 and Fig. 66), shows a rapid decrease in  $\alpha_{||}$  at temperatures below  $150^{\circ}\text{C}$ . Parallel expansion data for graphite reported by Riley (Ref. 123) show a similar decrease, however, the overall expansion values for pure graphite are somewhat higher than those observed in this study.

The higher expansion in the parallel plane over that in the perpendicular direction may be attributed to the layered structure of the polymer. The covalent linking within a layer is so strong that thermal vibrations perpendicular to the layers will be decreased; the larger mass of each layer is also significant in lowering the expansion of  $\alpha_{\perp}$ .

Heat capacity data from  $-100^{\circ}$  to  $600^{\circ}\text{C}$  were fitted to polynomial equations of the form  $c_p = a + bT$ . Values of the constants are shown in Table 44.

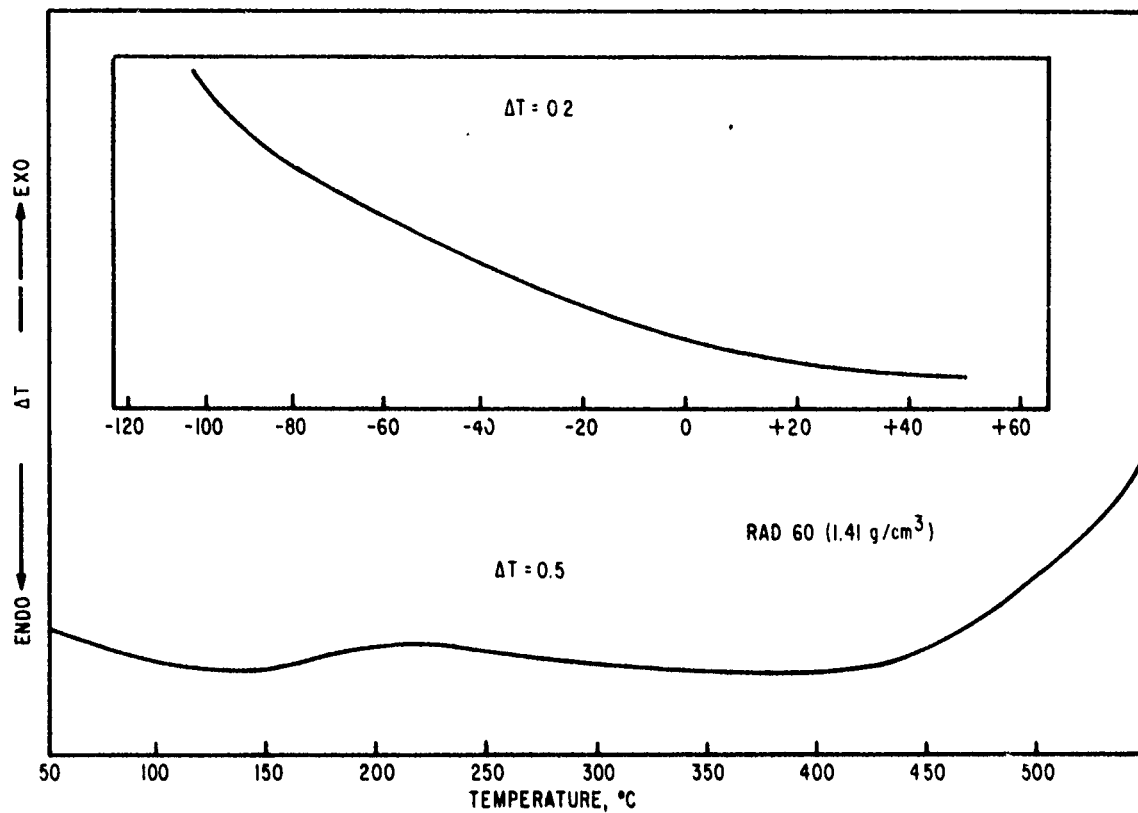


Figure 65. Differential Thermogram for Rad 60.

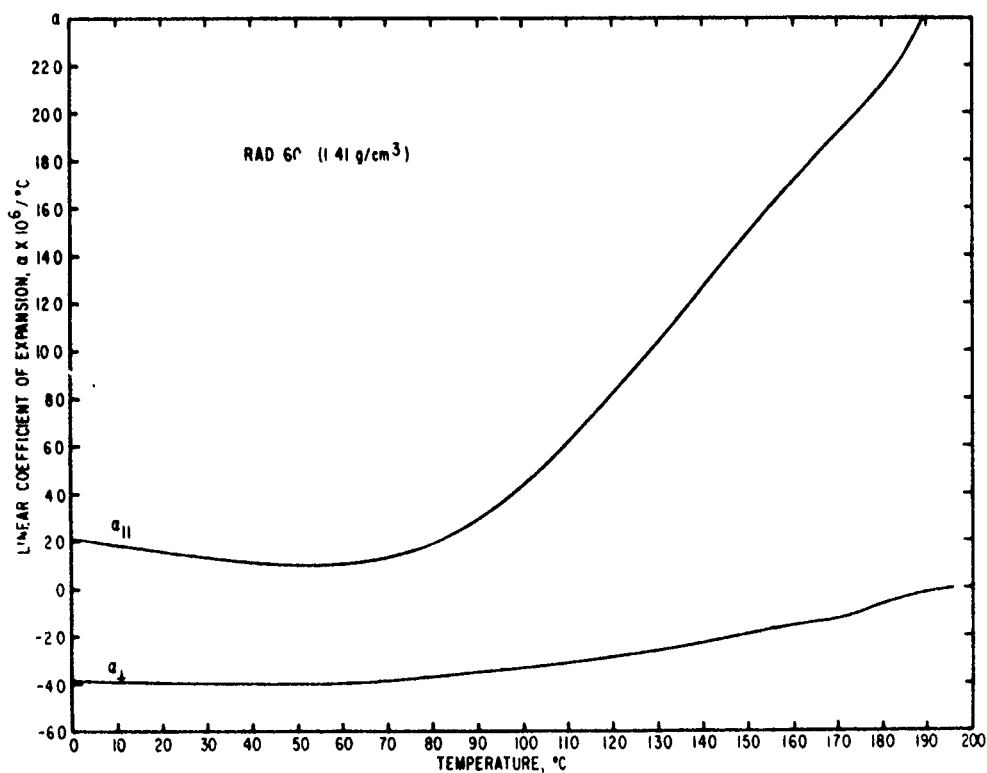


Figure 66. Linear Coefficient of Expansion Profiles For Rad 60 (Parallel and Perpendicular to the Axis).

Table 42  
HEAT CAPACITY DATA FOR TAPEWOUND NYLON PHENOLIC  
( $c_p = a + bT$ )

Temp. Range °C	a cal/g°C	b × 10 <sup>3</sup> cal/g°C <sup>2</sup>	Av Error $c_p \times 10^2$
-100 to 0	0.2956	1.21	0.13
25 to 200	0.2810	2.19	0.32
205 to 230	1.0212	-1.45	0.38
235 to 255	-1.2359	8.27	2.25
260 to 275	-8.6015	36.48	2.22
275 to 295	10.0638	-31.30	2.88
300 to 380	0.9403	-0.41	0.32
390 to 415	-5.5041	16.46	0.63
420 to 435	-0.4837	4.41	0.63
435 to 444	2.3029	-2.01	0.12
445 to 452	6.7370	-12.03	0.13

Thermal expansion data (Table 43 and Figure 66) obtained parallel and perpendicular to the plane are unusual in that expansivities in the perpendicular direction,  $\alpha_{\perp}$ , are negative to 190°C. This negative expansion may be because of the graphitic component  $[\alpha_{\perp} \text{ (Graphite - } 0^\circ \rightarrow 400^\circ\text{C)} = 1.58 \times 10^{-6}]$  present in the polymer; however, the data are subject to error for the limitations of the instrument may have been exceeded. Attempts were made to obtain expansivity data below 0°C, but values were not reproducible so they are not reported here. The values for the perpendicular expansion (Table 43) were obtained by averaging the results from five individual measurements, which agreed to within  $\pm 10$  percent.

Table 43  
 LINEAR THERMAL EXPANSION DATA FOR RAD 60

Temp. °C	$\alpha_{\perp} \times 10^6 / ^\circ\text{C}$	$\alpha_{  } \times 10^6 / ^\circ\text{C}$	Temp. °C	$\alpha_{\perp} \times 10^6 / ^\circ\text{C}$	$\alpha_{  } \times 10^6 / ^\circ\text{C}$
0	-3.83	2.02	110	-3.06	6.08
10	-3.95	1.79	120	-2.85	8.08
20	-4.00	1.52	130	-2.58	10.43
30	-4.01	1.25	140	-2.20	12.45
40	-4.10	1.02	150	-1.90	16.16
50	-4.05	0.91	160	-1.53	17.50
60	-4.00	1.02	170	-1.58	18.89
70	-3.90	1.43	180	-0.65	20.20
80	-3.76	1.99	190	-0.25	24.21
90	-3.56	3.03	200	+0.05	25.40
100	-3.36	4.39			

Polynomial Fit for the Coefficient of Expansion  
 $(\alpha = A + BT)$

Temp. Range °C	$A \times 10^6 \text{ } ^\circ\text{C}^{-1}$	$B \times 10^7 \text{ } ^\circ\text{C}^{-2}$
Parallel expansion, $\alpha_{  }$		
0 to 50	$2.00 \pm 0.04$	$-0.23 \pm 0.01$
60 to 100	$-4.30 \pm 0.82$	$0.83 \pm 0.10$
110 to 150	$-21.25 \pm 2.03$	$2.45 \pm 0.16$
150 to 200	$-16.78 \pm 4.15$	$2.11 \pm 0.23$
Perpendicular expansion, $\alpha_{\perp}$		
0 to 60	$-3.90 \pm 0.04$	$-0.03$
75 to 125	$-5.68 \pm 0.10$	$0.24$
140 to 200	$-7.79 \pm 0.63$	$0.39$



Table 44  
HEAT CAPACITY DATA FOR RAD 60  
( $c_p = a + bT$ )

Temp. Range °C	a cal/g°C	b × 10 <sup>3</sup> cal/g°C <sup>2</sup>	Av Error $c_p$ × 10 <sup>2</sup>
-100 to +20	0.2380	0.67	0.26
25 to 200	0.2346	0.92	0.32
225 to 350	0.3219	0.43	0.24
360 to 450	0.4034	0.19	0.12
460 to 600	0.5146	-0.06	0.07

### c. Thermal Properties of Refractories, Metals, and Alloys

#### (1) Pyrolytic Graphite

This material is a polycrystalline vapor-deposited form of graphite (density 2.19 g/cm<sup>3</sup>). It differs from normal graphite in atomic structure primarily in the mode of stacking in the basal planes, where the crystallites are stretched in a random fashion in the plane. This randomness in layer stacking destroys periodic repetition of the atoms in the direction perpendicular to the layers and appreciably alters those properties which depend on regularity of atomic arrangement, i.e., thermal expansion values.

The DTA thermogram (Fig. 67) shows no significant transitions except for slight changes in heat capacity, which cause the baseline to shift slightly. Heat capacity studies showed three distinct changes in the slope. These are illustrated by the linear least-squares data in Table 45. Results agree well with heat capacity data presented by Dugdale (Ref. 124).

The mean thermal expansion coefficients in the "c" direction,  $\alpha_{||}$ , are given in Table 46 and illustrated in Figure 68. The variation of the linear expansion with temperature agrees well with experimental and theoretical values obtained by Nelson and Riley (Ref. 125) and Entwisle (Ref. 126). The maximum expansion at 100°C in the "c" direction given in Reference 126 was  $2.50 \times 10^{-5}$  in/in°C; whereas, the value obtained in this study was  $2.52 \times 10^{-5}$  in/in°C.

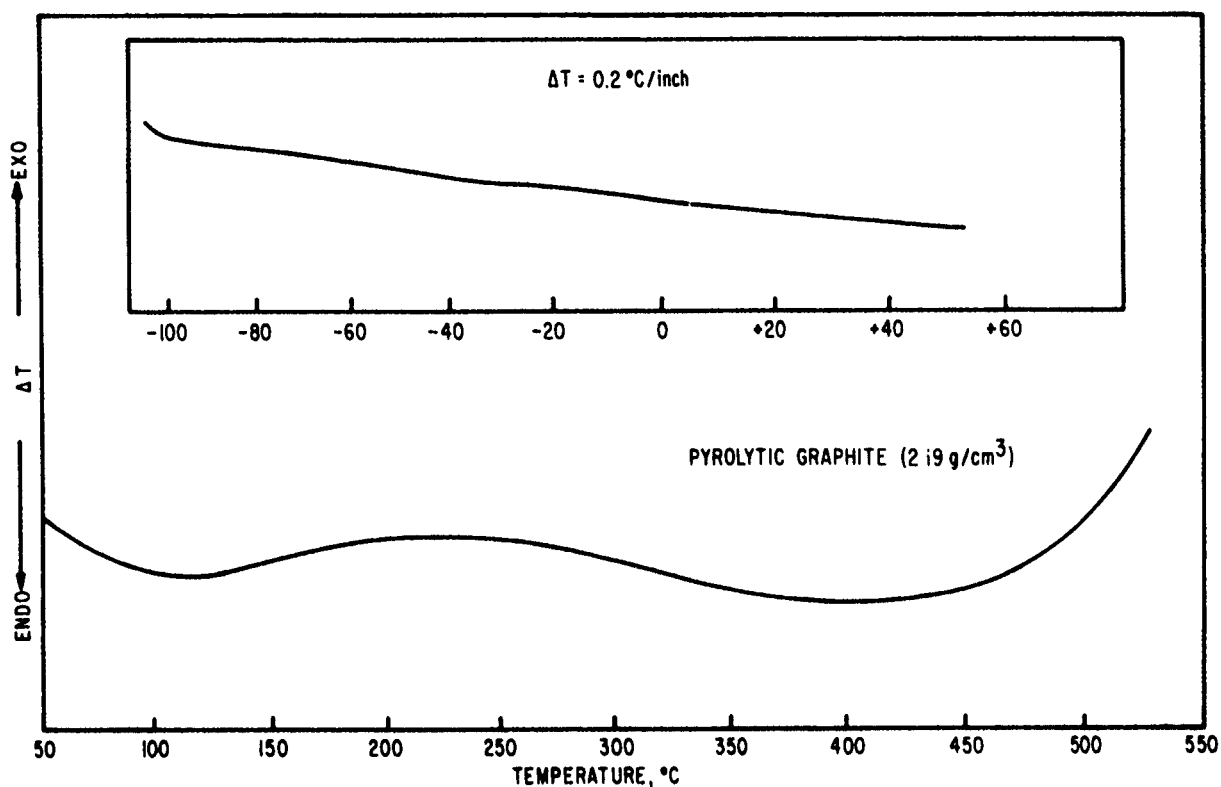


Figure 67. Differential Thermogram of Pyrolytic Graphite.

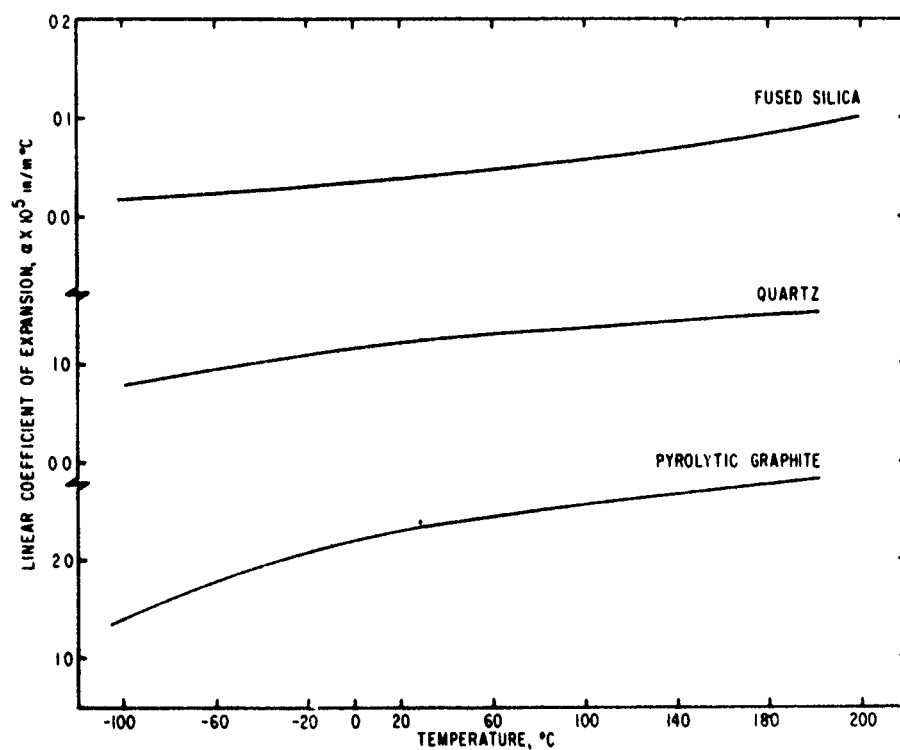


Figure 68. Linear Coefficient of Expansion Profiles For Pyrolytic Graphite, Quartz, and Fused Silica (Parallel to Axis).

Table 45  
HEAT CAPACITY DATA FOR PYROLYTIC GRAPHITE

$$c_p = a + bT$$

Temp. Range °C	a cal/g°C	b × 10 <sup>3</sup> cal/g°C <sup>2</sup>	Av Error c <sub>p</sub> × 10 <sup>2</sup>
-100 to 75	0.0318	1.27	0.64
75 to 225	0.0911	0.71	0.31
225 to 250	0.1910	0.26	0.47

Because of the limitations of the instrument, the expansion values in the "a" direction,  $\alpha_{\perp}$ , were impossible to obtain. Entwisle (Ref. 126) gives  $\alpha_{\perp} = -0.8 \times 10^{-6}$  in/in°C. Kingery (Ref. 127) has suggested that the low thermal expansivity of graphite is because of the high porosity. As the temperature is raised, the expansion is absorbed by the closing of the microfissures, rather than by gross changes in volume.

The explanation of the expansivity results given by Nelson and Riley (Ref. 125) emphasizes the importance of the layered structure. Elastic deformability parallel to the principal "c" axis will be much larger than that perpendicular to it, owing to the tighter interatomic bonding within the layers. In terms of the elastic moduli, this may be written as  $S_{33} \gg S_{11}$ . Under the influence of temperature and of zero-point energy the atoms will vibrate, and the limiting frequency in the parallel direction,  $\omega_c$ , will be greater than that perpendicular to it,  $\omega_a$ . Magnus (Ref. 128) has presented values for the two characteristic temperatures which are  $\theta_{\perp} = 2007^{\circ}\text{C}$  and  $\theta_{||} = 487^{\circ}\text{C}$  and are defined by the two limiting frequencies as

$$\theta_c = \frac{h}{k}(\omega_c); \quad \theta_a = \frac{h}{k}(\omega_a) \quad (25)$$

where  $h$  and  $k$  refer to the Plank and Boltzmann constants, respectively. At low temperatures, theory requires all the thermal energy to be absorbed in oscillations in the "c" direction because of the low value of  $\theta_{||}$  as compared with  $\theta_{\perp}$ . These parallel oscillations will therefore have the greater amplitude and  $\alpha_{||}$  will be greater than  $\alpha_{\perp}$ . The stretching of the lattice in one direction causes a lateral contraction in the other. At low temperatures, the small expansion within the layers will be lower than the lateral contraction and  $\alpha_{\perp}$  will be negative. At a higher temperature the lateral contraction and thermal expansion

Table 46  
 LINEAR THERMAL EXPANSION DATA FOR PYROLYTIC GRAPHITE  
 (PARALLEL TO THE AXIS)

Temp. °C	$\alpha_{  } \times 10^5 / ^\circ\text{C}$	Temp. °C	$\alpha_{  } \times 10^5 / ^\circ\text{C}$
-100	1.30	60	2.49
-90	1.38	70	2.50
-80	1.55	80	2.51
-70	1.72	90	2.52
-60	1.82	100	2.52
-50	1.90	110	2.56
-40	1.90	120	2.56
-30	1.89	130	2.59
-20	2.05	140	2.59
-10	2.16	150	2.66
0	2.16	160	2.69
10	2.22	170	2.73
20	2.23	180	2.90
30	2.26	190	2.94
40	2.43	200	2.96
50	2.44		

Polynomial Fit for Coefficient of Expansion

$$(\alpha = A + BT)$$

Temp. Range °C	$A \times 10^5 \text{ } ^\circ\text{C}^{-1}$	$B \times 10^6 \text{ } ^\circ\text{C}^{-2}$
Parallel expansion, $\alpha_{  }$		
-100 to 70	$2.123 \pm 0.02$	0.07
80 to 200	$2.122 \pm 0.06$	0.04

are balanced and  $\alpha_{\perp} = 0$ . A further increase in temperature causes the expansion to become greater than the lateral contraction, and  $\alpha_{\perp}$  will become positive and increase with temperature. Further relationships between the Debye temperature and the coefficient of expansion will be discussed in Section IV.

## (2) Quartz

A sample of X-cut quartz crystal, density  $2.65 \text{ g/cm}^3$ , was used to measure the linear thermal expansion parallel to the axis. Attempts to obtain expansivity measurements in the "a" direction,  $\alpha_{\perp}$ , were unsuccessful. Data for the expansion parallel to the axis are given in Table 47 and graphed as a function of temperature in Figure 69. Expansivity values increase linearly from a value of  $8.0 \times 10^{-6} \text{ in/in}^\circ\text{C}$  at  $-100^\circ\text{C}$  to  $15.0 \times 10^{-6} \text{ in/in}^\circ\text{C}$  at  $200^\circ\text{C}$ .

Heat capacity measurements were made on the sample from  $-100^\circ$  to  $300^\circ\text{C}$ . The best linear least-squares polynomial fit of the data may be represented by the constants in Table 48.

## (3) Fused Silica

The sample used here consisted of blocks of silicon dioxide formed by fusing quartz (rock crystal) in an electrically heated furnace above  $1710^\circ\text{C}$ . The material is easily supercooled to ordinary temperatures without crystallizing and exhibits very little change in volume with change in temperature. The calculated density was  $1.93 \text{ g/cm}^3$ .

The representative thermogram (Fig. 70) illustrates no significant transitions from  $-100^\circ$  to  $700^\circ\text{C}$ . However, a pronounced increase in heat capacity is evident at  $275^\circ\text{C}$ .

Thermomechanical measurements were made on the sample and experimental results indicate that fused silica has an average coefficient of expansion parallel to the plane of  $\sim 0.42 \times 10^{-6} \text{ in/in}^\circ\text{C}$  from  $-100^\circ$  to  $140^\circ\text{C}$  and  $\sim 0.62 \times 10^{-6} \text{ in/in}^\circ\text{C}$  from  $140^\circ$  to  $200^\circ\text{C}$ . (Values are subject to error due to the limitations of the instrument.) Values below  $0^\circ\text{C}$  were extrapolated. Data are listed in Table 49 and Figure 68.

Table 47  
 LINEAR THERMAL EXPANSION DATA FOR QUARTZ  
 (PARALLEL TO THE AXIS)

Temp. °C	$\alpha_{  } \times 10^6 \text{ in/in}^\circ\text{C}$	Temp. °C	$\alpha_{  } \times 10^6 \text{ in/in}^\circ\text{C}$
-100	8.00	60	13.00
-90	8.07	70	13.01
-80	8.50	80	13.23
-70	9.01	90	13.44
-60	9.25	100	13.50
-50	9.55	110	14.04
-40	9.99	120	14.24
-30	10.05	130	14.26
-20	11.02	140	14.30
-10	11.43	150	14.36
0	11.53	160	14.66
10	11.66	170	14.75
20	12.01	180	14.89
30	12.11	190	14.99
40	12.45	200	15.01
50	12.75		

Polynomial Fit for Coefficient of Expansion  
 $(\alpha = A + BT)$

Temp. Range °C	$A \times 10^6 \text{ }^\circ\text{C}^{-1}$	$B \times 10^7 \text{ }^\circ\text{C}^{-2}$
-100 to 60	$11.21 \pm 0.06$	0.33
70 to 200	$12.07 \pm 0.15$	0.16

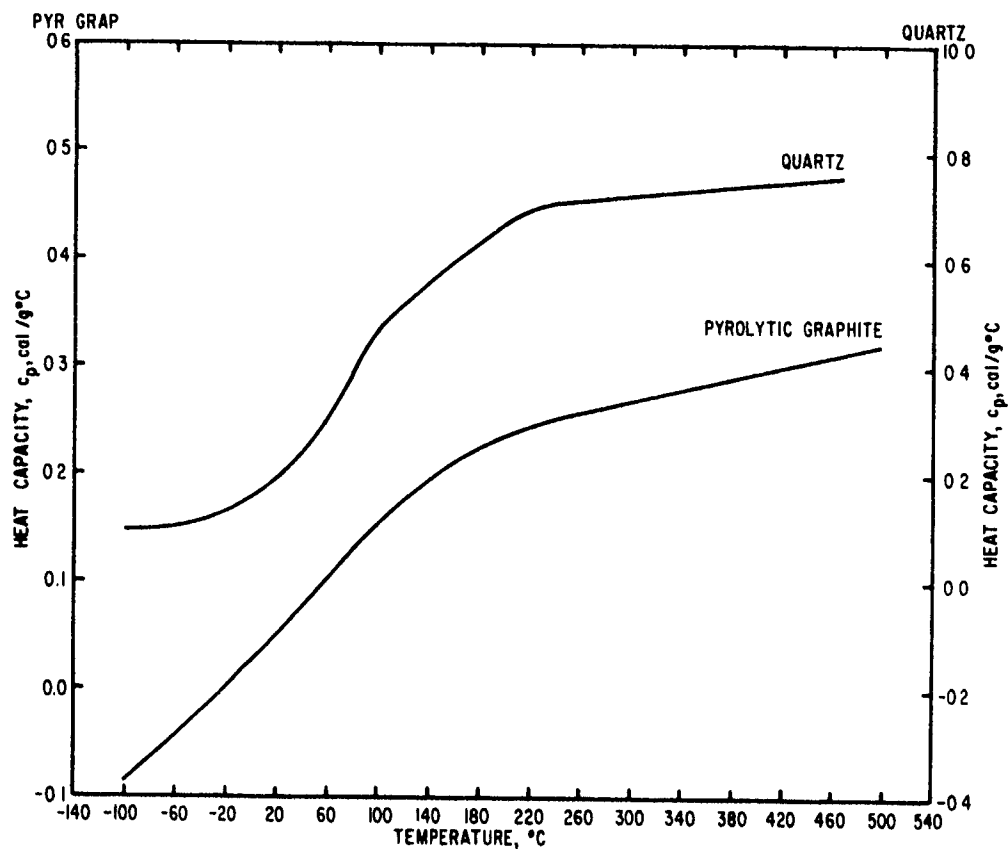


Figure 69. Heat Capacity Versus Temperature for Pyrolytic Graphite and Quartz.

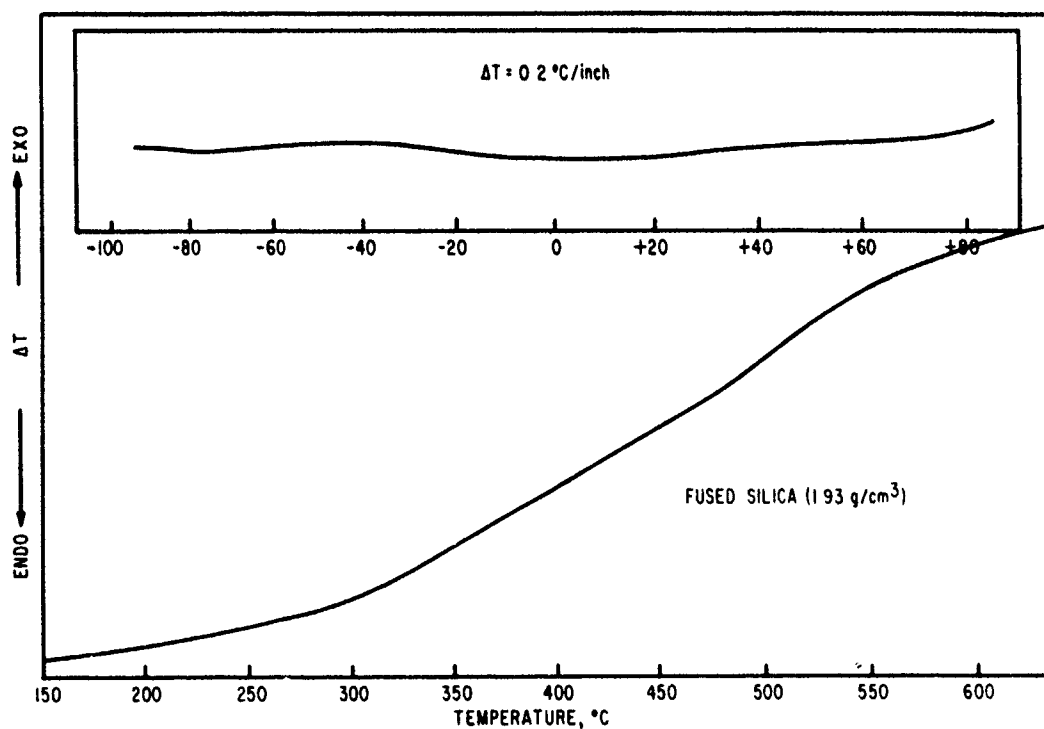


Figure 70. Differential Thermogram of Fused Silica.

Table 48  
HEAT CAPACITY DATA FOR QUARTZ  
( $c_p = a + bT$ )

Temp. Range °C	a cal/g°C	b × 10 <sup>3</sup> cal/g°C <sup>2</sup>	Av Error $c_p$ × 10 <sup>2</sup>
-100 to -50	0.1100	0.10	0.08
-40 to -10	0.1405	0.59	0.24
0 to 40	0.1265	1.87	1.27
50 to 80	0.0530	4.05	0.38
80 to 100	-0.0006	4.79	0.00
100 to 225	0.3073	1.64	1.62
225 to 300	0.3328	1.62	0.55

Table 49  
LINEAR THERMAL EXPANSION DATA FOR FUSED SILICA

Temp. °C	$\alpha \times 10^6$ in/in°C	Temp. °C	$\alpha \times 10^6$ in/in°C
-100	0.19	60	0.49
-90	0.21	70	0.49
-80	0.23	80	0.54
-70	0.25	90	0.56
-60	0.27	100	0.57
-50	0.28	110	0.59
-40	0.30	120	0.62
-30	0.33	130	0.68
-20	0.34	140	0.74
-10	0.36	150	0.75
0	0.38	160	0.78
10	0.40	170	0.82
20	0.42	180	0.86
30	0.44	190	0.92
40	0.46	200	0.99
50	0.48		



- (4) 1060 Aluminum, 6061-T6-Aluminum, HM-21A-Magnesium Thorium, Lead, and Gold

The chemical composition of the materials studied are given in Table 50. The complete thermal behavior of the metals and alloys in Table 50 was traced by applying thermodynamic relationships to basic data obtained by macroscopic measurements on the substances in question.

Anisotropy is generally expected for alloys; hence, coefficient of expansion values were measured for various specimen orientations. Since directional variations proved to be negligible, isotropy was assumed and Equation (36) was applicable. Ultrasonic studies for 6061-T6 aluminum (Table 5) show a longitudinal velocity parallel to the apparent stratification layer, which is approximately 0.4 percent higher than that across the layers. Since the thermo-mechanical analyzer gave dimensional accuracies of approximately  $\pm 3.0$  percent, this would account for the constant value of the expansion coefficient obtained parallel and perpendicular to the apparent stratification layers for this material.

Table 50  
CHEMICAL COMPOSITION OF METALS AND ALLOYS STUDIED  
(Density at 20°C)

Alloy	$\rho, \text{g/cm}^3$	Percent Composition
1060 Al	2.697	99.6% Aluminum
6061-T6-Al	2.700	98% Al with principal impurities Mg, Cr, Si, Cu
HM-21A-Mg-Th	1.782	Th 1.5% to 2.5%, Mn 0.45% to 1.1%, other impurities 0.30%, balance Mg
Block Lead	11.171	99.0%
Block Gold	18.959	99.0%

The ultrasonic data for 1060-aluminum and HM-21A magnesium-thorium alloy (Section II, paragraph (2) and Table 6) did not indicate a marked dependence of the velocities with direction of propagation along the axes of the cube. Since variations in the expansivity measurements in the "a" and "c" directions were also negligible, the condition of isotropy was more fully realized in these materials.

Heat capacity values determined from 0 to 400°C are tabulated in Table 51. Since the Grüneisen relation (Equation (36)) makes use of the isothermal bulk modulus,  $B^T$ , and since acoustical velocities were obtained under adiabatic conditions, the following relationship was substituted in Equation (36)

$$\frac{B^S}{B^T} = \frac{c_P}{c_V} \quad (26)$$

where  $B^S$  and  $B^T$  refer to the adiabatic and isothermal bulk moduli.

Grüneisen (Ref. 129) has shown experimentally that at temperatures below room temperature the coefficient of thermal expansion is approximately proportional to the specific heat such that

$$\beta/c_V = k \quad (27)$$

if it is assumed that the Grüneisen ratio,  $\gamma$ , is constant. Introducing the expression for  $c_V$  from equation (36) with the assumption that  $c_P = c_V$ , equation (27) becomes

$$k = \frac{\gamma \rho}{B^S} \quad (28)$$

As the bulk modulus does not vary much with temperature, the assumption of a constant  $\gamma$  leads to the approximate constancy of  $k$ . Tables 52, 53, and 54 summarize the properties used to calculate the Grüneisen ratio.

The ultrasonic data were fitted to an appropriate polynomial by the method of least squares and are represented in equation form in Section II, paragraph 2. The polynomial expansion for the shear velocity in lead is omitted because of the unreliability of the shear measurements due to the porosity of the sample (percent porosity = 21.2). The shear velocity value used in this study was given by Mason (Ref. 130) and limits the accuracy of  $\left(\frac{\partial B^S}{\partial T}\right)_0$  (Table 52).

Linear thermal expansion data (Table 53), and elongation data  $\left(\frac{l-l_0}{l_0}\right)$ , Table 54, agree well with reported values for similar materials. The elongation values for lead were compared to values presented by Nix and MacNair (Ref. 131) and Rubin, et al. (Ref. 132), in order to further define the accuracy of the method. A deviation of approximately 2.0 percent in  $\left(\frac{l-l_0}{l_0}\right)$  at -100°C decreased steadily to 1.6 percent at -20°C and an approximate overall deviation of 2.0 percent was retained to 200°C. The larger error below -20°C is the result

of using a sensitivity calibration obtained at room temperature; whereas, the very slight increase in error above 190° is probably due to the slight pressure exerted on the sample by the probe. Anomalies in lead are also associated with the high conductance of the material wherein the increased dissipation of heat is highly affected by the rate of sample heating.

The experimentally determined average expansions of  $3.1 \times 10^{-5}$  for lead and  $1.3 \times 10^{-5}$  for gold agree well with Hidnert and Krider's values (Ref. 133) of  $3.0 \times 10^{-5}$  and  $1.4 \times 10^{-5}$ , respectively.

Table 51

HEAT CAPACITY DATA FOR 1060 ALUMINUM, 6061-T6  
ALUMINUM, HM-21-A MAGNESIUM-THORIUM, LEAD, AND GOLD

(Units of  $c_p$  are cal/g°C)

Temp. °C	Mg-Th	Al 6061-T6	Al-1060	Pb	Au
0	0.248	0.210	0.200	0.030	0.030
25	0.252	0.211	0.202	0.031	0.031
50	0.259	0.216	0.204	0.032	0.031
75	0.267	0.219	0.206	0.301	0.031
100	0.268	0.224	0.207	0.032	0.031
125	0.269	0.228	0.209	0.032	0.032
150	0.275	0.233	0.210	0.032	0.032
175	0.276	0.236	0.220	0.032	0.032
200	0.279	0.241	0.226	0.032	0.032
225	0.285	0.248	0.234	0.033	0.032
250	0.288	0.253	0.236	0.034	0.032
275	0.288	0.256	0.240	0.034	0.032
300	0.289	0.260	0.247	0.034	0.032
325	0.294	0.268	0.249	MELT	0.033
350	0.296	0.274	0.254	TRAN	0.033
375	0.302	0.279	0.258	0.0400	0.034
400	0.302	0.281	0.263	0.0402	0.034

Table 52  
 LINEAR POLYNOMIAL EQUATIONS DESCRIBING THE EXPANSIVITY  
 DATA OF VARIOUS METALS AND ALLOYS  
 (Temperature Range 0° to 200°C)

Metal	Equation
1060 Al	$\alpha = 2.09 \times 10^{-5} \pm 1.9 \times 10^{-7} + (3.00 \times 10^{-8} \pm 1.6 \times 10^{-9}) T^{\circ}\text{C}$
6061-T6 Al	$\alpha = 2.10 \times 10^{-5} \pm 2.2 \times 10^{-7} + (3.06 \times 10^{-8} \pm 1.8 \times 10^{-9}) T^{\circ}\text{C}$
Au	$\alpha = 1.35 \times 10^{-5} \pm 2.1 \times 10^{-7} + (0.56 \times 10^{-9} \pm 1.8 \times 10^{-10}) T^{\circ}\text{C}$
Pb	$\alpha = 2.87 \times 10^{-5} \pm 8.6 \times 10^{-8} + (2.40 \times 10^{-8} \pm 7.3 \times 10^{-10}) T^{\circ}\text{C}$
HM-21A Mg-Th	$\alpha = 2.50 \times 10^{-5} \pm 1.7 \times 10^{-7} + (3.48 \times 10^{-8} \pm 1.5 \times 10^{-9}) T^{\circ}\text{C}$

Table 53  
 ELONGATION VERSUS TEMPERATURE FOR SEVERAL METALS AND ALLOYS

$$\text{Elongation} \left( \frac{l - l_0}{l_0} \times 10^3 \right)$$

Temp. °C	Mg-Th	Al 6061-T6	Al-1060	Pb	Au
-100	-2.35	-2.01	-2.12	-2.88	-1.30
-75	-1.95	-1.70	-1.79	-2.36	-1.07
-50	-1.51	-1.36	-1.44	-1.81	-0.82
-25	-1.04	-1.00	-0.98	-1.23	-0.55
0	-0.55	-0.51	-0.53	-0.62	-0.27
25	0.00	0.00	0.00	0.00	0.00
50	0.63	0.56	0.52	0.67	0.32
75	1.22	1.19	1.07	1.37	0.65
100	1.88	1.93	1.65	2.09	1.04
125	2.60	2.59	2.27	2.62	1.52
150	3.35	3.41	2.90	2.83	2.03
175	4.11	4.28	3.56	3.59	2.58
200	4.42	4.52	4.21	3.74	3.12

The expansion plots of the two aluminum alloys (Fig. 71) show a rapid decrease in expansion, whereas the magnesium-thorium expansion is much less. These results agree well with data for pure metals obtained by Borelius (Ref. 134) and are considered to be associated with low temperature phenomena; wherein,  $c_v$  and  $\beta$  approach zero as  $T \rightarrow 0^\circ\text{K}$ . The differences between the magnesium-thorium and aluminum alloys are probably associated with differences associated with cubical and hexagonal systems.

The measured values of thermal expansion (Table 52) and the specific heat data (Table 51), combined with ultrasonic measurements (Section II, paragraph 2) were then used to calculate the Grüneisen ratio,  $\gamma$ , (Table 54). Plots of  $\gamma$  versus  $T$  (Fig. 72) indicate slight variations in the Grüneisen ratio over the temperature range studied. These slight variations define the temperature dependency, or the anharmonicity of the crystal in much the same way as the Debye temperature,  $\theta$ , is taken to be a characteristic temperature.

According to the Debye Model,  $\gamma$  and  $\theta$  are related by

$$\gamma = - \frac{d \ln \theta}{d \ln V} \quad (29)$$

Barron (Ref. 135) has shown that Grüneisen's rule is obeyed at low temperatures when  $T \rightarrow 0^\circ\text{K}$  and at high temperatures when  $T \gg \theta$ , and hence, according to Equation (29),  $\theta$  is the limiting temperature. He has also proposed a model which suggests that the main variations of  $\gamma$  should occur for temperatures below  $0.3\theta$ .

No attempt has been made to calculate the Debye temperature because of insufficient data at low temperatures. The characteristic Debye temperatures for the pure metals given by Crawford (Ref. 136) for magnesium, aluminum, lead, and gold are, respectively  $87^\circ\text{C}$ ,  $117^\circ\text{C}$ ,  $-184^\circ\text{C}$ , and  $-84^\circ\text{C}$ .

The actual significance of the Grüneisen ratio on the equations of state of these solids, as opposed to previously estimated ratios, has not been studied. Rice, et al. (Ref. 137) report a Grüneisen ratio of 1.32 for pure magnesium metal obtained from dynamic measurements. The average value obtained in this study for the magnesium-thorium alloy was 1.45. If the value for the pure metal is used instead of the alloy, this would constitute an error of approximately 10 percent in this ratio.

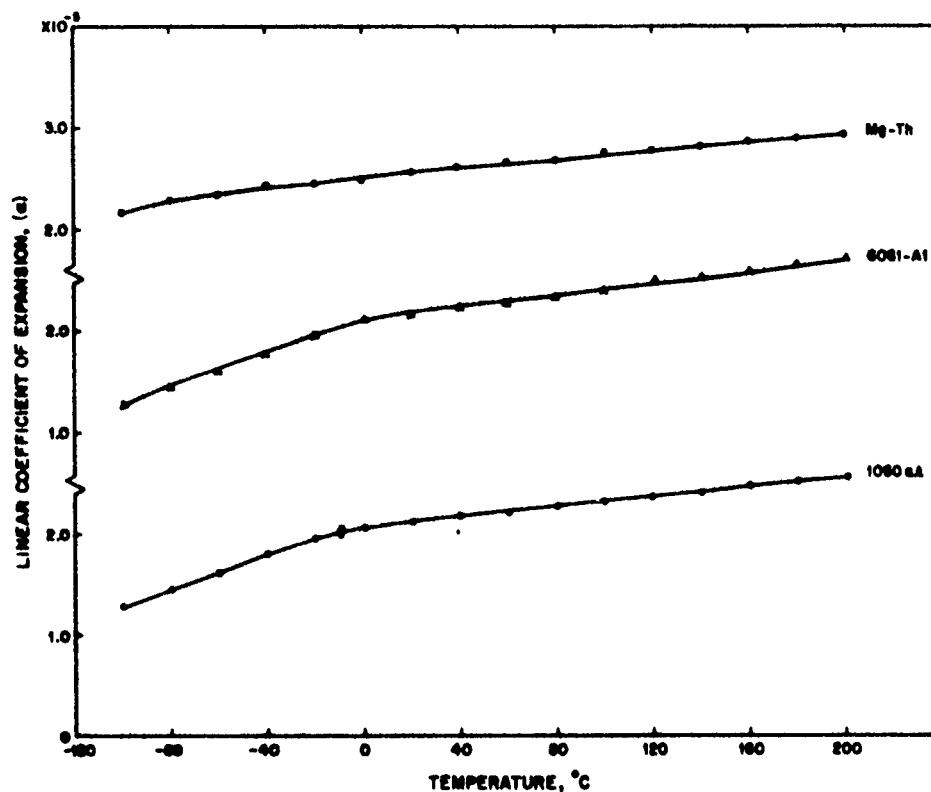


Figure 71. Expansivity Versus Temperature Curves for 6061-T6 Aluminum, 1060 Aluminum, and HM-21A Magnesium Thorium Alloys.

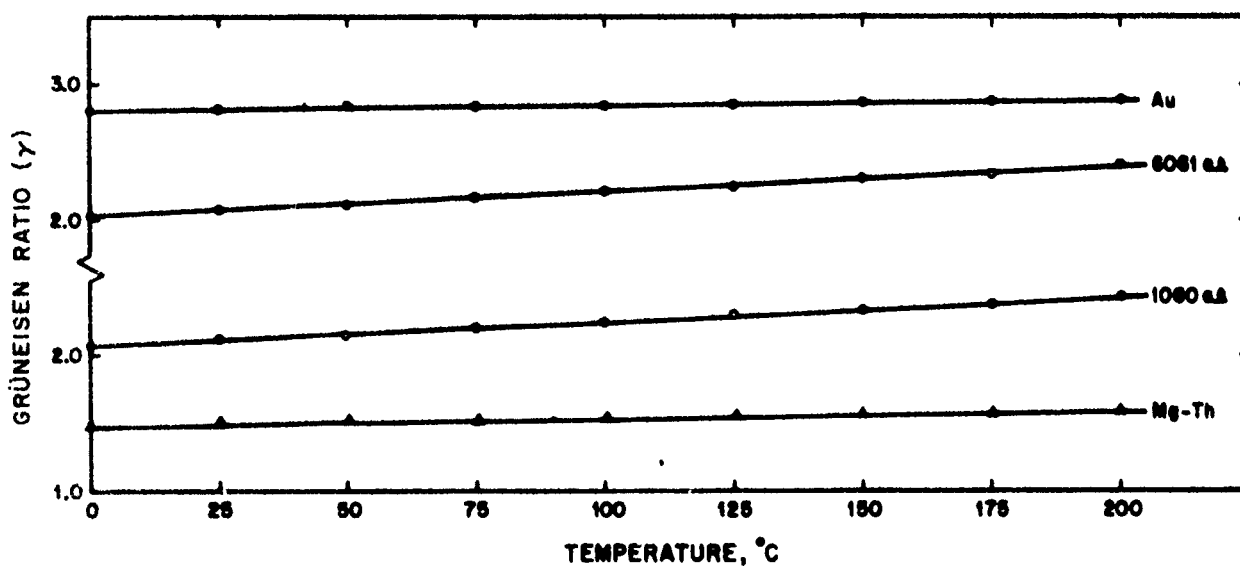


Figure 72. Grüneisen Ratio,  $\gamma$ , as a Function of Temperature For 1060 Aluminum, 6061-T6 Aluminum, HM-21A Magnesium Thorium, and Gold.

Table 54

COMPLETE TABULATION OF DATA USED TO CALCULATE THE  
GRÜNEISEN RATIO IN SEVERAL METALS AND ALLOYS

	Mg-Th	Al 6061	Al 1060	Pb	Au
Density, $\rho_0$ g/cm <sup>3</sup>	1.773	2.704	2.702	11.174	18.962
Volume Thermal Expansivity, $\beta_0 \times 10^5/^\circ\text{C}$	7.51	6.30	6.28	8.60	4.04
Grüneisen Constant, $\gamma_0$	1.45	2.03	2.06	2.20	2.80
Temperature Derivative of Expansivity, $\left(\frac{\partial\beta}{\partial T}\right)_0 \times 10^8/^\circ\text{C}$	6.11	9.17	0.00	7.32	2.27
Adiabatic Bulk Modulus, $B_0 \times 10^{11}$ dyne/cm <sup>2</sup>	3.55	7.51	7.43	5.26	16.70
Temperature Derivative of Modulus, $\left(\frac{\partial B}{\partial T}\right)_0$ kbars/ $^\circ\text{C}$	-0.046	-0.170	-0.216	-0.216	-0.307
Specific Heat, $\mathcal{C}_{P_0}$ , cal/g $^\circ\text{C}$	0.248	0.206	0.200	0.030	0.030
Temperature Derivative of Specific Heat, $\left(\frac{\partial \mathcal{C}_P}{\partial T}\right)_0 \times 10^4$ cal/g $^\circ\text{C}$	1.35	1.94	1.76	0.11	0.16
Grüneisen Temperature Derivative, $\left(\frac{\partial \gamma}{\partial T}\right)_0 \times 10^3/^\circ\text{C}$	0.62	1.91	1.92	2.51	0.45
Enthalpy, $\Delta H_{25^\circ\text{C}}$ cal/g	6.37	5.21	4.88	0.76	0.76
Entropy, $\Delta S_{25^\circ\text{C}}$ cal/g	0.06	0.05	0.04	0.01	0.01

Values for  $c_V$  (Table 55) were determined from the equation

$$c_P - c_V = -T \left( \frac{\partial P}{\partial V} \right)_T \times \left( \frac{\partial V}{\partial T} \right)_P^2 \quad (30)$$

which, upon proper substitution and rearrangement, becomes

$$c_V = c_P - \frac{VT\beta^2}{\chi^s} = c_P - \frac{\beta^2 TB^s}{\rho} \quad (31)$$

where  $\chi^s$  refers to the adiabatic compressibility.

Thermodynamic properties such as enthalpy,  $\Delta H$ , and entropy,  $\Delta S$ , (Table 54) were determined at 25°C by the application of suitable thermodynamic relations to the  $c_P$  data. (See Appendix VII.)

The adiabatic bulk modulus,  $B^s$ , (Table 54) was calculated from the ultrasonic longitudinal and shear velocities,  $V_\ell$  and  $V_t$ , according to Equation (4) and the density was obtained from a Maclaurin expansion retaining only the linear term in temperature. Zero subscripts refer to values obtained at 0°C.

The relative change in the bulk modulus with temperature,  $\left( \frac{\partial B^s}{\partial T} \right)_0$ , (Table 54) was obtained from the differentiation of Equation (4).

The value  $\left( \frac{\partial \alpha}{\partial T} \right)_0$ , was obtained by fitting linear least-square polynomial equations to the expansion data of Table 52.

The temperature derivative of the Grüneisen ratio  $\left( \frac{\partial \gamma}{\partial T} \right)_0$ , (Table 54) was obtained by differentiating each term of Equation (139) (Appendix III) which gave Equation (147) (Appendix III).



Table 55  
HEAT CAPACITY AT CONSTANT VOLUME  
( $c_V$ ) FOR THE METALS STUDIED

$$\left( \frac{\text{cal}}{\text{g}^\circ\text{C}} \right)$$

Temp. °C	Mg-Th	Al 6061-T6	Al-1060	Pb	Au
0	0.248	0.210	0.200	0.030	0.030
25	0.252	0.211	0.202	0.031	0.031
50	0.259	0.216	0.204	0.032	0.031
75	0.267	0.220	0.205	0.032	0.031
100	0.268	0.224	0.207	0.032	0.031
125	0.268	0.228	0.209	0.032	0.032
150	0.275	0.233	0.210	0.032	0.032
175	0.276	0.236	0.220	0.032	0.032
200	0.279	0.240	0.226	0.032	0.032

## SECTION IV

### APPLICATIONS

Many of the uses of ultrasonic and thermal data regarding application to equation of state parameters have been discussed in Reference 4. Basically these applications include estimations of shock impedances, bulk velocities, shock velocity-particle velocity slopes, and precise calculations of Grüneisen ratios in isotropic, elastic materials. This section will expand on existing applications and indicate further uses of ultrasonic and thermal data.

#### 1. The Theoretical and Experimental Determination of Grüneisen Ratios from Ultrasonic and Thermal Data

According to the Grüneisen theory (Ref. 129) the equation of state for solids is given by

$$P = - \frac{dU}{dV} + \gamma \frac{E_{VIB}}{V} \quad (32)$$

where  $P$  and  $V$  refer to the pressure and volume,  $E_{VIB}$  is the vibrational energy,  $U$  is the static lattice energy, and  $\gamma$  is the Grüneisen ratio, which in general is a slowly varying function of the volume.

Schuele and Smith (Ref. 138) rigorously define the Grüneisen ratio of Equation (32) as a weighed mean of individual gammas by

$$\gamma = \frac{\sum \gamma_i E_i(VIB)}{\sum E_i(VIB)} = \frac{\sum \gamma_i c_i}{\sum c_i} \quad (33)$$

where  $E_i(VIB)$ ,  $c_i$ , and  $\gamma_i$ , are respectively the  $i$ th normal mode of the vibrational energy, the classical Einstein heat capacity, and the individual Grüneisen ratio. The latter are defined by the equation

$$\gamma_i = - \frac{d \ln \omega_i}{d \ln V} \quad (34)$$

which expresses the volume dependence ( $V$ ) of the frequencies ( $\omega_i$ ) of the lattice modes.

For an ideal Debye solid, the atoms have a range of frequencies up to a maximum frequency,  $\omega_{\max} = k \theta / h$ , where  $\theta$  is a characteristic temperature, and  $h$  and  $k$  are the Planck and Boltzmann constants, respectively. For this type of solid, the specific heat at very low temperatures is proportional to the cube of the absolute temperature

$$c_V = \frac{12}{5} \pi^4 N k \left( \frac{T}{\theta} \right)^3 \quad (35)$$

which becomes

$$c_V = 464.4 \left( \frac{T}{\theta} \right)^3$$

expressed in cal/mole-degree. Equation (35) is valid for  $0 < T \lesssim \frac{\theta}{10}$ .

Since the Einstein frequency,  $\omega_E$ , is approximately related to the Debye temperature,  $\theta$ , by

$$\omega_E \sim \frac{3}{4} \frac{k}{h} \theta \sim \frac{3}{4} \omega_{\max}$$

then,  $\gamma_i = \gamma = -d \ln \omega_{\max} / d \ln V_0$ . For a real solid  $\gamma$  is approximately constant at high temperatures ( $T \geq \theta$  and  $\gamma = \gamma_\infty$ ) as the Dulong and Petit value ( $c_V = 3R$ ) is constant in this temperature range. Constancy is also expected at low temperatures ( $T \ll \theta$  where  $\gamma = \gamma_0 = -d \ln \theta / d \ln V$ ) (see Ref. 135). The main deviations in the Grüneisen constant are expected to occur below  $0.3 \theta$ .

As indicated in Reference (4), the thermodynamic relationship for the Grüneisen ratio,  $\gamma$ , can be expressed as

$$\gamma = \frac{\beta B^S}{\rho c_P} \text{ or } = \frac{\beta B^T}{\rho c_V} \quad (36)$$

where  $\beta$  is the volume coefficient of expansion,  $B^S$  and  $B^T$  are the adiabatic and isothermal bulk moduli,  $\rho$  is the density, and  $c_P$  and  $c_V$  are the specific heats at constant pressure and constant volume, respectively. If accurate experimental thermal and ultrasonic data as a function of temperature are employed to calculate  $\gamma$  by means of Equation (36), the resulting values will accurately represent the Grüneisen ratio in accordance with Equation (34).

For isotropic, elastic materials Equation (36) reduces to

$$\gamma = \frac{3\alpha}{\mathcal{C}_p} v_l^2 - \frac{4}{3} v_t^2 \quad (37)$$

where  $\alpha$  is the linear coefficient of expansion. However, many of the materials of current engineering interest are laminated structures, such as carbon phenolic or Fiberglas. In these cases, Equation (37) must be modified to correspond to the symmetry of the material. For most layered materials the model of transverse isotropy (which is similar to hexagonal symmetry) is a fair approximation to the actual symmetry of the specimen. As indicated in Section II, this model is easily checked through ultrasonic velocity measurements.

For a transversely isotropic medium, the adiabatic bulk modulus and its reciprocal, the compressibility  $\chi^s$ , are given in terms of the elastic stiffness coefficients as (See Appendix I)

$$\chi^s = \frac{c_{11} + c_{12} + 2c_{33} - 4c_{13}}{(c_{11} + c_{12})c_{33} - 2c_{13}^2} \quad (38)$$

$$\begin{aligned} B^s &= \frac{1}{\chi^s} \\ &= \frac{(c_{11} + c_{12})c_{33} - 2c_{13}^2}{c_{11} + c_{12} + 2c_{33} - 4c_{13}} \end{aligned} \quad (39)$$

A method for determining the elastic stiffness coefficients,  $c_{ij}$ , is also indicated in Section II. For transverse isotropy, the volume coefficient of expansion must likewise be modified. It is shown in Appendix VIII that this quantity can be estimated as

$$\beta = \alpha_{||} + 2\alpha_{\perp} \quad (40)$$

where  $\alpha_{||}$  is the linear coefficient of expansion in the z-direction (perpendicular to the layers), and  $\alpha_{\perp}$  is the expansion in either of the two other orthogonal directions.

If the Grüneisen ratio were a complete scalar function, the volume coefficient of expansion and the bulk modulus corresponding to the appropriate symmetry could be inserted into Equation (36) to yield a scalar result for this ratio. However, as recently pointed out by Key (Ref. 150) the Grüneisen ratio for anisotropic

materials must be considered as a tensor. Key shows that for transversely isotropic materials the Grüneisen tensor reduces to (see Appendix I)

$$\begin{bmatrix} \gamma_{xx} & \gamma_{xy} & \gamma_{zz} \\ \gamma_{xy} & \gamma_{yy} & \gamma_{yz} \\ \gamma_{xz} & \gamma_{yz} & \gamma_{zz} \end{bmatrix} = \frac{1}{\rho c_V} \begin{bmatrix} a & 0 & 0 \\ 0 & a & 0 \\ 0 & 0 & b \end{bmatrix} \quad (41)$$

where

$$a = c_{11} \alpha_{11} + c_{12} \alpha_{11} + c_{13} \alpha_{33}$$

$$b = c_{13} \alpha_{11} + c_{13} \alpha_{11} + c_{33} \alpha_{33}$$

In this notation  $\alpha_{11}$  is the linear coefficient of expansion along the layers (corresponding to  $\alpha_{\perp}$  in the earlier notation) and  $\alpha_{33}$  is the expansion coefficient perpendicular to the layers (corresponding to  $\alpha_{||}$ ). The elastic stiffness coefficients in Equation (41) are the isothermal coefficients. The equations for the conversion from the adiabatic to the isothermal coefficients and from the specific heat at constant pressure to that at constant volume are given in Appendix I. Equation (41) allows the calculation of the Grüneisen ratio for various directions in an anisotropic material. The scalar function of the spherical component of the Grüneisen ratio for transverse isotropy is given as

$$\alpha = \frac{1}{3\rho c_V} (2a + b) \quad (41a)$$

These equations are consistent with those given by Grüneisen and Goens in 1924 (Ref. 139).

Hydrostatic pressure measurements on the acoustic velocities yield another way of determining the Grüneisen ratio. Schreiber and Anderson (Ref. 24) give the Grüneisen ratio in terms of the hydrostatic pressure dependence of the longitudinal and shear modes in an isotropic medium as

$$\gamma_L = \frac{1}{3} + \frac{B_o^T}{V_\ell} \left( \frac{dV_\ell}{dP} \right) \quad (42)$$

$$\gamma_s = \frac{1}{3} + \frac{B_o^T}{V_s} \left( \frac{dV_s}{dP} \right) \quad (43)$$

and show that the Grüneisen ratios at low temperature,  $\gamma_{L.T.}$ , and at high temperature,  $\gamma_{H.T.}$ , are in this limit

$$\gamma_{L.T.} = \frac{1}{2 + \left(\frac{V_s}{V_l}\right)^3} \left[ \left(\frac{V_s}{V_l}\right)^3 \gamma_L + 2\gamma_s \right] \quad (44)$$

$$\gamma_{H.T.} = \frac{1}{3} (\gamma_L + 2\gamma_s) \quad (45)$$

They show that the use of Equations (44) and (45) compares well with the ratio calculated through the thermal relation (Equation (36)) for several of the ceramics and metals. There is not yet sufficient pressure data available on plastics to perform a similar comparison between the two approaches for these materials. However, the method possesses potential applications in equation of state investigations, because it permits another method of determining the Grüneisen ratio, and thus, serves as a check of the basic postulate of Grüneisen.

In the present study the Grüneisen ratio was determined for several metals, alloys and polymeric materials from 0° to 200°C by means of Equation (36). The temperature derivative of the Grüneisen ratio at 0°C,  $\left(\frac{\partial \gamma}{\partial T}\right)_0$ , was obtained by differentiating each term of Equation (36) which gives

$$\left(\frac{\partial \gamma}{\partial T}\right)_0 = \gamma_0 \left\{ \frac{1}{\beta} \left[ \left(\frac{\partial \beta}{\partial T}\right) + \beta^2 \right] + \frac{1}{B^s} \left(\frac{\partial B^s}{\partial T}\right) - \frac{1}{c_p} \left(\frac{\partial c_p}{\partial T}\right) \right\}_0 \quad (46)$$

where the zero subscripts represent 0°C. The relative change in the bulk modulus was obtained by differentiating Equation (4) for which the density was obtained assuming a linear expansion with temperature. The temperature variation of the specific heat and the thermal expansion was obtained from linear least-squares curves of the respective data.

The experimentally determined Grüneisen ratios are given in Table 56, and plotted as a function of temperature in Figure 73. The values obtained at 0°C for metals and alloys were taken from Table 54.

For the plastics the Grüneisen ratio was determined directly at each temperature through the defining Equation (36). This was necessary since many of the plastics undergo phase transitions throughout the region of interest. This is particularly true of Delrin Acetal in which a rotational transformation

Table 56

## GRÜNEISEN RATIO VERSUS TEMPERATURE FOR VARIOUS MATERIALS

Polymer	Temperature °C												
	0	10	20	30	40	50	60	70	80	90	100	110	120
													$\left[\left(\frac{\partial \gamma}{\partial T}\right)_0\right]$
Carbon Phenolic	0.51	0.44	0.37	0.34	0.24	0.23	0.21	0.17	0.19	0.21	0.25	0.21	0.23
GE Phenolic Fiberglass	0.29	0.32	0.32	0.35	0.37	0.37	0.37	0.36	0.38	0.38	0.37	0.39	0.37
Teflon				0.39	0.44	0.44	0.47	0.46	0.58	0.71	0.93	1.03	0.92
Nylon 6	0.94	0.84	0.91	1.05	1.82	3.30	2.43	1.62	1.23	0.97	0.90	0.82	0.75
Delrin Acetal	0.92	0.86	0.81	0.76	0.70	0.79	1.89	1.95	1.77	1.38	1.15		
Polyethylene (0.967 g/cm <sup>3</sup> )	1.19	1.19	1.12	1.19	1.37	1.54	1.60	1.69	1.55	1.64	1.66		
Polyethylene (0.922 g/cm <sup>3</sup> )	1.04	0.92	0.86	0.88	1.18	1.39	1.25	1.67	1.05	2.14	2.06		
Plexiglas	1.13	0.88	0.80	0.79	0.76	0.74	0.70	0.70	0.66	0.65	0.65		

\* Measured at 30°C

Metals and Alloys*	$\gamma_0$	$\left[\left(\frac{\partial \gamma}{\partial T}\right)_0\right] \times 10^3$
Gold	2.80	0.45
Lead	2.20	2.51
1060 Aluminum	2.06	1.92
6061-T6-Aluminum	2.03	1.91
HM-21-A Magnesium-Thorium	1.45	0.62

\* Data taken from Table 51.

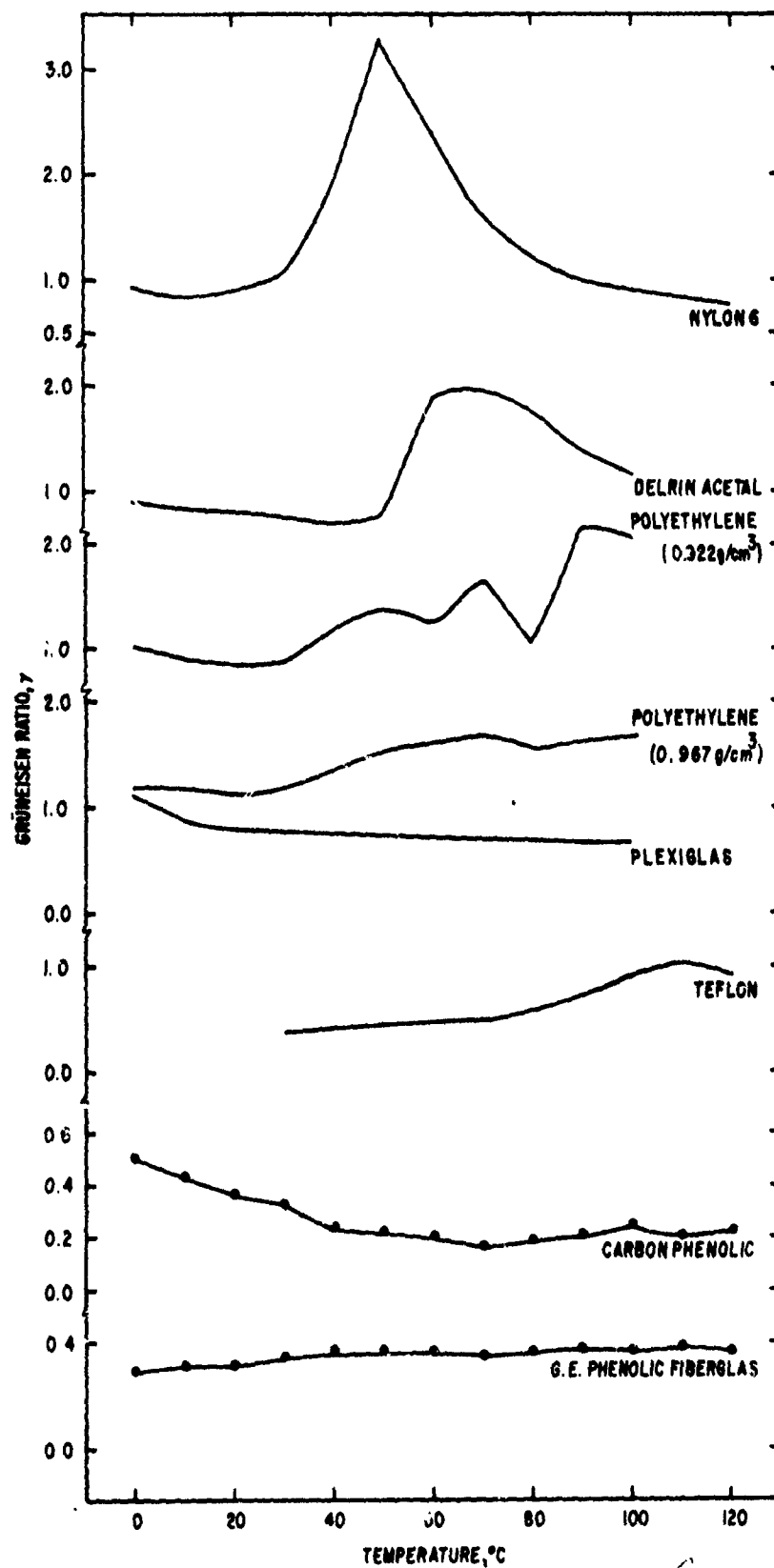


Figure 73. Gruneisen Ratios Versus Temperature for Various Materials.



begins at approximately 70°C. As shown in Figure 46 the linear expansion, and to a certain extent the specific heat, shows a marked increase at 70°C. Since the Grüneisen ratio was calculated by the thermal relation, it likewise follows the behavior of the thermal expansion in having a maximum at  $\sim 70^\circ\text{C}$  and dropping thereafter until the onset of melting. The validity of the thermal relation for the Grüneisen ratio through a major transition of this sort has not yet been studied. However, the values in Table 56 were calculated at all temperatures using the thermal relation.

For the two layered materials studied here (carbon phenolic and G.E. Fiberglas) the Grüneisen ratio was calculated by the two techniques previously mentioned. The solid line in Figure 73 corresponds to the use of the thermal relation (Equation (36)) which multiplies the volume coefficient of expansion and the bulk modulus as scalar quantities. The points were obtained by applying the tensor Equation (41a) to the experimental data, thereby obtaining the spherical component of the Grüneisen tensor. As illustrated in the figure, the results obtained from the two methods are in essential agreement for carbon phenolic, since this material is nearly isotropic (the anisotropy ratio  $2C_{44}/C_{11}-C_{12}$  is  $\sim 0.95$ , compared to 1 for complete isotropy). For GEFG the agreement is also good, even though this material is more anisotropic ( $2C_{44}/C_{11}-C_{12}$ )  $\sim 0.75$ ). These results emphasize the requirement for obtaining complete thermal and ultrasonic analyses on nose cone materials.

Another useful quantity is the pressure derivative of the Grüneisen ratio. This quantity can be determined by measuring the pressure derivatives of the various quantities appearing in Grüneisen's thermal equation (Equation (36)). However, most laboratories are not equipped at the present time to determine the pressure derivatives of  $\beta$  and  $c_p$ . By using the thermodynamic definitions of these two quantities it is shown in Appendix III that the pressure derivative of  $\gamma$  at atmospheric pressure can be estimated as

$$\left(\frac{\partial \gamma}{\partial P}\right)_{0,T} = \gamma_0 \left[ \frac{1}{\beta_0} \left(\frac{\partial \beta}{\partial P}\right)_{0,T} - \frac{1}{B_0^T} + \frac{1}{B_0^S} \left(\frac{\partial B^S}{\partial P}\right)_{0,T} - \frac{1}{c_p} \left(\frac{\partial c_p}{\partial P}\right)_{0,T} \right] \quad (47)$$

where the zero subscript refers to atmospheric pressure. The terms  $(\partial\beta/\partial P)_T$  and  $(\partial c_p/\partial P)$  can be estimated from ultrasonic and thermal data as

$$\left(\frac{\partial\beta}{\partial P}\right)_T = \frac{1}{(B^T)^2} \left(\frac{\partial B^T}{\partial T}\right)_P \quad (48)$$

$$\left(\frac{\partial c_p}{\partial P}\right)_T = -\frac{T}{\rho} \left[ \left(\frac{\partial \epsilon_r}{\partial T}\right)_P + \beta^2 \right] \quad (49)$$

The temperature derivative of the isothermal bulk modulus,  $(\partial B^T/\partial T)_P$ , can easily be obtained from the temperature derivative of  $B^S$ , as determined ultrasonically (see Appendix II). In Section IV, paragraph 2, a method is presented for estimating the pressure derivative of the bulk modulus from thermal and ultrasonic data obtained at atmospheric pressure, so that  $(\partial\gamma/\partial P)$  can be estimated without making pressure measurements. Through the use of Equations (48) and (49), (47) for  $\gamma'_0$  can be written to explicitly show the pressure dependence of  $\gamma$  at atmospheric pressure as

$$\left(\frac{\partial\gamma}{\partial P}\right)_{0,T} = \frac{\gamma_{0,T}}{B_0^S} \left[ \left(\frac{\partial B^S}{\partial P}\right)_{0,T} + \left(\frac{1 + \beta\gamma T}{B_0^S}\right) \left(\frac{\partial B^S}{\partial T}\right)_0 - 1 - \gamma - T \left(\frac{\partial\gamma}{\partial T}\right)_0 \right] \quad (50)$$

Most of the quantities in Equation (50) are normally reported for a given material, with perhaps the exception of  $(\partial B^S/\partial P)_T$ . As previously mentioned, this quantity can be easily measured ultrasonically or estimated with sufficient accuracy at atmospheric pressure (in the case of metals).

## 2. Determination of the High Pressure Equation of State from Ultrasonic Techniques

In an extremely important paper, Anderson (Ref. 23) has illustrated that determinations of the pressure derivatives of the acoustic velocities can be combined with the definition of the bulk modulus to yield the high pressure equation of state (see Appendix II for an outline of this technique). Essentially the technique is due to Murnaghan (Ref. 25) who assumed that the bulk modulus was linear in pressure. Then, the relation between the specific volume and pressure is given by

$$\ln\left(\frac{V_0}{V}\right) = \frac{1}{B_{0T}^T} \ln \left[ B_{0T}^T \left( \frac{P}{B_0^T} \right) + 1 \right] \quad (51)$$

In Equation (51) the superscript T refers to the isothermal bulk modulus, the prime refers to the pressure derivative, the subscript o represents atmospheric pressure, and the subscript T refers to the bulk modulus derivative evaluated at constant temperature. Equation (51) is the most important equation in this report and is the basis for most of the following derivations. Since all of the quantities on the right in Equation (51) can be determined ultrasonically as a function of pressure, this equation allows a comparison between the theoretical prediction of the Murnaghan equation of state and high pressure isothermal determinations of the equation of state. Equation (51) allows the extrapolation of the volume to pressures which are significantly higher than the pressure range over which the ultrasonic data are obtained, providing there are no phase changes over the extrapolated pressure range, and that the higher pressure derivatives of the bulk modulus are negligible. For comparisons with shock wave data,  $B_{OT}^{T'}$  and  $B_O^T$  are to be replaced by  $B_{OS}^{S'}$  and  $B_O^S$ , which are the pressure derivative of the adiabatic bulk modulus at constant entropy and at atmospheric pressure, and the atmospheric value of the adiabatic bulk modulus.

The ultrasonic data yields the adiabatic bulk modulus at all temperatures and pressures for which measurements are normally made. Therefore, ultrasonic pressure measurements at constant temperature yield the pressure derivative of the adiabatic modulus at constant temperature ( $B_{OT}^{S'}$ ). In comparing Equation (51) with shock measurements it is necessary to convert to the derivative of the adiabatic bulk modulus at constant entropy. As shown in Appendix II, this conversion is

$$B_{OS}^{S'} = B_{OT}^{S'} + \gamma \frac{\partial \ln B_O^S}{\partial \ln T} \quad (52)$$

where  $B_{OT}^{S'}$  is the ultrasonically determined pressure derivative of the adiabatic bulk modulus and T is the absolute temperature. The quantity  $B_{OT}^{S'}$  can be determined from the pressure derivatives of the adiabatic velocities in an isotropic medium as follows

$$B_O^S = \left[ \rho \left( V_l^2 - \frac{4}{3} V_t^2 \right) \right]_{OS} = \left( \rho \frac{\partial P}{\partial \rho} \right)_{OS} \quad (53)$$

$$B_O^T = \left( \rho \frac{\partial P}{\partial \rho} \right)_{OT} \quad (54)$$

$$\frac{B^S}{B^T} = 1 + \beta \gamma T \quad (55)$$

so that

$$\left(\frac{\partial B^S}{\partial P}\right)_{oT} = B_{oT}^{S'} = 2\rho_o \left( v_\ell' v_\ell - \frac{4}{3} v_t' v_t \right)_o + 1 + \beta\gamma T \quad (56)$$

where  $v_\ell$  and  $v_t$  are the longitudinal and shear velocities, respectively. The derivative as determined in Equations (52) and (56) must be used when comparing the Murnaghan equation with shock data.

In comparing Equation (51) with hydrostatic pressure measurements as obtained, e.g., in the Bridgman technique, the constant temperature derivative of the isothermal bulk modulus should be used. Anderson (Ref. 23) gives the correction from the adiabatic to the isothermal derivative at atmospheric pressure ( $P \approx o$ ) and constant temperature as follows

$$\begin{aligned} B_{o,T}^{T'} = B_{o,T}^{S'} + T\beta\gamma \left( \frac{B_o^T}{B_o^S} \right) \left[ 1 - \frac{2}{\beta B_o^T} \left( \frac{\partial B^T}{\partial T} \right)_o - 2B_{o,T}^{S'} \right] \\ + \left[ T\beta\gamma \left( \frac{B_o^T}{B_o^S} \right) \right]^2 \left[ B_{o,T}^{S'} - 1 - \frac{1}{\beta^2} \left( \frac{\partial \beta}{\partial T} \right)_o \right] \end{aligned} \quad (57)$$

As mentioned, the temperature derivatives of the velocities yield the temperature derivative of the adiabatic bulk modulus. However, the temperature derivative of the isothermal modulus at atmospheric pressure as required in Equation (57) is given, as shown in Appendix II, as

$$\begin{aligned} \left( \frac{\partial B_o^T}{\partial T} \right) = \frac{\left( \frac{\partial B_o^S}{\partial T} \right)}{(1 + \beta\gamma T)} - \frac{B_o^S \beta\gamma}{(1 + \beta\gamma T)^2} \\ - \frac{B_o^S \gamma T \left( \frac{\partial \beta}{\partial T} \right)_P}{(1 + \beta\gamma T)^2} - \frac{B_o^S \beta T \left( \frac{\partial \gamma}{\partial T} \right)_P}{(1 + \beta\gamma T)^2} \end{aligned} \quad (58)$$

The last term in Equation (58) can usually be neglected, as previously illustrated for aluminum, magnesium, and gold. However, in principle, all of the quantities appearing in Equations (57) and (58) can be obtained through ultrasonic and thermal experiments, yielding  $B_{o,T}^{T'}$  required in the Murnaghan relation (Equation (51)).

As Anderson (Ref. 23) indicates, the derivation of the Murnaghan equation relies upon the assumption of the linearity of the bulk modulus with pressure. He states that, generally the magnitude of  $B_o^{s''}$  is zero to at least two or three significant figures.\* This may not be true in all materials, particularly some of the plastics; however, contemporary ultrasonic pressure experiments easily yield the bulk modulus to one part in  $10^3$  so that a magnitude of  $B_o^{s''}$  as large as  $10^{-2}$  could be determined. In these cases, the approach used by Murnaghan could be modified to include the second derivative of B in Equation (51). In Appendix IV it is shown that the resulting equation can be written as

$$\frac{V_o}{V} = \left[ \frac{1 + aP}{1 + bP} \right]^{1/c} \quad (59)$$

where

$$a = \frac{B_o^{s''}}{B_o' - c}$$

$$b = \frac{B_o^{s''}}{B_o' + c}$$

$$c = \sqrt{(B_o')^2 - 2B_o B_o^{s''}}$$

The subscripts have been left off the bulk modulus and its derivatives with the understanding that either the adiabatic or isothermal values are used, depending on whether the hydrostat or adiabat is being determined.

Anderson (Ref. 23) also shows that the range of the Murnaghan equation is not restricted to the pressure range in which the bulk modulus is determined (3 to 10 kbars). In fact, he illustrates that this equation can be used to extrapolate the volume to several hundred kbars in metals, excepting phase changes. The applicability of the technique relies upon the accuracy with which  $B_o$  and  $B_o'$  can be determined, and upon the linearity of the bulk modulus.

---

\* It has recently been brought to the author's attention that Ruoff (Ref. 41) and Pastine (Ref. 26) have presented ways of estimating the second derivative of the bulk modulus from ultrasonic data combined with appropriate theoretical equations of state. They also discuss the effect of this derivative on the nonlinear behavior of the shock velocity versus particle velocity in metals and derive the resulting equation to quadratic terms in the particle velocity. This approach is outlined in Appendix V. A method is presented for estimating the order of magnitude of  $B_o^{s''}$ .

However, Equation (51) is fairly insensitive to uncertainties in the pressure derivative of the bulk modulus; a 1 percent error in  $B'_0$  changes the extrapolated volume at  $P = B_0$  by less than 1/2 percent.

As emphasized, the most accurate method for determining the bulk modulus and its pressure derivative is through an ultrasonic-hydrostatic pressure technique. However, the derivative can be estimated from a theoretical relation derived by Dugdale and MacDonald (Ref. 27). They give the pressure derivative of  $B$  in terms of the Grüneisen ratio as

$$B_{0,s}^{s'} \approx 2\gamma + 1 \quad (60)$$

As an example, the information in Table 57 has been obtained for 6061-T6 and 1060 Al at 25°C

Table 57  
THE RELATIONSHIP BETWEEN THE GRÜNEISEN RATIO  
AND THE PRESSURE DERIVATIVE OF THE BULK MODULUS IN ALUMINUM

	6061-T6	1060
$\gamma$	2.03	2.06
$B_{0,s}$	751 kbar	743 kbar
$B_{0,T}$	723 kbar	716 kbar
$B_{0,s}^{s'}$ (Eq. 53)	5.06	5.12
$B_{0,T}^{s'}$ (Eq. 49)	5.23	5.29

Figures 74 and 75 illustrate the applicability of using the Murnaghan equation in conjunction with the above data to estimate the high pressure equation of state of these two alloys. Also shown in Figure 74 for 6061 Al are some dynamically determined high pressure points by Lundergan and Herrmann (Ref. 28) and a least-squares compilation by Walsh, et al. (Ref. 29). As observed in the graph the agreement between the estimated curve and the actual data is particularly good to ~ 450 kbars considering that the pressure derivative was not directly measured. The same agreement is observed for 1060 Al in Figure 75, although experimental high pressure data for 1060 are somewhat lacking. However, this illustrates a fundamental advantage of this technique. That is, that the high pressure equation of state of materials as obtained through the Murnaghan equation

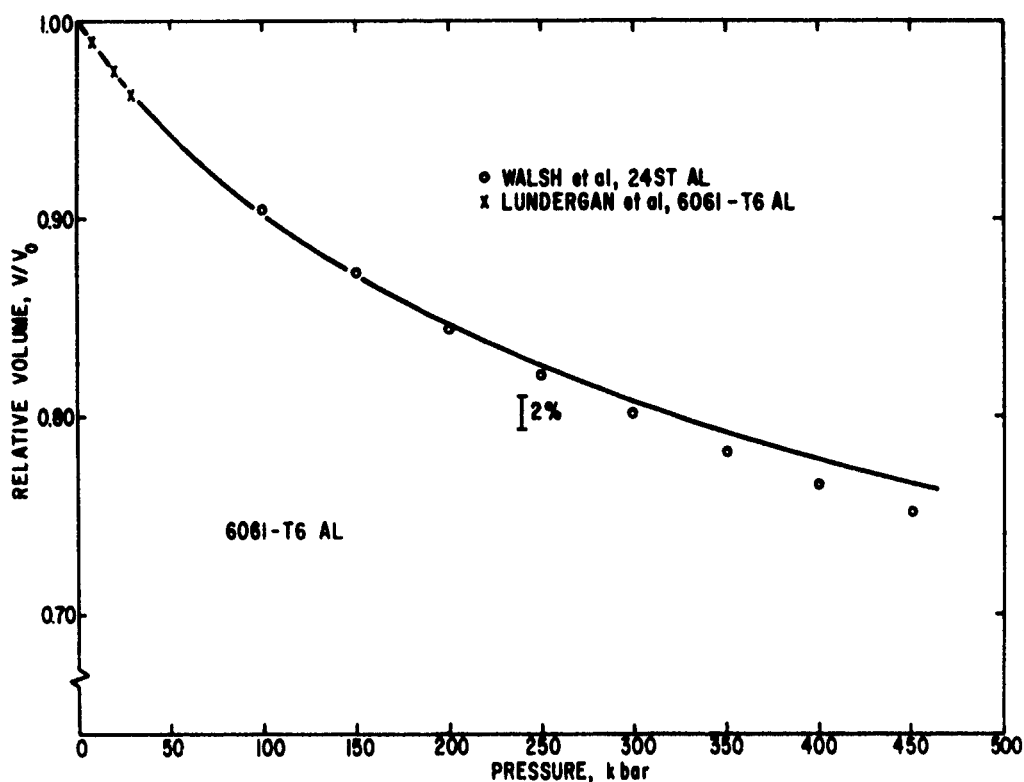


Figure 74. Relative Volume Versus Pressure for 6061-T6 Aluminum (Density, 2.704 g/cc at 25°C).

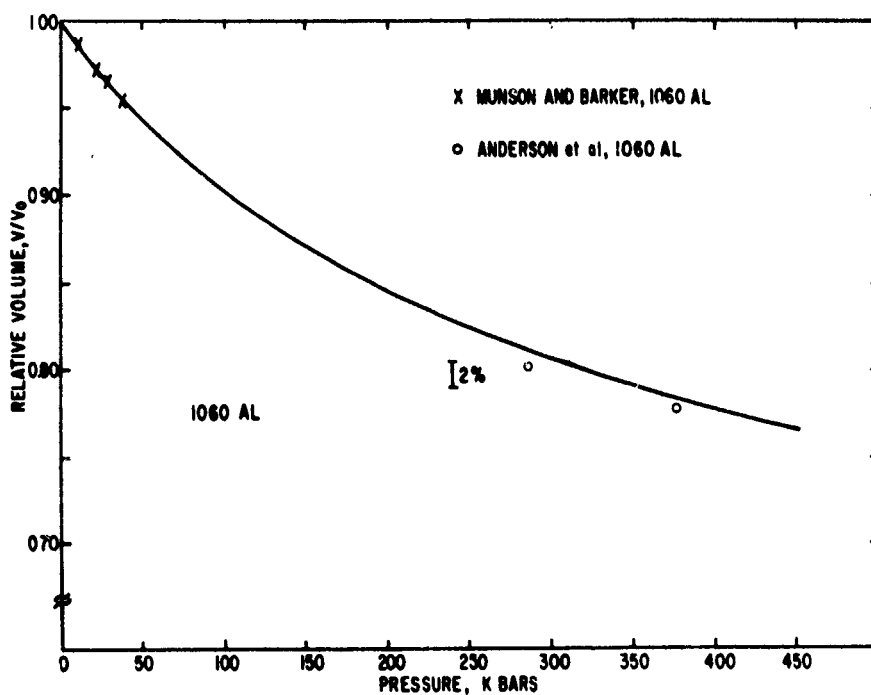


Figure 75. Relative Volume Versus Pressure for 1060 Aluminum (Density, 2.703 g/cc at 25°C).

can be checked by only a few experimental high pressure points to test for phase changes, and thus, to ensure the reliability of the estimated PVT relation. The experimental data in Figure 75 are those of C.D. Anderson, et al. (Ref. 30) and Munson and Barker (Ref. 31). The curves in Figures 74 and 75 were computed from the pressure derivatives of the isothermal bulk moduli at constant temperature, and therefore represent the hydrostats.

The technique is likewise expected to apply to the estimation of the high pressure equation of state in plastics. However, there are some reservations applicable to the use on this class of materials. First of all, the bulk modulus in plastics is significantly lower than that in metals ( $\sim 30$  to  $50$  kbars versus  $\sim 700$  kbars in metals). This places some restrictions on the pressure range within which the volume can be extrapolated within a prescribed degree of accuracy. Second, plastic materials generally exhibit a higher degree of viscoelasticity than do metals. This phenomenon leads to complex velocities of propagation, and consequently, to complex elastic moduli. To truly relate the Murnaghan theory to dynamic data in these cases, it will be necessary to evaluate the effect of temperature and pressure on the relaxation processes involved in viscous damping, and relate these mechanisms to the effective moduli for shock wave propagation (or to the moduli from isothermal compressibility experiments). This will necessitate the measurements of acoustic velocity and attenuation versus frequency for different values of the pressure and temperature. Third, the effect of the many transitions in plastics, such as glass transitions, should be studied regarding their effect on the equation of state. Last, some of the nose cone materials are extremely anisotropic, which might be resolved by determining the linear compressibilities and their pressure derivatives. If the compressibilities are linear in pressure, this fact could be used along with the definitions of the velocities and moduli to provide an analytical equation for the length change versus pressure. For reference purposes the linear compressibilities are presented here for a transversely isotropic medium. The compressibility along the  $x_i$  axis ( $i = 1, 2, 3$ ) is defined as

$$\chi_{x_i} = - \frac{1}{\ell(x_i)} \frac{\partial \ell(x_i)}{\partial P} \quad (61)$$

which is found from the total compressibility by separating  $V(x, y, z)$  into  $\ell(x_1) \ell(x_2) \ell(x_3)$ , where the  $\ell$ 's represent lengths along the three coordinate axes.



In Appendix I, it is shown that the compressibilities along the layers,  $\chi_{\perp}$ , and perpendicular to the layers,  $\chi_{||}$ , are given as

$$\chi_{\perp} = \frac{c_{33} - c_{13}}{c_{33} (c_{11} + c_{12}) - 2c_{13}^2} \quad (62)$$

$$\chi_{||} = \frac{c_{11} + c_{12} - 2c_{13}}{c_{33} (c_{11} + c_{12}) - 2c_{13}^2} \quad (63)$$

The total compressibility is then given as

$$\chi_T = \chi_{||} + 2\chi_{\perp} \quad (64)$$

as represented in Equation (38).

Figure 76 shows the predicted hydrostat for (TFE) Teflon (density 2.19 g/cc). First, it is noted that the agreement between the predicted curve and the experimental compressibility points of P.W. Bridgman (Ref. 32) is not good for pressures higher than about 10 kbars. However, Bridgman found a discontinuity in volume at  $\sim 6.5$  kbars, which he associated with a polymorphic transition.\* Therefore, the use of the Murnaghan equation is not reliable for pressures above this transition if the bulk modulus and its derivative are determined at lower pressures. The solution to this problem would be to make velocity measurements above 6.5 kbars, expand the bulk modulus about this pressure, and use the Murnaghan equation near this pressure, with the new values of  $B_0$  and  $B'_0$ . This would therefore require velocity measurements to be made over a pressure range of atmosphere to  $\sim 10$  kbars. It would also be worthwhile to evaluate the effect of temperature on this transition, because the pressure at which the transition occurs might be significantly decreased at higher temperatures. This is especially applicable to plastics, because the moduli in plastics are rather strong functions of temperature.

The Dugdale-MacDonald relation was used to obtain the pressure derivative of the bulk modulus in Teflon, and to thus obtain the curve in Figure 76. However, it is expected that this relation may not be generally valid in plastics. In particular, it gives a poor estimation of the derivative of the bulk modulus in polystyrene. Hughes and Kelly (Ref. 33) have measured the third-order elastic

---

\* Such transitions are ordinarily associated with a change in lattice structure which suggests some degree of crystallinity in Teflon.

constants in polystyrene, including the bulk modulus as a function of pressure. They found that the bulk modulus was linear to 9 kbars with a derivative of 8.89. The Grüneisen ratio calculated from their results and handbook values for  $\beta$  and  $c_p$  is 0.53, so that the derivative  $B_{os}^{s'}$  from the Dugdale relation is estimated as 2.06. There is thus a significant difference between the actual derivative and that estimated through the Dugdale-MacDonald relation, which emphasizes the need for a direct measurement of this derivative. Figure 77 shows the result of using the Murnaghan equation for the two different values of  $B'_0$  in polystyrene. The dashed line corresponds to the estimation of  $B_{o,s}^{s'}$  by the Dugdale equation, and the solid line represents the use of the actual derivative as determined by Hughes and Kelly.  $B_{OT}^{s'}$  was approximated as  $B_{os}^{s'}$  for these calculations because information was not available on the bulk modulus, specific heat, or volume coefficient of expansion versus temperature. Also shown in Figure 77 are some compressibility points by Bridgman (Ref. 32), some dynamic data by Wagner, et al. (Ref. 34), and Hauver, et al. (Ref. 35). This case shows that the Murnaghan equation equally applies to plastics. However, it also illustrates that the Dugdale-MacDonald relation is not necessarily valid for plastics.

These two examples illustrate the need for performing ultrasonic pressure measurements on plastics to predict the high pressure equation of state of these materials. Besides the isothermal measurements of Bridgman (Ref. 32) and the ultrasonic data of Hughes (Ref. 33) very little high pressure data (besides shock data) is available on plastics. Some older work on polyethylene and Lucite to  $\sim 1$  kbar has been reported by Hughes, Blankenship, and Mims (Ref. 37). Practically no information on the pressure derivatives of the elastic constants is available on the relatively new laminated materials, such as carbon phenolic.

It should be mentioned that shock measurements can be used to obtain the derivatives of the bulk modulus versus pressure. However, the derivative obtained in this technique is less accurate than the ultrasonic technique, because it involves the second derivative of the Hugoniot, whereas, the derivative obtained ultrasonically involves the first derivative of the velocities versus pressure. As shown in Section IV, paragraph 3, the ultrasonic technique can be used to estimate essentially all the parameters measured in the shock technique, such as shock velocity and particle velocity versus pressure. The estimations are restricted to pressure ranges in which transitions are not present. However, they illustrate the capabilities of the ultrasonic method and ways it can be used, in conjunction with shock techniques, to reduce analysis time and increase the available knowledge on the equation of state of solids.

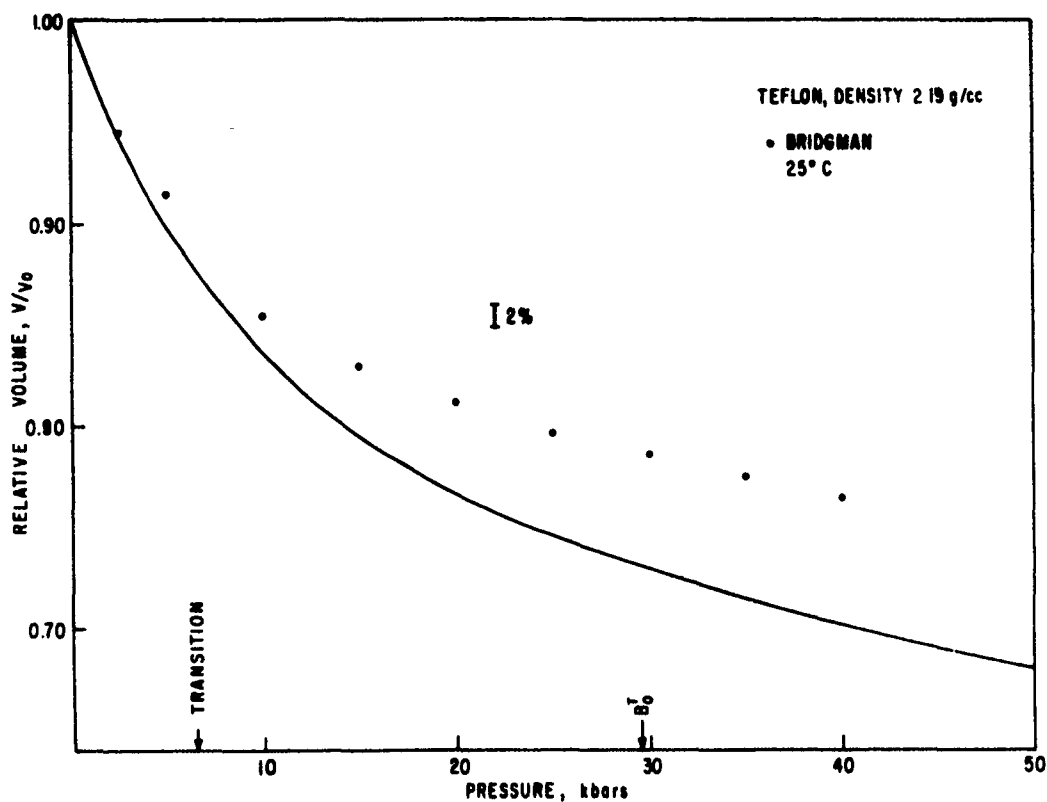


Figure 76. Relative Volume Versus Pressure for Teflon (Density 2.19 g/cc).

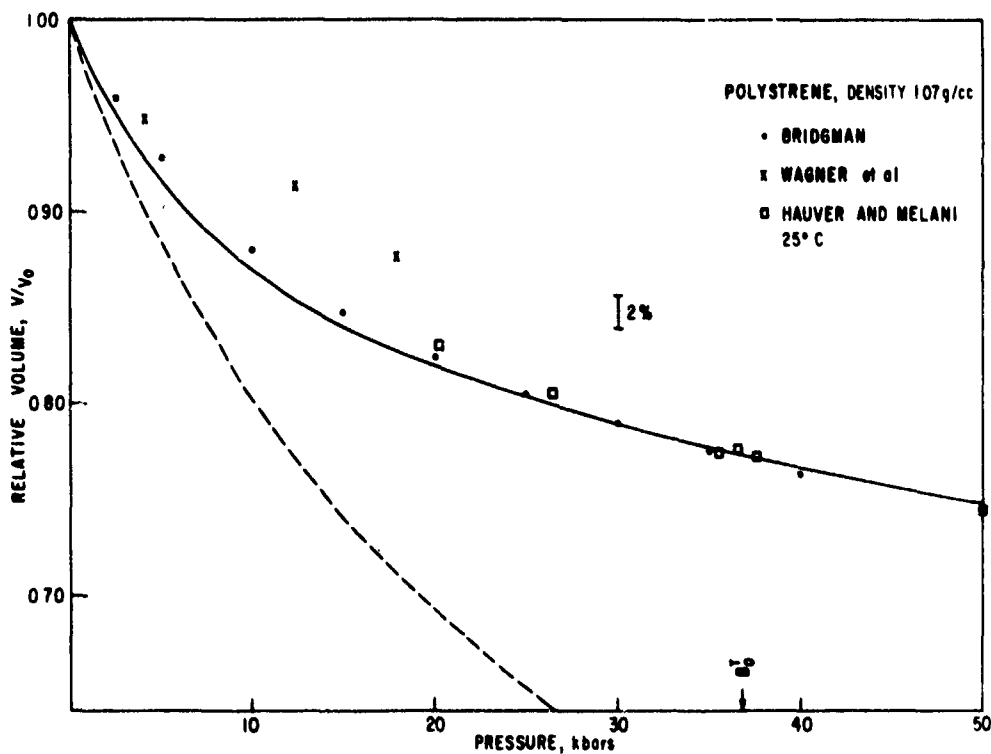


Figure 77. Relative Volume Versus Pressure for Polystyrene (Density, 1.07 g/cc). (The ultrasonic work of Hughes and Kelly (Ref. 33) was used to calculate the pressure dependence of the bulk modulus.)

### 3. Determination of the Shock Velocity and Particle Velocity Versus Pressure by the Ultrasonic Technique

Ruoff (Ref. 41) and Pastine (Ref. 26) have significantly increased the applicability of the ultrasonic technique by deriving the relation between shock velocity and particle velocity in terms of measurable quantities. In terms of the expansion of the shock velocity,  $U_s$ , to quadratic terms in the particle velocity,  $u_p$ ,

$$U_s(P) = a + bu_p + cu_p^2 \quad (65)$$

they give the coefficients  $a$ ,  $b$ , and  $c$  as

$$\begin{aligned} a &= U_s(P = 0) = \sqrt{\frac{B_o^s}{\rho}} \\ b &= \frac{1}{4} \left( 1 + B_{os}^{s'} \right) \\ c &= \frac{b}{6a} \left( 2 - b + \frac{B_{os}^s}{2b} + \gamma \right) \end{aligned} \quad (66)$$

(See Appendix V for the derivation of these constants.) All of the terms appearing in the constants  $a$ ,  $b$ , and  $c$  can be determined ultrasonically so that the shock velocity-particle velocity curve can be estimated by making pressure measurements of the acoustic velocities. For most materials the second derivative of the bulk modulus is very small (see Appendix V) so that the coefficient  $c$  is approximately zero and a linear relation represents the shock velocity, which is in agreement with shock measurements. However, the linear relation is only true on the average for the wide variety of materials studied with shock wave techniques, and there have been notable exceptions.

Both Ruoff (Ref. 41) and Pastine (Ref. 26) have used Equation (65) to explain the existence of curvature in the shock velocity versus particle velocity. Ruoff, in particular, has shown how the constant  $c$  can be evaluated from ultrasonic measurements on the alkali halides by assuming the Born model of the interaction potential to evaluate the derivative  $B''$ . This assumption is not necessary if the derivative can be determined directly. However, the bulk modulus is sufficiently linear with pressure for most materials so that contemporary ultrasonic techniques are not sensitive enough to detect the second derivative of the bulk modulus. The sensitivity of the ultrasonic approach can be extended by increasing the pressure range over which measurements are normally made, or by using materials

with small bulk moduli. Plastics should allow the determination of the second derivative of the bulk modulus, and thus, allow comparison of Equation (66) with shock wave data over a large pressure range.

The shock velocity and particle velocity can also be expressed in terms of the pressure. If the Murnaghan logarithmic equation is a valid representation of the equation of state for most solids, which is somewhat confirmed by the good agreement between the experimental and theoretical data for most materials when phase changes are not encountered over the region of application, this equation can be used to predict the shock velocity and particle velocity versus pressure. To derive these quantities the conservation laws for mass and momentum are needed. These are

$$\rho (U_s - u_p) = \rho_o U_s \quad (67)$$

$$P - P_o = \rho_o u_p U_s \quad (68)$$

Here,  $u_p$  is the particle velocity behind the shock front,  $U_s$  is the shock velocity,  $\rho$  and  $\rho_o$  are the respective densities behind and in front of the shock, and  $P$  and  $P_o$  are the corresponding pressures. It is shown in Appendix IV that the shock and particle velocities can then be written as

$$U_s(P) = \sqrt{\frac{A \cdot P \times 10^9}{\rho_o B}} \quad (69)$$

$$u_p(P) = \sqrt{\frac{B \cdot P \times 10^9}{\rho_o A}} \quad (70)$$

where

$$A = \left[ B_{os}^{s'} \left( \frac{P}{B_o^s} \right) + 1 \right]^{\frac{1}{B_{os}^s}}$$

$$B = \left[ B_{os}^{s'} \left( \frac{P}{B_o^s} \right) + 1 \right]^{\frac{1}{B_{os}^{s'}}} - 1$$

Equations (69) and (70) are written so that for  $P$  and  $B_o^s$  in kbars and  $\rho_o$  in g/cc, the velocities are in units of cm/sec. The important point about the two equations is that the three required quantities  $(B_{os}^s, B_{os}^{s'}, \rho_o)$  can all be evaluated at atmospheric pressure by ultrasonic techniques. The applicability

of these two equations in predicting the shock and particle velocities at high pressure rests upon the same assumptions involved in predicting the relative volume versus pressure; namely, that the bulk modulus is linear in pressure and that the material does not exhibit transitions over the extrapolated pressure range.

Figures 78 through 88 illustrate the agreement between the estimated shock and particle velocities versus pressure, and the actual experimental data. The graphs in these figures represent compressible and incompressible materials, alloys, single crystals, and one plastic. With the exception of polystyrene, the values of  $B_0^s$  and  $B_{os}^{s'}$  were taken from Reference (23). The pressure measurements of Hughes and Kelly (Ref. 33) were used to evaluate  $B_0^s$  and  $B_{ot}^{s'}$  for polystyrene. The shock wave data in all these figures were taken from the Lawrence Radiation Laboratory's compilation, "Compendium of Shock Wave Data" (Ref. 36).

The agreement between the extrapolated curve and actual data for potassium and sodium is particularly good to about 300 to 400 kbars, considering the relatively low bulk modulus in these materials. The shock velocity for NaCl (Figure 81) is extrapolated to only  $\sim 250$  kbars because of a transition in the region 220 to 270 kbars. The dashed line in Figure 81 shows the result of extrapolating beyond the transition.

The agreement between the extrapolated curve and the experimental data for  $Al_2O_3$  is not as good. The curve in Figure 82 was calculated for polycrystalline  $Al_2O_3$ . However, it falls between McQueen's experimental data for single crystal and polycrystalline  $Al_2O_3$ .

The agreement for polystyrene, which in comparison to other materials presented here is more compressible, is fairly good to  $\sim 150$  kbars. The data illustrated in Figure 85 suggest a transition in the region of 150 kbars.

The extrapolations for magnesium and iron are good; however, the maximum pressure to which the shock velocity for iron can be extrapolated is  $\sim 130$  kbars because of a transition at this pressure.

The extrapolated curve of shock velocity for aluminum is within  $\sim 3$  percent of the experimental data at 450 kbars and within  $\sim 5$  percent at 800 kbars. Figure 88 shows the estimated particle velocity in aluminum versus pressure. The agreement between the experimental values and the theory is within  $\sim 5$  percent to 800 kbars. The experimental shock data shown in Figures 87 and 88 for aluminum

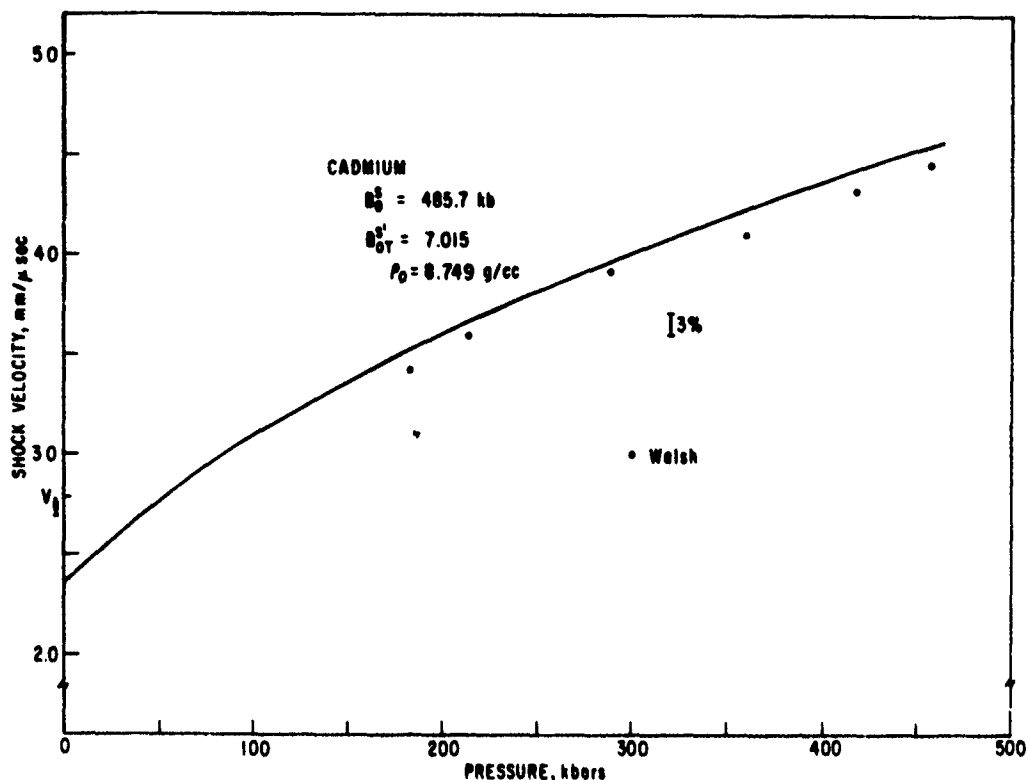


Figure 78. Shock Velocity Versus Pressure in Cadmium.

were obtained from a number of investigations on different alloys of aluminum. No correction was made for the difference in density between the reported experimental data and the value used here (2.70 g/cc).

Figures 76 through 88 illustrate that the Murnaghan equation can, in many instances, be combined with the laws of conservation of mass and momentum to yield fair predictions of the shock and particle velocities at high pressures, providing the ultrasonic data at atmospheric pressure is not used to extrapolate across a phase transition. The agreement between the theoretical and experimental data provide further confidence in using the Murnaghan equation to extrapolate data, obtained over the pressure range of 0 to 10 kbars, to significantly higher pressures. The evaluation of the second derivative of the bulk modulus will allow a more accurate estimation of the density versus pressure (Equation 59), and should thus improve the agreement of the shock velocity and particle velocity versus pressure through the use of Equations (67) and (68).

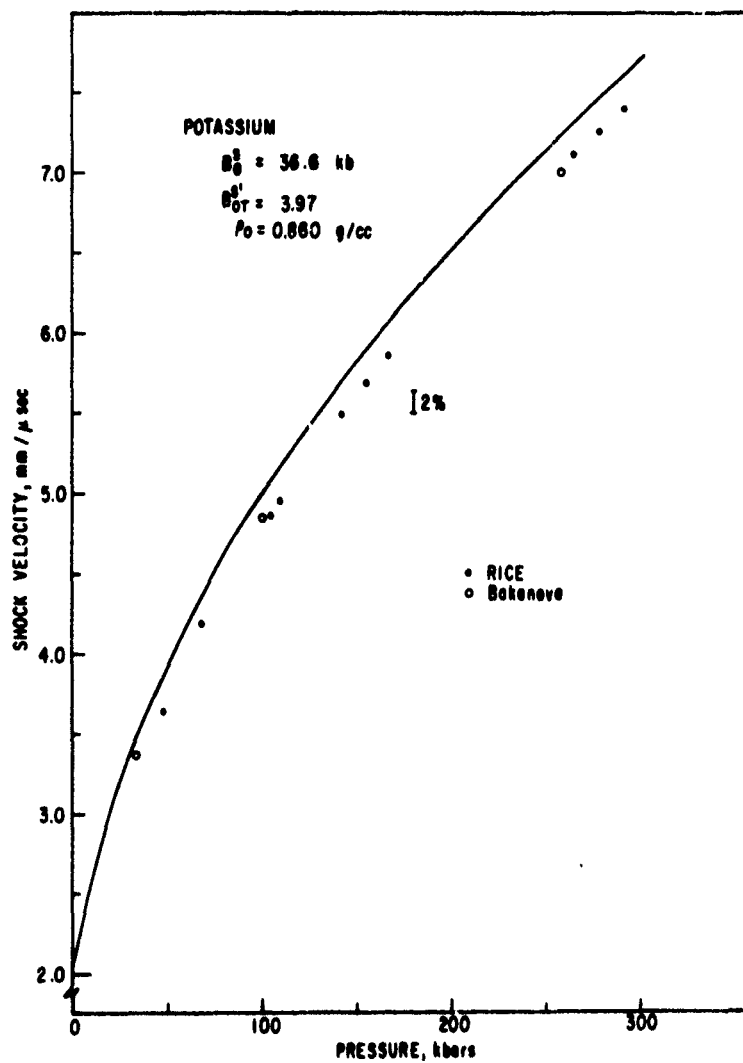


Figure 79. Shock Velocity Versus Pressure in Potassium.



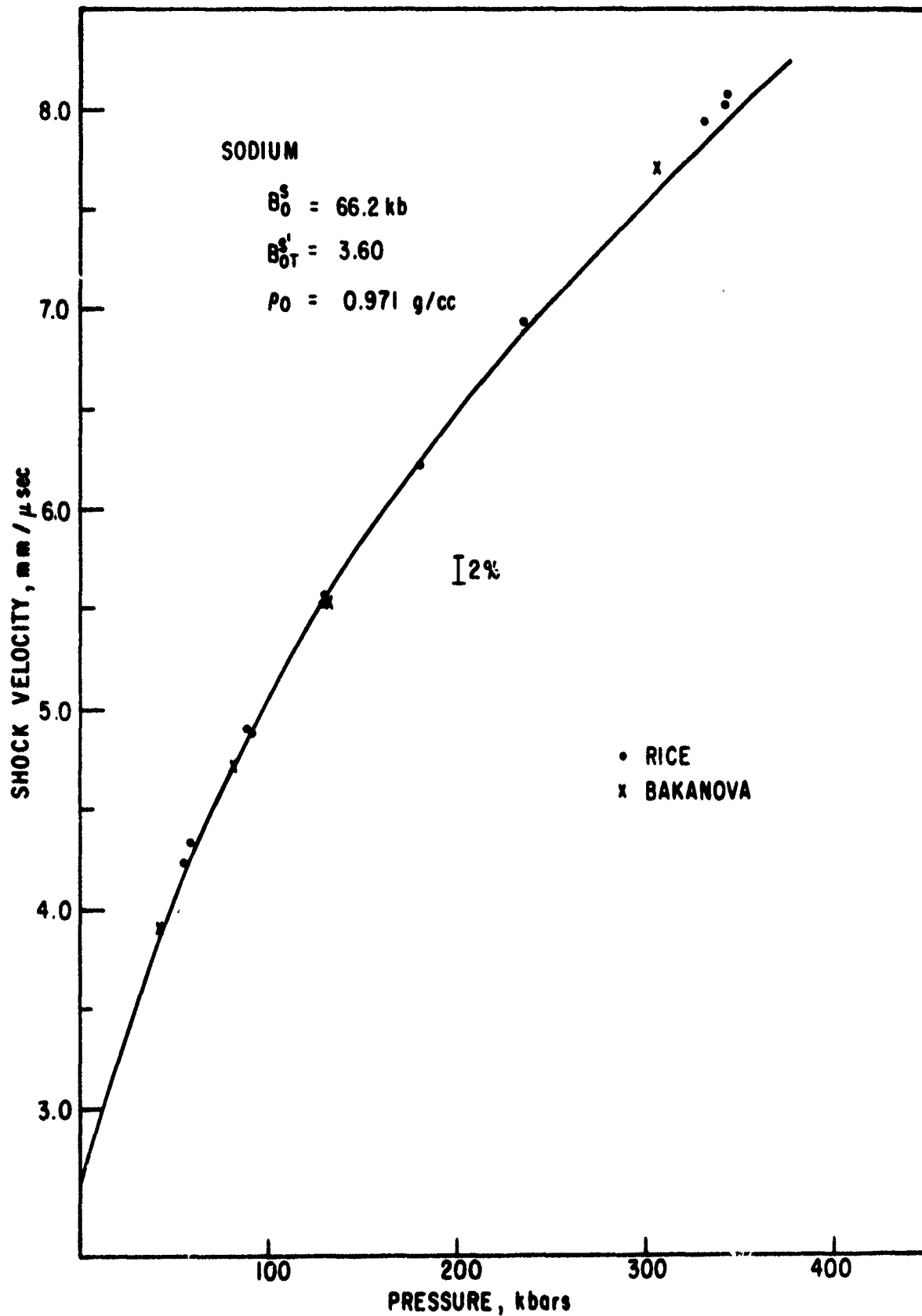


Figure 80. Shock Velocity Versus Pressure in Sodium.

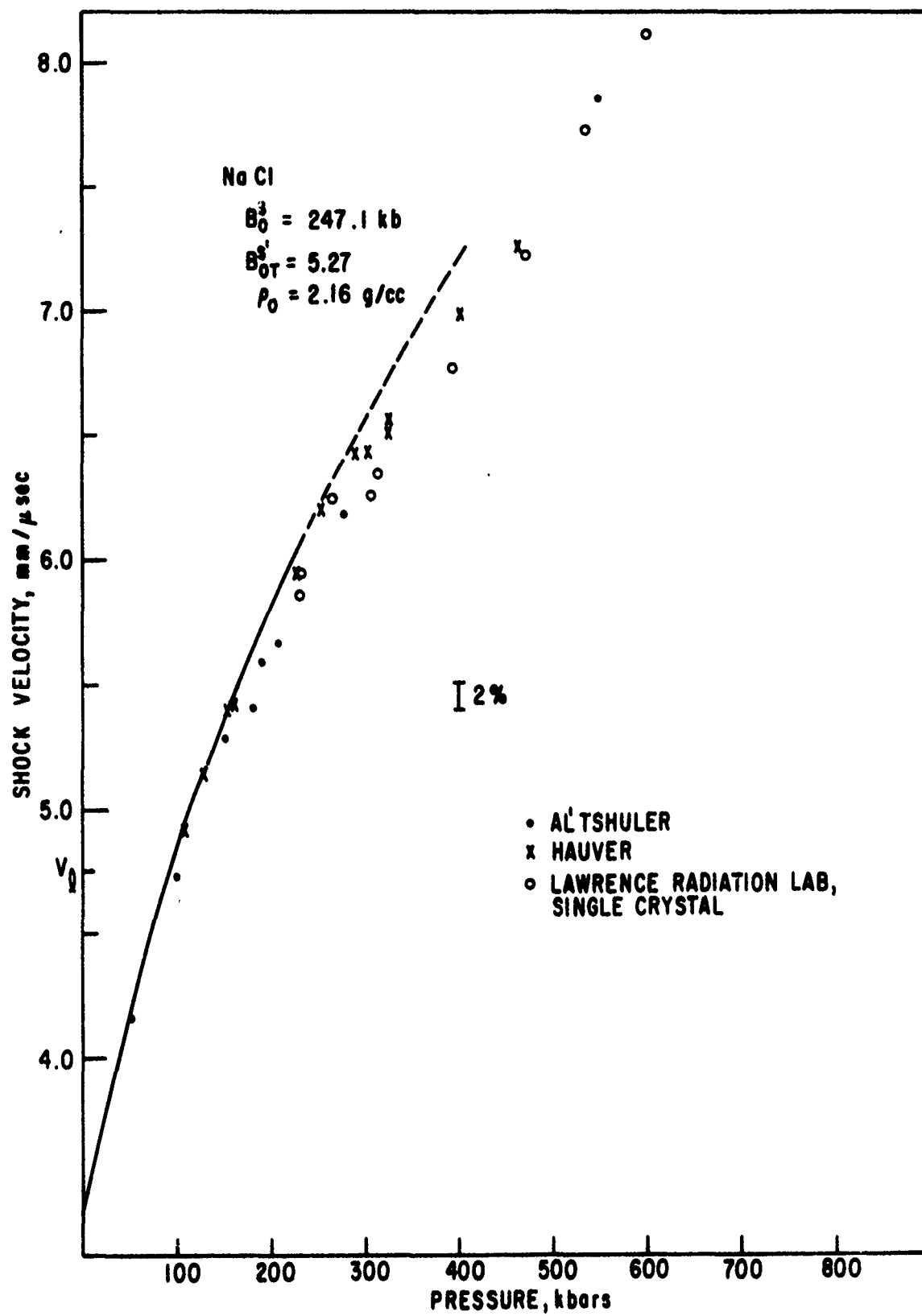


Figure 81. Shock Velocity Versus Pressure in Sodium Chloride.

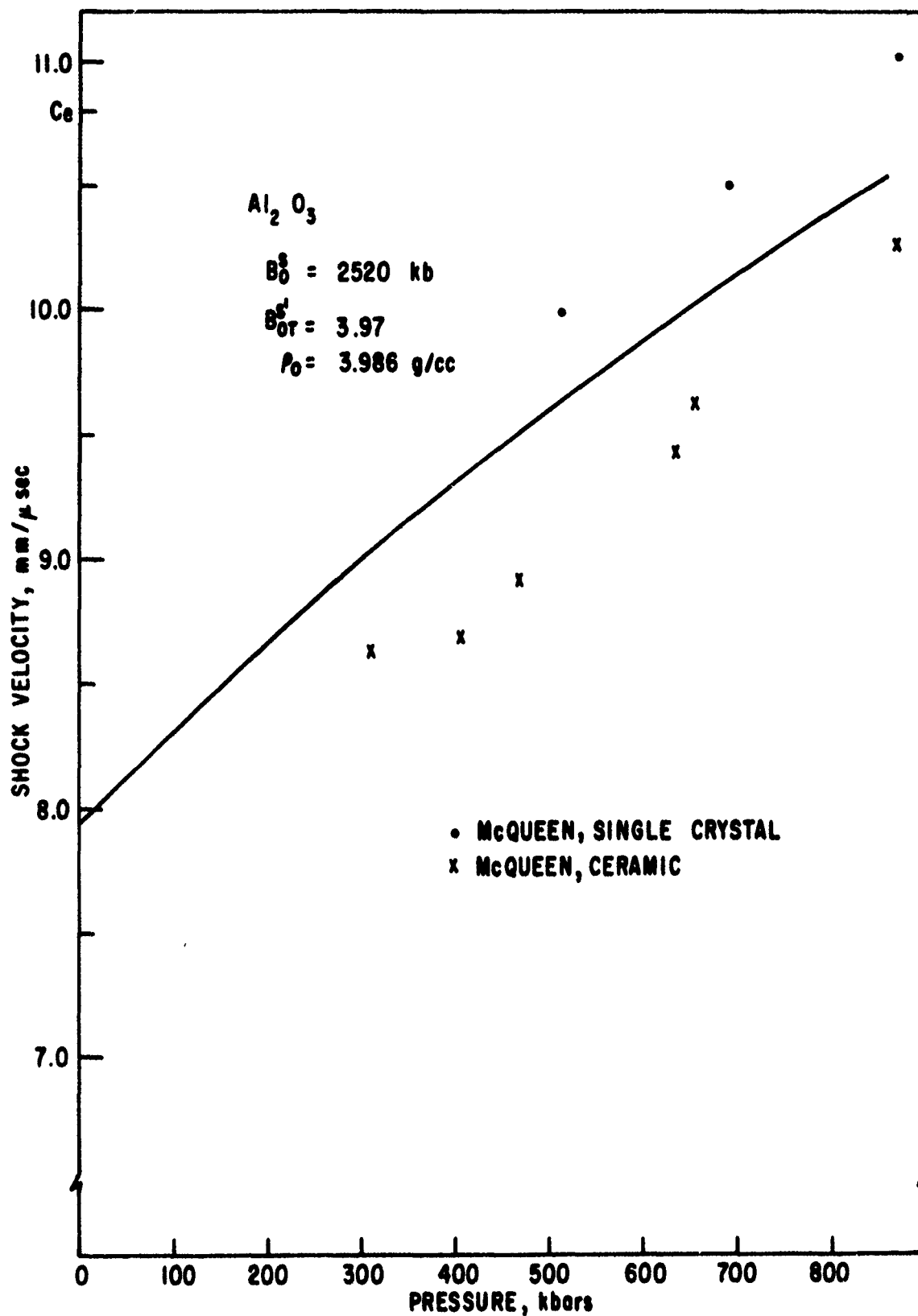


Figure 82. Shock Velocity Versus Pressure in Aluminum Oxide.

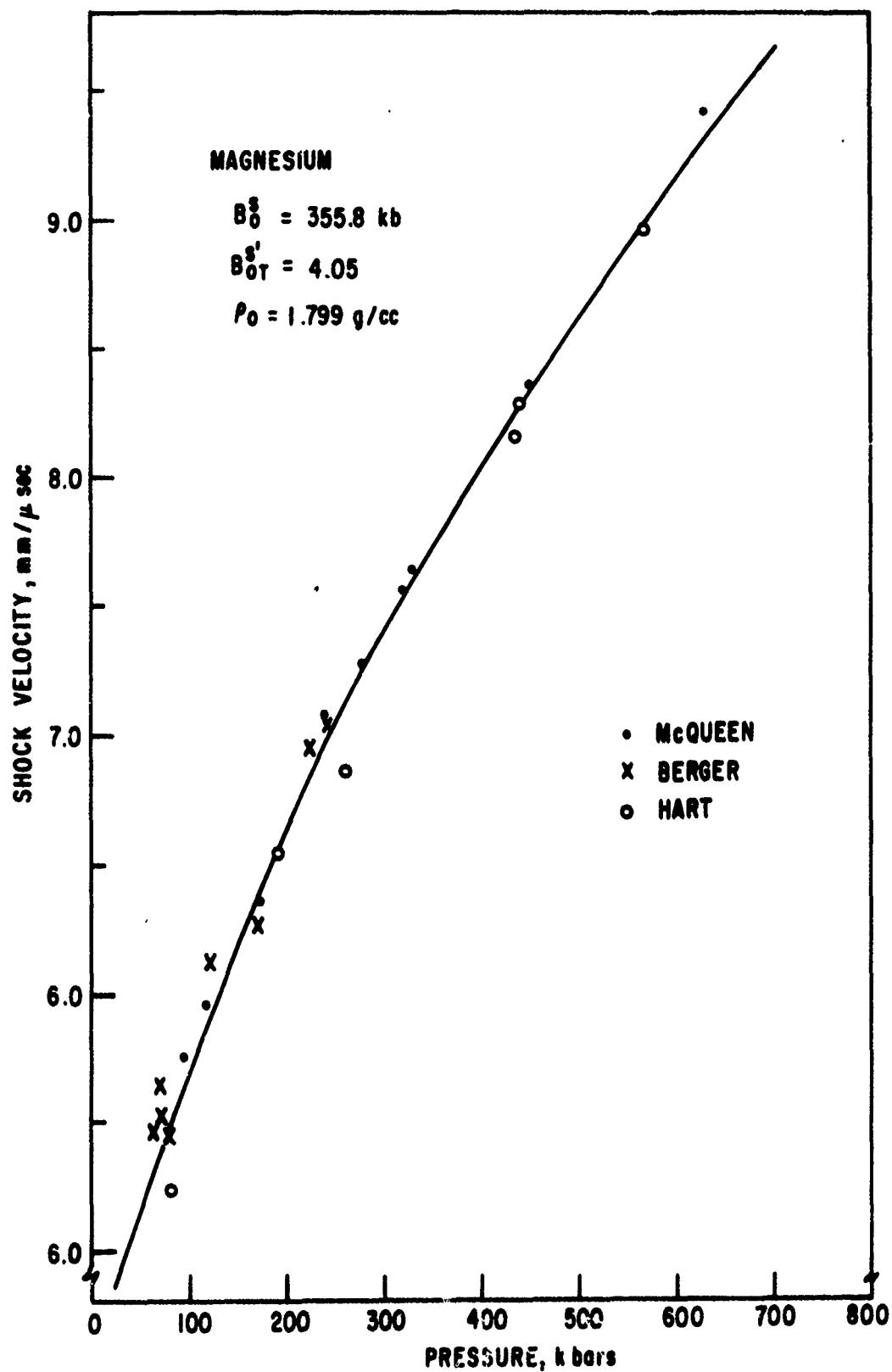


Figure 83. Shock Velocity Versus Pressure in Magnesium.

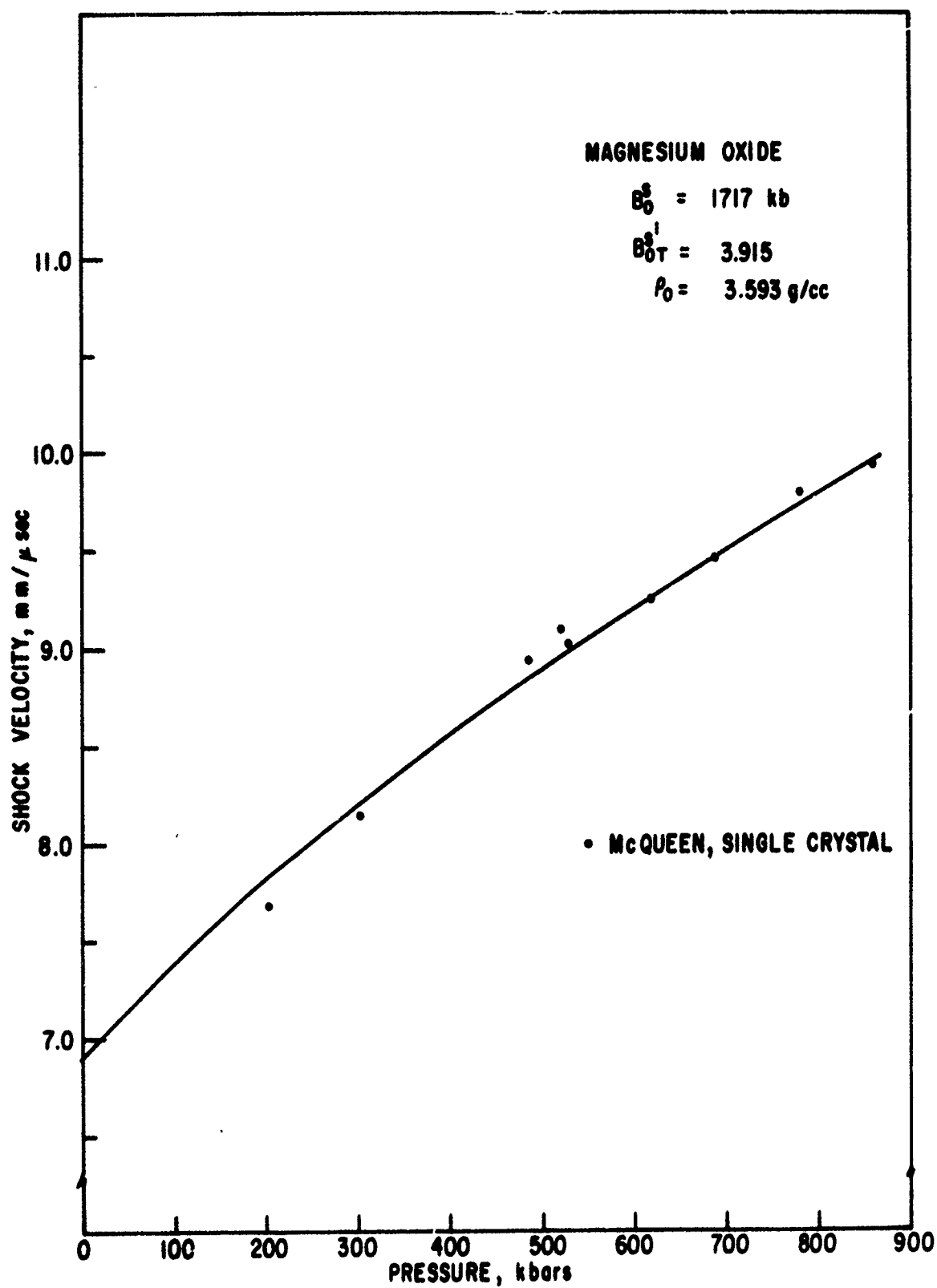


Figure 84. Shock Velocity Versus Pressure in Magnesium Oxide.

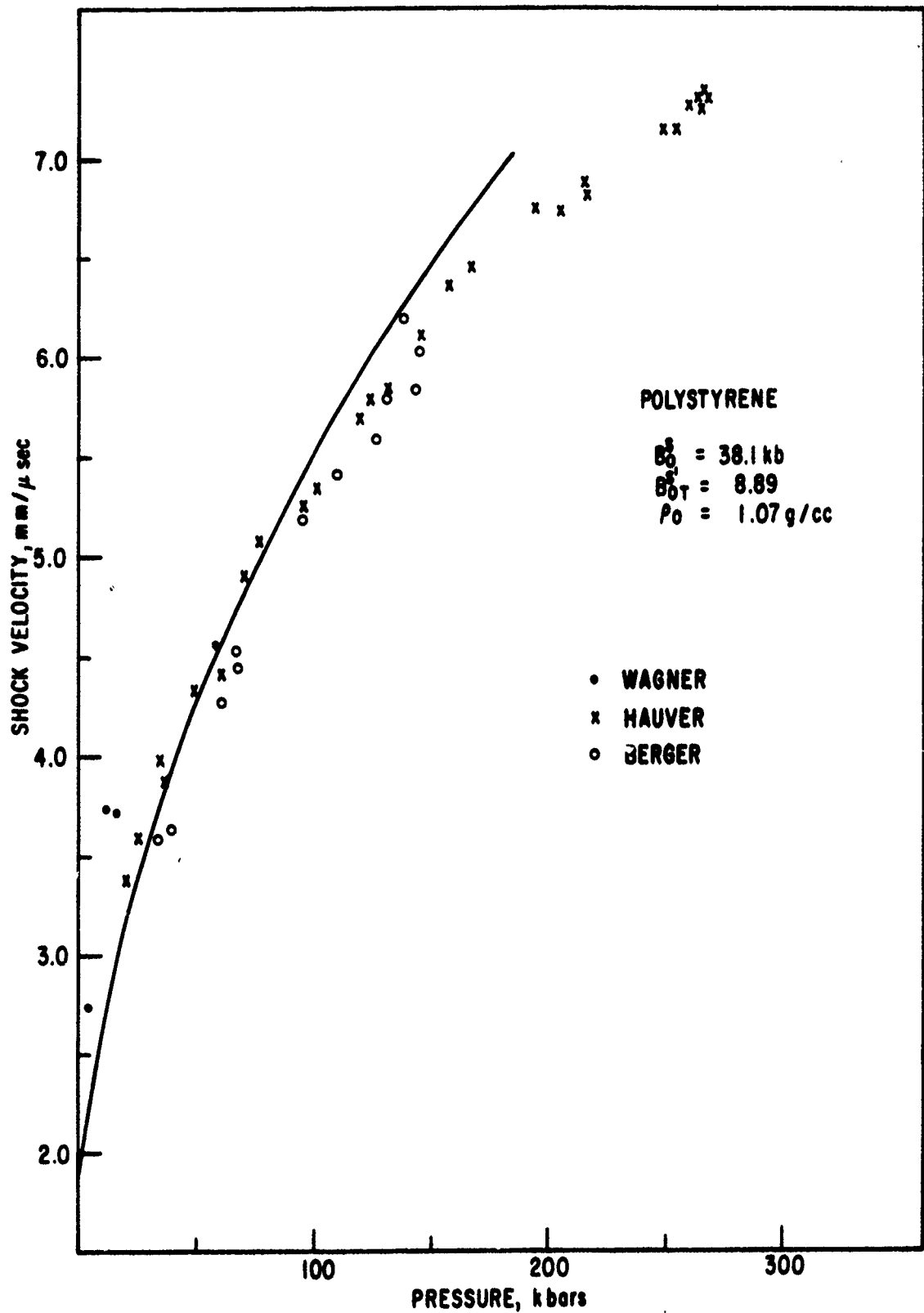


Figure 85. Shock Velocity Versus Pressure in Polystyrene.

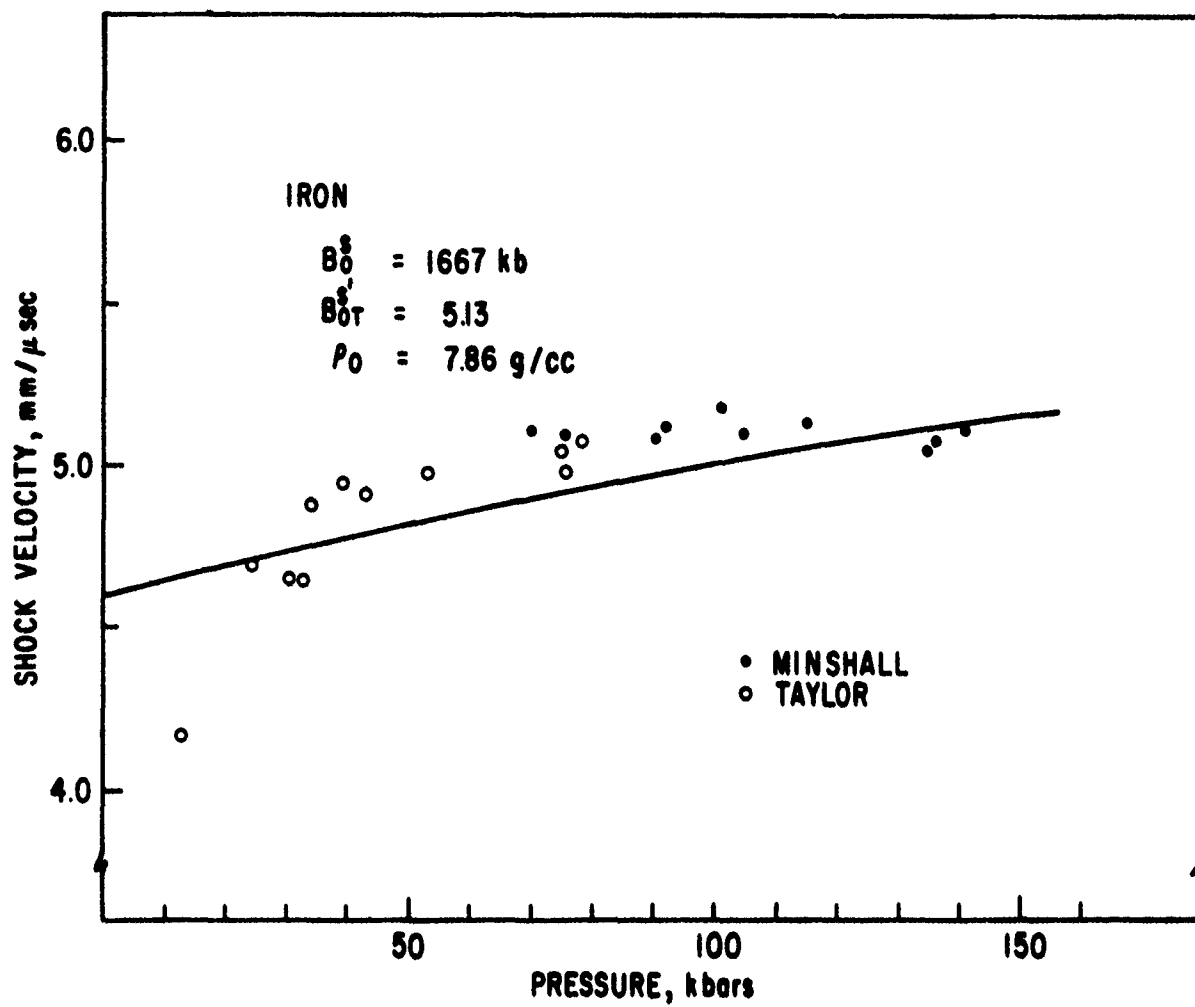


Figure 86. Shock Velocity Versus Pressure in Iron.

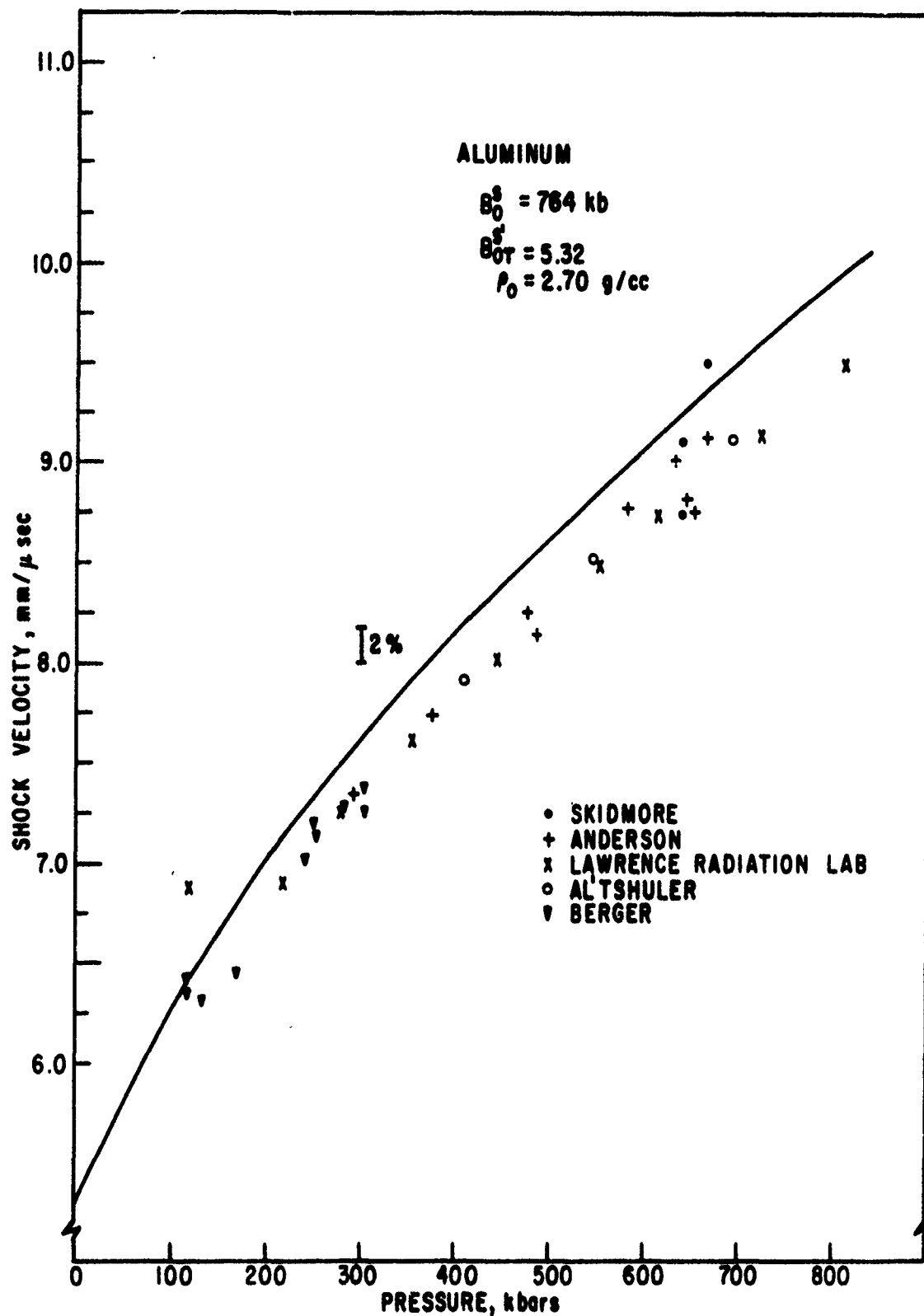


Figure 87. Shock Velocity Versus Pressure in Aluminum.



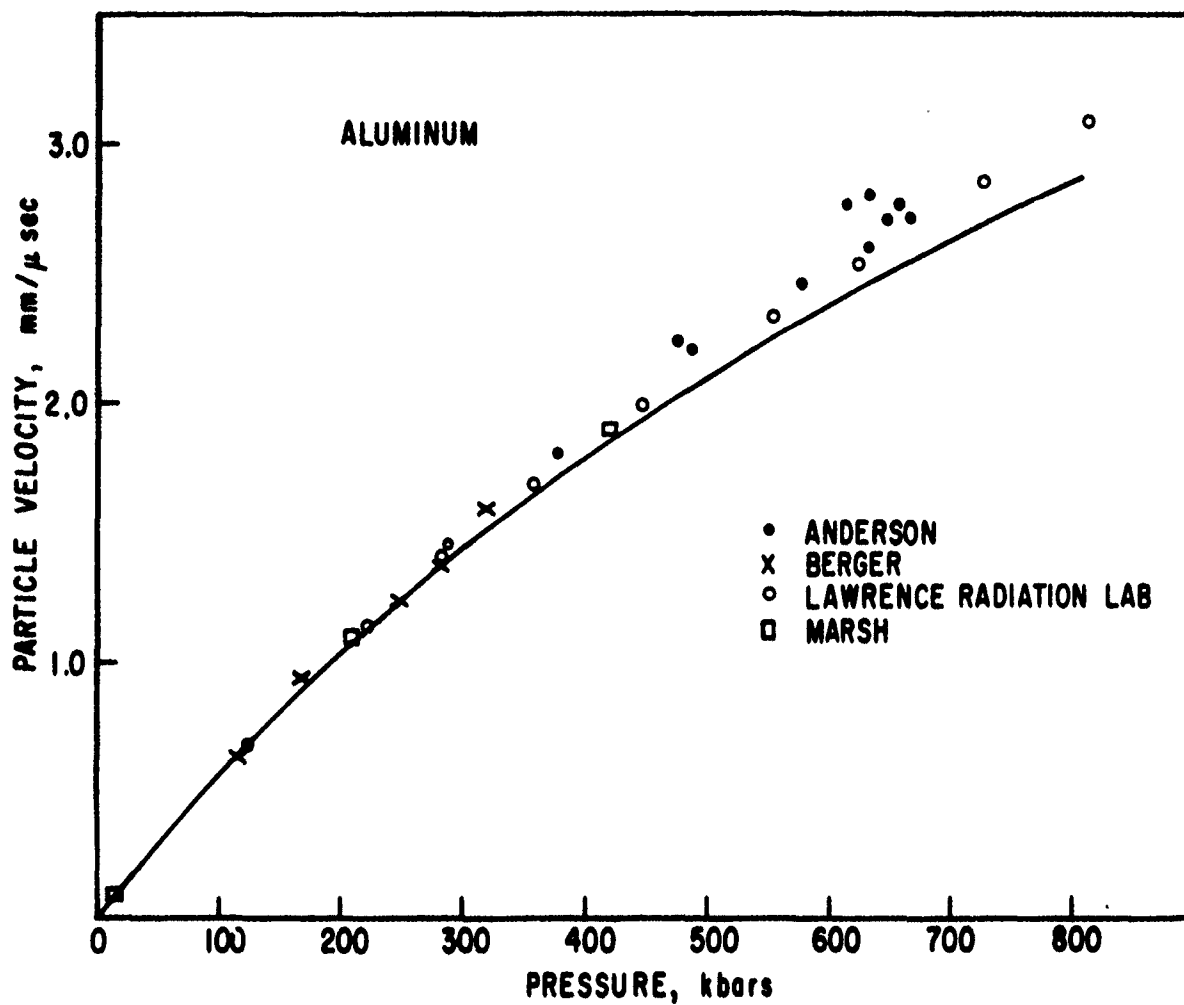


Figure 88. Particle Velocity Versus Pressure in Aluminum.

#### 4. Additional Thermodynamic Applications To the Equation of State

This last discussion on applications is to further illustrate some of the ways in which experimental ultrasonic and thermal data can be used to obtain many other thermodynamic parameters. Although some of these are not presently in wide use regarding thermodynamic studies on operational materials, it is expected that such refinements may be required as material characterization programs become more exact.

##### a. Debye Temperatures

One such parameter falling in the above class is the Debye temperature,  $\theta$ . Although this parameter is not generally considered in response physics as applied to present day technology, it is important in the fact that it indicates the temperature range in which mechanical and thermal properties such as the bulk modulus, expansion coefficient, and specific heat approach fairly constant behavior. It is also important in the physics of condensed states, because the classical theory of solids gives relationships between separate physical parameters in terms of  $\theta$  on which the pressure depends. The Debye temperature may be determined ultrasonically and expressed in terms of the corresponding rate of propagation of elastic oscillations by

$$\theta^3 = \frac{h}{k} \left( \frac{9N}{4\pi v} \right) \left[ \frac{1}{\left( \frac{2}{V_t^3} \right) + \left( \frac{1}{V_l^3} \right)} \right] \quad (71)$$

where  $N$  is Avogadro's number,  $v$  is the volume per mole, and  $V_l$  and  $V_t$  are the longitudinal and transverse velocities.

Ryabinin, et al. (Ref. 140) have expressed Equation (71) in terms of the bulk modulus,  $B^T$ , and the Poisson coefficient,  $\sigma$ , by

$$\theta = \frac{h}{k} \left( \frac{9N}{4\pi} \right)^{1/3} \frac{(B^T)^{1/2} V^{1/6}}{M^{1/2} f^{1/3}(\sigma)} \quad (72)$$

where  $M$  is the mass,  $f(\sigma)$  is the function of  $\sigma$ , and the other symbols have their usual significance. If the pressure and temperature dependence of the volume and Poisson coefficient are known, one could calculate the Debye temperature ultrasonically, and then use it to express the variation with the coefficient of expansion, melting point, or other physical parameters.

## b. Specific Heat at Constant Volume

Another quantity of significant interest is the specific heat at constant volume,  $c_v$ . As shown here and in Appendix I, this quantity can be calculated from the experimentally determined values of the specific heat at constant pressure, the expansion coefficient, and the bulk modulus. The pressure derivative of  $c_v$  may be expressed as

$$\left(\frac{\partial c_v}{\partial P}\right)_T = -Tv\beta^2 \left[ \frac{1}{\beta^3} \left(\frac{\partial \beta}{\partial T}\right)_P - \frac{2}{\beta \chi T} \left(\frac{\partial \chi}{\partial T}\right)_P - \frac{1}{\beta^2} \left(\frac{\partial \beta}{\partial T}\right)_P \right] \quad (73)$$

The difference in the heat capacities ( $c_p - c_v$ ), may be determined by subtracting Equation (73) from Equation (48) which gives the following expression:

$$\left[ \frac{\partial (c_p - c_v)}{\partial P} \right]_T = -Tv\beta^2 \left[ 1 + \frac{2}{\beta \chi T} \left(\frac{\partial \beta}{\partial T}\right)_P + \frac{1}{(\chi T)^2} \left(\frac{\partial \chi}{\partial P}\right)_T \right] \quad (74)$$

Therefore, to calculate the pressure derivative of ( $c_p - c_v$ ), one must know the dependence of the compressibility on pressure and the variation of the coefficient of expansion with temperature.

Heat capacity at constant volume data can be obtained from experimentally determined  $c_p$  data by the relation

$$c_v = c_p - \frac{T\beta^2 B}{\rho} \quad (75)$$

However, at low temperatures, the formula for the heat capacity as given by Equation (35) is more useful in estimating  $c_v$ , due to the difficulty of measuring  $\beta$  and  $B$  at very low temperatures.

## c. Volume Coefficient of Expansion

If the variation of the bulk modulus, density, and heat capacity with pressure is known at very low temperatures, the variation of the coefficient of expansion can be calculated from the thermal Grüneisen ratio (Eq. 36) because at these low temperatures  $\gamma$  is assumed to be constant and independent of pressure. Ryabinin, et al. (Ref. 141) have shown that the dependence of the coefficient of thermal expansion on pressure can also be calculated if the relationships  $v = v(P)$  and  $\theta = \theta(P)$  are known. Since the thermodynamic potential  $\phi$  is

$$\phi = \phi_0(P) + \theta f\left(\frac{T}{\theta}\right) \quad (76)$$

the volume is given by the relationship

$$V = \frac{\partial \Phi}{\partial P} = V_0(P) + \frac{\partial \theta}{\partial P} \left( f - \frac{T}{\theta} f' \right) \quad (77)$$

and the coefficient of expansion by

$$\beta = - \frac{T}{V\theta^2} \frac{d\theta}{P} \cdot f'' \quad (78)$$

In the above formulas, the quantities  $f'$  and  $f''$  are the first- and second-pressure derivatives, respectively, of the function  $f$  describing the functional dependence of the Debye temperature.

Thermal expansion data at high pressure presented by Ryabinin, et al. (Ref. 140) serves to illustrate that the expansion coefficient decreases with an increase in pressure. For pressures up to 30,000 kg/cm<sup>2</sup>, he measured the percent decrease in the expansion coefficient for iron, copper, and silver as 6.1, 10.4, and 16.4, respectively.

#### d. Entropy

The application of thermodynamic relations to changes in properties of solids as a function of temperature at constant pressure are illustrated in Appendix VII. Similar thermodynamic relationships may be derived to express property changes as a function of temperature and pressure, e.g., the variation of entropy,  $S$ , with pressure at constant temperature is given by

$$\left( \frac{\partial S}{\partial P} \right)_T = - \left( \frac{\partial V}{\partial T} \right)_P = - \beta V \quad (79)$$

whereas the entropy variation with volume is given as

$$\left( \frac{\partial S}{\partial V} \right)_T = \left( \frac{\partial P}{\partial T} \right)_V = \beta B^T \quad (80)$$

These equations illustrate the usefulness of thermal and ultrasonic data in obtaining these relationships.

If  $\beta$  is negative in the preceeding equations, i.e.,  $(\partial S/\partial P)_T > 0$  and  $(\partial S/\partial V)_T < 0$ , the entropy must necessarily increase with increasing pressure and decreasing volume. (Negative expansion coefficients are common for certain glasses, as well as pyrolytic graphite.) If  $\beta$  is positive, the entropy must

decrease with increasing pressure and decreasing volume. A decrease in entropy indicates the material is attaining a greater degree of order and the integration of Equation (79) at constant temperature gives the difference in entropy at pressure  $P$  and atmospheric pressure,  $P_o$ , by

$$(S_P - S_{P_o}) = - \int_{P_o}^P \left( \frac{\partial v}{\partial T} \right)_P dP = - \int_{P_o}^P \beta v dP \quad (81)$$

Therefore, from the variation of the coefficient of expansion with pressure, ( $\beta = a + dP$ ), and the variation of volume with pressure, the entropy can be calculated as a function of pressure.

#### e. Energy Relations

The variation of internal energy is given by  $dU = TdS - PdV$  where  $-PdV$  represents the work of compression and is dependent on the internal energy and the entropy changes. For an adiabatic compression, the work is dependent only on changes in the internal energy, and results in an increase in temperature. This temperature increase may be calculated by

$$dT = \frac{\beta v T}{c_p} dP \quad (82)$$

The variation of free energy,  $\Delta F$ , of a solid with pressure at constant temperature, increases with an increase in pressure, because  $\Delta F = - \int PdV$  (which is the work of compression sometimes defined as the Helmholtz free energy,  $A$ ). The latter is related to the Gibbs free energy,  $G$ , by  $G = A + PV$  or  $dG = VdP - SdT$ . Proper manipulation of thermodynamic equations shows that the variation of the Gibbs free energy with pressure, is expressed as

$$\left( \frac{\partial G}{\partial P} \right)_T = V = V_o (1 + \beta \Delta T) \quad (83)$$

which makes use of the volume and the volume coefficient of expansion as a function of temperature.

#### f. Fusion Temperatures

The Grüneisen ratio at the fusion temperature,  $\gamma_f$ , can be determined by the equation

$$\gamma_f = \frac{\beta_f B_f^T}{c_{v,f} \cdot \rho_f} = \frac{\beta_f B_f^S}{c_{p,f} \cdot \rho_f} \quad (84)$$

if all parameters are measured at the fusion temperature. Furthermore, the volume coefficient of expansion at fusion,  $\beta_f$ , may be approximated from

$$\beta_f = \beta_{(\text{solid})} - \beta_{(\text{liquid})} \quad (85)$$

The bulk modulus at fusion,  $B_f^s$ , could be obtained from ultrasonic measurements made close to the melting temperature, or approximated from the following relation

$$B_f^s = B_o^s \left[ 1 - n \beta (T_f - T_o) \right] \quad (86)$$

where temperatures are given in °C and the constant  $n$  obtained from

$$n = \frac{B^s}{\beta} \left( \frac{\partial \beta}{\partial P} \right)_T \quad (87)$$

varies from approximately 3 to 10 for most solids. Therefore, knowing  $B^s$ ,  $\beta$  and the dependence of the coefficient of expansion on pressure, the melting point at a different pressure could be derived as follows

$$\frac{T_f^P}{T_f^{P_o}} = \frac{v_f^P / B_f^{S,P}}{v_f^{P_o} / B_f^{S,P_o}} = \frac{v_{T_o}^P / B_{T_o}^{S,P}}{v_{T_o}^{P_o} / B_{T_o}^{S,P_o}} \cdot Z \quad (88)$$

where the superscripts  $P$  and  $P_o$  refer to some pressure-- $P$ , different from atmospheric pressure,  $P_o$ . The constant,  $Z$ , can be calculated if we know the variation of the volume and bulk modulus with temperature. Since  $v$  and  $B^s$  change very little with temperature, the error involved in using Equation (88) will be no greater than the error observed in determining the melting point under high pressure, which is approximately  $\pm 10$  percent (Ref. 147). By the use of Equation (88) and with the assumption that  $Z = 1$  (Ref. 135), Strong (Ref. 147), and Butuzov (Ref. 148) calculated the variation of melting point with pressure up to 30,000 kg/cm<sup>2</sup>. The difference between the experimental and theoretical results was 0.2 percent for aluminum while for iron it was 1.70 percent.

Since the Lindemann law (Ref. 142) equates the frequency,  $\omega_f$ , in terms of fusion parameters with an Einstein or Debye frequency corresponding to normal temperatures, a direct relationship between the Grüneisen and Lindemann theories may be established. If the Grüneisen ratio at fusion,  $\gamma_f$ , is evaluated

by its definition from the Debye frequency of a solid, the use of Lindemann's law and the Clapeyron equation permits one to express  $\gamma_f$  in terms of the bulk modulus, the volume change, and the heat of fusion,  $\Delta H_f$  (Ref. 143). In equation form this becomes

$$\gamma_f = \frac{1}{3} + \frac{1}{2} q B_f^T \frac{\Delta v}{\Delta H_f}$$

where

$$q = 1 + B_f^T \beta_f T_f \frac{\Delta v}{\Delta H_f} = 1 + \gamma_f c_{v,f} T_f \frac{\Delta v}{v_f \Delta H_f} \quad (89)$$

and Equation (89) gives a direct connection between the Lindemann and Grüneisen theories.

With  $q$  defined by Equation (89) the variation of the fusion temperature with pressure becomes

$$\frac{dT_f}{dP_f} = 2 \left( \gamma_f - \frac{1}{3} \right) T_f / q B_f^T \quad (90)$$

which permits the evaluation of the slope and curvature of a fusion curve as a function of  $\gamma_f$ . According to Gilvarry (Ref. 143), equation (90) signifies that if  $\gamma_f > \frac{1}{3}$ , and the fusion temperature,  $T_f$ , is an increasing function of the fusion pressure,  $P_f$ , then the fusion curve slope is in agreement with that proposed by Bridgman (Ref. 144). If  $\gamma_f = \frac{1}{3}$  at finite pressure, the fusion temperature rises to a maximum and then falls, as predicted by Tammann (Ref. 145). If  $\gamma_f \rightarrow \frac{1}{3}$  for large  $P_f$ , an asymptotic fusion temperature exists which is in accord with the hypothesis proposed by Schames (Ref. 146).

According to Bridgman (Ref. 144) the fusion curve for all substances is concave to the pressure axis; that is,  $d^2 T_f / dP_f^2$  is negative. Equation (90) then becomes

$$\frac{d^2 T_f}{dP_f^2} = - 2 \left( \gamma_f - \frac{1}{3} + \frac{d\gamma_f}{d \ln v_f} \right) T_f q^2 / B_f^T \quad (91)$$

if  $\gamma_f > \frac{1}{3}$  and  $\gamma_f - \frac{1}{3} \frac{d\gamma_f}{d \ln v_f} > 0$ .

## SECTION V

## CONCLUSIONS AND RECOMMENDATIONS

Some of the possible applications of ultrasonic and thermal investigations with respect to the determination of the high pressure and temperature regions of the equation of state of solids are related in this section. With regard to the ultrasonic approach, it is shown that it is extremely useful to measure the dependence of the acoustic velocities versus hydrostatic pressure at several temperatures. This would allow the determination of the pressure derivative of the adiabatic bulk modulus at several different temperatures. Section IV shows that the Murnaghan equation could then be used to estimate the high pressure equation of state at each temperature; thus, mapping out the complete PVT surface (neglecting phase changes). In principle, this approach could also yield estimations of dynamic quantities, such as the shock velocity-particle velocity curves and the Hugoniot.

A study should be made regarding the agreement obtained between the extrapolated ultrasonic pressure data and the shock data on several different materials, particularly the plastics and reinforced materials. This study might then allow an estimation of the magnitude of the second pressure derivative of the bulk modulus. However, every effort should be made to evaluate this quantity experimentally through ultrasonics or some other approach, since it may improve the agreement between the predicted and actual equation of state.

For the viscoelastic type materials a study should be made of the contributions of the imaginary to the real part of the elastic moduli. These contributions to the moduli could possibly be correlated with static and dynamic equation of state measurements to determine the effect of compressional or bulk viscosity on the high pressure equation of state. This approach would necessitate the measurements of longitudinal and shear wave attenuation coefficients over wide pressure and temperature changes, and likewise require a model to relate the complex moduli to the static and dynamic cases.

Another extremely important consideration is the effect of porosity on the agreement of the static (e.g., compressibility measurements), dynamic (such as shock wave determinations), and the ultrasonic equation of state determinations.



The effect of porosity is expected to be significantly enhanced for some of the reinforced materials. It will therefore be necessary to relate the data obtained in the three different techniques so that comparisons can be made between the three. For example, the differences in the high pressure equation of state presented here for aluminum oxide with regard to the shock and ultrasonic techniques are thought to arise from the differences in density of the specimens used in the two approaches.

With respect to thermal analyses, it is necessary to determine the temperature derivative of the thermal expansion coefficient with more precision. This could probably be accomplished through the employment of an optical technique to determine very small length changes with temperature. The temperature derivative,  $\frac{d\alpha}{dT}$ , is necessary to determine the temperature derivative of the Grüneisen ratio, and likewise to estimate the pressure dependence of the specific heat. For many of the reinforced materials, the thermal expansion coefficient is extremely small ( $\sim 10^{-6}$  to  $10^{-5}/^{\circ}\text{C}$ ) so that the differential technique used here does not yield good results. However, an optic technique should significantly improve the precision with which this quantity can be determined. Also, it may be worthwhile to establish a technique for determining the pressure derivatives of the thermal expansion and specific heat. These quantities, in addition to the pressure derivative of the bulk modulus, are necessary to calculate the pressure dependence of the Grüneisen ratio. Although they can be estimated through thermodynamic relations between the pressure and temperature derivatives, it would be advantageous to measure the pressure derivatives directly.

In conclusion, this report illustrates the use of thermal and ultrasonic data to obtain the high pressure equation of state. The proposed approach is expected to be particularly useful to shock wave investigations because it is nondestructive, relatively inexpensive, and rapid. In addition, the approach allows an easy determination of the complete pressure-volume-temperature equation of state.

## APPENDIX I

THE RELATIONSHIP BETWEEN THE BULK MODULUS AND THE ACOUSTIC  
VELOCITIES FOR TRANSVERSE ISOTROPIC MEDIA

In Reference 4 it was shown that the stress strain matrix for an elastic medium of arbitrary symmetry is

$$\begin{pmatrix} c_{11} & c_{12} & c_{13} & c_{14} & c_{15} & c_{16} \\ c_{21} & c_{22} & c_{23} & c_{24} & c_{25} & c_{26} \\ c_{31} & c_{32} & c_{33} & c_{34} & c_{35} & c_{36} \\ c_{41} & c_{42} & c_{43} & c_{44} & c_{45} & c_{46} \\ c_{51} & c_{52} & c_{53} & c_{54} & c_{55} & c_{56} \\ c_{61} & c_{62} & c_{63} & c_{64} & c_{65} & c_{66} \end{pmatrix} \quad (92)$$

In the case of complete isotropy all of the coefficients are zero except  $c_{11}$  and  $c_{12}$  and the matrix in Equation (92) becomes

$$\begin{pmatrix} c_{11} & c_{12} & c_{12} & 0 & 0 & 0 \\ c_{12} & c_{11} & c_{12} & 0 & 0 & 0 \\ c_{12} & c_{12} & c_{11} & 0 & 0 & 0 \\ 0 & 0 & 0 & \frac{c_{11} - c_{12}}{2} & 0 & 0 \\ 0 & 0 & 0 & 0 & \frac{c_{11} - c_{12}}{2} & 0 \\ 0 & 0 & 0 & 0 & 0 & \frac{c_{11} - c_{12}}{2} \end{pmatrix} \quad (93)$$

The relations between the stiffness constants and the Lamé constants  $\lambda$  and  $\mu$  are

$$c_{11} = \lambda + 2\mu$$

$$c_{12} = \lambda$$

For the case of isotropic symmetry the adiabatic bulk modulus is given as

$$B^S = \lambda^S + 2/3\mu$$

$$= \rho \left( v_l^2 - 4/3 v_t^2 \right) \quad (94)$$

The Grüneisen ratio then takes the simple thermodynamic form

$$\gamma = \frac{\beta B^S}{\rho c_p} \quad (95)$$

where  $\beta$  is the volume coefficient of thermal expansion and can be approximated by three times the linear expansion for isotropic materials. For nonisotropic materials both  $\beta$  and  $B^S$  represent different functions of the linear expansion and sound velocities, respectively.

For materials exhibiting transverse or hexagonal symmetry the appropriate stress strain matrix is (Ref. 5)

$$\begin{pmatrix} c_{11} & c_{12} & c_{13} & 0 & 0 & 0 \\ c_{12} & c_{11} & c_{13} & 0 & 0 & 0 \\ c_{13} & c_{13} & c_{33} & 0 & 0 & 0 \\ 0 & 0 & 0 & c_{44} & 0 & 0 \\ 0 & 0 & 0 & 0 & c_{44} & 0 \\ 0 & 0 & 0 & 0 & 0 & \frac{c_{11} - c_{12}}{2} \end{pmatrix} \quad (96)$$

There are thus 5 independent elastic stiffness coefficients. The equations of motion for displacements,  $u$ ,  $v$ ,  $w$  in the directions  $x$ ,  $y$ ,  $z$ , respectively, then become

$$\rho \frac{\partial^2 u}{\partial t^2} = \lambda_{11} \frac{\partial^2 u}{\partial s^2} + \lambda_{12} \frac{\partial^2 v}{\partial s^2} + \lambda_{13} \frac{\partial^2 w}{\partial s^2}$$

$$\rho \frac{\partial^2 v}{\partial t^2} = \lambda_{12} \frac{\partial^2 u}{\partial s^2} + \lambda_{22} \frac{\partial^2 v}{\partial s^2} + \lambda_{23} \frac{\partial^2 w}{\partial s^2} \quad (97)$$

$$\rho \frac{\partial^2 w}{\partial t^2} = \lambda_{13} \frac{\partial^2 u}{\partial s^2} + \lambda_{23} \frac{\partial^2 v}{\partial s^2} + \lambda_{33} \frac{\partial^2 w}{\partial s^2}$$

where  $s = lx + my + nz$ ,  $t$  is the time, and

$$\begin{aligned}
 \lambda_{11} &= l^2 c_{11} + m^2 \left( \frac{c_{11} - c_{12}}{2} \right) + n^2 c_{44} \\
 \lambda_{12} &= lm \left( \frac{c_{11} + c_{12}}{2} \right) \\
 \lambda_{13} &= nl (c_{13} + c_{44}) \\
 \lambda_{23} &= mn (c_{13} + c_{44}) \\
 \lambda_{22} &= l^2 \left( \frac{c_{11} - c_{12}}{2} \right) + m^2 c_{11} + n^2 c_{44} \\
 \lambda_{33} &= l^2 c_{44} + m^2 c_{44} + n^2 c_{33}
 \end{aligned} \tag{98}$$

( $l$ ,  $m$ , and  $n$  are the direction cosines of the normal to the plane wave.) The velocities corresponding to the three solutions of Equation (97) must satisfy a determinant of the form

$$\begin{vmatrix}
 \lambda_{11} - \rho V^2 & \lambda_{12} & \lambda_{13} \\
 \lambda_{12} & \lambda_{22} - \rho V^2 & \lambda_{23} \\
 \lambda_{13} & \lambda_{23} & \lambda_{33} - \rho V^2
 \end{vmatrix} = 0 \tag{99}$$

Substituting in the values of the  $\lambda_{ij}$  from Equation (98) gives

$$\begin{vmatrix}
 l^2 c_{11} + m^2 \left( \frac{c_{11} - c_{12}}{2} \right) + n^2 c_{44} - \rho V^2 & lm \left( \frac{c_{11} + c_{12}}{2} \right) & nl (c_{13} + c_{44}) \\
 lm \left( \frac{c_{11} + c_{12}}{2} \right) & l^2 \left( \frac{c_{11} - c_{12}}{2} \right) + m^2 c_{11} + n^2 c_{44} - \rho V^2 & mn (c_{13} + c_{44}) \\
 nl (c_{13} + c_{44}) & mn (c_{13} + c_{44}) & (l^2 + m^2) c_{44} - n^2 c_{33} - \rho V^2
 \end{vmatrix} = 0 \tag{100}$$

Let the axis perpendicular to the layers to be identified as the z-axis. Then waves transmitted along this direction ( $n = 1, l = m = 0$ ) have velocities

$$v_{l,z} = \sqrt{\frac{c_{33}}{\rho}}, \text{ displacement along the z-direction}$$

$$(v_{s,z})_x = \sqrt{\frac{c_{44}}{\rho}}, \text{ displacement in any direction in the z-plane}$$

Now, consider propagation along the x-direction (e.g.,  $l = 1, m = n = 0$ ). The three possible waves are

$$v_{l,x} = \sqrt{\frac{c_{11}}{\rho}}, \text{ displacement along x-direction}$$

$$(v_{s,x})_z = \sqrt{\frac{c_{44}}{\rho}}, \text{ displacement in z-direction}$$

$$(v_{s,x})_y = \sqrt{\frac{c_{11} - c_{12}}{2\rho}}, \text{ displacement in y-direction}$$

To determine the fifth constant, a wave is transmitted along an axis 45 degrees between the x- and z-directions, i.e.,  $l = n = \frac{1}{\sqrt{2}}, m = 0$ . The two solutions of Equation (100) are then

$$(v_{s,45})_y = \frac{c_{11} - c_{12} + c_{44}}{4\rho}, \text{ displacement in y-direction}$$

$$v_{l,45} = \sqrt{\frac{\frac{c_{11} + c_{33} + 2c_{44}}{2} + \sqrt{\left(\frac{c_{11} - c_{33}}{2}\right)^2 + (c_{13} + c_{44})^2}}{2\rho}}$$

where the particle velocity for the last wave velocity has the direction cosine

$$\alpha = \gamma \left[ \frac{c_{11} - c_{33}}{2(c_{13} + c_{44})} + \sqrt{1 + \left(\frac{c_{11} - c_{33}}{2(c_{13} + c_{44})}\right)^2} \right]$$

where the displacement  $\xi$  has components

$$\xi = \alpha\mu + \beta v + \gamma w$$

Hence, measurements of  $v_{l,x}$ ,  $v_{l,z}$ ,  $v_{l,45}$ ,  $(v_{s,z})_x$ , and  $(v_{s,x})_y$  allow a determination of all five constants. For arbitrary angle of incidence with the z-axis the longitudinal velocity is given as

$$\begin{aligned}
2\rho V_{l,\phi}^2 = & c_{11} \sin^2 \phi + c_{33} \cos^2 \phi + c_{44} \\
& + \left\{ \left[ (c_{11} - c_{44}) \sin^2 \phi - (c_{33} - c_{44}) \cos^2 \phi \right]^2 \right. \\
& \left. + 4 \sin^2 \phi \cos^2 \phi (c_{13} + c_{44})^2 \right\}^{1/2}
\end{aligned} \quad (101)$$

where  $\phi$  is the angle between the direction of propagation and the z-axis. The five elastic constants corresponding to the symmetry condition of transverse isotropy can then be obtained through Equation (96).

The matrix specifying the strains as functions of the stress is similar to the  $6 \times 6$  matrix in Equation (92), except that the entries are the adiabatic compliance coefficients  $s_{ij}$ . The adiabatic compressibility of a solid is defined as

$$\chi^s = - \frac{1}{v} \left( \frac{\partial v}{\partial P} \right)_s \quad (102)$$

where  $v$  is the specific volume and  $P$  is the pressure. In terms of the compliance coefficients the general formula for arbitrary symmetry is

$$\chi_s = s_{11} + s_{22} + s_{33} + 2 (s_{12} + s_{13} + s_{23}) \quad (103)$$

The adiabatic bulk modulus is defined as

$$\begin{aligned}
B^s &= - v \left( \frac{\partial P}{\partial v} \right)_s \\
&= \frac{1}{\chi^s} \\
&= \frac{1}{s_{11} + s_{22} + s_{33} + 2(s_{12} + s_{13} + s_{23})} \quad (104)
\end{aligned}$$

Therefore, the bulk modulus can be obtained for any specimen of arbitrary symmetry by using the values of  $\rho V^2$  to solve for the stiffness coefficients  $c_{ij}$ , inverting the matrix (Equation (92)) to obtain the compliance coefficients  $s_{ij}$  and using Equation (104). For transverse isotropy the resulting expression for the adiabatic bulk modulus is

$$B^s = \frac{(c_{11} + c_{12})c_{33} - 2c_{13}^2}{c_{11} + c_{12} + 2c_{33} - 4c_{13}} \quad (105)$$

Because of the radical in the third relation in Equation (101) there is some ambiguity associated with the proper choice of the plus or minus sign, and hence, in the value of  $c_{13}$  in the case of crystals. The correct choice is determined by lattice stability conditions. For a solid to be stable, the elastic stress should have a minimum at zero stress. As Alers and Neighbours show, (Ref. 38), the criterion is satisfied if all the principal minor determinants of the matrix (Eq. (92)) are positive. For hexagonal symmetry or transverse isotropy they show that the following equalities must hold

$$\begin{aligned} c_{11}^2 - c_{12}^2 &> 0 \\ c_{33}(c_{11} + c_{12}) - 2c_{13}^2 &> 0 \\ c_{11}c_{33} - c_{13}^2 &> 0 \end{aligned} \quad (106)$$

These conditions allow the correct determination of  $c_{13}$  in metals satisfying this symmetry class. However, for the layered structures considered here, it is advantageous to check these criteria by comparing the results obtained through their use with results obtained in other experiments. For example, to predict the high pressure equation of state from ultrasonic measurements, it is necessary to know the bulk modulus. The resulting extrapolated equation of state can be compared with the dynamic measurements to determine the proper value of the bulk modulus, and hence, to check the inequality relations. The outlined method then provides a way of calculating the Grüneisen ratio in Equation (95), when the volume coefficient of expansion is properly determined.

As mentioned in Section IV, paragraph 1, the values of the volume coefficient of expansion and the bulk modulus cannot simply be inserted into Equation (95) to calculate the Grüneisen ratio in anisotropic materials. Instead, as Key shows (Ref. 150), the Grüneisen ratio must be considered a tensor. Key gives a derivation of the tensor relations for various symmetry classes. A somewhat different approach will be used to derive the tensor relationship for transverse isotropy.

Equation (95) can be written as

$$\begin{aligned} \gamma &= \frac{\beta B^T}{\rho c_V} \\ &= \frac{1}{\rho c_V} \left( \frac{\partial P}{\partial T} \right)_V \end{aligned} \quad (107)$$

since

$$\beta B^T = \left[ \frac{1}{V} \left( \frac{\partial V}{\partial T} \right)_P \right] \left[ -V \frac{\partial P}{\partial V} T \right] = \left( \frac{\partial P}{\partial T} \right)_V$$

Generalizing Equation (107) gives matrix elements of the Grüneisen ratio as

$$\gamma_{ij} = \frac{1}{\rho c_V} \left( \frac{\partial \sigma_{ij}}{\partial T} \right)_V \quad (108)$$

where the stress matrix for transverse isotropy is given in Equation (94).

In Equation (108), the volume of the reference condition is to be held constant so that the dilatational strains from equilibrium are zero. The coefficient  $\gamma_{xx}$  can be computed from Equation (108) as

$$\gamma_{xx} = \frac{1}{\rho c_V} \left( \frac{\partial \sigma_{xx}}{\partial T} \right)_{\epsilon_{xx} = 0} \quad (109)$$

$\sigma_{xx}$  is given from Equation (96) as

$$\sigma_{xx} = c_{11} \epsilon_{xx} + c_{12} \epsilon_{yy} + c_{13} \epsilon_{zz} \quad (110)$$

By virtue of Equation (107) the stiffness coefficients in Equation (110) are isothermal. Equation (109) for the 11 matrix element of  $\gamma$  then becomes at zero strain

$$\gamma_{xx} = \frac{1}{\rho c_V} \left[ \frac{\partial}{\partial T} (c_{11} \epsilon_{xx} + c_{12} \epsilon_{yy} + c_{13} \epsilon_{zz}) \right]_{\epsilon = 0} \quad (111)$$

or

$$\gamma_{xx} = \frac{1}{\rho c_V} \left[ c_{11} \frac{\partial \epsilon_{xx}}{\partial T} + c_{12} \frac{\partial \epsilon_{yy}}{\partial T} + c_{13} \frac{\partial \epsilon_{zz}}{\partial T} \right]_{\epsilon = 0} \quad (112)$$

But from the generalized definition of the expansion coefficients (Ref. 39)

$$\alpha_{ij} = \left( \frac{\partial \epsilon_{ij}}{\partial T} \right)_{\epsilon = 0} \quad (113)$$



so that Equation (112) becomes

$$\begin{aligned}\gamma_{xx} &= \frac{1}{\rho c_V} \left[ c_{11} \alpha_{xx} + c_{12} \alpha_{yy} + c_{13} \alpha_{zz} \right] \\ &= \frac{1}{\rho c_V} \left[ c_{11} \alpha_{11} + c_{12} \alpha_{11} + c_{13} \alpha_{33} \right]\end{aligned}\quad (114)$$

Similarly,

$$\begin{aligned}\gamma_{yy} &= \gamma_{xx} \\ \gamma_{zz} &= \frac{1}{\rho c_V} \left[ 2c_{13} \alpha_{11} + c_{33} \alpha_{33} \right]\end{aligned}\quad (115)$$

Since the thermal expansion matrix for transverse isotropy is diagonal in the principal axes, the off-diagonal components for the Grüneisen tensor are zero. Therefore, the complete matrix for transverse isotropy is

$$\begin{bmatrix} \gamma_{11} & \gamma_{12} & \gamma_{13} \\ \gamma_{21} & \gamma_{22} & \gamma_{23} \\ \gamma_{31} & \gamma_{32} & \gamma_{33} \end{bmatrix} = \begin{bmatrix} \gamma_{xx} & 0 & 0 \\ 0 & \gamma_{xx} & 0 \\ 0 & 0 & \gamma_{zz} \end{bmatrix}\quad (116)$$

and the spherical component is

$$\gamma = \frac{1}{3} (2\gamma_{xx} + \gamma_{zz})\quad (117)$$

Key (Ref. 150) gives the conversion from the specific heat at constant pressure to that at constant volume for transverse isotropy as

$$c_V = c_P - \frac{T}{\rho} \left[ 2\alpha_{11}^2 (c_{11} + c_{12}) + 4\alpha_{11} \alpha_{33} c_{13} + \alpha_{33}^2 c_{33} \right]\quad (118)$$

where the  $c_{ij}$  are the isothermal constants. He also gives the conversion from the adiabatic compliance coefficients  $s_{ij}$  to the isothermal ones as

$$\begin{aligned}
 s_{11}^T &= s_{11}^s + \frac{\alpha_{11}^2 T}{\rho c_p} \\
 s_{12}^T &= s_{12}^s + \frac{\alpha_{11}^2 T}{\rho c_p} \\
 s_{13}^T &= s_{13}^s + \frac{\alpha_{11} \alpha_{33} T}{\rho c_p} \\
 s_{33}^T &= s_{33}^s + \frac{\alpha_{33}^2 T}{\rho c_p}
 \end{aligned} \tag{119}$$

In Equations (118) and (119),  $\alpha_{11}$  and  $\alpha_{33}$  correspond to  $\alpha_{\perp}$  and  $\alpha_{||}$ , respectively as used earlier.

Once the adiabatic stiffness coefficient matrix is obtained through the equations presented earlier in this appendix, the matrix is inverted to find the adiabatic compliance matrix. Relations in Equation (119) are then applied to find the isothermal compliance matrix (the only other coefficient needed for transverse isotropy is  $s_{44}^T$  which is equal to  $s_{44}^s$ ), and this matrix is then inverted to obtain the isothermal stiffness coefficients needed in Equations (114), (115), and (118).

This method then allows the determination of the Grüneisen tensor for materials which are not isotropic.

## APPENDIX II

## DERIVATION OF THE MURNAGHAN EQUATION

The Murnaghan logarithmic equation, as normally used, is based upon the linearity of the bulk modulus with pressure. This equation is generally derived through the definition of the isothermal bulk modulus, defined as

$$B^T(P) = -v(P) \left( \frac{\partial P}{\partial v(P)} \right)_T \quad (120)$$

If the bulk modulus is linear with pressure, Equation (120) can be written as

$$-v \left( \frac{\partial P}{\partial v} \right)_T = B_o^T + B_{oT}^{T'} P \quad (121)$$

which upon integrating between the limits  $v_o$  and  $v$  and  $P_o$  and  $P$  becomes

$$- \int_{v_o}^v \frac{dv}{v} = \int_{P_o}^P \frac{dP}{B_o^T + B_{oT}^{T'} P}$$

which on integration, yields

$$\ln \left( \frac{v_o}{v} \right) = \frac{1}{B_{oT}^{T'}} \ln \left[ \frac{B_o^T + B_{oT}^{T'} P}{B_o^T + B_{oT}^{T'} P_o} \right] \quad (122)$$

Since  $P_o$  is approximately 1 bar, Equation (122) can be written to a good approximation as

$$\ln \frac{v_o}{v} = \frac{\ln}{B_{oT}^{T'}} \left[ 1 + B_{oT}^{T'} \left( \frac{P}{B_o^T} \right) \right]$$

$$\frac{\rho}{\rho_o} = \left[ B_{oT}^{T'} \left( \frac{P}{B_o^T} \right) + 1 \right]^{\frac{1}{B_{oT}^{T'}}} \quad (123)$$

Equation (123) can then be used to estimate the hydrostat to pressures beyond the range of experimental investigation providing that (1) the bulk modulus is linear in pressure, (2) that no phase changes exist over the extrapolated pressure range, and (3) that the isothermal bulk modulus and its pressure derivative at constant temperature are precisely evaluated at atmospheric pressure. Isothermal compression experiments yield one method of determining  $B_o^T$  and  $B_{oT}^{T'}$ . However, the pressure derivative is found only by differentiating a curve fitted to the pressure dependence of the change in volume. Hence, the accuracy with which  $B_{oT}^{T'}$  can be determined suffers with this method. A much more accurate way of determining the bulk modulus and its isothermal pressure derivative is through the determination of the adiabatic sound velocities versus pressure. Although this technique yields the adiabatic bulk modulus and its isothermal derivative, the data are easily converted as follows. The isothermal modulus is given in terms of the adiabatic modulus as

$$B^T(P, T) = \frac{B^S(P, T)}{1 + \beta \gamma T} \quad (124)$$

where  $\beta$  is the volume coefficient of expansion,  $\gamma$  is the Grüneisen ratio, and  $T$  is the absolute temperature. The pressure derivative of the adiabatic bulk modulus at constant temperature is easily obtained for an isotropic medium. From the definition of the bulk modulus for an isotropic medium,

$$B^S = \rho \left[ v_\ell^2 - \frac{4}{3} v_t^2 \right] \quad (125)$$

Differentiating Equation (125) at constant temperature yields

$$\left( \frac{\partial B^S}{\partial P} \right)_T = 2\rho \left[ v_\ell v'_\ell - \frac{4}{3} v_t v'_t \right]_T + \left[ v_\ell^2 - \frac{4}{3} v_t^2 \right]_T \left( \frac{\partial \rho}{\partial P} \right)_T \quad (126)$$

The isothermal bulk modulus is defined as

$$B^T = -v \left( \frac{\partial P}{\partial v} \right)_T = \rho \left( \frac{\partial P}{\partial \rho} \right)_T \quad (127)$$

so that by Equations (124) and (127), Equation (126) evaluated at  $P=0$  becomes

$$B_{oT}^{S'} = 2\rho_o \left[ v_\ell v'_\ell - \frac{4}{3} v_t v'_t \right]_{P=0} + (1 + \beta \gamma T) \quad (128)$$

$B_{oT}^{S'}$  is the quantity normally measured in ultrasonic-pressure measurements.

Anderson (Ref. 23) shows that the conversion to the isothermal pressure derivative of the isothermal bulk modulus is given as follows

$$B_{OT}^{T'} = B_{OT}^{S'} + \beta \gamma T \left( \frac{B_O^T}{B_O^S} \right) \left[ 1 - \frac{2}{\beta B_O^T} \left( \frac{\partial B_O^T}{\partial T} \right)_P - 2B_{OT}^{S'} \right] + \left[ \beta \gamma T \left( \frac{B_O^T}{B_O^S} \right) \right]^2 \left[ B_{OT}^{S'} - 1 - \frac{1}{\beta^2} \left( \frac{\partial \beta}{\partial T} \right)_P \right] \quad (129)$$

where the temperature derivative of  $B_O^T$  is obtained from the temperature derivative of  $B_O^S$  by differentiating Equation (124) with respect to temperature

$$\begin{aligned} \left( \frac{\partial B_O^T}{\partial T} \right)_P &= \frac{\partial}{\partial T} \left( \frac{B_O^S}{1 + \beta \gamma T} \right)_P \\ &= \frac{\left( \frac{\partial B_O^S}{\partial T} \right)_P}{1 + \beta \gamma T} - \frac{B_O^S \beta \gamma}{(1 + \beta \gamma T)^2} - \frac{B_O^S \gamma T \left( \frac{\partial \beta}{\partial T} \right)_P}{(1 + \beta \gamma T)^2} - \frac{B_O^S \partial T \left( \frac{\partial \gamma}{\partial T} \right)_P}{(1 + \beta \gamma T)^2} \end{aligned} \quad (130)$$

All of the quantities appearing on the right in Equations (129) and (130) can hence be determined through thermal or ultrasonic experiments.

Frequently, it is desirable to estimate the high pressure equation of state as determined normally by dynamic techniques. While the Murnaghan equation is still applicable, a better approximation to dynamic data is obtained by using the adiabatic bulk modulus and its adiabatic pressure derivative. The applicable formulas in this instance are

$$\frac{\rho}{\rho_O} = \left[ B_{OS}^{S'} \left( \frac{P}{B_O^S} \right) + 1 \right]^{\frac{1}{B_{OS}^{S'}}} \quad (131)$$

The quantity  $B_{OS}^{S'}$  can be determined from the ultrasonically determined pressure derivative of the adiabatic bulk modulus,  $B_{OT}^{S'}$ , by writing

$$\begin{aligned} B^S &= B^S(P, T) \\ dB^S &= \left( \frac{\partial B^S}{\partial P} \right)_T dP + \left( \frac{\partial B^S}{\partial T} \right)_P dT \\ \left( \frac{dB^S}{dP} \right)_S &= \left( \frac{\partial B^S}{\partial P} \right)_T + \left( \frac{\partial B^S}{\partial T} \right)_P \left( \frac{dT}{dP} \right)_S \end{aligned}$$

Or at atmospheric pressure

$$B_{os}^{s'} = B_{oT}^{s'} + \left( \frac{\partial B^s}{\partial T} \right)_o \left( \frac{dT}{dP} \right)_s \quad (132)$$

Thurston (Ref. 39) gives the quantity  $\left( \frac{\partial T}{\partial P} \right)_s$  as

$$\left( \frac{dT}{dP} \right)_s = \frac{T\beta}{\rho c_p} \quad (133)$$

or by the definition of the Grüneisen ratio

$$\gamma = \frac{\beta B^s}{\rho c_p} \quad (134)$$

$$\left( \frac{dT}{dP} \right)_s = \frac{T}{B^s} \gamma \quad (135)$$

so that Equation (132) becomes

$$\begin{aligned} B_{os}^{s'} &= B_{oT}^{s'} + \left( \frac{\partial B^s}{\partial T} \right)_P \frac{T\gamma}{B^s} \\ &= B_{oT}^{s'} + \gamma \frac{\partial \ln B^s}{\partial \ln T} \end{aligned} \quad (136)$$

where, as previously mentioned,  $B_{oT}^{s'}$  is the ultrasonic pressure derivative of the adiabatic bulk modulus at atmospheric pressure and constant temperature.

The technique outlined here is not restricted to cases in which the bulk modulus is linear in pressure. If the ultrasonic data are of sufficient precision to allow a determination of the second derivative of the bulk modulus, a corresponding higher order expression can be defined as follows. From the definition of either the isothermal or adiabatic modulus

$$\begin{aligned} B(v, P) &= -v \left( \frac{\partial P}{\partial v} \right) \\ &= B_o + B_o' P + \frac{1}{2} B_o'' P^2 \end{aligned} \quad (137)$$

where either the adiabatic or the isothermal moduli and their derivatives are to be used in Equation (137), depending on the desired application. Integrating

Equation (137) between the limits  $v_0$  and  $v$ , and  $P=0$  and  $P$  gives

$$\frac{\rho}{\rho_0} = \left[ \frac{1 + aP}{1 + bP} \right]^{\frac{1}{c}} \quad (138)$$

where

$$a = \frac{B'_0}{B'_0 - c}$$

$$b = \frac{B''_0}{B'_0 + c}$$

$$c = \sqrt{B'^2_0 - 2B'_0 B''_0}$$

Equation (138) may be more appropriate to equation of state of solids, especially plastics which generally exhibit low bulk moduli.

## APPENDIX III

ESTIMATION OF THE PRESSURE DERIVATIVE  
OF THE GRÜNEISEN RATIO

One way to obtain the pressure dependence of the Grüneisen ratio is to use hydrostatic pressure to measure the pressure dependence of the various quantities in the Grüneisen formula

$$\gamma = \frac{\beta B^S}{\rho c_p} \quad (139)$$

The quantity  $B^S/\rho$  can easily be determined experimentally by using an ultrasonic approach as shown in the text. However, the experimental determinations of the pressure derivatives of the volume coefficient of expansion and the specific heat are difficult at high pressure. This Appendix outlines a technique for estimating the pressure derivative of the Grüneisen ratio. In the following it is assumed that the material is isotropic, and that no phase changes occur over the pressure range of interest.

Thurston (Ref. 40) shows that the pressure derivatives of  $\beta$  and  $c_p$  at constant temperature are related to the mechanical properties of an isotropic solid as

$$\begin{aligned} \left(\frac{\partial \beta}{\partial P}\right)_T &= - \left(\frac{\partial \chi^T}{\partial T}\right) \\ &= \frac{1}{(B^T)^2} \left(\frac{\partial B^T}{\partial T}\right)_P \end{aligned} \quad (140)$$

$$\left(\frac{\partial c_p}{\partial P}\right)_T = - \frac{T}{\rho} \left[ \left(\frac{\partial \beta}{\partial T}\right)_P + \beta^2 \right] \quad (141)$$

where the superscript T refers to the isothermal moduli and the temperature T is absolute. If one has the means of measuring the temperature dependence of the bulk modulus and the expansion coefficient, Equations (140) and (141) allow an estimation of the pressure derivatives of  $\beta$  and  $c_p$ .



Consider the derivative of Equation (139) with respect to pressure and at constant temperature,

$$\begin{aligned} \left(\frac{\partial \gamma}{\partial P}\right)_T &= \frac{\partial \gamma}{\partial \rho} \left(\frac{\partial \rho}{\partial P}\right)_T + \frac{\partial \gamma}{\partial c_P} \left(\frac{\partial c_P}{\partial P}\right)_T + \frac{\partial \gamma}{\partial \beta} \left(\frac{\partial \beta}{\partial P}\right)_T + \frac{\partial \gamma}{\partial B^S} \left(\frac{\partial B^S}{\partial P}\right)_T \\ &= -\frac{\beta B^S}{\rho^2 c_P} \left(\frac{\partial \rho}{\partial P}\right)_T - \frac{\beta B^S}{\rho c_P^2} \left(\frac{\partial c_P}{\partial P}\right)_T + \frac{B^S}{\rho c_P} \left(\frac{\partial \beta}{\partial P}\right)_T + \frac{\beta}{\rho c_P} \left(\frac{\partial B^S}{\partial P}\right)_T \end{aligned} \quad (142)$$

The quantity  $\left(\frac{\partial \rho}{\partial P}\right)_T$  can be reduced as follows.

$$\rho = \frac{1}{v}, \text{ where } v \text{ is the specific volume.}$$

So that

$$\left(\frac{\partial \rho}{\partial P}\right)_T = -\frac{1}{v^2} \left(\frac{\partial v}{\partial P}\right)_T \quad (143)$$

From the definition of the isothermal compressibility

$$\begin{aligned} \chi^T &\equiv -\frac{1}{v} \left(\frac{\partial v}{\partial P}\right)_T \\ &= \frac{1}{B^T} \end{aligned} \quad (144)$$

Equation (143) can be written as

$$\left(\frac{\partial \rho}{\partial P}\right)_T = \frac{\rho}{B^T}$$

Using the defining Equation (139) for the Grüneisen ratio, Equation (142) at atmospheric pressure can then be expressed as

$$\left(\frac{\partial \gamma}{\partial P}\right)_{O,T} = \gamma_O \left[ -\frac{1}{B_O^T} - \frac{1}{c_P} \left(\frac{\partial c_P}{\partial P}\right)_{O,T} + \frac{1}{\beta} \left(\frac{\partial \beta}{\partial P}\right)_{O,T} + \frac{1}{B_O^S} \left(\frac{\partial B^S}{\partial P}\right)_{O,T} \right] \quad (145)$$

As previously illustrated, the adiabatic bulk modulus,  $B_O^S$ , can be determined ultrasonically to within 1 percent in metals. The isothermal bulk modulus at atmospheric pressure,  $B_O^T$ , can thus be deduced through the following relation,

$$B_O^T = B_O^S / (1 + \beta \gamma T) \quad (146)$$

Also, the pressure derivative  $\left(\frac{\partial B^S}{\partial P}\right)_{0,T}$  can be determined ultrasonically or estimated fairly accurately through the Dugdale-MacDonald relation (Appendix II). Therefore, if one uses Equations (140) and (141) to estimate the derivatives of  $\beta$  and  $c_p$ , an estimation of the pressure dependence of  $\gamma$  can be obtained.

Generally, the bulk modulus is linear in pressure, as are the temperature derivatives of the bulk modulus and expansion coefficient. Furthermore, it is expected that the dependence of the Grüneisen ratio with pressure is small, so that the determination of the various quantities at atmospheric pressure on the right side in Equation (145) represent the derivative of  $\gamma$  for all pressures (excepting phase changes).\*

As an example, the ultrasonic and thermal data reported here are used to estimate the Grüneisen ratio in 6061-T6 Al at 100 kbars. The quantities required in Equation (145) are given in the text as

$$\begin{aligned}\gamma_0 &= 2.06 \\ B_0^S &= 7.51 \times 10^{11} \text{ dynes/cm}^2 \\ B_0^T &= 7.19 \times 10^{11} \text{ dynes/cm}^2 \\ \left(\frac{\partial B^S}{\partial T}\right)_P &= -1.70 \times 10^8 \text{ dynes/cm}^2\text{°C} \\ \left(\frac{\partial B^T}{\partial T}\right)_P &= -3.04 \times 10^8 \text{ dynes/cm}^2\text{°C} \\ c_p &= 0.22 \text{ cal/gm}^\circ\text{C} = 9.21 \times 10^6 \text{ ergs/gm}^\circ\text{C} \\ \beta &= 6.9 \times 10^{-5}/^\circ\text{C} \\ \left(\frac{\partial \beta}{\partial T}\right)_P &= 9 \times 10^{-8}/^\circ\text{C}^2\end{aligned}$$

From the Dugdale-MacDonald relation

$$\left(\frac{\partial B^S}{\partial P}\right)_{0,T} \approx 5.1$$

---

\*It is not necessary to make this assumption if the pressure derivatives in Equation (145) are determined experimentally over the pressure range of interest.

From Equations (140) and (141)

$$\left(\frac{\partial c_p}{\partial P}\right)_{o,T} = 1.05 \times 10^{-5} \text{ cm}^3/\text{gm}^\circ\text{C}$$

$$\left(\frac{\partial \beta}{\partial P}\right)_{o,T} = 5.88 \times 10^{-16} \text{ cm}^2/\text{dyne}^\circ\text{C}$$

All of the above calculations correspond to 300°K. Then by Equation (145)

$\left(\frac{\partial \gamma}{\partial P}\right)_T$  is given as

$$\left(\frac{\partial \gamma}{\partial P}\right)_T = -3.7 \times 10^{-12} \text{ cm}^2/\text{dynes}$$

$$= -3.7 \times 10^{-3}/\text{kbar}$$

Therefore, the Grüneisen ratio at 100 kbars in 6061-T6 Al is estimated as

$$\gamma_{100} = \gamma_o + \left(\frac{\partial \gamma}{\partial P}\right)_{o,T} P$$

$$\approx 2.14 - 3.7 \times 10^{-1}$$

$$\approx 1.77$$

which is approximately a 17 percent decrease in this value over that at atmospheric pressure.

The foregoing analysis allows an estimation of the pressure derivative of  $\gamma$  when thermal and ultrasonic data at atmospheric pressure are available.

Equation (145) for  $\gamma'$  can be put in a form more suitable in using experimental data by referring to the definition of the temperature derivative of  $\gamma$ .

$$\begin{aligned} \left(\frac{\partial \gamma}{\partial T}\right)_P &= \frac{\partial \gamma}{\partial \rho} \left(\frac{\partial \rho}{\partial T}\right)_P + \frac{\partial \gamma}{\partial B^S} \left(\frac{\partial B^S}{\partial T}\right)_P + \frac{\partial \gamma}{\partial \beta} \left(\frac{\partial \beta}{\partial T}\right)_P + \frac{\partial \gamma}{\partial c_p} \left(\frac{\partial c_p}{\partial T}\right)_P \\ &= \gamma \left[ \frac{1}{\beta} \left(\frac{\partial \beta}{\partial T}\right)_P + \frac{1}{B^S} \left(\frac{\partial B^S}{\partial T}\right)_P + \beta - \frac{1}{c_p} \left(\frac{\partial c_p}{\partial T}\right)_P \right] \\ &= \gamma \left[ \frac{1}{\beta} \left\{ \left(\frac{\partial \beta}{\partial T}\right)_P + \beta^2 \right\} + \frac{1}{B^S} \left(\frac{\partial B^S}{\partial T}\right)_P - \frac{1}{c_p} \left(\frac{\partial c_p}{\partial T}\right)_P \right] \end{aligned} \quad (147)$$

Then by Equations (140) and (141), Equation (145) for the pressure derivative of  $\gamma$  becomes

$$\left(\frac{\partial \gamma}{\partial P}\right)_T = \frac{\gamma}{B^s} \left[ \left(\frac{\partial B^s}{\partial P}\right)_T + \left(\frac{1 + \beta \gamma T}{\beta B^s}\right) \left(\frac{\partial B^s}{\partial T}\right)_P - 1 - \gamma - T \left(\frac{\partial \gamma}{\partial T}\right)_P \right] \quad (148)$$

Since all of the quantities in Equation (148) are normally determined experimentally, except perhaps  $\frac{\partial B^s}{\partial P}$ , this relation allows a more convenient estimation of  $\gamma'$ .

## APPENDIX IV

THE USE OF THE MURNAGHAN EQUATION IN  
ESTIMATING THE SHOCK AND PARTICLE  
VELOCITIES AT HIGH PRESSURE

The shock velocity and particle velocity are calculated as a function of pressure in this section by assuming that the Murnaghan logarithmic equation represents the equation of state of the material under investigation. The resulting equations are expressed in terms of quantities which can be determined at the low pressure region (to 10 kbars) by ultrasonic techniques. However, the derivation relies upon the absence of phase transition in the pressure range of interest to which the extrapolation will be carried.

In Appendix II the Murnaghan equation representing adiabatic conditions was expressed as

$$\ln \left( \frac{v_o}{v} \right) = \frac{1}{B_{os}^{s'}} \ln \left[ B_{os}^{s'} \left( \frac{P}{B_o^s} \right) + 1 \right] \quad (149)$$

In the present case, it is assumed that the shock conditions are more closely approximated by the adiabat rather than the isothermal. For hydrodynamic flow the continuity equations for mass and momentum are

$$\rho (U_s - u_p) = \rho_o U_s \quad (150)$$

$$P - P_o = \rho_o u_p U_s$$

where  $U_s(P)$  is the shock velocity at pressure  $P$ , and  $\rho$  and  $u_p$  correspond to the density and particle velocity, respectively.  $P_o$  and  $\rho_o$  are the initial pressure and density.

Solving these two equations for  $U_s$  and  $u_p$  yields

$$U_s(P) = \left[ \frac{\rho}{\rho_o} \cdot \frac{(P - P_o)}{(\rho - \rho_o)} \right]^{1/2} \quad (151)$$

$$u_p(P) = \left[ \frac{\rho - \rho_o}{\rho} \right] U_s \quad (152)$$

Substituting in Equation (150) for the density and dropping  $P_0$  gives Shock Velocity:

$$U_s(P) = \left[ \frac{a \cdot P \times 10^9}{b \cdot \rho_0} \right]^{1/2} \quad (153)$$

Particle Velocity:

$$u_p(P) = \left[ \frac{b \cdot P \times 10^9}{a \cdot \rho_0} \right]^{1/2} \quad (154)$$

where

$$a = \left[ B_{os}^{s'} \left( \frac{P}{B_o^s} \right) + 1 \right]^{\frac{1}{B_{os}^{s'}}}$$

$$b = a - 1$$

Equations (153) and (154) have been written for pressure and bulk modulus in kbars; then the velocities will be in terms of cm/sec.

The important point about Equations (153) and (154) is that only ultrasonically determined quantities are necessary to estimate the two velocities at high pressure. The velocities could likewise be determined for the equation of state containing the second derivative of the bulk modulus at zero pressure (Equation 138), Appendix II).

Figures 78 through 88 in the text show the result of using these two equations to testimate the velocities at high pressures ( $\sim 1$  Mbar in some cases). In general, the agreement between the extrapolated curves and the actual dynamic data is good.

## APPENDIX V

DERIVATION OF THE NONLINEAR RELATION BETWEEN  
SHOCK VELOCITY AND PARTICLE VELOCITY

Appendix IV shows that the shock velocity is given in terms of the pressure as

$$U_s^2 = \frac{P}{\rho_o (1 - \rho_o/\rho)} \quad (155)$$

where  $P$  is the pressure along the Hugoniot. The particle velocity is likewise given as

$$u_p^2 = \frac{P(1 - \rho_o/\rho)}{\rho_o} \quad (156)$$

Differentiating these two equations gives

$$2U_s dU_s = \frac{\left(\frac{\partial P}{\partial \rho}\right) d\rho}{\rho_o (1 - \rho_o/\rho)} - \frac{P d\rho}{\rho^2 (1 - \rho_o/\rho)^2} \quad (155a)$$

$$2u_p du_p = \left(\frac{\partial P}{\partial \rho}\right) \frac{(1 - \rho_o/\rho)}{\rho_o} d\rho + P \frac{d\rho}{\rho^2} \quad (156a)$$

It is desired to express the shock velocity in terms of the particle velocity as

$$\begin{aligned} U_s &= U_o + \left(\frac{\partial U_s}{\partial u_p}\right)_o u_p + \frac{1}{2} \left(\frac{\partial^2 U_s}{\partial u_p^2}\right) u_p^2 \\ &= a_1 + a_2 u_p + \frac{1}{2} a_3 u_p^2 \end{aligned} \quad (157)$$

where the zero subscript implies that the derivatives are evaluated at zero pressure and initial density  $\rho_o$ . The constant  $a_1$  is given by

$$\begin{aligned} a_1 &= \lim_{\substack{u_p \rightarrow 0 \\ P \rightarrow 0 \\ \rho \rightarrow \rho_o}} (U_s) \\ &= \lim_{\substack{P \rightarrow 0 \\ \rho \rightarrow \rho_o}} \frac{P}{\rho_o (1 - \rho_o/\rho)} \end{aligned}$$

Applying L'Hospitals' rule to this relation gives

$$\begin{aligned}
 a_1 &= \left( \frac{\Delta P}{\frac{\rho_o}{\rho^2} \Delta \rho} \right)_{\substack{P \rightarrow 0 \\ \rho \rightarrow \rho_o}} \\
 &= \left( \frac{\partial P}{\partial \rho} \right)_{\substack{P \rightarrow 0 \\ \rho \rightarrow \rho_o}}
 \end{aligned} \tag{158}$$

which, by definition of the adiabatic bulk modulus, yields the constant  $a_1$  as

$$a_1 = \sqrt{\frac{B_o}{\rho_o}} \tag{159}$$

The constant  $a_2$  is given by

$$a_2 = \lim_{u_p \rightarrow 0} \left( \frac{dU_s}{du_p} \right)$$

which from Equations (155a) and (156a), becomes

$$a_2 = \lim_{\substack{P \rightarrow 0 \\ \rho \rightarrow \rho_o}} \left[ \frac{\left( \frac{\partial P}{\partial \rho} \right) - \frac{\rho_o P}{\rho^2 (1 - \rho_o/\rho)}}{\left( \frac{\partial P}{\partial \rho} \right) (1 - \rho_o/\rho) + (\rho_o/\rho^2) P} \right] \tag{160}$$

Applying L'Hospitals' rule twice to Equation (160) and passing to the limit gives

$$\begin{aligned}
 a_2 &= \frac{\frac{1}{\rho_o} \left( \frac{\partial^2 P}{\partial \rho^2} \right)_o + \frac{2}{\rho_o^2} \left( \frac{\partial P}{\partial \rho} \right)_o}{\frac{4}{\rho_o^2} \left( \frac{\partial P}{\partial \rho} \right)_o} \\
 &= \frac{\rho_o \left( \frac{\partial^2 P}{\partial \rho^2} \right)_o + 2 \left( \frac{\partial P}{\partial \rho} \right)_o}{4 \left( \frac{\partial P}{\partial \rho} \right)_o}
 \end{aligned} \tag{161}$$

Since the bulk modulus is defined as

$$\begin{aligned}
 B &= -v \left( \frac{\partial P}{\partial v} \right) \\
 &= \rho \left( \frac{\partial P}{\partial \rho} \right)
 \end{aligned} \tag{162}$$



and the pressure derivative of B is

$$\begin{aligned}\left(\frac{\partial B}{\partial P}\right) &= B' = 1 + \rho \left(\frac{\partial^2 P}{\partial \rho^2}\right) \left(\frac{\partial \rho}{\partial P}\right) \\ &= 1 + \frac{\rho^2}{B} \left(\frac{\partial^2 P}{\partial \rho^2}\right)\end{aligned}\quad (163)$$

Equation (161) becomes

$$\begin{aligned}a_2 &= \frac{\frac{B}{\rho} (B' - 1) + \frac{2B}{\rho}}{\frac{4B}{\rho}} \\ &= \frac{1}{4} (B' + 1)\end{aligned}\quad (164)$$

Finally, the constant  $a_3$  is given by

$$\begin{aligned}a_3 &= \lim_{\substack{P \rightarrow 0 \\ \rho \rightarrow \rho_0}} \frac{d^2 U_s}{du_p^2} \\ &= \lim_{\substack{P \rightarrow 0 \\ \rho \rightarrow \rho_0}} \frac{d}{d\rho} \left( \frac{dU_s}{du_p} \right) \left( \frac{d\rho}{du_p} \right) \\ &= \lim_{\substack{P \rightarrow 0 \\ \rho \rightarrow \rho_0}} \frac{d}{d\rho} \left[ \frac{\rho^2 (1 - \rho_0/\rho) \left(\frac{\partial P}{\partial \rho}\right) - \rho_0 P}{\rho^2 (1 - \rho_0/\rho)^2 \left(\frac{\partial P}{\partial \rho}\right) + \rho_0 (1 - \rho_0/\rho) P} \right] \left( \frac{d\rho}{du_p} \right)\end{aligned}$$

which, upon applying successive applications of L'Hospitals' rule, yields

$$\frac{d^2 U_s}{du_p^2} = \frac{1}{a_1} \left\{ \frac{\rho_0 \frac{\partial P}{\partial \rho} + \rho_0^2 \frac{\partial^2 P}{\partial \rho^2} + \frac{1}{6} \rho_0^3 \frac{\partial^3 P}{\partial \rho^3}}{\rho_0 \left(\frac{\partial P}{\partial \rho}\right)} - \frac{3}{16} \left[ \frac{2\rho_0 \frac{\partial P}{\partial \rho} + \rho_0^2 \frac{\partial^2 P}{\partial \rho^2}}{\left(\rho_0 \frac{\partial P}{\partial \rho}\right)} \right]^2 \right\}$$

Using Equation (163) and

$$\begin{aligned}\frac{\partial^2 B}{\partial P^2} &= \left(\frac{\partial^2 P}{\partial \rho^2}\right) \left(\frac{\partial \rho}{\partial P}\right)^2 + \rho \left(\frac{\partial^3 P}{\partial \rho^3}\right) \left(\frac{\partial \rho}{\partial P}\right) + \rho \left(\frac{\partial^2 P}{\partial \rho^2}\right) \left(\frac{\partial^2 \rho}{\partial P^2}\right) \\ B'' &= 2 \frac{\rho^2}{B^2} \left(\frac{\partial^2 P}{\partial \rho^2}\right) + \frac{\rho^3}{B^2} \left(\frac{\partial^3 P}{\partial \rho^3}\right) - \frac{\rho^2}{B^2} \left(B' \frac{\partial^2 P}{\partial \rho^2}\right) \\ &= 2 \frac{B' - 1}{B} + \frac{\rho^3}{B^2} \left(\frac{\partial^3 P}{\partial \rho^3}\right) - \frac{B'(B' - 1)}{B}\end{aligned}$$

so that

$$\rho^3 \frac{\partial^3 P}{\partial \rho^3} = B [BB'' + (B' - 1)(B' - 2)] \quad (165)$$

Therefore,  $\frac{d^2 U_s}{du_p^2}$  becomes

$$\begin{aligned}\frac{d^2 U_s}{du_p^2} &= \frac{1}{a_1} \left\{ 1 + B' - 1 + \frac{1}{6} [BB'' + (B' - 1)(B' - 2)] - \frac{3}{16} (B' + 1)^2 \right\} \\ &= \frac{1}{a_1} \left\{ \frac{(1 + B')(7 - B')}{48} + \frac{BB''}{6} \right\} \quad (166)\end{aligned}$$

when evaluated at the origin along an isentrope.

Pastine (Ref. 26) shows that the volume derivative when evaluated at the origin along a Hugoniot is equal to the volume derivative along an isentrope to second order. However, he shows that the third derivative of the pressure with respect to volume along the Hugoniot differs from the respective derivative along the isentrope by a factor  $\frac{B}{2} (B' + 1)\gamma$ , where  $\gamma$  is the Grüneisen ratio. Therefore, Equation (165) evaluated on the Hugoniot becomes

$$\left(\rho^3 \frac{\partial^3 P}{\partial \rho^3}\right)_{P=0} = B [BB'' + (B' - 1)(B' - 2) + \frac{1}{2} (B' + 1)\gamma]$$

and Equation (166) for the constant  $a_3$  is thus modified to

$$\begin{aligned}a_3 &= \frac{1}{a_1} \left\{ \frac{(1 + B')(7 - B')}{48} + \frac{BB''}{6} + \frac{(B' + 1)\gamma}{12} \right\} \\ &= \frac{1 + B'}{48a_1} \left\{ \frac{8BB''}{(1 + B')} + 7 + 4\gamma - B' \right\}_{P=0} \quad (167)\end{aligned}$$

Both Ruoff (Ref. 41) and Pastine (Ref. 26) have used Equation (167) to explain the nonlinearity between shock velocity and particle velocity in some of the metals and alkali halides. Ruoff has devised a unique technique for estimating  $B''$ , and thus, obtaining  $a_3$  by using ultrasonic determinations of  $B'$  and the Born model to estimate  $B''$  in alkali halides. This technique can be used only for crystals satisfying the Cauchy-Love relations and has not yet been generalized to a material satisfying an arbitrary potential function.

Since the shock velocity is almost linear in particle velocity for a wide variety of materials, Equation (167) can be used to estimate the order of magnitude of  $B''_0$ . Setting the quantity in brackets in Equation (167) equal to zero yields

$$B'' = -\frac{B' + 1}{8B} [4\gamma + 7 - B'] \quad (168)$$

Since  $B$  is always positive and  $B'$  is generally positive, Equation (168) implies that  $B''$  will be negative providing  $B'$  is less than  $4\gamma + 7$ . In this case, the shock velocity will be linear in particle velocity. If  $B'$  is more positive (or negative) than this value, the curvature of the shock velocity curve will be positive (or negative).

Table 58 gives the values of  $B''_0$ , as estimated from Equation (166), for a number of materials. The elastic constants were taken from Reference 23. Ruoff has estimated the second derivative of the bulk modulus in sodium, using the Born model, and obtained a value of  $-0.063$  kbar. Pastine used hydrostatic compression data to calculate  $B''$  as  $-0.051$  kbar $^{-1}$ . The value of  $-0.089$  as estimated here illustrates the technique of obtaining an order of magnitude estimate of the second derivative of the bulk modulus and suggests that the shock velocity-particle velocity curve is concave upward, in agreement with Ruoff's and Pastine's treatments. Ruoff and Pastine both showed by the outlined technique that the velocity curve is concave upward with quadratic coefficients of  $+0.005$   $\mu\text{sec}/\text{mm}$  and  $+0.016$   $\mu\text{sec}/\text{mm}$ , respectively. The value of  $B''_0$  reported in Table 58 thus indicates an approximate order of magnitude of  $B''_0$  to be expected in ultrasonic pressure measurements.

Table 58

ESTIMATION OF THE SECOND DERIVATIVE OF THE ADIABATIC  
BULK MODULUS FOR SEVERAL MATERIALS

Material	$B_o^{s''}$ (kbar <sup>-1</sup> )
Magnesium	-0.016
Sodium	-0.089
Sodium Chloride	-0.022
Potassium	-0.13
Cadmium	-0.018
Iron	-0.0040
Aluminum	-0.012
Magnesium Oxide	-0.0027
Aluminum Oxide	-0.0021

## APPENDIX VI

THEORETICAL EQUATIONS OF DIFFERENTIAL  
THERMAL ANALYSIS

Vold (Ref. 42) has developed a simplified mathematical treatment relating the area and shape of a thermogram to the heat of reaction,  $\Delta H$ . The increase in enthalpy of the sample,  $c_{P(s)} dT_{(s)}$ , is equal to the heat transferred from the surroundings to the cell. Thus, for the time interval,  $dt$ ,

$$c_{P,S} dT_S = dH + K_S (T_B - T_S) dt \quad (169)$$

where  $K_S$  is the heat transfer coefficient of the sample,  $c_{P,S}$  is the heat capacity of the sample,  $dH$  is the heat of reaction, and  $T_B$  and  $T_S$  are the temperature of the bath and sample, respectively.

Similarly for the reference cell,

$$c_{P,R} dT_R = K_R (T_B - T_R) dt \quad (170)$$

where  $K_R$  is the heat transfer coefficient of the reference cell. With proper choice of reference material, sample cells, and the level of the sample packing, equilibrium is reached when

$$c_{P,S} = c_{P,R} = c_P \text{ and } K_S = K_R = K \quad (171)$$

Subtracting Equation (170) from Equation (169) and substituting  $\Delta T$  for  $T_S - T_R$ , leads to

$$dH = c_P d(\Delta T) + K \Delta T dt \quad (172)$$

In order to obtain an expression for the total heat transferred, Equation (172) is integrated between  $t = 0$  and  $t = \infty$  giving

$$\Delta H = c_P (\Delta T_{\infty} - T_0) + K \int_0^{\infty} \Delta T dt \quad (173)$$

Because  $T$  is zero at  $t = 0$  and  $t = \infty$ , the first term in Equation (173) also becomes zero. The integral is equal to the total area,  $A$ , under the curve, so that

$$\Delta H = K \int_0^{\infty} \Delta T \, dt = K \quad (174)$$

$K$  is characteristic of the apparatus and can be evaluated by carrying out a reaction with known heat effects, allowing calibration of the apparatus.

Specifically, peak areas resulting from phase changes in a known weight of material were measured by means of a polar planimeter. The calibration coefficient was calculated from

$$K = \frac{\Delta H_f \cdot M \cdot R}{A \cdot \Delta T_S \cdot T_S} \quad (175)$$

where

$K$  = calibration coefficient, g cal/°C min

$A$  = peak area, sq. in.

$M$  = sample mass, g

$R$  = heating rate, °C/min

$\Delta T_S$  = y-axis sensitivity, °C/in

$T_S$  = x-axis sensitivity, °C/in

$\Delta H_f$  = known heat of fusion of a reference standard, cal/g

The heat of fusion or transition of unknown materials may be obtained by proper substitution of experimentally determined  $K$  values and rearrangement of Equation (175).

Since the heat evolved in a short time interval is proportional to the number of moles of sample reacting

$$dH = - (KA/n_o) dn \quad (176)$$

where  $-dn$  is the number of moles of sample reacted and  $KA/n_o$  is the heat of reaction per mole. Combining Equations (176) and (172) and differentiating with respect to time, yields the rate of reaction,  $-\left(\frac{dn}{dt}\right)$ , by

$$-\left(\frac{dn}{dt}\right) = n_o / KA \left[ c_p \, d(\Delta T) / dt + K \Delta T \right] \quad (177)$$

where  $\Delta T$  refers to the height and  $d(\Delta T)/dt$  to the slope of a thermogram at a given time,  $t$ , or temperature,  $T$ .

The number of moles of sample,  $n$ , remaining at any instant is equal to the initial number of moles,  $n_o$ , minus the number that have reacted:

$$n = n_o - \int_0^t - \left( \frac{dn}{dt} \right) dt \quad (178)$$

Substitution of  $\frac{dn}{dt}$  from Equation (176) into Equation (178) gives

$$n = n_o - (n_o/Ka) \left[ c_p \int_0^t (d\Delta T/dt) dt + K \int_0^t \Delta T dt \right] \quad (179)$$

which upon integration becomes

$$n = n_o - (n_o/Ka) [c_p \Delta T + Ka] \quad (180)$$

where  $a$  is the area under the thermogram up to time  $t$ . See Figure 89.

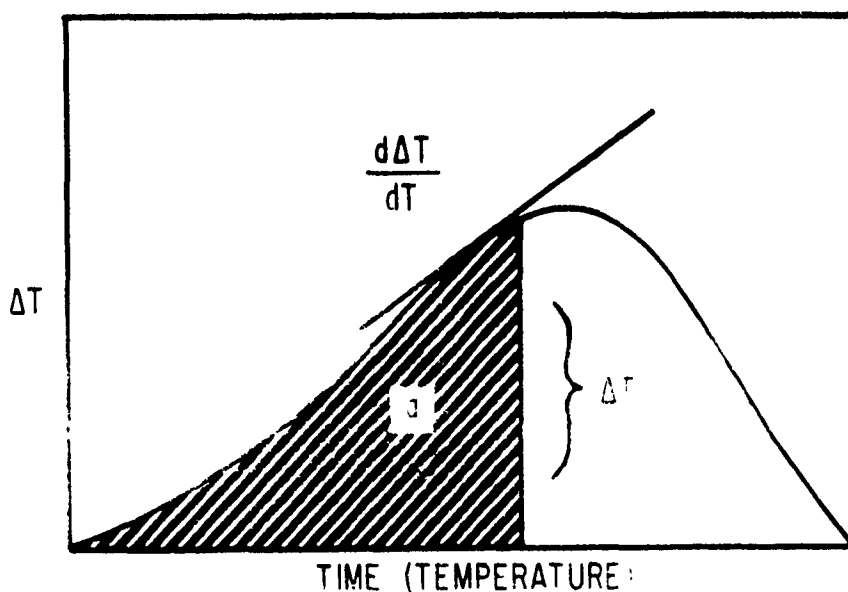


Figure 89. Differential Temperature Versus Time Curve Illustrating Reaction Rates.

## APPENDIX VII

## THERMAL CALCULATIONS AND THERMODYNAMIC APPLICATIONS

The determination of thermodynamic properties requires accurate numerical techniques for arriving at interpolated values of a function of one or two variables and for obtaining differentiated properties at interpolation points. This Appendix illustrates the determination of temperature derivatives from experimentally determined specific heat, thermal expansion, density and ultrasonic sound velocity measurements.

Specific heat values were computed at 5-degree temperature intervals from the values of the observed differential temperature, heating rate, sample mass, and instrumental calibration constant by

$$c_p \left( \frac{\text{Millicalories}}{\text{mg} \cdot ^\circ\text{C}} \right) = \frac{(\Delta T_S - \Delta T_B) E_T}{M \cdot R} \quad (181)$$

where

- $c_p$  = Specific heat at constant pressure
- $\Delta T_S$  = Absolute differential temperature for sample,  $^\circ\text{C}$
- $\Delta T_B$  = Absolute differential temperature for blank,  $^\circ\text{C}$
- $E_T$  = Calibration coefficient at temperature, T, mcal/ $^\circ\text{C}$  min
- $M$  = Sample mass, mg
- $R$  = Heating rate,  $10^\circ\text{C}/\text{min}$

From the computer plots of the specific heat as a function of temperature,  $c_p$  values were obtained from the straight line portions of the curve which were used to calculate the temperature derivative of the specific heat,  $[\partial c_p / \partial T]$ , according to

$$c_p = A + BT$$

and

$$\left[ \frac{\partial c_p}{\partial T} \right] = B \quad (182)$$

where A and B are constants calculated by the computer and T refers to the temperature in  $^\circ\text{C}$ .



By definition, the linear thermal expansion coefficient,  $\alpha$ , is given by the differentiation of the length curve by

$$\alpha = \frac{1}{l_0} \frac{\partial l}{\partial t} \quad (183)$$

$$l = A + BT + CT^2$$

$$\left[ \frac{\partial l}{\partial t} \right] = B + 2CT$$

and for the instrument used, Equation (183) becomes

$$\alpha = S/l_0 (B + 2CT) \text{ and } \left[ \frac{\partial \alpha}{\partial T} \right] = 2C \quad (184)$$

where  $S$  is the sensitivity of the instrument, and  $l_0$  refers to the original sample length measured at room temperature. Due to the inherent limitations of the cubic curve fit caused by the round-off errors of the computer and by the fact that the second derivative is limited to a linear variation between adjacent junction points, Equation (184) could not be used directly.

More reliable linear expansion coefficients were obtained from

$$\alpha = \left[ \left( \frac{h_2 - h_1}{T_2 - T_1} \right) S - \left( \frac{l_2 - l_1}{T_2 - T_1} \right) B \right] \frac{S}{l_0} \quad (185)$$

where  $l_2$  and  $l_1$ , and  $h_2$  and  $h_1$  refer to the heights of the blank and the sample, respectively, at a temperature interval  $T_2 - T_1$ , where  $T_2$  was five degrees higher than  $T_1$ , and  $S$  and  $l_0$  have the same significance as above.

The temperature derivative,  $\left[ \frac{\partial \alpha}{\partial T} \right]$ , was obtained by choosing the best  $\alpha$  values from the  $\alpha$  versus  $T$  plot and calculating the linear least-squares as done for the  $c_p$  data.

Densities were measured at room temperature and the density at  $0^\circ\text{C}$ ,  $\rho_0$ , was obtained from

$$\rho = \rho_0 - \beta \rho_0 T = 1 - 3\alpha_0 T \quad (186)$$

where the zero subscript refers to  $0^\circ\text{C}$ ,  $\beta$  is the volume coefficient of expansion, and  $\alpha$  is the linear expansion coefficient.

The adiabatic bulk modulus,  $B^s$ , obtained from ultrasonic studies (Section I) by

$$B^s = \rho \left( V_l^2 - \frac{4}{3} V_t^2 \right) \quad (187)$$

was differentiated with respect to temperature to give

$$\left( \frac{\partial B^s}{\partial T} \right)_P = 2\rho \left[ V_l \left( \frac{\partial V_l}{\partial T} \right) - \frac{4}{3} V_t \left( \frac{\partial V_t}{\partial T} \right) \right] - \beta \cdot B^s \quad (188)$$

where  $V_l$  and  $V_t$  refer to the longitudinal and transverse velocities, respectively.

The thermal Grüneisen ratio,  $\gamma$ , given by

$$\gamma = \frac{\beta \cdot B^s}{c_p \cdot \rho} \quad (189)$$

was differentiated with respect to temperature to yield

$$\left( \frac{\partial \gamma}{\partial T} \right)_{P,0} = \gamma_0 \left\{ \frac{1}{\beta} \left[ \left( \frac{\partial \beta}{\partial T} \right) + \beta^2 \right] + \frac{1}{B^s} \left( \frac{\partial B^s}{\partial T} \right) - \frac{1}{c_p} \left( \frac{\partial c_p}{\partial T} \right) \right\}_0 \quad (190)$$

in which proper experimental values were inserted to allow a determination of the temperature derivative of  $\gamma$  in materials which did not exhibit phase changes.

Substitution of experimental data into known thermodynamic relationships permitted the calculation of other physical properties, such as  $\left( \frac{\partial H}{\partial T} \right)_P$ ,  $\left( \frac{\partial V}{\partial T} \right)_P$ , and  $\left( \frac{\partial V}{\partial P} \right)_T$ . Enthalpy,  $\Delta H$ , and entropy,  $\Delta S$ , values were determined from calorimetric data. Since  $\left( \frac{\partial H}{\partial T} \right)_P = c_p$ , then

$$\begin{aligned} \Delta H &= \int_{T_0}^T c_p \, dT \\ &= \int_{T_0}^T (a + bT) \, dT = \left[ aT + \frac{bT^2}{2} \right]_{T_0}^T \end{aligned} \quad (191)$$

and since  $\left( \frac{\partial S}{\partial T} \right)_P = \frac{c_p}{T}$  then

$$\begin{aligned} \Delta S &= \int_{T_0}^T \left( \frac{c_p}{T} \right) dT = \int_{T_0}^T \left( \frac{a + bT}{T} \right) dT \\ &= \left[ a \ln T + bT \right]_{T_0}^T \end{aligned} \quad (192)$$

where  $a$  and  $b$  refer to the constants obtained from heat capacity data.

The transformation of one phase into another, generally in the form of a solid-solid, solid-liquid, or liquid-vapor transition, involves an equilibrium reaction at a given temperature and pressure. Since the system is in equilibrium, the Gibbs' free energy,  $G = G_B - G_A = 0$  and the temperature is now altered by an amount  $dT$ . If the system is to be maintained in equilibrium, the pressure must be altered by some quantity,  $dP$ . Nevertheless, if equilibrium is maintained at the new temperature,  $T'$

then

$$T' = T + \Delta T$$

and

$$\Delta G'_{p', T'} = G'_B - G'_A = 0 \quad (193)$$

From this it is obvious that

$$d(\Delta G) = d(G_B - G_A) = 0 \quad (194)$$

and  $dG_B - dG_A = 0$  which in differential form becomes

$$dG_A = V_A dP - S_A dT \quad (195)$$

$$dG_B = V_B dP - S_B dT$$

Setting up the equality demanded by Equation (194) and upon rearrangement, Equation (195) leads to

$$(V_B - V_A) dP = (S_B - S_A) dT$$

or

$$\frac{dP}{dT} = \frac{S_B - S_A}{V_B - V_A} \quad (196)$$

The value of the derivative,  $\left(\frac{dP}{dT}\right)$ , at the specified temperature and pressure of the transition is obtained from the entropy change of a phase transition, which is defined as  $\Delta S = S_B - S_A - \Delta H_{TR}/T$ ; so that Equation (196) now becomes

$$\frac{dP}{dT} = \frac{\Delta H_{TR}}{T(V_B - V_A)} \quad (197)$$

which is known as the Clapeyron equation and which is applicable to equilibrium between any two phases of one component.

If the equilibrium reaction results in a gas and condensed phase (liquid or solid), so that  $V_B - V_A = V_{\text{gas}} - V_{\text{cond.}}$ , then since  $V_{\text{gas}} \gg V_{\text{cond.}}$ , the latter may be neglected and Equation (197) becomes

$$\ln \left( \frac{P_2}{P_1} \right) = - \frac{\Delta H_{\text{TR}}}{R} \left[ \frac{1}{T_2} - \frac{1}{T_1} \right] \quad (198)$$

which is the well-known Clausius-Clapeyron equation. This equation may be used to obtain  $\Delta H$  from known values of vapor pressure as a function of temperature or vice versa, to predict vapor pressures of a liquid (or a solid) when the heat of vaporization (or sublimation) and one vapor pressure is known.

The temperature dependence of the heat of a phase transition,  $\Delta H_{\text{TR}}$ , is generally given as

$$\left( \frac{\partial \Delta H}{\partial T} \right)_P = \Delta c_P \quad (199)$$

however, the vapor pressure does not remain constant but it is also a function of the temperature. This may be represented by the total differential

$$\begin{aligned} d(\Delta H) &= \left( \frac{\partial \Delta H}{\partial T} \right)_P dT + \left( \frac{\partial \Delta H}{\partial P} \right)_T dP \\ &= \Delta c_P dT + \left( \frac{\partial H_B}{\partial P} - \frac{\partial H_A}{\partial P} \right)_T dT \end{aligned} \quad (200)$$

where A and B refer to the two phases at equilibrium. Since the free energy function defines the pressure derivative as

$$\left( \frac{\partial H}{\partial P} \right)_T = V - T \left( \frac{\partial V}{\partial T} \right)_P \quad (201)$$

Equation (200) becomes

$$\frac{d(\Delta H)}{dT} = \Delta c_P + \frac{\Delta H}{T} - \Delta H \left( \frac{\partial \ln \Delta V}{\partial T} \right)_P \quad (202)$$

which is applicable to all types of phase transitions. However, when both A and B are condensed phases, the third term of Equation (202) is small compared to the other terms in the equation and may be neglected.

Equation (202) then becomes

$$\frac{\partial(\Delta H_{TR})}{\partial T} = \Delta c_P + \frac{\Delta H}{T} \quad (203)$$

If the phase transition is a vaporization or sublimation,  $\Delta V \approx V_{\text{gas}} = RT/P$  and the third term of Equation (202) cancels the second and

$$\frac{\partial(\Delta H_{TR})}{\partial T} \approx \Delta c_P \quad (204)$$

Although Equations (199) and (204) are formally alike, they refer to different types of processes. The former is strictly true for a process occurring at constant pressure throughout a range of temperatures and the latter applies to a vaporization or sublimation where the condensed phase is small as compared to the gas phase.

The change in free energy,  $\Delta G$ , for a phase change is readily obtained from the relation

$$\Delta G = \Delta H_{TR} - T\Delta S_{TR} \quad (205)$$

when  $\Delta H_{TR}$  and  $\Delta S_{TR}$  are the enthalpy and entropy of transition at constant temperature.

The temperature derivative of the free energy,  $\left[\frac{\partial(\Delta G/T)}{\partial T}\right]_P$ , may be derived by differentiating the fundamental definition  $G/T = H/T - S$  as a function of temperature and at constant pressure. The equation becomes

$$\left[\frac{\partial(G/T)}{\partial T}\right]_P = H \left[\frac{\partial(1/T)}{\partial T}\right]_P + \frac{1}{T} \left(\frac{\partial H}{\partial T}\right)_P - \left(\frac{\partial S}{\partial T}\right)_P \quad (206)$$

which may be reduced to

$$\left[\frac{\partial(\Delta G/T)}{\partial T}\right]_P = -\frac{\Delta H}{T^2} \quad (207)$$

An equation for  $G$  may also be obtained from the integration of

$$\left(\frac{\partial \Delta G}{\partial T}\right)_P = -\Delta S \quad (208)$$

where the expression for  $\Delta S$  as a function of temperature, for substitution into the preceeding equation may be derived from

$$\left(\frac{\partial \Delta S}{\partial T}\right)_P = \frac{\Delta c_P}{T} \quad (209)$$

## APPENDIX VIII

DEFINITIONS AND APPLICATION OF THERMAL  
EXPANSIVITY MEASUREMENTS

In an elastic region the effect of temperature on strain appears in two ways; first, by causing a modification in the elastic constants as a result of the angular stresses originating in the material, and second, by directly producing a temperature strain even in the absence of an external stress. The former, the elastic shear strain,  $\epsilon_s^l$ , originating from the angular distortion of the material is generally small and is given by

$$\epsilon_s^l = \tan \phi \quad (210)$$

where  $\phi$  is the tangent of the angle resulting from the distortional stress. The longitudinal strain or elongation,  $\epsilon_l^t$ , is the result of pure thermal strains brought about by the temperature rise and is defined by

$$\epsilon_l^t = \frac{l - l_0}{l_0} \alpha T \quad (211)$$

where  $l_0$  is the original sample length which differs from the new length  $l$ , and  $\alpha$  is the linear coefficient of expansion.

The total strain,  $\epsilon$ , at any point in an elastic body is the sum of the shear or elastic strain,  $\epsilon_s^l$ , and thermal or longitudinal strain,  $\epsilon_l^t$ , given by

$$\epsilon = \epsilon_s^l + \epsilon_l^t \quad (212)$$

If the length increases in the direction of the x-axis, the mean length,  $\left(\frac{\Delta l}{l_0}\right)$ , or the total strain may be referred to this axis so that Equation (212) becomes

$$\begin{aligned} \epsilon_x &= \epsilon_{xx} + \alpha T \\ &= \frac{\sigma_{xx}}{M} - S \cdot \frac{\sigma_{yy}}{M} - S \cdot \frac{\sigma_{zz}}{M} + \alpha T \end{aligned} \quad (213)$$

where  $\sigma$ ,  $S$ , and  $M$  refer respectively to the stress, Poisson's ratio, and an effective elastic modulus. Referring to cartesian coordinates, if the stress

components at the point are  $\sigma_{xx}$ ,  $\sigma_{yy}$ ,  $\sigma_{zz}$ ,  $\sigma_{xy}$ ,  $\sigma_{yz}$ ,  $\sigma_{zx}$ , the strain components are therefore,

$$\begin{aligned}\epsilon_{xx} &= \frac{1}{M} \left[ \sigma_{xx} - S(\sigma_{yy} + \sigma_{zz}) \right] + \alpha T \\ \epsilon_{yy} &= \frac{1}{M} \left[ \sigma_{yy} - S(\sigma_{xx} + \sigma_{zz}) \right] + \alpha T \\ \epsilon_{zz} &= \frac{1}{M} \left[ \sigma_{zz} - S(\sigma_{xx} + \sigma_{yy}) \right] + \alpha T\end{aligned}\quad (214)$$

For an isotropic cubic material, symmetry arguments show that the thermal strain must be a pure expansion or contraction with no shear-strain components referred to any set of axes. The total strains for a temperature change are

$$\begin{aligned}\epsilon_x^t &= \epsilon_y^t = \epsilon_z^t = \alpha(T - T_0) \\ \sigma_{xy}^t &= \sigma_{yz}^t = \sigma_{zx}^t = 0\end{aligned}\quad (215)$$

where  $\alpha = \alpha_x = \alpha_y = \alpha_z$  which indicates that the crystal expands equally along the three cubic axes and the thermal expansion is isotropic. Therefore, cubic materials need only one coefficient of expansion obtained in any direction to describe them.

It has been shown that the three principal elastic stiffness constants necessary to describe a cubic structure are  $c_{11}$ ,  $c_{12}$ , and  $c_{44}$ . These constants may be determined from the velocities of three waves: (1) a longitudinal wave which propagates along a cube axis with velocity  $(c_{11}/\rho_0)^{1/2}$ ; where  $\rho_0$  is the density; (2) a shear wave which propagates along a cube axis with velocity  $(c_{44}/\rho_0)^{1/2}$ ; and (3) a shear wave with particle motion along a  $110$  direction which propagates along a  $1\bar{1}0$  direction with velocity  $[(c_{11} - c_{12})/2\rho_0]^{1/2}$ . If the elastic constants are defined by

$$c_{11} - c_{12} = 2c_{44}, \quad (216)$$

this relation is the condition that the crystal should be elastically isotropic; that is, the waves should propagate in all directions with equal velocities and be independent of orientation.



The anisotropy factor, A, is highly dependent upon crystal orientation. For a cubic crystal it is defined by Kittel (Ref. 152) as the square of the ratio of velocities of the shear waves propagating in the [100] and [110] directions:

$$A = \frac{2c_{44}}{(c_{11} - c_{12})} \quad (217)$$

Alexander (Ref. 151) has shown the relationship between anisotropy and thermal expansion by assuming that each crystal has a cubic symmetry with thermal expansion coefficients  $\alpha_a$ ,  $\alpha_b$ , and  $\alpha_c$  in the a-, b-, and c-directions. For a temperature rise,  $\Delta T$ , the macroscopic thermal expansion of a polycrystalline bar must be  $1/3 \Delta T (\alpha_a + \alpha_b + \alpha_c)$ . Each grain is assumed to be restricted in each direction by that amount. Thus, the crystal tries to expand in the a-direction by an amount  $\alpha_a \Delta T$ , but can only expand  $1/3 \Delta T (\alpha_a + \alpha_b + \alpha_c)$ . Thus, a compressive (negative tensile) stress is induced in the grain in that direction corresponding with a tensile strain of

$$\epsilon_a = - \alpha_a \Delta T - \frac{1}{3} \Delta T (\alpha_a + \alpha_b + \alpha_c) \quad (218)$$

Therefore,

$$\begin{aligned} \epsilon_a &= \frac{1}{3} (\alpha_b + \alpha_c - 2\alpha_a) \\ \epsilon_b &= \frac{1}{3} \Delta T (\alpha_c + \alpha_a - 2\alpha_b) \end{aligned} \quad (219)$$

and

$$\epsilon_c = \frac{1}{3} \Delta T (\alpha_a + \alpha_b - 2\alpha_c)$$

For an anisotropic material like  $\alpha$ -uranium,  $\alpha_a = \alpha_c$  so that the strains become

$$\begin{aligned} \epsilon_a &= \frac{1}{3} \Delta T (\alpha_b - \alpha_a) \\ \epsilon_b &= \frac{2}{3} \Delta T (\alpha_a - \alpha_b) = -2\epsilon_a \\ \epsilon_c &= \frac{1}{3} \Delta T (\alpha_b - \alpha_a) = \epsilon_a \end{aligned}$$

that is,

$$\epsilon_a = \epsilon_c = -\frac{1}{2} \epsilon_b \quad (220)$$

where

$$\epsilon_b = \frac{2}{3} \Delta T (\alpha_a - \alpha_b) \quad (221)$$

If the stresses remain within the elastic range, they may be determined from Hooke's law. Since  $\sigma_a = \sigma_c = -\frac{1}{2} \sigma_b$ , by symmetry then

$$\begin{aligned} \epsilon_b &= \frac{1}{M} [\sigma_b - 2 S \sigma_a] = -\frac{2}{M} [\sigma_a (1 - S) - S \sigma_b] \\ &= \frac{\sigma_b}{M} (1 + S) \end{aligned} \quad (222)$$

and the strain may be expressed in terms of the modulus,  $M$ , the strain,  $\epsilon$ , and Poisson's ratio,  $S$ . The maximum stress induced may then be defined as

$$\sigma_b = \left( \frac{M}{1 + S} \right) \left( \frac{2}{3} \Delta \alpha \Delta T \right) \quad (223)$$

where  $\Delta \alpha = \alpha_a - \alpha_b$ .

The volume coefficient of a gas is generally calculated from the equation of state, or from any empiric equation representing the relationship between volume and temperature at constant pressure.

The volume expansivity of liquids and solids may be calculated from an empiric equation representing the relationship between density and temperature at constant pressure. Since the specific volume,  $v$ , is the reciprocal of the density,  $\rho$ , it follows that

$$\beta = -\frac{1}{\rho} \left( \frac{\partial \rho}{\partial T} \right)_P \quad (224)$$

Since density data for the solid over a wide temperature range were not available, the volume expansivities were calculated from linear expansivities. For most crystals, there can be found three mutually perpendicular directions such that if a cube is cut out of the crystal with its sides parallel to these directions and heated, the angles will remain right angles, though the sides will become unequal. These directions are called the principal axis of dilatation,

and the coefficients of expansion in these directions are denoted by  $\alpha_x$ ,  $\alpha_y$ , and  $\alpha_z$ . Such a cube of sides,  $l_0$ , will, on being heated to  $T^\circ\text{C}$ , become a rectangular solid whose sides will be given by  $l_x$ ,  $l_y$ , and  $l_z$ , and whose edges will be given by

$$\begin{aligned} l_x &= l_0 (1 + \alpha_x T) \\ l_y &= l_0 (1 + \alpha_y T) \\ l_z &= l_0 (1 + \alpha_z T) \end{aligned} \quad (225)$$

The volume of this isotropic solid is given by

$$V = (l_x) (l_y) (l_z) \approx l_0^3 [1 + (\alpha_x + \alpha_y + \alpha_z)T] \quad (226)$$

which, as a function of temperature becomes

$$\frac{\partial V}{\partial T} = l_y l_z \left( \frac{\partial l_x}{\partial T} \right) + l_x l_z \left( \frac{\partial l_y}{\partial T} \right) + l_x l_y \left( \frac{\partial l_z}{\partial T} \right)$$

or

$$\frac{1}{V} \frac{\partial V}{\partial T} = \frac{1}{l_x} \frac{\partial l_x}{\partial T} + \frac{1}{l_y} \frac{\partial l_y}{\partial T} + \frac{1}{l_z} \frac{\partial l_z}{\partial T} \quad (227)$$

and

$$\beta = \alpha_x + \alpha_y + \alpha_z$$

Since for a cubic structure  $\alpha_x = \alpha_y = \alpha_z = \alpha$ , the volume coefficient of expansion,  $\beta$ , becomes

$$\beta = 3\alpha = \frac{3}{l_0} \frac{l - l_0}{T - T_0} \quad (228)$$

which represents the volume expansivity of the crystal.

The volume coefficients of expansion of the anisotropic materials in this report were calculated from

$$\beta = \alpha_{||} + 2\alpha_{\perp} \quad (229)$$

where  $\alpha_{||}$  and  $\alpha_{\perp}$  represent the linear coefficients of expansion parallel and perpendicular to the chain alignment of the polymer.

Since the degree of crystallinity, % C, may be expressed by

$$\% C = \frac{\beta_a - \beta_s}{\beta_a - \beta_c} \quad (230)$$

expansivity data present a direct means of calculating the crystallinity of the polymeric materials. In Equation (230), the term  $\beta_s$  is the volume expansivity of the sample studied, and  $\beta_a$  and  $\beta_c$  refer to the expansivities of the amorphous and crystalline regions, respectively. The  $\beta_a$  term may be obtained from measurements made after the glass-transition temperature, whereas,  $\beta_c$  may be obtained from measurements made on the pure crystalline polymer.

This page intentionally left blank.

## REFERENCES

1. Bridgman, P.W., The Physics of High Pressure, G. Bell and Sons, London, 1952.
2. Lazarus, D., Phys. Rev. 76, p. 545, 1949.
3. Brugger, K., J. Appl. Phys. 36, p. 759, 1965.
4. Asay, J. R., Dorr, A. J., Arnold, N. D., and Guenther, A. H., Ultrasonic Wave Velocity-Temperature Studies in Several Plastics, Plastic Foams, and Nose-Cone Materials, AFWL-TR-65-188, Air Force Weapons Laboratory, New Mexico, 1966.
5. Mason, W.P., Physical Acoustics and the Properties of Solids, D. Van Nostrand Co., Inc., New Jersey, 1958.
6. Cedrone, N.P., and Curran, D.R., J. Acoust. Soc. Amer. 26, p. 963, 1954.
7. Barthel, R., and Nolle, A.W., J. Acoust. Soc. Amer. 24, p. 8, 1951.
8. Bogardus, E.H., J. Appl. Phys. 36, p. 2504, 1965.
9. Kolsky, H., Stress Waves in Solids, Dover Publication, 1963.
10. Arnold, N.D., and Guenther, A.H., J. Appl. Polymer Sci. 10, p. 731, 1966.
11. Estes, P.H., Machine Design 38, p. 77, 1966.
12. Davidse, P.D., Watterman, H.I., and Westerdijk, J.B., J. Polymer Sci. 59, p. 389, 1962.
13. Kunze, R.J., Machine Design 38, p. 75, 1966.
14. Horio, M., and Onogi, S., J. Appl. Phys. 22, p. 971, 1951.
15. Lucks, C.F., and Deem, H.W., Thermal Properties of Thirteen Metals, ASTM STP No. 227, 1958.
16. Fenn, R.W., Young's Modulus of Magnesium Alloys as a Function of Temperature and Metallurgical Variables, The Dow Chemical Co., pp 22-27, 1959.
17. Fahey, N.H., Ultrasonic Determination of Elastic Constants at Room and Low Temperatures, Technical Report No. WAL TR 118, 1/1, Watertown Arsenal, 1960.
18. Cady, W.G., Piezoelectricity, Dover Publication, 1964.
19. Brugger, K., Phys. Rev. 133, p. A1611, 1964.
20. Cook, R.K., J. Acoust. Soc. Amer. 29, p. 445, 1956.
21. Breazeale, M.A., and Ford, J., J. Appl. Phys. 36, p. 1624, 1965.

## REFERENCES (cont'd)

22. Smith, R.T., Stern, R., and Stephens, R.W.B., J. Acoust. Soc. Amer. 40, p. 1002, 1966.
23. Anderson, O.L., J. Phys. Chem. Solids 27, p. 547, 1966.
24. Schreiber, E., and Anderson, A.L., J. Am. Ceram. Soc. 49, p. 184, 1966.
25. Murnaghan, F.D., Proc. Natn. Acad. Sci. 30, p. 244, 1944.
26. Pastine, D.J., and Piacesi, D., J. Phys. Chem. Solids 27, p. 1783, 1966.
27. Dugdale, J.S., and MacDonald, D.K.C., Phys. Rev. 89, p. 832, 1953.
28. Lundergau, C.D., and Herrmann, W. J., J. Appl. Phys. 34, p. 2046, 1963.
29. Walsh, J.M., Rice, M.H., McQueen, R.C., and Yarger, F.L., Phys. Rev. 108, p. 196, 1957.
30. Anderson, C.D., Doran, D.G., and Fahrenbuck, A.L., Equation of State of Solids: Aluminum and Teflon, AFWL Technical Report 65-147, Kirtland AFB, New Mexico, 1965.
31. Munson, D.E., and Barker, L.M., J. Appl. Phys. 37, p. 1652, 1966.
32. Bridgman, P.W., Collected Experimental Papers, Vol. VI, Harvard University Press, p. 3848, 1964.
33. Hughes, D.S., and Kelly, J.L., Phys. Rev. 92, p. 1145, 1953.
34. Wagner, M.H., Waldorf, W.F., and Louie, N.A., Determination of Hugoniot Equations of State for Polymers and Reentry Vehicle Materials and Investigations of Fracture Phenomena, AFSWC-TDR-62-66, Vol. I, Aerojet-General Corp., 1962.
35. Hauver, G.E., and Melani, A., Shock Compression of Plexiglas and Polystyrene, BRL Report No. 1259, Aberdeen Proving Ground, Maryland, 1964.
36. Van Thiel, M. Compendium of Shock Wave Data, UCRL-50108, Vol. I and II, Lawrence Radiation Laboratory, Livermore, Calif., 1966.
37. Hughes, D.S., Blankenship, E.G., and Mims, R.L., J. Appl. Phys. 21, p. 294, 1950.
38. Alers, G.A., and Neighbours, J.R., J. Appl. Phys. 28, p. 1514, 1957.
39. Thurston, R.N., Physical Acoustics, W.P. Mason, Editor, Vol. I, Part A, p. 47, Academic Press, New York and London, 1964.
40. Thurston, R.N., Proceedings of the IEEE 53, p. 1320, 1965.
41. Ruoff, A.L., On The Relationship Between the Equation of State at High Pressures as Determined From Ultrasonic Data and Shock Data, Sandia Corporation Technical Report, SC-RR-66-676, 1966.

## REFERENCES (cont'd)

42. Vold, M.S., Anal. Chem. 21, p. 683, 1949.
43. Laquer, H.L., and Head, E.L., AECU-2161, Tech. Inf. Serv., AEC, Oak Ridge, Tennessee, 1952.
44. Deeg, E., Ber. Deut. Keram. Ges. 33, p. 321, 1956.
45. Houldsworth, H.S., and Cobb, J.W., Tran. Brit. Ceram. Soc. 22, p. 111, 1922.
46. Nolle, A.W., J. Polymer Sci., 5, p. 1, 1950.
47. Nielsen, L.E., Buckdahl, R., Levreault, J., J. Appl. Phys. 31, p. 607, 1950.
48. Leska, J.W., Ind. Eng. Chem. 36, p. 40, 1940.
49. Clash, R.F., Berg, R.M., Symposium on Plastics A.S.T.M., 1944.
50. Wilhout, R.C., and Dole, M., J. Phys. Chem. 57, p. 14, 1953.
51. Ke, B., Sisko, A.W., J. Poly. Sci. 1, p. 87, 1961.
52. O'Neil, M.J., Anal. Chem., 36, p. 1238, 1964.
53. Boyer, R.F., and Spencer, R.S., Advances in Colloid Science II; Interscience Publishers, Inc., New York, pp. 1-55, 1946.
54. Boyer, R.F. Simha, R., J. Chem. Physics 37, p. 1003, 1962.
55. Dannis, M.L., J. Appl. Poly. Sci. 1, p. 121, 1959.
56. Wiley, R.H., and Brauer, G.M., J. Polymer Sci. 3, p. 455, 1948.
57. Fuoss, R., J. Am. Chem. Soc. 61, p.2334, 1939; 63, p. 2401, 2410, 2832, 1941.
58. Davies, J.M., Miller, R.F., and Busse, W.F., J. Am. Chem. Soc. 63, 361, 1941.
59. Corruccini, R.J., and Gniewek, J.J., Natl. Bur. Standards Monogram 29, May 19, 1961.
60. Scott, A.H., J. Res. National Bur. Standards 4, p. 99, 1935.
61. Schallamach, A., Proc. Phys. Soc. London 53, p. 214, 1941.
62. Werner, A.J., ASTM Bull. No. 165, p. 53, 1950.
63. Gordon, M., and Taylor, J.S., J. Appl. Chem. 2, p. 493, 1952.
64. Fox, T.G., and Loshaek, S., Bull. Amer. Phys. Soc. II 1, p. 123, 1956.
65. Mandelkern, L., Martin, G.M., and Quinn, F.A., J. Res. National Bur. Standards 58, p. 137, 1957.
66. Buchdahl, R., and Nielsen, L.C., J. Polymer Sci. 15, p. 1, 1955.



## REFERENCES (cont'd)

67. Deutsch, K., Hoff, E.A.W., and Reddish, W., J. Poly. Sci. 13, p. 565, 1954.
68. Hoff, E.A.W., Robinson, D.W., and Willbourn, A.H., J. Poly. Sci. 18, p. 161, 1955.
69. Muris, L.T., McCrum, N.G., and McGrew, F.C., Soc. Plastics Eng. J. 15, p. 368, 1959.
70. Willbourn, R.H., and Brauer, G.M., J. Poly. Sci. 3, p. 647, 1948.
71. Alfrey, T. Mechanical Behavior of High-Polymers, Interscience Pub., Inc., N.Y., 1946.
72. Boyer, R.F., and Spencer, R.S., J. Appl. Phys. 16, p. 594, 1945.
73. Nielsen, L.E., Mechanical Properties of Polymers, Reinhold Pub. Co., New York, p. 33, 1962.
74. Kline, D.E., Sauer, J.A., Woodward, A.E., J. Poly. Sci. 22, p. 455, 1956.
75. Oakes, W.G., and Robinson, D.W., J. Poly. Sci. 14, 505, 1954.
76. Schmieder, K., and Wolf, K., Kolloid Z. 134, p. 149, 1953.
77. Nielsen, L.E., J. Appl. Phys. 25, p. 1209, 1954.
78. Rempel, R.C., Weaver, A.E., Sands, R.H., and Miller, R.L., J. Appl. Phys. 28, p. 1082, 1957.
79. Swan, P.R., J. Poly. Sci. XLII, p. 525, 1960.
80. Gubler, M.G., and Kovacs, A.J., J. Poly. Sci. 34, p. 551, 1959.
81. Bunn, C.W., Proc. Roy. Soc. A 180, p. 82, 1942.
82. Wunderlich, B., Chem. Phys. 37, p. 1203, 1962.
83. Wunderlich, B., and Dole, M., J. Poly. Sci. XXIV, p. 201, 1957.
84. Inoue, W., J. Poly. Sci. 1, p. 2697, 1963.
85. Nielsen, L.E., J. Appl. Poly. Sci. 2, p. 351, 1959.
86. Raine, H.C., Richards, R.B., Ryder, H., Proc. Roy. Soc. 180, p. 56, 1942.
87. Nielsen, L.E., Soc. Plastics Eng. J. 16, p. 525, 1960.
88. Hunter, E., and Oakes, W.G., Proc. Roy. Soc. (London) A 182, p. 49, 1944
89. Coffman, D.D., Berchet, G.J., Peterson, W.R., Spanagel, P.W., J. Poly. Sci. 2, p. 306, 1947

# REFERENCES (cont'd)

90. Vogelsong, D.C., J. Poly. Sci. Part A, 1, p. 1055, 1963.
91. Schwender, B.F. Zuccarello, R.K., J. Poly. Sci. Part C, Polymer Symposia, No. 6, N.Y., September 1967.
92. McCall, D.M., and Anderson, E.W., J. Chem. Phys. 32, p. 237, 1960.
93. Dole, M., and Wunderlich, B., J. Poly. Sci. 24, p. 139, 1957.
94. Rigby, H.A., and Bunn, C.W., Nature 164, p. 583, 1949.
95. Quinn, F.A., Roberts, D.E., and Work, R.N., J. Appl. Phys. 22, p. 1085, 1951.
96. Furukawa, G.T., McCoskey, R.E., and King, G.J., J. Res. Natl, Bur. Standards 49, p. 273, 1952.
97. Bridgman, P.W., Proc. Am. Acad. Arts Sci. 76, p. 55, 1948.
98. Weir, C.E., J. Res. N.B.S. 50, p. 95, 1953.
99. Bunn, C.W., Nature 174, p. 549, 1954.
100. Marx, P., and Dole, M., J. Amer. Chem. Soc. 77, p. 4771, 1955.
101. Roff, W.J., Fibers, Plastics, and Rubbers, Butterworth, Inc., London, 1956.
102. Starkweather, H.W., and Boyd, R.H., J. Phys. Chem. 64, p. 410, 1960.
103. Siegel, J.C., Muus, L.T., Lin, T.P., and Larsen, H.A., J. Poly. Sci. 2A, p. 391, 1964.
104. Lupton, J.M., 134th Meeting of the Amer. Chem. Soc., Chicago, Sept 1958.
105. Douglas, T.B., and Harman, A.W., J. Res. N.B.S. 69A, p. 149, 1965.
106. Becker, G.W., Kolloid Z. 140, p. 1, 1955
107. Heydeman, P., and Grucking, H.D., Kolloid Zeit. 1, p. 16, 1963.
108. Deutsch, K., Hoff, E.A.W., and Reddish, W., J. Poly. Sci. 13, p. 565, 1954.
109. Koppelman, J., Kolloid Z. 164, p. 31, 1959.
110. Fox, R.B., Isaacs, L.G., and Stokes, S., J. Poly. Sci. Part A, 1, p. 1079, 1963.
111. Cowley, P.R.E., and Melville, H.W., Proc. Roy. Soc. A 210, p. 153, 1955.
112. Ehrenfest, P., Proc. Roy. Acad. 36, p. 153, 1933.
113. Hammer, C.F., Koch, T.A., and Whitney, J.F., J. Appl. Poly. Sci. 1, p. 169, 1959.

## REFERENCES (cont'd)

114. Linton, W.H., and Goodman, G., J. Poly. Sci. 1, p. 179, 1959.
115. Tang, W.K., and Neill, W.K., J. Poly. Sci. Part C, 6, p. 65, 1964.
116. Ke, B., J. Appl. Poly. Sci. VI, p. 624, 1962.
117. Cobbs, W.H., Jr., and Burton, R.L., J. Poly. Sci. 10, p. 275, 1953.
118. Eiermann, K., J. Poly. Sci., Pt. C, 6, p. 157, 1963.
119. Mead, M., D&R Pilot Plants, Inc., Hazardville, Conn., private communication.
120. Wunderlich, B., and Bodily, D.M., J. Poly. Sci. Pt. C, 6, p. 137, 1963.
121. Partington, J.R., An Advanced Treatise on Physical Chemistry of Solids, Longmans, Green & Co., N.Y., p. 155, 1952.
122. Rads Material Property Data, June 6, 1966.
123. Riley, D.P., Proc. Phys. Soc. (London) 57, p. 486, 1945.
124. Dugdale, J.J., Morrison, J.A., Patterson, D., Proc. Roy. Soc. (London) A 224, p. 228, 1954.
125. Nelson, J.B., and Riley, D.P., Proc. Phys. Soc. (London) 57, p. 477, 1945.
126. Entwisle, F., Phys. Letters 2, p. 236, 1962.
127. Kingery, W.D., Proceedings of International Symposium on High Temperature Technology, McGraw-Hill, N.Y., 1960.
128. Magnus, A., Ann. Phys. Lpz. 70, p. 303, 1923.
129. Grüneisen, E., Handbuch der Phys. 10, p. 1, 1926.
130. Mason, W.P., Physical Acoustics and the Properties of Solids, D. Van Nostrand, Inc., New York, 1958.
131. Nix, F.C., and MacNair, D., Phys. Rev. 61, p. 74, 1942.
132. Rubin, T., Johnston, H.L., and Altman, H.W., J. Phys. Chem. 66, p. 266, 1962.
133. Hidnert, P., and Fritzer, H.S., Amer. Inst. of Phys. Handbook, p. 4-51, 1957.
134. Borelius, G., and Johansson, C.H., Ann. Phys. 75, p. 23, 1924.
135. Barron, T.H.K., Ann. of Phys. 1, p. 77, 1957, Phil. Mag. 46, p. 720, 1955.
136. Crawford, F.H., Heat, Thermodynamics and Statistical Physics, Harcourt, Brace and World, Inc., 1963.
137. Rice, M.H., McQueen, R.G., and Walsh, J.M., Solid State Phys. 6, p. 1, 1958.

## REFERENCES (cont'd)

138. Schuele, D.E., and Smith, C.S., J. Phys. Chem. Solids 25, p. 801, 1964.
139. Grüneisen, E., and Goens, E., Physik 29, p. 141, 1924.
140. Ryabinin, Y.N., Rodionov, K.P., and Alekseev, E.S., Sov. Phys. - Tech. Phys. 9, p. 1477, 1965.
141. Ryabinin, Y.N., Rodionov, K.P., and Alekseev, E.S., Phys of Metals and Metallography 10, p. 150, 1960.
142. Lindemann, F.A., Phys. Z. 11, p. 609, 1910.
143. Gilvarry, J.J., Phys. Rev. 102, p. 308, 1956.
144. Bridgman, P.W., Revs. Mod. Phys. 7, p. 1, 1935.
145. Tammann, G., Kristallisieren und Schmelzen (Verlag von J.A. Barth), Leipzig, p. 90, 1903.
146. Schames, L., Ann. Phys. 38, p. 850, 1912; 39, p. 887, 1912.
147. Strong, H.M., Nature 183, p. 1381, 1959.
148. Butuzov, V.P., Sov. Phys.-Crystallography 2, p. 533, 1957.
149. Morgan, D.T., and Overall, J.P., RTD TDR-63-3018.
150. Key, S.W., J. Appl. Phys. 38, p. 2923, 1967.
151. Alexander, J.M., Thermal Stress, edited by Benham, P.P., Hoyle, R., and Ford, H., Pitman and Sons, Ltd., London, 1964, p. 264.
152. Kittel, C., Introduction to Solid State Physics, John Wiley and Sons, Inc., London, 1956.

# DISTRIBUTION

No. cys

## HEADQUARTERS USAF

Hq USAF, Wash, DC 20330

- 1 (AFTAC/TD-3, Capt Herman)
- 1 USAF Dep IG (AFIDI), Norton AFB, Calif 92409
- 1 USAF Dir Nuc Safety (AFINS), Kirtland AFB, NM 87117

## MAJOR AIR COMMANDS

AFSC, Andrews AFB, Wash, DC 20331

- 1 (SCTSW)
- 1 (SCTSE)
- 1 (SCNC)
- 1 AUL (SE)-67-464, Maxwell AFB, Ala 36112
- USAFA, Colo 80840
- 1 (DFLBA)
- 1 (FJSRL, OAR)

## AFSC ORGANIZATIONS

- 1 AFSC STLO, R&T Div, AFUPO, Los Angeles, Calif 90045
- 1 AFSC STLO (RTSAS), Suite 104, 363 S. Taafe Ave, Sunnyvale, Calif 94086
- 1 FTD (TDBTL), Wright-Patterson AFB, Ohio 45433
- 1 AF Materials Lab, Wright-Patterson AFB, Ohio 45433
- 1 AF Avionics Lab, Wright-Patterson AFB, Ohio 45433
- 1 AF Flight Dynamics Lab, Wright-Patterson AFB, Ohio 45433
- 1 ORA (RRRD), Holloman AFB, NM 88330
- 1 SAMSO (SMT), AFUPO, Los Angeles, Calif 90045
- 1 ESD (ESTI), L.G. Hanscom Fld, Bedford, Mass 01730
- 1 APGC (PGBPS-12), Eglin AFB, Fla 32542
- 1 RADC (EMLAL-1), Griffiss AFB, NY 13442
- 1 AFRPL (RPI), Edwards AFB, Calif 93523

## KIRTLAND AFB ORGANIZATIONS

AFSWC, Kirtland AFB, NM 87117

- 1 (SWEH)
- 1 (SWT)

# DISTRIBUTION (cont'd)

## No. cys

AFWL, Kirtland AFB, NM 87117

5 (WLIL)  
1 (WLAW)  
1 (WLDC)  
50 (WLRE)  
10 (WLRP)  
1 (WLX)  
1 (WLF)

## OTHER AIR FORCE AGENCIES

Director, USAF Project RAND, via: AFLO, The RAND Corp, 1700 Main St,  
Santa Monica, Calif 90401

1 (RAND Physics Div)  
1 (RAND Library)  
1 (Dr. O. Nance)  
1 SAAMA (SAW), Dir Spec Weapons, Kelly AFB, Tex 78241  
1 Hq OAR (RROS), 1400 Wilson Blvd, Arlington, Va 22209  
1 AFOSR, 1400 Wilson Blvd, Arlington, Va 22209  
1 AFCLRL, L.G. Hanscom Fld, Bedford, Mass 01731

## ARMY ACTIVITIES

1 Commanding Officer (SMUPA-VC1), Picatinny Arsenal, Dover, NJ 07801  
1 Director, Army Research Office, 3045 Columbia Pike, Arlington, Va 22204  
2 Director, USAERDL (STINFO Br), Ft Belvoir, Va 20260  
1 Commanding General, White Sands Missile Range (Technical Library),  
White Sands, NM 88002

## NAVY ACTIVITIES

1 Commanding Officer, Naval Research Laboratories (ATTN: L.C. Cardinal),  
Wash, DC 20390  
1 Superintendent, US Naval Postgraduate School, (Code 2124, Technical  
Reports), Monterey, Calif 93940  
1 Commanding Officer and Director, Naval Applied Science Laboratory,  
Brooklyn, NY 11251  
Commander, Naval Ordnance Laboratory, White Oak, Silver Spring,  
Md 20910  
1 (Code 730)  
1 (R. W. Warfield, Chemical Research Dept 4-156)

DISTRIBUTION (cont'd)

No. cys

OTHER DOD ACTIVITIES

20 DDC (TIAAS), Cameron Sta, Alexandria, Va 22314

AEC ACTIVITIES

1 USAEC (Library), Rm J-004, Wash, DC 20545  
1 Sandia Corporation (Information Distribution Div), Box 5800,  
Sandia Base, NM 87117  
1 Sandia Corporation (Tech Library), P.O. Box 969, Livermore,  
Calif 94551  
1 Director's Office, University of California Lawrence Radiation  
Laboratory, P.O. Box 808, Livermore, Calif 94551  
1 University of California Lawrence Radiation Laboratory (Technical  
Information Div), Berkeley, Calif 94720  
1 Director, Los Alamos Scientific Laboratory, P.O. Box 1663 (Helen  
Redman, Report Library), Los Alamos, NM 87554  
1 Oak Ridge National Laboratory (Technical Library), Oak Ridge, Tenn 37831  
1 Courant Institute of Mathematical Science, AEC Computing and Applied  
Mathematics Center (Technical Library), 251 Mercer Street, New York,  
NY 10012

OTHER

1 Aerospace Corporation (Acquisitions Group), P.O. Box 95085,  
Los Angeles, Calif 90045  
1 Aerospace Corporation, San Bernardino Operations (A.M. Naqvi),  
P.O. Box 1308, San Bernardino, Calif 92402  
1 Allied Research Associates, Inc., (D.C. Knodel), Virginia Road,  
Concord, Mass 01742  
1 Applied Physics Laboratory, Johns Hopkins University, 8621 Georgia Ave,  
Silver Spring, Md 20910  
1 Avco Missile Systems Division (Research Library), 201 Lowell St,  
Wilmington, Mass 01887  
1 Battelle Memorial Institute, 505 King Avenue, Columbus, Ohio 43201  
1 Gulf General Atomic, Inc., (Library), P.O. Box 608, San Diego,  
Calif 92112  
1 General Atomic Div, General Dynamics Corp (Chief, Tech Info Services),  
P.O. Box 1111, San Diego, Calif 92112  
1 General Electric Co., MSD, Rm M9120 (F.A. Lucy), P.O. Box 8555,  
Philadelphia, Pa 19101  
1 Lockheed Missiles and Space Co., Div Lockheed Aircraft Corporation,  
(Dr. D. Moffatt), 1111 Lockheed Way, Sunnyvale, Calif 94086  
1 Massachusetts Institute of Technology, P.O. Box 73, Lexington, Mass 02173  
1 Princeton University, Forrestal Research Center Library, Aeronautical  
Sciences Bldg, Princeton, NJ 08540

## DISTRIBUTION (cont'd)

No. cys

1 Research Analysis Corporation (M.L. Emerson, Lib), McLean, Va 22101

1 Stanford Research Institute (G-037, External Reports), Menlo Park, Calif 94025

1 TRW, Inc., TRW Systems Group (Technical Library, Acquisitions), One Space Park, Redondo Beach, Calif 90276

2 Librarian, University of Albuquerque, St. Joseph Place, N.W., Albuquerque, New Mexico 87105

1 Mother M. Barbara Ann, O.S.F., Sisters of St. Francis, Mount St. Francis, Box 1060, Colorado Springs, Colo 80901

1 Librarian, St. Francis College, 2701 Spring St., Fort Wayne, Indiana 46808

1 Dr. D. J. Baumann, Creighton University, Chemistry Dept, 2500 California St, Omaha, Nebr 68131

1 Dr. J. L. Walter, C.S.C., Chemistry Dept, University of Notre Dame, Notre Dame, Ind 46556

1 Sr. Celine Martin, O.S.F., St. Francis Convent, Mount Alverno, Mishawaka, Ind 46615

1 Sr. Michael Schafer, S.P., St. Mary of the Woods College, St. Mary of the Woods, Ind 47876

1 Stanford Research Institute, ATTN: Dr. G.R. Abrahamson, Menlo Park, Calif 94025

1 Shock Hydrodynamics, Inc., ATTN: R. Bjork, Sherman Oaks, Calif 91403

1 Union Carbide, ATTN: Dr. Conrad Troulsen, Tarrytown, N.Y. 10591

1 General Motors, ATTN: R. Lingle, Manufacturing Development, 12 Mile and Mound Road, Warren, Mich 48089

1 Aerospace Corporation, ATTN: Dr. Paul Rausch, 1111 Mill St, Room 1120, Bldg. B1. San Bernardino, Calif 92408

1 Aeronutronics, Division of Philco, ATTN: W. Hackler, Ford Road, Research Laboratory, Room 223, Newport Beach, California 92660

1 Lowell Technical Institute, ATTN: Prof. Steve Seradian, Mechanical Engineering Dept, Lowell, Mass 01853

1 Official Record Copy (WLRE/Lt Asay)



This page intentionally left blank.

Unclassified

Security Classification

DOCUMENT CONTROL DATA - R&D		
(Security classification of title, body of abstract and indexing annotation must be entered when the overall report is classified)		
1 ORIGINATING ACTIVITY (Corporate author) Air Force Weapons Laboratory (WLRE) Kirtland Air Force Base, New Mexico		2a REPORT SECURITY CLASSIFICATION Unclassified
		2b GROUP
3 REPORT TITLE ULTRASONIC AND THERMAL STUDIES OF SELECTED PLASTICS, LAMINATED MATERIALS, AND METALS		
4 DESCRIPTIVE NOTES (Type of report and inclusive dates) September 1965 to June 1967		
5 AUTHOR(S) (Last name, first name, initial) Asay, Lt James R.; Urzendowski, Dr. S.R.; Guenther, Dr. Arthur H.		
6 REPORT DATE January 1968	7a TOTAL NO. OF PAGES 266	7b. NO. OF REFS 151
8a. CONTRACT OR GRANT NO. F29(601)-67-C-0042	8a ORIGINATOR'S REPORT NUMBER(S) AFWL-TR-67-91	
b. PROJECT NO. 5710		
c. Subtask 15.018	8b OTHER REPORT NO(S) (Any other numbers that may be assigned this report)	
d.		
10. AVAILABILITY/LIMITATION NOTICES APPROVED FOR PUBLIC RELEASE, DISTRIBUTION UNLIMITED.		
11. SUPPLEMENTARY NOTES	12. SPONSORING MILITARY ACTIVITY AFWL (WLRE) Kirtland AFB, N.M. 87117	
13. ABSTRACT (Distribution Limitation Statement No. 2) Ultrasonic and thermal investigations of several common plastics, nose cone materials, and alloys are presented. The ultrasonic data consist of measurements of the acoustic shear and longitudinal velocities in the frequency range of 1 to 10 MHz and as a function of temperature (to ~ 125°C for most of the plastics and to ~ 250°C for most of the alloys). Some information is presented regarding the dependence of acoustic velocities on uniaxial stress in two aluminum alloys. The temperature dependent ultrasonic data are used to calculate the temperature dependence of the elastic moduli for the materials studied. The thermal analyses describe a differential thermal technique (DTA) used to study the phase transitions and chemical transformations of the reported materials. This approach was used to measure the linear coefficient of expansion and the specific heat at constant pressure over a temperature range of ~ -100 to 200°C for the expansion characteristics, and ~ -100 to 700°C for the specific heat measurements. In addition, heats of fusion are reported. In some cases, the thermal behavior of the reported materials is listed to approximately 1200°C. The thermal and ultrasonic data are combined to calculate the Grüneisen ratio as a function of temperature. The application of ultrasonic and thermal investigations to the determination of the equation of state of solids is also presented. The present study shows that such applications are of significant importance to high pressure equation-of-state determinations. The study also illustrates that many more applications to the equation of state can be obtained through ultrasonic and thermal measurements as a function of hydrostatic pressure.		

DD FORM 1473  
1 JAN 64

Unclassified

Security Classification

14	KEY WORDS	LINK A		LINK B		LINK C	
		ROLE	WT	ROLE	WT	ROLE	WT
	Ultrasonic properties Acoustic sound velocities Elastic properties of solids Equation of state of solids Thermal properties of solids Specific heats of plastics and nonplastics Thermal expansion coefficients for solids DTA studies of plastics						

## INSTRUCTIONS

1. **ORIGINATING ACTIVITY:** Enter the name and address of the contractor, subcontractor, grantee, Department of Defense activity or other organization (*corporate author*) issuing the report.

2a. **REPORT SECURITY CLASSIFICATION:** Enter the overall security classification of the report. Indicate whether "Restricted Data" is included. Marking is to be in accordance with appropriate security regulations.

rectiv  
the gr  
marki  
ized.

1. Enter the report title at optional marking as authorized.

3. **REPORT TITLE:** Enter the complete report title in all capital letters. Titles in all cases should be unclassified. If a meaningful title cannot be selected without classification, show title classification in all capitals in parenthesis immediately following the title.

4. **DESCRIPTIVE NOTES:** If appropriate, enter the type of report, e.g., interim, progress, summary, annual, or final. Give the inclusive dates when a specific reporting period is covered.

5. **AUTHOR(S):** Enter the name(s) of author(s) as shown on or in the report. Enter last name, first name, middle initial. If military, show rank and branch of service. The name of the principal author is an absolute minimum requirement.

6. **REPORT DATE:** Enter the date of the report as day, month, year, or month, year. If more than one date appears on the report, use date of publication.

7a. **TOTAL NUMBER OF PAGES:** The total page count should follow normal pagination procedures, i.e., enter the number of pages containing information.

7b. **NUMBER OF REFERENCES:** Enter the total number of references cited in the report.

8a. **CONTRACT OR GRANT NUMBER:** If appropriate, enter the applicable number of the contract or grant under which the report was written.

8b, 8c, & 8d. **PROJECT NUMBER:** Enter the appropriate military department identification, such as project number, subproject number, system numbers, task number, etc.

9a. **ORIGINATOR'S REPORT NUMBER(S):** Enter the official report number by which the document will be identified and controlled by the originating activity. This number must be unique to this report.

9b. **OTHER REPORT NUMBER(S):** If the report has been assigned any other report numbers (*either by the originator, or by the sponsor*), also enter this number(s).

10. **AVAILABILITY/LIMITATION NOTICES:** Enter any limitations on further dissemination of the report, other than those

imposed by security classification, using standard statements such as:

- (1) "Qualified requesters may obtain copies of this report from DDC."
- (2) "Foreign announcement and dissemination of this report by DDC is not authorized."
- (3) "U. S. Government agencies may obtain copies of this report directly from DDC. Other qualified DDC requesters shall request through \_\_\_\_\_."
- (4) "U. S. military agencies may obtain copies of this report directly from DDC. Other qualified users shall request through \_\_\_\_\_."
- (5) "All distribution of this report is controlled. Qualified DDC users shall request through \_\_\_\_\_."

If the report has been furnished to the Office of Technical Services, Department of Commerce, for sale to the public, indicate this fact and enter the price, if known.

11. **SUPPLEMENTARY NOTES:** Use for additional explanatory notes.

12. **SPONSORING MILITARY ACTIVITY:** Enter the name of the departmental project office or laboratory sponsoring (*paying for*) the research and development. Include address.

13. **ABSTRACT:** Enter an abstract giving a brief and factual summary of the document indicative of the report, even though it may also appear elsewhere in the body of the technical report. If additional space is required, a continuation sheet shall be attached.

It is highly desirable that the abstract of classified reports be unclassified. Each paragraph of the abstract shall end with an indication of the military security classification of the information in the paragraph, represented as (TS), (S), (C), or (U).

There is no limitation on the length of the abstract. However, the suggested length is from 150 to 225 words.

14. **KEY WORDS:** Key words are technically meaningful terms or short phrases that characterize a report and may be used as index entries for cataloging the report. Key words must be selected so that no security classification is required. Identifiers, such as equipment model designation, trade name, military project code name, geographic location, may be used as key words but will be followed by an indication of technical context. The assignment of links, rules, and weights is optional.